

**CFD-Enabled Optimisation for Microfluidic
Heat Transfer Systems**

**Submitted in accordance with the requirements for the degree of Doctor of
Philosophy in Mechanical Engineering**

By

MUYASSAR EDRIS ISMAEEL

The University of Leeds

School of Mechanical Engineering

Institute of ThermoFluids (iTF)

January 2021

The candidate confirms that the work submitted is his own, except where work formed jointly-authored publication has been included. The contribution of the candidate and other authors to this work has been explicitly indicated overleaf. The candidate confirms that appropriate credit has been given within the thesis where reference has been made to the work of others. This copy has been supplied on the understanding that it is copyright material and that no quotation from the thesis may be published without proper acknowledgement.

© 2021 The University of Leeds and Muyassar Edris Ismaeel.

This work is dedicated to:

My Country Iraq,

My beloved parents,

My beloved wife, Saja, and our children Osama,

Anas, and Razan,

My dear brothers and sisters.

Work appearing in Jointly Authored Publications

Peer Reviewed Conference Proceedings and Poster

1. M. Ismaeel, N. Kapur, Z. Khatir and H. Thompson, “Robust Optimisation of Serpentine Fluidic Heat Sinks for High-Density Electronics Cooling”, Proceedings 16th UK Heat Transfer Conference (UKHTC2019), Nottingham, 8-10 Sep. 2019,
2. M. Ismaeel, N. Kapur, Z. Khatir and H. Thompson, “Optimisation Under Uncertainty for a Serpentine Heat Sink”, Poster, School of Mechanical Engineering, University of Leeds, Leeds, UK.

Acknowledgements

In the Name of Allah, the Most Beneficent, the Most Merciful. All the praises and thanks be to Allah, the Lord of 'Alamin.

I would like to thank the Iraqi Ministry of Higher Education and Scientific Research (MOHESR), and the Mechanical Engineering Department, University of Mosul, Iraq for the financial support of this work.

I would like also to express my sincere gratitude to my supervisors, Professor Harvey Thompson, Professor Nikil Kapur and Dr Zinedine Khatir for their advice, supportive guidance and encouraging me to be an independent researcher Throughout my study journey.

I am most thankful to my dear wife, children, and my big family, for their continual support, encouragement and understanding during my study.

Last but not least, I wish to express my gratitude to my friends and colleagues for their support during the years of my study.

Abstract

Rapid developments in the electronics industry have led to an increase in the densities of integrated circuits, therefore, finding effective cooling methods to keep the temperature of the electronic components during operation below their critical temperature has become a necessity. Consequently, the current study aims to enhance and optimise the hydrothermal performance for the serpentine minichannel heat sink. Accordingly, a set of objectives have been proposed, and the CFD methodology has been adopted to achieve this aim. Deterministic and probabilistic optimisation strategies have also been employed to find global and robust designs for the considered heat sink.

To enhance the hydrothermal performance of the serpentine minichannel heat sink with plate fins (*SMCHS – PF*), the effect of the channel width, $1.0 \leq W_c \leq 2.0 \text{ mm}$, and height, $1.0 \leq H_c \leq 3.0 \text{ mm}$, have been investigated. The results showed that the pressure drop (ΔP) and thermal resistance (R_{th}) could be reduced up to, respectively, 94.92% and 10.22% through setting the $W_c = 1.5 \text{ mm}$, $H_c = 3 \text{ mm}$ for mass flow rate (\dot{m}) of 2 g/s . Besides, vortex generators (*VGs*) with different size and arrangements were utilised to enhance the performance of *SMCHS – PF*, and the study exhibited that the existence of the *VGs* enhanced the heat transfer, but this came at the expense of an increase in pressure losses. The performance evaluation criteria (PEC) has also been used to assess the benefit of adding the *VGs*. The study has revealed that the *SMCHS – PF* with vertical in-lined vortex generators (*VIVGs*) design, which abbreviated as *SMCHS – PF – VIVGs*, has a superior performance among the studied designs within the range for the vortex generators generator's radius (r_{VG}). Regarding the optimisation task implemented for the *SMCHS – PF*, the results showed that the robust design could be produced with R_{th} and ΔP higher than those of the global design by 5.7% and 4.3%, respectively.

The current study has also explored the impact of the fin length (F_l) to the secondary channel length (l_{sc}) ratio (R_{FS}), fins offset (F_o) and the number of fins (F_n) on the hydrothermal performance of the microchannel heat sink with chevron fins *SMCHS – CF*. On the one hand, the study revealed that the pressure drop for the *SMCHS – CF*, in comparison to the *SMCHS – PF*, could be reduced by 28% via increasing F_n from 6 to 18 for $l_{sc} = 0.25 \text{ mm}$, but this reduction was not exceeded

10% for $l_{sc} = 1.0 \text{ mm}$ for the same range of F_n . On the other hand, R_{FS} has a small effect on thermal resistance (R_{th}), and the findings show that the maximum reduction in R_{th} was 7%. Furthermore, the results revealed that lowering the R_{FS} from 3 to 1 can reduce the pressure drop by 14%. The probabilistic optimisation results indicated that thermal resistance and pressure drop of the robust design were higher than those of the global optimum design by 8.2% and 43%, respectively. In the current work, hybrid elliptical-rectangular fins have been proposed to replace the chevron fins for the serpentine minichannel heat sink (*SMCHS – EF*). The effect of the fin parameters, i.e. the semi-minor axis (R_f), the number of fins (F_n) and the fin length to the secondary channel length (R_{FS}), on the hydrothermal performance have been explored. Introducing the hybrid fins helped in reducing the overall thermal resistance and pressure drop by 10% and 60% in comparison to those for the *SMCHS – PF*. Besides, increasing R_{FS} from 3 to 13 has led to reducing the R_{th} by 7%, which was accompanied by raising ΔP by 47%.

Table of Contents

Work appearing in Jointly Authored Publications	i
Acknowledgements	ii
Abstract	iii
Table of Contents	v
List of Figures	ix
List of Tables	xv
Nomenclature	xvii
Chapter 1 Introduction	- 1 -
1.1 Background.....	- 1 -
1.2 Thermal Management Technologies.....	- 1 -
1.3 Classification of Cooling Techniques.....	- 2 -
1.4 Emerging Cooling Techniques.....	- 3 -
1.5 Microchannels Classification.....	- 4 -
1.6 Thermo-hydraulic Performance of Microchannel Heat Sinks.....	- 5 -
1.7 Motivation of the current study.....	- 5 -
1.8 Scope of Research.....	- 6 -
1.9 Main contributions (Original contributions of this work).....	- 7 -
1.10 Chapter Summary.....	- 7 -
1.11 Thesis Overview.....	- 8 -
Chapter 2 Literature Review	- 10 -
2.1 Introduction.....	- 10 -
2.2 Single-Phase Microchannel Heat Sinks	- 10 -
2.3 Active Enhancement of Heat Transfer in <i>MCHSs</i>	- 13 -
2.3.1 Forced Convection	- 13 -
2.3.2 Nanofluid Technology	- 14 -
2.4 Passive Enhancement of Heat Transfer in <i>MCHSs</i>	- 14 -
2.4.1 The effect of Coolant Type	- 16 -
2.4.2 Effect of substrate thickness and structural material.....	- 17 -
2.4.3 Double layers (Multi-layers Heat Sink)	- 18 -
2.4.4 Flow Passages Filled with Porous Materials	- 19 -
2.4.5 Effect of the Geometry of the Heat Sink Microchannel.....	- 20 -
2.4.6 Vortex generators (Turbulators)	- 23 -
2.5 Serpentine Microchannel Heat Sinks.....	- 27 -
2.6 Optimisation of Microchannel Heat Sinks.....	- 34 -
2.6.1 Deterministic Optimisation of Microchannel Heat Sinks.....	- 34 -
2.6.2 Robust Design.....	- 38 -
2.7 Gaps in knowledge and the aims of the current research.....	- 44 -
Chapter 3 Heat Transfer and Fluid Flow Fundamentals	- 46 -
3.1 Introduction.....	- 46 -
3.2 Heat Transfer Basics.....	- 46 -

3.3	Fluid Flow Basics	- 48 -
3.4	Boundary layer concept	- 49 -
3.4.1	Hydrodynamic boundary layer	- 50 -
3.4.2	Thermal boundary layers.....	- 50 -
3.4.3	Significance of the Prandtl Number	- 52 -
3.5	Flow Entrance Region Characteristics	- 53 -
3.6	Conjugate Heat Transfer Problems.....	- 55 -
3.7	Governing Equations for microchannel heat sinks	- 56 -
3.8	Assumptions and Boundary Conditions	- 57 -
3.9	Chapter Summary.....	- 58 -
Chapter 4 Computational and Optimisation Methodologies		- 59 -
4.1	Introduction.....	- 59 -
4.2	Computational Fluid Dynamics (CFD) Methods	- 59 -
4.2.1	Pre- processing.....	- 59 -
4.2.2	Processing.....	- 60 -
4.2.3	Post-processing.....	- 61 -
4.3	Formulation of Optimisation Problems	- 61 -
4.4	Classification of Optimisation Problems.....	- 62 -
4.5	Optimisation Algorithms	- 63 -
4.5.1	Derivative Based Optimisation Methods	- 63 -
4.5.2	Derivative Free Based Optimisation Methods	- 64 -
4.5.3	Optimisation software Used.....	- 65 -
4.5.4	Surrogate-Based Optimisation.....	- 65 -
4.5.5	Design of Experiments (DoE):.....	- 66 -
4.5.6	Monte Carlo Sampling Method.....	- 67 -
4.5.7	Latin Hypercube Sampling Method.....	- 67 -
4.5.8	Surrogate Model: Gaussian Process (GP).....	- 68 -
4.5.9	Surrogate Model Validation: Efficiency and Accuracy	- 69 -
4.6	Robust Optimisation.....	- 70 -
4.6.1	Random Variables	- 70 -
4.6.2	Uncertainty Quantification	- 71 -
4.6.3	Monte Carlo Simulations (<i>MCS</i>).....	- 72 -
4.6.4	Optimisation under uncertainty.....	- 72 -
4.7	Chapter Summary.....	- 73 -
Chapter 5 CFD-enabled Optimisation of the Serpentine Minichannel Heat Sinks		- 75 -
5.1	Introduction.....	- 75 -
5.2	CFD Simulation Setup:	- 75 -
5.2.1	Geometry description and boundary Conditions	- 75 -
5.2.2	Mesh Independency Test	- 77 -
5.2.3	Validation of the Numerical Simulation Model.....	- 78 -
5.3	Effect of Channel Width and Channel Depth.....	- 80 -
5.4	Effect of Vortex Generators.....	- 85 -

5.4.1	Vertical Transverse Vortex Generators Attached to the Sidewalls.....	- 87 -
5.4.2	Horizontal Transverse Vortex Generators Attached to the Channel Base.....	- 94 -
5.5	Deterministic Optimisation of the Serpentine Minichannel Heat Sinks.....	- 102 -
5.5.1	Single-Objective Deterministic Optimisation.....	- 102 -
5.5.2	Multi-Objective Functions Deterministic Optimisation	- 105 -
5.6	Deterministic Optimisation of SMCHS – PF – VGS	- 107 -
5.6.1	Single-objective Optimisation for SMHS – PF – VSVGs and SMHS – PF – HVGs	- 107 -
5.6.2	Multi-objective optimisation for SMHS – PF – VSVGs and SMHS – PF – HVGs	- 114 -
5.7	Optimisation under Uncertainty for SMCHS – PF	- 117 -
5.7.1	Uncertainty Quantification for the Performance of SMCHS – PF	- 117 -
5.7.2	Single-Objective Optimisation for $\sigma_{R_{th}}$ and $\sigma_{\Delta P}$	- 120 -
5.7.3	Multi-Objective Function Optimisation for $\mu_{R_{th}}$, $\sigma_{R_{th}}$, $\mu_{\Delta P}$ and $\sigma_{\Delta P}$	- 122 -
5.8	Chapter Summary.....	- 127 -
Chapter 6 Effect of Chevron Fins on the Performance of Serpentine Minichannel Heat Sinks		- 129 -
6.1	Introduction.....	- 129 -
6.2	CFD Analysis of the SMCHS – CF	- 129 -
6.2.1	CFD Modelling	- 129 -
6.2.2	Mesh Independence tests and Validation	- 131 -
6.3	Characteristics of Fluid Flow and Heat Transfer.....	- 135 -
6.3.1	Effect of Number of Fins (F_n).....	- 135 -
6.3.2	Effect of Fins Offset (F_o).....	- 142 -
6.3.3	Effect of Fin Length to Secondary Channel Length Ratio (R_{FS}).....	- 146 -
6.4	Deterministic and Probabilistic Optimisation for MCHSs with Chevron Fins.....	- 151 -
6.4.1	Deterministic Single-Objective Optimisation.....	- 152 -
6.4.2	Deterministic Multi-Objective Optimisation for SMHS – CF -	160 -
6.4.3	Probabilistic Optimisation for Minichannels Heat sink with Chevron Fins (SMCHS – CF)	- 163 -
6.5	Chapter Summary.....	172
Chapter 7 Serpentine Minichannel Heat Sink with Hybrid Elliptical-Rectangular Fins.....		- 174 -
7.1	Introduction.....	- 174 -
7.2	CFD Analysis of the SMCHSs with Hybrid Elliptical-Rectangular Fins	- 174 -
7.2.1	CFD Modelling	- 174 -
7.2.2	Mesh Independency and Validation	- 176 -

7.3	Influence of Introducing Hybrid Elliptical-Rectangular Fins in SMCHSs	- 179 -
7.4	The Benefit of using Hybrid Elliptical-Rectangular Shape Fins with SMCHSs	- 180 -
7.5	Characteristics of Fluid Flow and Heat Transfer	- 182 -
7.5.1	Effect of the semi-minor axis (R_f) of the hybrid fin	- 182 -
7.5.2	Effect of Number of Fins (F_n)	- 184 -
7.5.3	Effect of Fin Length to Secondary Channel Length Ratio (R_{FS})	- 185 -
7.6	Deterministic Optimisation for the SMCHS – EF	- 187 -
7.6.1	Single-Objective Optimisation	- 187 -
7.6.2	Multi-Objective Optimisation	- 195 -
7.7	Chapter Summary	- 197 -
Chapter 8 Conclusions and Future Works		- 199 -
8.1	Introduction	- 199 -
8.2	Conclusions	- 199 -
8.2.1	Minichannel Geometrical Parameters of the SMHS – PF	- 199 -
8.2.2	Vortex generators	- 200 -
8.2.3	Fin Parameters of the SMCHS – CF	- 200 -
8.2.4	Fin Parameters of the SMCHS – EF	- 201 -
8.3	Recommendations for Future Works	- 202 -
REFERENCES		- 203 -

List of Figures

Fig. 1-1 Structure of the current thesis.	- 9 -
Fig. 2-1 The geometry of the straight microchannel heat sink with a magnifying view.	- 11 -
Fig. 2-2 Schematic diagram of the heat sink showing (a) the involved heat transfer modes and (b) the thermal resistance network.	- 15 -
Fig. 2-3 Schematic diagram of the designed double-layered microchannels heat sink proposed by Vafai and Zhu, 1999.	- 19 -
Fig. 2-4 Schematic of microchannel heat sink with different channel shapes investigated by Gunnasegaran <i>et al.</i> (2010).	- 21 -
Fig. 2-5 Schematic of wavy microchannels (a) characteristic dimensions and (b) change in relative wavy amplitude along the flow direction of the novel designs: i) constant wavy amplitude, ii) increased relative wavy amplitude, and iii) locally higher at high heat flux regions wave amplitude (Reproduced from Sui <i>et al.</i> , (2010) with permission).	- 22 -
Fig. 2-6 Schematic of the heat sink with serpentine channel: (a) top view, (b) side view, and (c) isometric view (Reproduced from Li <i>et al.</i> , 2013 with permission).	- 29 -
Fig. 2-7 Different minichannel heat sinks studied by Al-Neama <i>et al.</i> (2017): (a) <i>SRMs</i> and (b) <i>SPSMs</i> , <i>DPSMs</i> and <i>TPSMs</i> (Reproduced with permission).	- 30 -
Fig. 2-8 Geometries investigated by Al-Neama <i>et al.</i> (2018): serpentine rectangular with plate fins, <i>SMCHS – PF</i> (left), and serpentine rectangular with chevron fins, <i>SMCHS – CF</i> (Right) (Reproduced with permission).	- 31 -
Fig. 2-9 The four configurations of the serpentine microchannel heat sinks studied by Imran <i>et al.</i> (2018) (Reproduced with permission).	- 32 -
Fig. 2-10 Half domain of the micro pin-fins heat sink with: (a) circular, (b) symmetric airfoil, and (c) symmetric convex cross sections (Reproduced from Reddy <i>et al.</i> (2017) with permission).	- 35 -
Fig. 2-11 Schematic diagram of the microchannel heat sink (a) 3D full geometry (b) computational domain and (c) top view of the computational domain (Reproduced from Shi <i>et al.</i> (2019)) with permission).	- 37 -
Fig. 2-12: Comparison between robust and reliable design concepts in terms of PDF.	- 39 -
Fig. 3-1. Schematic of typical boundary layer (a) external flow and (b) internal flow.	- 50 -
Fig. 3-2. Thermal boundary layer of cold flow: (a) over flat plate and (b) inside pipe.	- 51 -
Fig. 3-3. Conjugate boundary conditions between the solid and fluid.	- 55 -
Fig. 4-1 Latin hypercube sampling (a) Five samples (b) Ten samples.	- 67 -
Fig. 4-2 Schematic for the concept of the: global optimal design (point A) and robust design (point B).	- 71 -
Fig. 5-1 Geometrical model: (a) 3-D geometry, (b) top view and (c) side view.	- 76 -
Fig. 5-2 Mesh techniques for the mesh independency study: (a) hybrid mesh and (b) unstructured mesh.	- 78 -

Fig. 5-3 Comparison of the present work against the work of Al-Neama (2018): (a) R_{th} and (b) ΔP	- 80 -
Fig. 5-4 The variation in (a) thermal resistance and (b) pressure drop due to change in channel width for different mass flow rate and $H_c = 2\text{ mm}$	- 82 -
Fig. 5-5 The variation in (a) thermal resistance and (b) pressure drop due to change in channel depth for different mass flow rate and $W_c = 1.5\text{ mm}$	- 83 -
Fig. 5-6 Velocity vectors at the middle of the minichannels, i.e. $z = 0.5H_c$ and the middle of the first channel for: (a) $H_c = 1.25\text{ mm}$ and (b) $H_c = 3.0\text{ mm}$ both at $W_c = 1.5\text{ mm}$ and $m = 1.25\text{ g/s}$	- 84 -
Fig. 5-7 Velocity vectors at the middle of the minichannels, i.e. $z = 0.5H_c$ for: (a) $W_c = 1.0\text{ mm}$ and (b) $W_c = 2.0\text{ mm}$ both at $H_c = 2.0\text{ mm}$ and $m = 1.25\text{ g/s}$	- 85 -
Fig. 5-8 Serpentine minichannel heat sink equipped with vertical traverse vortex generators: (a) 3D view showing the VGs , (b) top view with an enlarged view $SMCHS - PF - VSVGs$ and (c) top view with an enlarged view for $SMCHS - PF - VIVGs$	- 89 -
Fig. 5-9 Effect of Reynolds number on: (a) R_{th} , (b) ΔP and (c) PEC for $SMCHS -$ $PF - VSVGs$	- 90 -
Fig. 5-10 Effect of Reynolds number on: (a) R_{th} , (b) ΔP and (c) PEC for $SMCHS -$ $PF - VIVGs$	- 91 -
Fig. 5-11 Velocity vectors in the $xy -$ plane at $z = 3\text{ mm}$, for staggered $VVGs$ at $Re = 1750$ with: (a) smooth channel (b) $r_{VG} = 1.5\text{ mm}$ and (c) $r_{VG} = 3.0\text{ mm}$	- 93 -
Fig. 5-12 Velocity field in the $yz -$ plane at $z = 3.75\text{ mm}$, for in-lined $VVGs$ at $Re = 1750$ with: (a) $r_{VG} = 1.5\text{ mm}$ and (b) $r_{VG} = 3.0\text{ mm}$	- 94 -
Fig. 5-13 Serpentine minichannel heat sink equipped with horizontal traverse vortex generators at the base of the minichannels ($SMCHS - PF - HVG$): (a) 3D view showing the channel base with $HVGs$, (b) side view of the channel and (c) top view with an enlarged view for the $HVGs$	- 95 -
Fig. 5-14 Effect of Reynolds number on: (a) thermal resistance, (b) pressure drop and (c) PEC for $SMCHS - PF - HVG$	- 96 -
Fig. 5-15 Temperature distribution in the $yz -$ plane at $x = 7.75\text{ mm}$ and at $Re = 1000$ for: (a) smooth serpentine and $HVGs$ with (b) $r_{VG} = 0.1\text{ mm}$ and (c) $r_{VG} = 0.25\text{ mm}$	- 98 -
Fig. 5-16 Velocity vectors in the $yz -$ plane at $x = 7.75\text{ mm}$ and at $Re = 1000$ for: (a) smooth serpentine and $HVGs$ with (b) $r_{VG} = 0.1\text{ mm}$ and (c) $r_{VG} = 0.25\text{ mm}$	- 99 -
Fig. 5-17 Vortical structures in the $xz -$ plane at different y values and at $Re = 1000$ for: (a) smooth serpentine and $HVGs$ with (b) $r_{VG} = 0.2\text{ mm}$ and (c) $r_{VG} = 0.3\text{ mm}$	- 100 -
Fig. 5-18 Temperature distribution in the $xy -$ plane at $z = 2.05\text{ mm}$, and at $Re = 1000$ for: (a) smooth serpentine and $HVGs$ with (b) $r_{VG} = 0.2\text{ mm}$ and (c) $r_{VG} = 0.3\text{ mm}$	- 101 -
Fig. 5-19 Design of experiments and validation points used to build the surrogate model for the $SMCHS - PF$ design.....	- 103 -

Fig. 5-20	Surrogate model for the performance criteria of <i>SMCHS – PF</i> design: (a) R_{th} and (b) ΔP . The red points are the training points, while the black (Labeled as CP _i) points are the validation points.....	- 104 -
Fig. 5-21	Pareto front for the pressure drop and thermal resistance of the <i>SMCHS – PF</i>	- 106 -
Fig. 5-22	Design of experiments and validation points used to build the surrogate model for the: (a) <i>SMCHS – PF – VSVGs</i> and (b) <i>SMCHS – PF – HVGs</i> designs.	- 109 -
Fig. 5-23	Surrogate model for the performance criteria of <i>SMCHS – PF – VSVGs</i> design: (a) R_{th} , (b) ΔP and (c) PEC.....	- 111 -
Fig. 5-24	Surrogate model for the performance criteria <i>SMCHS – PF – HVGs</i> design: (a) R_{th} , (b) ΔP and (c) PEC.....	- 112 -
Fig. 5-25	Pareto front for the pressure drop and thermal resistance: (a) <i>SMCHS – PF – VSVGs</i> and (b) <i>SMCHS – PF – HVGs</i>	- 115 -
Fig. 5-26	(a) the mean and (b) the Std Dev of R_{th} and ΔP as a function of the number of samples N_s	- 118 -
Fig. 5-27	Surrogate model for the Std Dev of (a) the thermal resistance ($\sigma_{R_{th}}$) and (b) the pressure drop ($\sigma_{\Delta P}$) with the DoE points and the optimum at min σ as a function of the two design variables, W_c and H_c	- 119 -
Fig. 5-28	(a) thermal resistance and (b) pressure drop surrogate model showing the global minimum (red point) and the robust design at the minimum σ (green point).....	- 121 -
Fig. 5-29	(a) Pareto front and (b) surrogate model of R_{th} showing the global minimum (red point) and the robust design at the minimum σ (green points).	- 123 -
Fig. 5-30	(a) Pareto front and (b) surrogate model of ΔP showing the global minimum (red point) and the robust design at the minimum σ (green points).	- 124 -
Fig. 5-31	Pareto front for the $f_{R_{th}}$ and $f_{\Delta P}$	- 126 -
Fig. 5-32	Surrogate models for (a) thermal resistance and (b) pressure drop showing the global minimum (green point) and the three selected points from Pareto front.	- 126 -
Fig. 6-1	Geometry of the serpentine microchannels heatsink with secondary channels: (a) 3D view, (b) side view, (c) top view showing the main dimensions and (d) detailed fin dimensions (Reproduced from Al-Neama <i>et al.</i> (2018)with permission).....	- 130 -
Fig. 6-2	Mesh quality of the <i>SMCHS – CF</i> used in the mesh sensitivity test: (a) full meshed geometry and (b) magnifying view for a part of the meshed geometry.	- 132 -
Fig. 6-3	Validation of the present work against previous study for serpentine minichannel heat sink with chevron fins, (Al-Neama , 2018).	- 134 -
Fig. 6-4	Influence of the number of fins on Pressure drop (ΔP) at Reynolds number $Re = 1500$ for different secondary channel length.....	- 135 -
Fig. 6-5	Influence of the number of fins on thermal resistance (R_{th}) at $Re =1500$ for different secondary channel lengths.	- 137 -

Fig. 6-6	Temperature distribution (K) at the mid-depth plane of the channel ($Z = 0.5 H_c$) for: (a) $F_n = 6$ & $l_{sc} = 1.0$ mm, (b) $F_n = 6$ & $l_{sc} = 0.25$ mm, (c) $F_n = 18$ & $l_{sc} = 1.0$ mm, and (d) $F_n = 18$ & $l_{sc} = 0.25$ mm.	138 -
Fig. 6-7	Velocity distribution (m/s) at the mid-depth plane of the channel ($Z = 0.5 H_c$) for: (a) $F_n = 6$ & $l_{sc} = 1.0$ mm, (b) $F_n = 6$ & $l_{sc} = 0.25$ mm, (c) $F_n = 18$ & $l_{sc} = 1.0$ mm, and (d) $F_n = 18$ & $l_{sc} = 0.25$ mm.	139 -
Fig. 6-8	Influence of the Reynolds number on overall thermal resistance for different numbers of fins with: (a) $l_{sc} = 0.25$ mm, and (b) $l_{sc} = 0.75$ mm.	140 -
Fig. 6-9	Influence of Reynolds number on pressure losses for different numbers of fins with: (a) $l_{sc} = 0.25$ mm, and (b) $l_{sc} = 0.75$ mm.	141 -
Fig. 6-10	Geometry of the CFD model: (a) Top view, (b) magnifying view for fins without offset and (c) magnifying view showing the fins offset variable, F_o [mm].	143 -
Fig. 6-11	Influence of fin offset on: (a) thermal resistance and (b) pressure losses for different values of Reynolds number.	144 -
Fig. 6-12	Influence of Reynolds number on: (a) thermal resistance and (b) pressure losses for different values of fin offset.	145 -
Fig. 6-13	Velocity distribution for: (a) $F_o = 0$ and (b) $F_o = 2.0$ [mm].	145 -
Fig. 6-14	Magnifying view illustrating the fin length to the secondary channel length ratio $R_{FS} = \frac{F_l}{l_{sc}}$ for: (a) $R_{FS} = 0.5$ and (b) $R_{FS} = 5.0$	147 -
Fig. 6-15	(a) A single minichannel cell with its secondary microchannels and (b) percentage of the mass flow rate at the corresponding channels for different R_{FS} and $Re = 1500$	147 -
Fig. 6-16	Influence of the fin length to secondary channel length ratio on: (a) Thermal resistance, (R_{th}) and (b) Pressure drop (ΔP).	149 -
Fig. 6-17	Influence of the fin length ratio, R_{FS} , and numbers of fins F_n on: (a) the overall thermal resistance and (b) the pressure drop penalty.	150 -
Fig. 6-18	The geometry of the <i>SMCHS – CF</i> with $F_n = 6$ and $R_{FS} = 1$	151 -
Fig. 6-19	Design of experiments points (red points) used to build the metamodel and validation points (black points) for the <i>SMCHS – CF</i> with W_c , l_{sc} and θ as design variables.	153 -
Fig. 6-20	Metamodel for the thermal resistance (R_{th}) as a function of two design variables, W_c and l_{sc} , at $\theta = 20.04$ at which the minimum thermal resistance happen.	155 -
Fig. 6-21	Metamodel for the pressure drop (ΔP) as a function of two design variables, W_c and l_{sc} , at $\theta = 34.75$ at which the minimum pressure drop take place.	155 -
Fig. 6-22	Geometries for the optimum design of the <i>SMCHS – CF</i> with W_c , l_{sc} and θ as design variables obtained with <i>soga</i> for: (a) minimum thermal resistance and (b) minimum pressure drop.	156 -
Fig. 6-23	Design of experiments points (red points) used to build the metamodel and validation points (black points) for the <i>SMCHS – CF</i> with F_n , F_o and R_{FS} as design variables.	157 -
Fig. 6-24	Metamodel for the thermal resistance (R_{th}) as a function of the two design variables, F_o and R_{FS} , at $F_n = 17$ at which the minimum thermal resistance occurs.	159 -

Fig. 6-25 Metamodel for the pressure drop (ΔP) as a function of the two design variables, F_o and R_{FS} , at $F_n = 5$ at which the minimum pressure drop occurs.	- 159 -
Fig. 6-26 Geometries for the optimum design of the <i>SMCHS – CF</i> with F_n , F_o and R_{FS} as design variables obtained with <i>soga</i> for: (a) minimum thermal resistance and (b) minimum pressure drop.	- 160 -
Fig. 6-27 Pareto front for the pressure drop and thermal resistance of the <i>SMCHS – CF</i> with W_c , l_{sc} and θ as design variables.....	- 161 -
Fig. 6-28 Pareto front for the pressure drop and thermal resistance of the <i>SMCHS – CF</i> with R_{FS} , F_o and F_n as design variables.....	- 163 -
Fig. 6-29 (a) the mean μ and (b) the Std Dev σ of R_{th} and ΔP as a function of the number of samples N_s	- 164 -
Fig. 6-30 Surrogate models for the Standard deviations as a function of W_c , l_{sc} and θ_{opt} for: (a) the thermal resistance ($\sigma_{R_{th}}$) and (b) the pressure drop ($\sigma_{\Delta P}$).	- 165 -
Fig. 6-31 Pareto front for the $\mu_{R_{th}}$ and $\sigma_{R_{th}}$ for the <i>SMCHS – CF</i>	169
Fig. 6-32 Pareto front for $\mu_{\Delta P}$ and $\sigma_{\Delta P}$ for the <i>SMCHS – CF</i>	170
Fig. 6-33. Pareto front for $f_{\Delta P}$ and $f_{R_{th}}$ of the <i>SMCHS – CF</i>	172
Fig. 7-1 Geometry of the serpentine minichannels heatsink provided with hybrid elliptical-rectangular fins (<i>SMCHS – EF</i>): (a) 3D view, (b) side view and (c) Top view showing the related dimensions.	- 175 -
Fig. 7-2 Mesh quality of the <i>SMCHS – EF</i> used in the mesh sensitivity test: (a) full meshed geometry and (b) magnifying view for a part of the meshed geometry.	- 177 -
Fig. 7-3 Comparison between the serpentine minichannel heat sink with plate fin, <i>SMCHS – PF</i> , (Al-Neama , 2018) and the one with hybrid elliptical-rectangular fins, <i>SMCHS – EF</i> : (a) R_{th} and (b) ΔP	- 179 -
Fig. 7-4 Comparison between <i>SMCHS – PF</i> (Al-Neama , 2018) and <i>SMCHS – EF</i> : (a) R_{th} and (b) ΔP	- 181 -
Fig. 7-5 Selected fins used with the <i>SMCHS – EF</i> showing the difference in fin tips for: (a) $R_f = 0.2 \text{ mm}$, (b) $R_f = 0.35 \text{ mm}$ and (c) $R_f = 0.5 \text{ mm}$	- 182 -
Fig. 7-6 The relationship between (a) R_{th} and (b) ΔP , and the Reynolds number (Re) for different values of the semi-minor axis, R_f , for the <i>SMCHS – EF</i>	- 183 -
Fig. 7-7 Effect of Re and F_n on: (a) R_{th} and (b) ΔP for the <i>SMCHS – EF</i>	- 184 -
Fig. 7-8 The effect of fin length ratio (R_{FS}) on: (a) the overall thermal resistance, R_{th} and (b) pressure drop, ΔP at different values of Re for the <i>SMCHS – EF</i>	- 186 -
Fig. 7-9 Comparison between designs with different R_{FS} showing the secondary channel length (l_{sc}) for: (a) $R_{FS} = 3$ and (b) $R_{FS} = 13$	- 187 -
Fig. 7-10 3D scatter plots for the DoE points used to build the surrogate models for the responses of the <i>SMCHS – EF</i> with F_o , F_n , R_f and R_{FS} as design variables visualised in: (a) F_o , R_f and R_{FS} planes and (b) F_n , R_f and R_{FS} planes.....	- 189 -
Fig. 7-11 Single-objective optimisation for R_{th} of the <i>SMCHS – EF</i> as a function of: (a) F_o and R_f and (b) F_n and R_{FS} as design variables.	- 191 -

- Fig. 7-12 Single-objective optimisation for R_{th} of the *SMCHS – EF* as a function of:
 (a) R_{FS} and R_f and (b) R_{FS} and F_o as design variables..... - 192 -
- Fig. 7-13 Single-objective optimisation for ΔP of the *SMCHS – EF* as a function of:
 (a) R_{FS} and R_f and (b) F_o and R_{FS} as design variables..... - 193 -
- Fig. 7-14 Single-objective optimisation for R_{FS} as design variables..... - 194 -
- Fig. 7-15 Geometries for the optimum design of the *SMCHS – EF* with F_o , F_n , R_f and R_{FS} as design variables obtained using *soga* for: (a) minimum thermal resistance and (b) minimum pressure drop. - 195 -
- Fig. 7-16 Pareto front for the pressure drop and thermal resistance of the *SMCHS – EF* with F_o , F_n , R_f and R_{FS} as design variables..... - 196 -

List of Tables

Table 1-1 Classification of channels adopted from (Dixit and Ghosh, 2015)...	4 -
Table 3-1 Types of hydrodynamic and thermal boundary layers developments in duct flow (Rohsenow <i>et al.</i> , 1998).....	53 -
Table 5-1 Mesh dependence test for the serpentine microchannels heat sink.	79 -
Table 5-2 Comparison of the responses evaluated by the CFD simulation and the approximation surrogate model (cross-validation).....	105 -
Table 5-3 Global surrogate-based single-objective optimisation results for the thermal resistance and pressure drop.....	105 -
Table 5-4 Validation of the metamodeling method for the <i>SMCHS – PF</i>	107 -
Table 5-5 Surrogate model validation for the <i>SMCHS – PF – VSVGs</i> design	110 -
Table 5-6 Surrogate model validation for the <i>SMCHS – PF – HVGs</i> design.-	110 -
Table 5-7 Global surrogate-based single-objective optimisation results for R_{th} , ΔP and PEC of the <i>SMCHS – PF – VSVGs</i> design.....	113-
Table 5-8 Global surrogate-based single-objective optimisation results for R_{th} , ΔP and PEC of the <i>SMCHS – PF – HVGs</i> design.....	113 -
Table 5-9 Performance of the <i>SMCHS – PF – VSVGs</i> for the selected optimum designs located on the Pareto front, P ₁ to P ₅ as shown in Fig. 5 22.-	116 -
Table 5-10 Performance of the <i>SMCHS – PF – HVGs</i> for the selected optimum designs located on the Pareto front, HP ₁ to HP ₅ as shown in Fig. 5-25.	116 -
Table 5-11 The uncertainty associated with the input design variables.....	117 -
Table 5-12 Surrogate-based single-objective optimisation results for $\sigma_{R_{th}}$ and $\sigma_{\Delta P}$	120 -
Table 5-13 Comparison between the global optimum and the robust optimum for the thermal resistance and pressure drop evaluated at $(W_c)_{Robust}$ and $(H_c)_{Robust}$	121 -
Table 6-1 Boundary and operating conditions for mesh dependence analysis.	131 -
Table 6-2 Results of the mesh independency study.....	133 -
Table 6-3 Comparison of the responses evaluated by the CFD simulation and the approximation surrogate model (cross-validation).....	154 -
Table 6-4 Surrogate-based single-objective optimisation results for the thermal resistance and pressure drop of the <i>SMCHS – CF</i> with W_c , l_{sc} and θ as design variables.....	154 -
Table 6-5 Comparison of the responses evaluated by the CFD simulation and the approximation surrogate model (cross-validation).....	158 -
Table 6-6 Surrogate-based single-objective optimisation results for the thermal resistance and pressure drop of the <i>SMCHS – CF</i> with F_n , F_o and R_{FS} as design variables.....	158 -
Table 6-7 Validation of the Pareto front results for the <i>SMCHS – CF</i> . -	161 -
Table 6-8 Validation of the Pareto front results for the <i>SMCHS – CF</i> with R_{FS} , F_o and F_n as design variables.	162 -

Table 6-9	The uncertainty associated with the input design variables.....	- 164 -
Table 6-10	Surrogate-based single-objective optimisation results for the standard deviations of the R_{th} and ΔP for the <i>SMCHS – CF</i> with W_c, l_{sc} and θ as design variables.....	167
Table 6-11	Comparison between the single-objective deterministic global optimum design with the three selected point from the Pareto front results for thermal resistance of the <i>SMCHS – CF</i>	169
Table 6-12	Comparison between the single-objective deterministic global optimum design with the three selected point from the Pareto front results for pressure drop of the <i>SMCHS – CF</i>	170
Table 6-13	Comparison between the multi-objective deterministic optimum designs with their corresponding designs from the Pareto front results for $f_{\Delta P}$ and $f_{R_{th}}$ of the <i>SMCHS – CF</i>	172
Table 7-1	Detailed dimensions of the minichannel heat sink with hybrid elliptical-rectangular fins (<i>SMCHS – EF</i>). These dimensions were selected to be comparable to those heat sinks studied in the previous chapters.-	175 -
Table 7-2	Results of the mesh independency study.....	- 178 -
Table 7-3	Comparison of the responses evaluated by the CFD simulation and the approximation surrogate model for cross-validation.....	- 188 -
Table 7-4	Surrogate-based single-objective optimisation results for R_{th} and ΔP of the <i>SMCHS – EF</i> with F_o, F_n, R_f and R_{FS} as design variables....	- 190 -
Table 7-5	Validation of the Pareto front results for the <i>SMCHS – EF</i> with F_o, F_n, R_f and R_{FS} as design variables.....	- 197 -

Nomenclature

Symbol	Quantity	SI Unit
A	Area	m^2
D	Diameter, Characteristics length	m
h	Heat transfer coefficient	$W/(m^2 \cdot K)$
H	Height	m
k	Thermal conductivity	$W/(m \cdot K)$
L	Length	m
N_s	number of samples	
P	Pressure drop, wetted perimeter	Pa, m
\mathcal{P}	Pumping power	W
q	Generated heat	W
Q	Volumetric flow rate	m^3/s
\dot{Q}	Rate heat transfer	W
R	Resistance	K/W
t	Thickness	m
T	Temperature	K or $^{\circ}C$
V	Velocity	m/s
W	Width	m
w	velocity component in z-direction	m/s
x	x-direction	m
y	y-direction	m
z	z-direction	m
Greek symbols		
θ	Oblique angle of the fins	degree
μ	Dynamic viscosity, the statistical mean	$kg/m \cdot s$
ρ	Density	kg/m^3
ν	Kinematic viscosity	m^2/s
σ	The standard deviation	
λ	Free path length	m
Δ	Difference	

Non-dimensional Numbers

Kn	Knudsen number, λ/L_{char}
Pr	Prandtl number, $c_p\mu/k$
Re	Reynolds number, $4\dot{m}/\mu P_{er}$
Nu	Nusselt number, $h L/k$

Subscripts and superscripts

b	Base
c	Characteristics, cross-sectional, critical
ch	Channel
$cond$	Conduction
$conv$	Convection
eff	Effective
h	Hydraulic
max	Maximum
min	Minimum
in	Inlet
ou	Outlet
s	Solid, Surface, Heat sink, sample
cTM	Case-to-thermal material
jc	Junction-to-case
TMs	Thermal material-to-heat sink
sf	Heat sink-to-cooling fluid
th	Thermal
w	Wall

Abbreviations

$SMCHS - PF$	Serpentine minichannel heat sink with plate fins
$SMCHS - PF - HVGs$	$SMCHS - PF$ with vertical horizontal vortex generators
$SMCHS - PF - VIVGs$	$SMCHS - PF$ with vertical in-lined vortex generators
$SMCHS - PF - VSVGs$	$SMCHS - PF$ with vertical staggered vortex generators
$SMCHS - CF$	Serpentine microchannel heat sink with chevron fins
$SMCHS - EF$	$SMCHS - PF$ with hybrid elliptical-rectangular fins

Chapter 1 Introduction

1.1 Background

Since the invention of the integrated circuits (ICs) in 1958 (Woodford, 2017), the number of transistors per square millimetre on integrated circuits have increased dramatically. From a careful observation of this trend, in 1965 Gordon Moore, the co-founder of Intel Corporation, noticed that the number of transistors per chip were doubled for every couple of years and expected that this tendency would continue for the new generations of integrated circuits. This has been known as Moore's law and it is still valid to date.

The rapid development in the electronics industry has led to significant increases in the densities of integrated circuits. The literature shows that the average heat flux in the period from 2010 to 2012 has increased dramatically from $50 W/cm^2$ to around $250 W/cm^2$, (Ahmed *et al.*, 2018), and it is expected that the dissipated heat from these components will increase up to more than $800 W$ by 2026 (Al-Neama, 2018). This led to an increase in cooling system requirements so that the processors' temperatures remain within the allowable range, 85 to 100 °C, to ensure reliability and elongate the life span. The studies show that a rise in temperature of chip for 1°C will degrade its reliability by 5% and reduce the life span significantly (Ahmed *et al.*, 2018). Consequently, finding effective cooling technologies to ensure that the chips and electronic equipment operate below the critical temperature is becoming increasingly urgent, and this can be achieved using thermal management.

1.2 Thermal Management Technologies

Efficient thermal management for electronic components helps in improving the reliability and preventing premature failure for such devices by avoiding overheating protecting against critical temperature fluctuations and preventing the formation of condensates (Shabany, 2009; Murshed, 2016; Ahmed *et al.*, 2018). Several techniques can be employed for cooling electronic devices such as heat pipes, jet impingement and heat sinks, to name a few. The primary modes of heat transfer that are used in thermal devices for cooling electronics are conduction and

convection while the radiation participates in removing only a small fraction of the overall thermal load. The design strategies of these thermal management techniques can be typically classified into two categories, namely passive and active devices. The first category requires no external means to circulate the coolant; however, it utilises gravitational force and capillary forces to complete the process of heat transfer. This makes it simple and cheap as it does not need maintenance. In contrast, the second type of cooling systems needs a pump or fan for driving the working fluid to achieve higher cooling capacity and improving the performance of the cooling system (Murshed, 2016 and KAWA., 2011).

1.3 Classification of Cooling Techniques

The work principle of the cooling techniques which are used in thermal management for cooling electronic devices could be divided into four main types (Murshed and De Castro, 2017 and Anandan and Ramalingam, 2008):

1. Radiation and free convection,
2. Forced air-cooling,
3. Forced liquid cooling, and
4. Liquid evaporation.

For low heat flux applications ($0.155 - 1.55 \text{ kW}/\text{m}^2$), the heat sink designs that make use of natural convection are preferable to provide adequate cooling due to simplicity, reliability and low cost. In contrast, the forced air-cooling system will be a good candidate for cooling a higher heat flux electronic component ($0.8 - 16 \text{ kW}/\text{m}^2$) such as those used for cooling the PCs and laptops. When the air-cooling system becomes inadequate to dissipate the generated heat from the chips ($11 - 930 \text{ kW}/\text{m}^2$), the air is replaced by a liquid (e.g. water) to enhance the overall cooling performance since liquids have greater heat transfer coefficient than air (Murshed and De Castro, 2017). Furthermore, the liquid evaporation method has also been used for the electronic components with very high heat flux ($15.5 - 1400 \text{ kW}/\text{m}^2$). This method is superior to the other approaches as it exploits the latent heat of evaporation to remove more heat from the electronics (Anandan and Ramalingam, 2008).

1.4 Emerging Cooling Techniques

During the last four decades, a considerable effort has been put to innovate and develop new technology for controlling the temperature in micro applications like micro-electronic circuits packaging, micro-fuel cell, concentrated solar cells, infrared detectors, etc. (Murshed, 2016). Among these technologies are heat pipe, spray cooling, jet impingement cooling and the microchannel heat sinks. As this study concentrates on serpentine minichannel heat sink, a brief description of the microchannel heat sinks will be given below.

The pioneering work of Tuckerman and Pease (1981) is considered as the real onset of research in the field of the liquid-cooled microchannel heat transfer since microchannel heat sinks represents a promising choice for cooling the small areas that generate high heat fluxes. The heat transfer process within the heat sink is accomplished by transferring the generated heat from the electronic system to the substrate and the walls of the heat sink by conduction, and then it is taken away by convection to the surrounding via the working fluid. Based on the state of the working fluid, there are two main types of the heat sink structures which have been commonly employed for cooling electronic devices, namely air-cooled and liquid-cooled heat sinks.

Despite the fact that air-cooled heat sinks are used widely in cooling the electronic devices, recent studies have shown that liquid-cooled heat sinks are more efficient for high heat flux electronics cooling as they can offer heat transfer coefficients of one to two orders larger than those from air-cooled devices (Adham *et al.*, 2013 and Joshi and Wan, 2018). This has motivated a lot of researches towards further investigations for the liquid-cooled heat sinks used in cooling the high flux electronics (on the order of $10^2 - 10^3 \text{ W/cm}^2$) which is encountered, for example, in aircraft, military avionics, Radio Frequency (RF) Power Amplifier and microwave (MW) applications (Ruiz, M., 2015 and Agarwal *et al.*, 2017).

There are two kinds of the liquid-cooled technique used for removing heat flux from electronics components, i.e. single-phase and two-phase (boiling) microfluidic heat sink. Two-phase microchannel heat sinks (MCHS) can offer many advantages over single-phase systems, for example, achieving high heat transfer coefficients through exploiting the working fluid's latent heat. This helps in reducing the amount of the coolant used in such cooling systems. It also helps in maintaining uniformity for the

temperature along the walls of the heat sink (Mudawar, 2011; Murshed and De Castro, 2017 and Joshi and Wan, 2018). However, there are some disadvantages for the two-phase microchannel heat sinks such as flow instabilities and dry-out (Joshi and Wan, 2018). The present study focussed on single-phase *MCHSs*.

1.5 Microchannels Classification

The working principle of many heat transfer equipment has been inspired by human organs such as lung, brain, kidney and liver. These parts of the human body have micro- and minichannels that provide very high mass and heat transfer. This fact has been employed to create microchannel cooling systems for removing the high heat flux that is encountered in some application like electronic components and high-power laser diode arrays (Kandlikar, 2003 and Furmański *et al.*, 2018). Among these cooling equipments is the microchannel heat sink which was first suggested by Tuckerman and Pease (1981)

To distinguish the (micro-scale) microchannels from the conventional size (macro-scale) channels, Kandlikar (2003) and Mehendale *et al.* (2000) proposed two different classifications, Table 1-1. The former has been based on the Knudsen number and manufacturing constraints in classifying, while the latter classification was based on arbitrary sorting (Dixit and Ghosh, 2015). Knudsen number is defined as the ratio of the mean free path length, λ , to the characteristic length of the system, L_c , (Rapp, 2016). This work will follow the one suggested by Kandlikar (2003).

Table 1-1 Classification of channels adopted from (Dixit and Ghosh, 2015).

(Mehendale et al. 2000)	(Kandlikar, 2003)
Conventional channels $D_h > 6 \text{ mm}$	Conventional channels $D_h > 3 \text{ mm}$
Compact Passages $1 \text{ mm} < D_h \leq 6 \text{ mm}$	Minichannels $200 \mu\text{m} < D_h \leq 3 \text{ mm}$
Meso-channels $100 \mu\text{m} < D_h \leq 1 \text{ mm}$	Microchannels $10 \mu\text{m} < D_h \leq 200 \mu\text{m}$
Micro-channels $1 \mu\text{m} < D_h \leq 100 \mu\text{m}$	Transitional channels $0.1 \mu\text{m} < D_h \leq 10 \mu\text{m}$
	Molecular nanochannels $D_h \leq 0.1 \mu\text{m}$

D_h : The hydraulic diameter of the conduit.

1.6 Thermo-hydraulic Performance of Microchannel Heat Sinks

As mentioned in the previous sections, the aim of using the heat sink mainly is to manage the heat generated within the electronics components and prevent it from rising beyond the allowable limits of the working conditions. Therefore, the heat sink needs to convey the generated heat and reject it away with minimum thermal resistance, R_{th} . As a designer, to assess the effectiveness of the cooling system, it is useful to calculate its overall thermal resistance which could be written in the following form (Kode *et al.*, 2018):

$$R_{th} = \frac{T_{max} - T_{in}}{q} \quad \text{Equ. 1-1}$$

where T_{max} , T_{in} and q are the maximum temperature of the heat sink, inlet temperature of the working fluid and the dissipated heat.

For the active microchannel heat sinks technology, forced convection is used to circulate the working fluid. So, it is necessary to calculate the pumping power needed to achieve the required level of cooling. As can be seen from Equ. 1-2, the pumping power is directly proportional to volumetric flow rate, Q , and pressure drop, Δp , of the coolant (Husain *et al.*, 2008).

$$\mathcal{P} = Q \cdot \Delta P \quad \text{Equ. 1-2}$$

The microchannel heat sink designs with minimum pressure drop and thermal resistance are desirable in order to minimise each of the temperature rises of the electronic equipment per each watt of the dissipated heat and the pumping power needed to circulate the coolant.

1.7 Motivation of the current study

In spite of the fact that the convection heat transfer and fluid flow in microchannels heat sinks have been extensively investigated experimentally and numerically (Adham *et al.*, 2013 and Ahmed *et al.*, 2018), there is still a need to improve the performance of the microchannel heat sink to overcome the increase in the power density of the electronic devices. Despite the fact that numerous previous studies have addressed the optimisation problems, there are, to the best author's

knowledge, limited studies that have dealt with the performance robustness of the microchannel heat sinks when there is a margin of uncertainty associated with the manufacturing process and the operating conditions. A thorough review of the related literature is presented later (Chapter 2). It is worth stating here that Al-Neama (2018) achieved good results in reducing the overall thermal resistance by 10% and pressure drop by 60% for the serpentine minichannel heat sinks by introducing chevron fins and secondary channels. Therefore, replacing the chevron fins with a simpler geometrical shape may offer a better performance for the heat sink. In addition, taking into consideration the variability in geometrical parameters of the serpentine minichannel heat sink due to the manufacturing process could lead to producing a robust design.

1.8 Scope of Research

This study is aimed at trying to improve the performance and produce a robust design of the serpentine minichannel heat sink provided with secondary channels which has been proposed by Al-Neama (2018). To achieve these aims, the following objectives are set:

1. Examining the effect of the channel width and depth of the main channel for the smooth serpentine minichannel heat sinks without secondary microchannels (*SMCHS – PF*). (Chapter 5)
2. Exploring the influence of adding vortex generators to the sidewalls and to the base of the minichannels for the *SMCHS – PF*. (Chapter 5)
3. Performing deterministic optimisation by formulating a design optimisation problem with the overall thermal resistance (R_{th}) and pressure drop (ΔP) as the objective minimisation functions to explore the best design variables for the *SMCHS – PF*. (Chapter 5)
4. Formulating an optimisation under uncertainty problem, with design objectives of minimizing the mean (μ) and standard deviation (σ) for the responses, i.e. $\mu_{R_{th}}$, $\sigma_{R_{th}}$, $\mu_{\Delta P}$ and $\sigma_{\Delta P}$, to investigate the best design variables for the *SMCHS – PF*. (Chapter 5)
5. For the serpentine minichannel heat sinks with chevron fins (*SMCHS – CF*), investigating the effect of the number of fins (F_n), the fin offset (F_o), the

impact of the fin to secondary channel lengths ratio ($R_{FS} = \frac{F_l}{l_{sc}}$) on its thermal resistance (R_{th}) and pressure drop (ΔP). (Chapter 6)

6. Conducting a deterministic optimisation for the *SMCHS – CF* performance in terms of the R_{th} and ΔP , to find the best design variables. (Chapter 6)
7. Formulating the optimisation under uncertainty problem for the *SMCHS – CF* to produce the optimum design with $\min \mu_{R_{th}}, \sigma_{R_{th}}, \mu_{\Delta P}$ and $\sigma_{\Delta P}$. (Chapter 6)
8. Investigating the performance of the serpentine minichannel heat sink with hybrid elliptical-rectangular fins (*SMCHS – EF*). (Chapter 7)
9. Performing deterministic optimisation by formulating a design optimisation problem aiming at minimizing the design objectives, i.e. R_{th} and ΔP , explore the best design variables for the *SMCHS – EF*. (Chapter 7)

1.9 Main contributions (Original contributions of this work)

The specific contributions of this thesis can be summarised as:

1. Providing robust designs for the serpentine minichannel heat sink with and without secondary channels. Chapters (6-7)
2. Extending the investigations of minichannel heat sinks with secondary channels, first studied by Al-Neama (2018), to cover some aspects, e.g. number of fins (F_n), the fin length to the secondary channel length (R_{FS}) and the fins offset (F_o), that have not been examined. Chapter (6)
3. Exploring new fin design for the serpentine heat sink aiming at the enhancement of its performance. Chapter (7)

1.10 Chapter Summary

In this chapter an overview about the thermal management for electronic components and its related methodologies has been presented. The serpentine minichannel heat sink with chevron fins and secondary channels has been mentioned in this chapter as it is considered a promising cooling system for high heat flux applications. In Al-Neama study (2018), it has been demonstrated that this design has good hydro-thermal performance over the designs without secondary

channels. Consequently, this has motivated the researcher to further explore and improve this design.

1.11 Thesis Overview

The remaining chapters of this thesis are presented as shown in the following diagram:

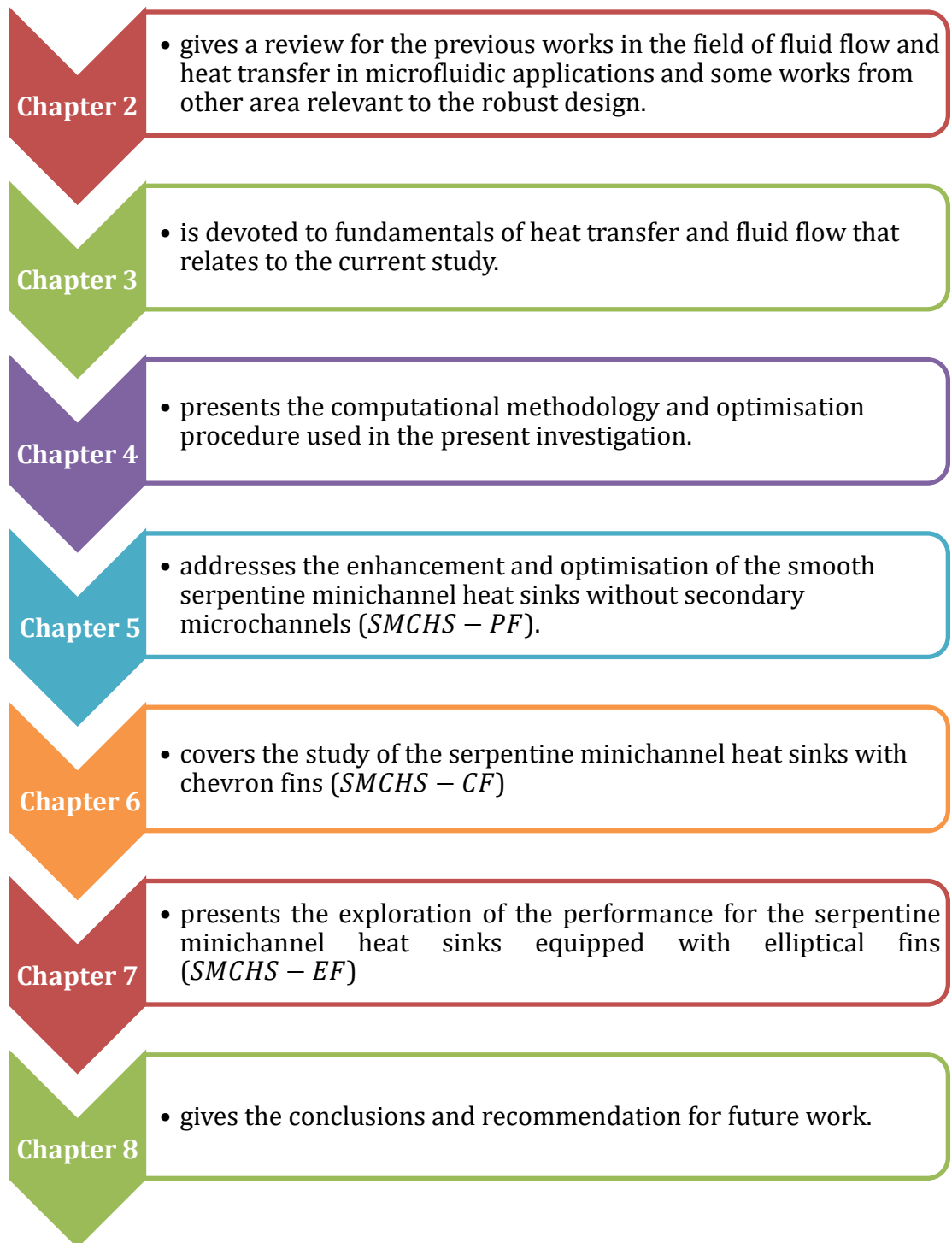


Fig. 1-1 Structure of the current thesis.

Chapter 2 Literature Review

2.1 Introduction

Microchannels have been used widely for the purpose of cooling microelectronic components because they have shown a good thermal performance as they have small volume and large heat transfer surface to volume ratio. A considerable number of studies have been conducted to investigate the flow and heat transfer characteristics of microchannels and improve their performance. Different factors can affect the performance of microchannel heat sinks such as the shape of the channel, fluid properties, the cavities machined on the channel surface and surface roughness of the channel walls (Tullius *et al.*, 2011).

This chapter presents the relevant works to the microchannel heat sinks technology used for cooling electronic systems. It is organised as follows: section 2.2 gives an overview about single-phase microchannel heat sinks (*MCHSs*). A review of the active and passive techniques of enhancing the heat transfer in *MCHSs* is presented respectively in section 2.3 and section 2.4. A review of the studies that addressed the serpentine microchannel heat sink is presented in section 2.5. After that, the focus is turned to review the articles that dealt with optimisation of *MCHSs*, sections 2.6, which is subdivided into two main subsections: investigations dealt with the deterministic optimisation of *MCHSs*, section 2.6.1, and the studies that related to robust design methodology, section 2.6.2. Finally, the gaps in knowledge will be given in section 2.7.

2.2 Single-Phase Microchannel Heat Sinks

In their experimental and theoretical pioneering study, Tuckerman and Pease (1981) suggested the concept of single-phase flow microchannel heat sink (*MCHS*) for cooling very-large-scale integrated (*VLSI*) circuits. They manufactured and tested a very compact heat sink which has a base area ($L \times W$) of 1 cm^2 and made of silicon with an array of straight channel is chemically etched in it with height (H_c) and width (W_c) of respectively $302 \text{ }\mu\text{m}$ and $50 \text{ }\mu\text{m}$ and separated by $50 \text{ }\mu\text{m}$ thick wall (W_w), Fig. 2-1. They employed water as a working fluid.

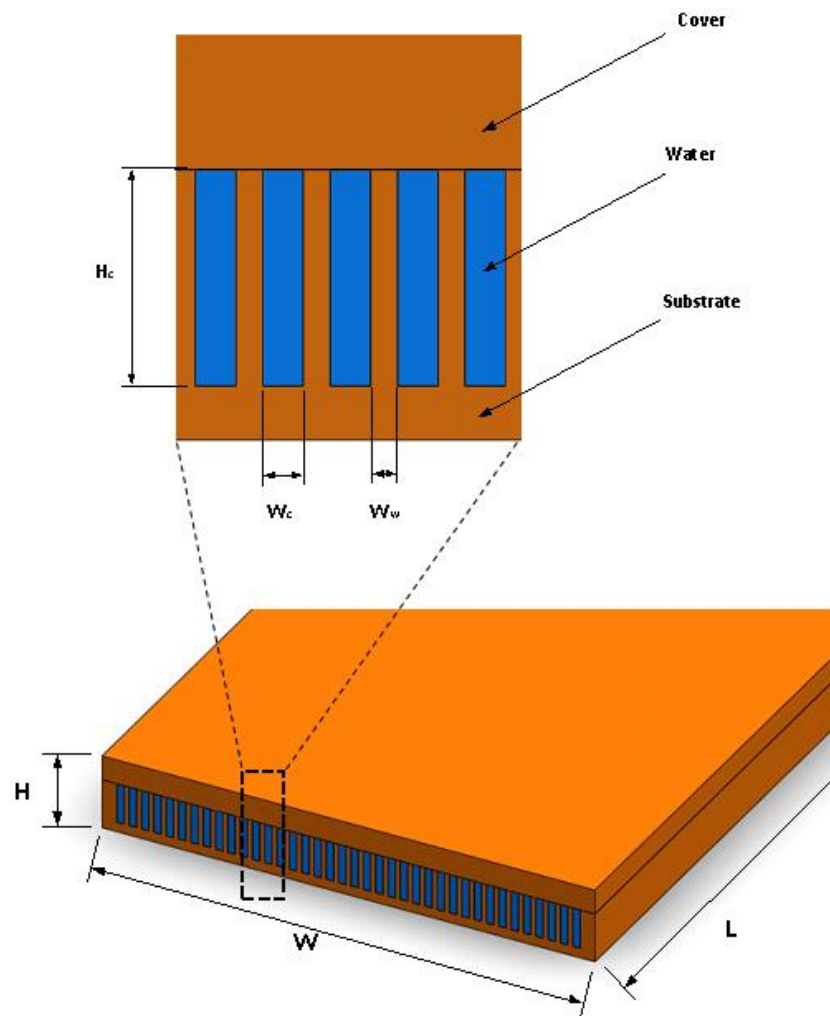


Fig. 2-1 The geometry of the straight microchannel heat sink with a magnifying view.

They concluded that manufacturing cooling channels with micro-scale dimensions leads to a high heat transfer rate, i.e. the heat transfer coefficient of laminar flows within small channels is inversely proportional to the hydraulic diameter of the channel. They also demonstrated that this design could dissipate 790 W/cm^2 while keeping the maximum difference between the substrate temperature and the water inlet temperature less than 71°C . It is worth mentioning that the thermal resistance and the pressure drop were respectively as low as 0.09 K/W.cm^2 and 2.2 bar . This pioneering work was followed-up by a number of researches to improve the hydrothermal performance of the *MCHS*. For example, Phillips *et al.* (1990) extended the theoretical work of Tuckerman by conducting an experimental investigation to study small, moderate and large aspect ratios of channels for different flow conditions, i.e. fully developed and developing flow in the laminar and turbulent regimes. The substrate for heat sink was made from indium phosphide

(InP) while water was used as the coolant. The dimensions of the microchannel heat sink were $H_c = 165 \mu m$, $W_c = 220 \mu m$, $W_w = 155 \mu m$ and $L_c = 0.97 cm$. He also developed a computer model (*MICROHEX*) to enable numerical computations for the hydrothermal performance of the considered heat sink. He obtained an excellent thermal performance with thermal resistance was as low as of $0.072 K/W.cm^2$ allowing load dissipation as high as $1056 K/W.cm^2$.

Kawano *et al.* (1998) conducted combined three-dimensional numerical simulations and experiments to explore the fluid flow and heat transfer in a straight rectangular microchannel heat sink (*MCHS*). They selected silicon as the material for the substrate and water as the refrigerant. In their experimental setup, the manufactured substrate had dimensions of $15 mm \times 15 mm$ with an array of 110 microchannels. Two designs have been tested where both had a channel width of $57 \mu m$ while channel height was either $180 \mu m$ or $370 \mu m$. To simplify the numerical simulations, they assumed that the flow was laminar and fully developed. For the experimental pressure loss measurements, they did not apply heat to the chip. The results showed there was a good matching between the numerical results and the experimental measurements of the pressure drop for the range of Reynolds number of $0 < Re < 200$. For the same range of Reynolds number, however, there was a discrepancy in the thermal resistance values at the entrance of the microchannels. This discrepancy had been attributed to heat losses from the heat sink block to the surrounding while implementing the experiments. For higher Reynolds number, i.e. $Re > 300$, they also highlighted that the values of the pressure losses in the experimental part were higher than that predicted using the numerical simulation.

Xu *et al.* (2000) conducted an interesting experimental investigation for water flow friction in a rectangular microchannel heat sink with a hydraulic diameter ranging from $29.59 \mu m$ to $344.3 \mu m$ and ratio of the width to the depth ranging from 0.041 to 1.716. Their experimental results were presented for Reynolds numbers ranging from 20 to 4000. Two different types of microchannels have been fabricated and tested. The first type had microchannels machined in an aluminium substrate using micro-end-mills while the second one had microchannels structures in silicon wafers made by etching. The comparison of their results with the available data from literature showed that the conventional theories, i.e. Navier-Stokes equations, are

suitable to predict the flow characteristics in the microchannel with the range of hydraulic diameters studied.

During the last four decades, considerable efforts have been put to improve the performance of conventional microchannel heat sinks for cooling the microelectronics (Anandan and Ramalingam 2008, Tullius *et al.*, 2011, Adham *et al.*, 2013, Dixit and Ghosh, 2015, Murshed and De Castro 2017, Ahmed *et al.*, 2018). Mainly, the heat transfer augmentation techniques could be active or passive. For the first technique, the improvement in heat transfer happens with the aid of an external power such as jet impingement, surface vibration, electrostatic field etc. (Anandan and Ramalingam 2008). In contrast, the intensification of heat transfer using the second technique occurs as a result of increasing the heat transfer area or improve the thermophysical properties for the heat sink material or the working fluid, like extended surface, treated surface, swirl flow devices, vortex generators ... etc. (Léal *et al.*, 2013 and Al-Asadi 2018). The designers might use the active technique, passive technique, or a combination of both of them. A brief review of the active and passive heat transfer augmentation techniques will be given in the following sections.

2.3 Active Enhancement of Heat Transfer in MCHSs

2.3.1 Forced Convection

In thermal management, the thermal convection is the main mode of heat transfer utilised to cool the electronic components. This kind of heat transfer can be forced convection or natural convection, depending on whether there is an external means to move the fluid or not. The heat sinks under natural convection have been used extensively, such as such the study of Yazicioğlu and Yüncü (2007); Ismail *et al.* (2008); Yu *et al.* (2010) and Huang *et al.* (2014). However, the heat sinks utilising the forced convection has become more prevalent and regarded as a promising solution in thermal management due to its ability to cool the electronics is superior to that of the natural convection (Pi *et al.*, 2018). Several studies, like the work of Peles *et al.* (2005), Ho *et al.* (2010) and Soheli *et al.* (2014), have employed this mechanism with heat sinks to tackle the problem of high heat flux generated within electronic components.

Furthermore, fluid flow within heat sinks could be laminar or turbulent; however, studies of the microchannel under laminar flow was the dominate (Adham *et al.*, 2013 and Ahmed *et al.*, 2018). The reason behind that could be attributed to the belief of the researchers that the performance of microchannel heat sinks is better with laminar flow than turbulent flow.

2.3.2 Nanofluid Technology

Nanoparticles have also been investigated as a mean of enhancing the heat transfer (Palm *et al.*, 2006); however, recent results showed that the increase in thermal conductivity of the nanofluids comes at the price of pressure drop and also do not deliver these benefits in practice (Alkasmoul *et al.*, 2018). Besides, other studies have shown that the nanoparticles' presence causes some issues like erosion, particle sedimentation, nanoparticle agglomeration, clogging the channel over time and fouling (Lee and Mudawar, 2007 and Yu *et al.*, 2008).

2.4 Passive Enhancement of Heat Transfer in MCHSs

Heat sinks have been used as an effective cooling technique for electronic systems. The modes of heat transfer involved to cool the electronic chips are mainly conduction and convection. Basically, the heat is transferred from the electronic component to the base of the heat sink by conduction. This heat, then, conducts from the bottom of the heat sink to its fins. These fins are in contact with the cooling fluid that, in turn, convey the heat away by convection, free or forced convection, Fig. 2-2 (a).

In the heat sink research community, researchers have chosen the concept of thermal resistance as a criterion to assess heat sink. Researcher groups aim to reduce the overall thermal resistance, thus improving the heat transfer and maintaining the junction temperature of the electronic components within safe working temperature of 85 to 100 °C (Ahmed *et al.*, 2018). The thermal resistance network for the heat sink is depicted in Fig. 2-2 (b).

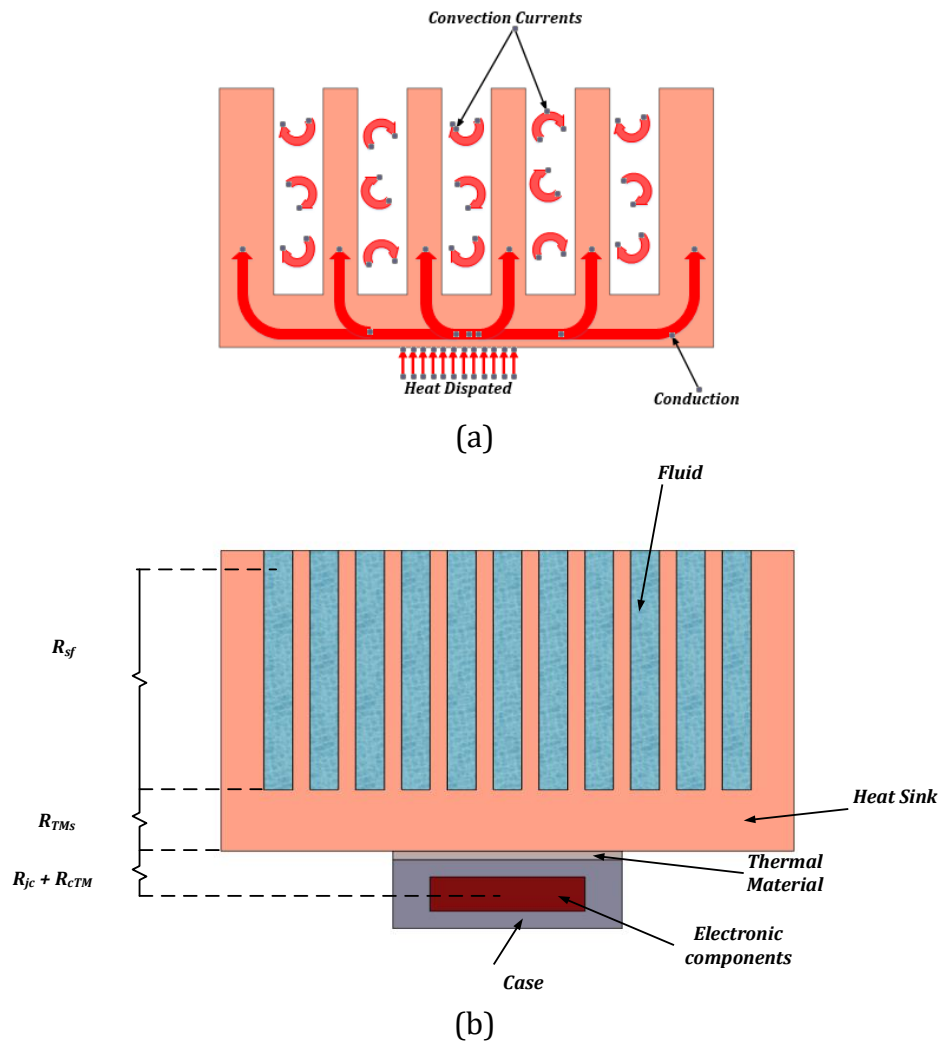


Fig. 2-2 Schematic diagram of the heat sink showing (a) the involved heat transfer modes and (b) the thermal resistance network.

The summation of the individual thermal resistance of all the layers of the heat sink is equivalent to its overall thermal resistance. So that the total junction-to-fluid thermal resistance (R_{th}) consists of the junction-to-case (R_{jc}), the case-to-thermal material (R_{cTM}), the thermal material-to-heat sink (R_{TMs}), and the heat sink-to-coolant (R_{sf}). Thus, the overall thermal resistance could be expressed mathematically as in the following equation:

$$R_{th} = \frac{T_{max} - T_{in}}{q} = R_{jf} = R_{jc} + R_{cTM} + R_{TMs} + R_{sf} \quad \text{Equ. 2-1}$$

To improve the heat sink performance, it is necessary to enhance its heat transfer mechanisms by reducing the thermal resistance of conduction and convection modes. The conduction thermal resistance for the heat sink base can be written as

the ratio of its substrate thickness (H_b) to the thermal conductivity (k) and the area of the heat sink (A_s) as shown below:

$$R_{cond} = \frac{H_b}{k \cdot A_s} \quad \text{Equ. 2-2}$$

So, reducing this thermal resistance needs to minimise the H_b and/or maximise the A_s and k (Koşar 2010).

On the other hand, the convective thermal resistance of the heat sink can be defined as the reciprocal of the heat transfer coefficient (h) times the effective heat transfer area (A_{eff}) as stated bellow:

$$R_{conv} = \frac{1}{h \cdot A_{eff}} \quad \text{Equ. 2-3}$$

As a result, to augment the convective heat transfer it is required to mitigate this thermal resistance which can be achieved by maximizing the h and/or A_{eff} .

In the literature, there is a good review for the passive techniques used to enhance the heat transfer for microchannel heat sink which has been accomplished recently by Sidik *et al.* (2017). In the following subsections, however, a review of some previous works devoted to investigating the effect of the coolant type, substrate material, shape of the channels and other factors on the performance of microchannel heat sinks will be presented.

2.4.1 The effect of Coolant Type

Air-cooled heat sinks are used widely to cool electronic system due to their simplicity, reliability, and low cost (Al-damook, 2016). Numerous studies have been conducted to investigate and improve the performance of the air-cooling heat sinks like the recent studies of Al-Damook *et al.* (2015), Sakanova and Tseng (2018), Khoshvaght-Aliabadi *et al.* (2018) and Aghakhani *et al.* (2019); furthermore, an interesting review can be found in an article by Khattak and Ali (2019). As the power of electronic systems increased, the performance of the traditional air-cooled heat sinks become limited and insufficient to meet the recent and future cooling requirements of the electronic circuitry of the forthcoming years. They also suffer from noise problem. They also suffer from noise problem (Khattak and Ali, 2019 and

Wang, 2017). Therefore, researchers are trying to find alternative solutions to eliminate these shortcomings.

One of the attempts is to use liquid coolant instead of air to overcome the shortcomings of air-cooled heat sinks. In early 1980s, Tuckerman and Pease suggested water as a coolant in microchannel heat sinks for cooling high heat flux devices which have better performance and compact size in comparison with the forced air-cooled system. This superior performance is due to the fact that water has higher specific heat capacity and higher thermal conductivity than air, and thus has a high heat transfer coefficient (Salman *et al.*, 2014). Also, water-cooled systems need much lower flow rates. However, using water as a coolant for cooling electronic devices is risky due to the possibility of leakage issue that causes system damage. Therefore, considerable attention to design the water-cooled heat sinks should be given (Adham *et al.*, 2012).

Other studies have employed alternative coolants like the study of Adham *et al.* (2012) who reported an analytical optimisation study of the hydrothermal performance of a rectangular heat sink using ammonia gas as working fluid. Their results demonstrated ammonia gas as a coolant for the rectangular microchannel heat sink is promising. The results also showed an enhancement in heat removal capability where the thermal resistance reduced significantly from 0.266 K/W for air to 0.218 K/W for ammonia gas under the same operating conditions. Furthermore, they achieved a substantial reduction in the total pressure drop from 5.36 mbar and 9.52 mbar for ammonia and air respectively.

2.4.2 Effect of substrate thickness and structural material

Some researchers have investigated the effect of substrate thickness and structural material on the thermal performance of the microchannel heat sink. For example, Koşar (2010) analyzed numerically the conjugate heat transfer of water flow inside rectangular *MCHS* to explore the effect of the material type and wall thickness on the heat transfer characteristics. He modelled conjugate heat transfer in microchannels of size ($200\mu\text{m} \times 200\mu\text{m}$) with substrate thickness (H_b) in the range of $100\mu\text{m} - 1000\mu\text{m}$ made of different materials, i.e. Polyimide, Silica Glass, Quartz, Steel, Silicon and Copper. The flow has been assumed to be laminar with Reynolds number $Re < 2000$. He concluded that the thermal conductivity and

thickness of the substrate have a crucial effect on the heat transfer as it increases with increasing thermal conductivity and decreasing the substrate thickness.

The study of Léal *et al.* (2013) reported a numerical analysis of the conjugate heat transfer of water flow inside partially heated microtubes. They considered two wall thicknesses ($d_i/d_o = 0.1/0.3$ and $0.1/0.5$) and three different materials (stainless steel, copper and silicon). They assumed laminar flow with Reynolds number up to 200. Their major findings confirmed that the heating source position has a significant effect on the behaviour of the local Nusselt number while the wall thickness, wall material and the Reynolds number did not affect it.

Another study by Shkariah *et al.* (2013) explored numerically the effect of three different substrate materials, i.e. silicon, aluminium and graphene, on the thermal performance of a single-phase microchannel heat sink. Water was used as the coolant fluid with non-temperature-dependent thermal properties. Three-dimensional CFD simulations based on the finite volume method (*FVM*) using *FLUENT* 14 were performed for solving the governing equations of the straight microchannel heat sink. The study revealed that graphene offered the lowest thermal resistance among the investigated materials.

Gunnasegaran *et al.* (2010) conducted a numerical analysis research on heat transfer and pressure drop in trapezoidal microchannel heat sinks using different types of base nanofluids and four types of *MCHS* substrate materials (copper, aluminium, steel, and titanium). They employed the finite volume method to solve the three-dimensional steady, laminar flow and heat transfer governing equations. They reported that great heat transfer enhancement can be achieved by manufacturing the heat sink substrate from steel (high thermal diffusivity material) and using water-based nanofluids (low Prandtl number, Pr) as coolant.

2.4.3 Double layers (Multi-layers Heat Sink)

To produce reliable microelectronic devices with long lifetime, the issue of non-uniform wall temperature distribution should be addressed. One of the proposed solutions is the concept of a double-layered microchannel heat sink (*DL – MCHS*), Fig. 2-3, which has been suggested by Vafai and Zhu (1999). They used a counter current flow arrangement for the cooling purpose. The study analysed the thermal performance and the temperature distribution for the proposed structure and

optimised the geometrical design parameters. In comparison with the one-layered structure, the two-layered design can substantially reduce the streamwise temperature rise on the base surface and the pressure drop. This study has been followed by several investigations that employed multi-layers to enhance the performance and obtain uniform wall temperatures of the heat sinks such as the studies of Wei and Joshi (2003), Skandakumaran et al. (2004), Levac *et al.* (2011), Deng *et al.* (2019).

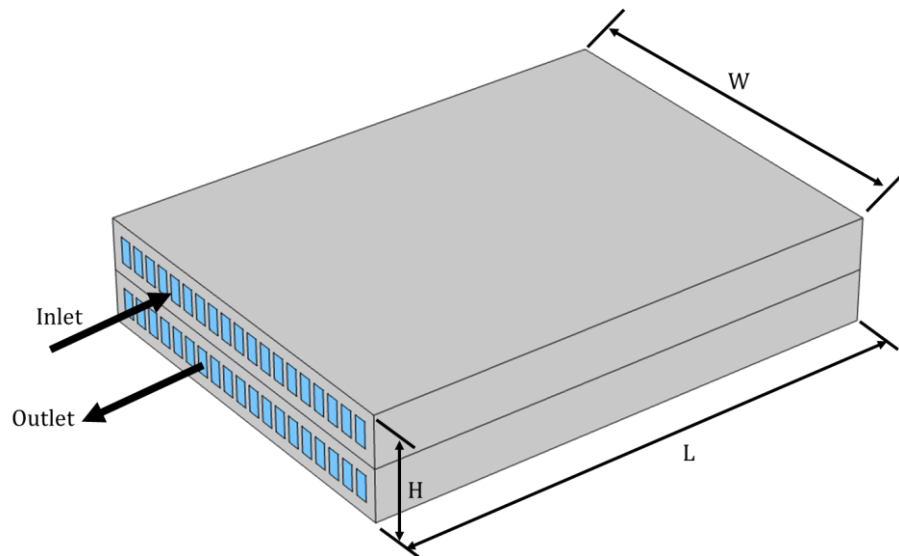


Fig. 2-3 Schematic diagram of the designed double-layered microchannels heat sink proposed by Vafai and Zhu, 1999.

2.4.4 Flow Passages Filled with Porous Materials

The hydraulic and thermal performances of the porous-microchannel heat sinks (porous-*MCHSs*) for electronics cooling have been given considerable attention by researchers. The idea behind inserting porous metallic materials into a microchannel is to increase both the local velocity mixing of the cooling fluid and the surface contact area-to-volume ratio which lead to improving convective heat transfer (Singh *et al.*, 2009). Significant effort has been devoted to determining the effect of configurations and porosity conditions on the hydrothermal performance of porous-*MCHSs*, such as the work of Jiang *et al.* (2001), Hung and Yan (2013), Hung *et al.* (2013) and Dehghan *et al.* (2016).

2.4.5 Effect of the Geometry of the Heat Sink Microchannel

As can be seen in the literature, several attempts have been made to improve the overall thermal performance of microchannel heat sinks through modifying its channel shape. This has been done by employing different microchannel geometries such as rectangular (Kawano *et al.*, 1998; Vafai and Zhu, 1999 and Xu *et al.*, 2000), circular (Nonino *et al.*, 2009, Singh *et al.*, 2009 and Sohel *et al.*, 2013), square (Mo *et al.*, 2005, Raimondi *et al.*, 2013 and Abdollahi *et al.*, 2014) and trapezoidal (McHale and Garimella, 2010, Chai *et al.*, 2012 and Qu *et al.*, 2001). The purpose of these changes was to increase the effective area available for heat transfer and mitigate convective thermal resistance (Adham *et al.*, 2013). For instance, to study the influence of geometrical parameters on microchannel heat sink performance, Gunnasegaran *et al.* (2010) carried out a three-dimensional numerical analysis of conjugate heat transfer and fluid flow in channels with a rectangular, triangular and trapezoidal cross-sections, Fig. 2-4. Water was used to remove the heat from the hot surface of the heat sink. The governing equations were solved using the finite volume method and the investigations of the steady-state laminar flow were performed in the range of Reynolds number 100-1000. The authors disclosed that the heat sinks having the smallest hydraulic diameter have better thermal-hydraulic performance.

Later, Wang *et al.* (2016) investigated numerically the effect of different geometries, i.e. rectangular, trapezoidal and triangular shapes on the heat transfer and fluid flow characteristics of microchannel heat sinks. The coolant was de-ionised water while the material of the heat sink was oxygen-free copper. They showed that the rectangular microchannel has the best performance compared to the other geometries.

As seen in the open literature, another direction of improving the performance of *MCHSs* is by using curved path channels. For instance, one of the studies that investigated the effect of the path shape of the microchannel on the heat sink performance has been done by Mohammed *et al.* (2011). They examined numerically the effect of zigzag, curvy, and step channel shapes on the heat transfer and fluid flow in the microchannel channel heat sink made of aluminium and cooled by water. They concluded that the zigzag shape, in comparison with other configurations, has the best heat transfer but this at the expense of high pressure

drop. Furthermore, the pressure drop in all the studied shapes was higher than that of the conventional straight *MCHS*.

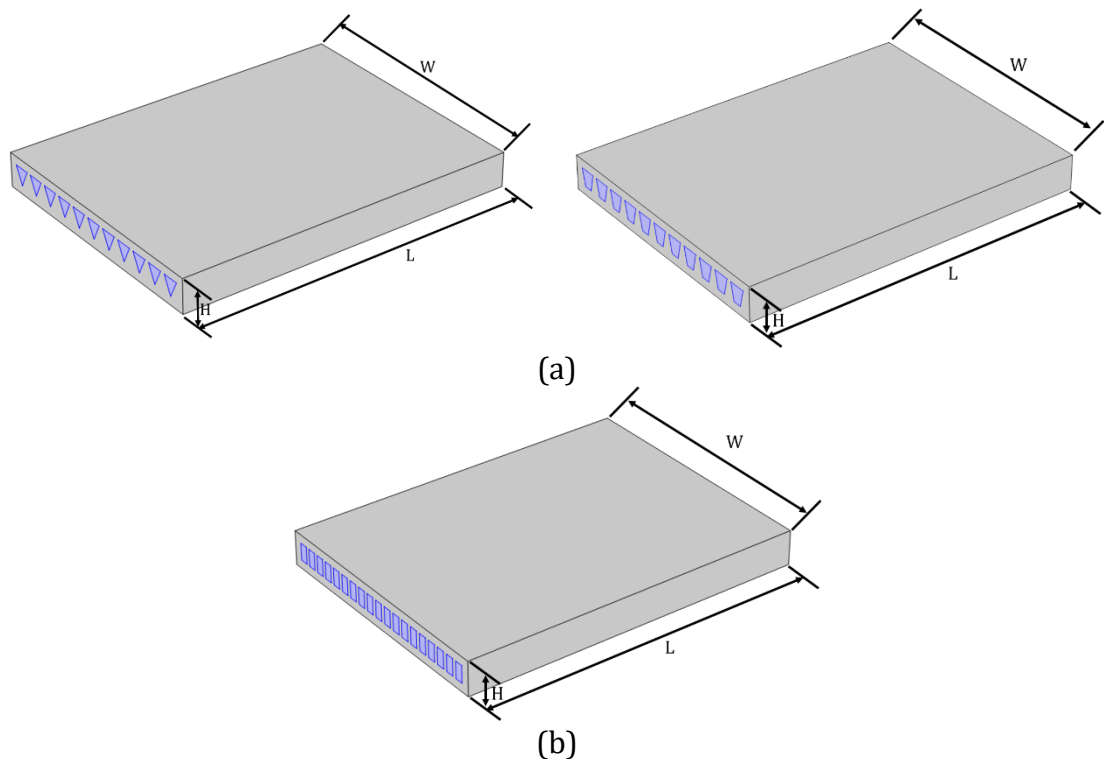


Fig. 2-4 Schematic of microchannel heat sink with different channel shapes investigated by Gunnasegaran *et al.* (2010).

Some researchers tried to improve the performance of the conventional microchannel heat sink by replacing the straight channels with sinusoidal channels such as the study by Sui *et al.* (2010). They reported a three-dimensional numerical simulation for laminar liquid-water flow and heat transfer to assess wavy microchannels with a rectangular cross section, Fig. 2-5 (a). They assumed the substrate to be silicon and the applied heat flux to be constant. The numerical results revealed that there was a considerable improvement in the heat transfer performance of the wavy microchannels in comparison with that of straight channels for the same cross section. According to the authors, the augmentation in heat transfer is due to generating secondary flow (Dean Vortices) with variable patterns, i.e. changing in number and location of the vortices, along the flow direction which creates chaotic advection and enhances the convective fluid mixing. Besides, they noticed that the pressure drop penalty was small in comparison to the significant enhancement in the overall heat transfer. They also investigated the changing in the relative wavy amplitude Fig. 2-5 (b - ii & iii). They found that

increasing the waviness along the flow direction can lead to an increase in heat transfer performance and consequently a reduction in the temperature rise of the chip along the flow direction. They were also able to increase the waviness at specific locations of higher heat flux to promote the heat transfer, which is beneficial for addressing hot spot issue. For the two new designs, Fig. 2-5 (b – ii & iii), it is of interesting to highlight that the authors also recorded an improvement for the heat transfer enhancement factor and pressure factor with values from (1.71 to 2.95) and (1.38 to 2), respectively.

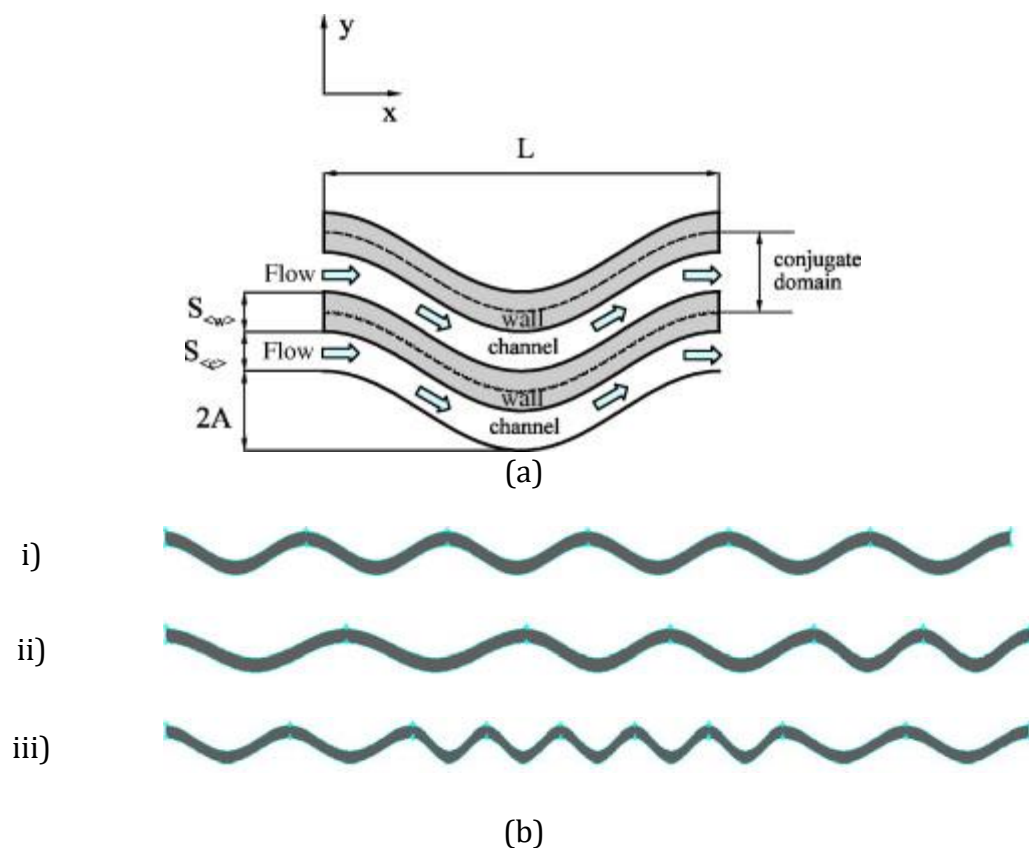


Fig. 2-5 Schematic of wavy microchannels (a) characteristic dimensions and (b) change in relative wavy amplitude along the flow direction of the novel designs: i) constant wavy amplitude, ii) increased relative wavy amplitude, and iii) locally higher at high heat flux regions wave amplitude (Reproduced from Sui *et al.*, (2010) with permission).

Interestingly, the same authors conducted an experimental study Sui *et al.* (2011) to investigate the hydrothermal performance of sinusoidal microchannels with rectangular cross sections. They used de-ionised water to cool the copper heat sinks that containing 60-62 wavy channels. Each microchannel consisted of 10 identical wavy units with average width, depth and wavelength of about $250 \mu\text{m}$, $404 \mu\text{m}$ and 2.5mm , respectively, while wavy amplitude was changing between 0 and $259 \mu\text{m}$.

The range of Reynolds numbers considered in their experiments was from around 300 to 800. They also performed a conjugate heat transfer simulation, using the CFD software package (*FLUENT*), for the specified test geometries and boundary conditions used in the experimental part of their study and compared the results from the two methodologies. The comparison showed a reasonably good agreement between the experimental and numerical results. They also demonstrated that the heat transfer performance of the wavy microchannel that they studied was superior to that of straight baseline microchannel and the pressure drop penalty was noticeably less than the heat transfer enhancement. The enhancement in the hydrothermal performance confirmed the conclusions of their previous work (Sui *et al.*, 2010) about the advantages of using a heat sink with wavy microchannels over those using straight channels.

2.4.6 Vortex generators (Turbulators)

Researchers have conducted several studies to enhance the heat transfer in conventional microchannel heat sink by adding different geometrical features, which are termed as vortex generators (*VGs*). These geometrical modifications increase the cooling surface area for convection heat transfer mechanism and play a role in disturbing the flow and forming vortices in the stream (Ebrahimi *et al.*, 2016 and Al-Asadi 2018). The vortex generators could be formed in different shapes such as grooves, wings, winglets, fins ... etc (Aris *et al.*, 2011). According to the orientation of the vortices' axes with respect to the fluid flow, vortex generators can be classified into two categories. The first kind is named transverse vortex generators (*TVG*) in which the rotating axes of *TVs* are perpendicular to the direction of the main fluid flow. The other type is termed as longitudinal vortex generators (*LVG*) in which the rotating axes of *LVs* are parallel with the main fluid flow's axis, therefore it is also known as stream wise vortices. It has also been shown that using (*LVGs*) augments the heat transfer performance better than employing (*TVGs*) (Wang *et al.*, 2002, Wu and Tao, 2008 and Ahmed *et al.*, 2012).

The literature is rich with the studies that investigated the use of vortex generators such as Hsiao *et al.* (2014), Kim *et al.* (2011), Datta *et al.* (2016), Al-Asadi *et al.* (2016), Li *et al.* (2016), Zhang *et al.* (2019) and Datta *et al.* (2017). Recently, Chai and Tassou (2018) presented a comprehensive review of the experimental and

numerical studies that addressed vortex generators of variant types to enhance the thermal performance of the airside surface of heat exchangers. A review for the more relevant researches in the field of microchannel heat sink is given below.

Wang *et al.* (2007) experimentally studied the heat transfer and pressure drop in narrow rectangular mini-channels with length (L), width (W) and height (H) of $940 \times 40 \times 2.5 \text{ mm}$, respectively, while the length (L_v), width (W_v) and height (H_v) of the *LVGs* were $10 \text{ mm} \times 2 \text{ mm} \times 1.1 \text{ mm}$ with an angle of attack of $\beta = 50^\circ$. They used de-ionised water as working fluid with Prandtl number $Pr = 4 - 5$. Their findings showed that heat transfer could be enhanced by 10 - 45% if longitudinal vortex generators *LVGs* are used, but it will be accompanied by a larger friction factor than that for the smooth channel.

Cheng (2007) conducted computational fluid dynamics (CFD) simulation of fluid flow and heat transfer in a stacked two-layer microchannel heat sink with enhanced mixing passive microstructures. The width (W_{ch}), height ($H_{ch1,2}$), length (L), fin width (W_{fin}) and base thickness ($t_{1,2}$) of the microchannels were $30 \mu\text{m}$, $100 \mu\text{m}$, $5000 \mu\text{m}$, $30 \mu\text{m}$ and $30 \mu\text{m}$ respectively. The rib height (h) had taken the values 10, 20 and $30 \mu\text{m}$ and the rib pitch was $10 \cdot h$. The researcher employed the 3D conjugated model to simulate the conjugate heat transfer between the heat sink and fluid. He studied the effect of the ratio of embedded structure height to microchannel height (h/H_{ch1}) and fluid property on the thermal performance of microchannel heat sink in their investigation. The Reynolds number was fixed at 14.8 while the ratio (h/H_{ch2}) was changed from 0.13 to 0.26. He compared his results with previous works and concluded that the stacked two-layered microchannel heat sink with multiple passive microstructures has a better performance than those of smooth microchannel, single and double-layer. Cheng attributed that to the presence of the multiple passive microstructures which enhance the mixing mechanism and thus augment the heat transfer and reduce the thermal resistance. Furthermore, increasing the ratio (h/H_{ch1}) leads to a decrease in thermal resistance. Liu *et al.* (2011) conducted experimental research on the hydrothermal performance in a rectangular microchannel with longitudinal vortex generators and cooled by de-ionised water for Reynolds numbers in the range from 150 to 1200. The dimensions of the height (H), width (W), and length (L) of the rectangular microchannels were respectively $100 \mu\text{m}$, $1500 \mu\text{m}$, and $20,000 \mu\text{m}$. In their

investigation, six different configurations of the microchannel test chips with a different number of pairs and angles of attack of the *LVGs* were considered. They also highlighted that the rectangular microchannel with *LVGs* could enhance heat transfer up to 12% for laminar flow and up to 90% for turbulent flow, compared with the smooth rectangular microchannel, while causing more significant pressure drop which might reach 83% for laminar flow and 169% for turbulent flow.

Chen *et al.* (2014) extended the work of Liu *et al.*, (2011) by exploring experimentally the hydraulic and thermal characteristics of rectangular microchannels having longitudinal vortex generators (*LVGs*). The de-ionised water was the working fluid, and the Reynolds number varied from 350 to 1500. They designed and fabricated ten rectangular microchannel test chips to study the effect of the height of *LVGs* and the aspect ratio on the heat transfer and pressure drop of rectangular microchannels with passive microstructure. The rectangular microchannels were manufactured in two aspect ratios 0.25 and 0.0667. Their results showed that the enhancement in heat transfer performance was 12.3–73.8% and 3.4–45.4% for microchannels with aspect ratios of 0.0667 and 0.25, respectively but the penalties for pressure drop were raised 40.3–158.6% and 6.5–47.7%, respectively.

Ebrahimi *et al.* (2015) performed three-dimensional simulations using an open-source computational fluid dynamics code, *OpenFOAM*, to explore the effects of the Reynolds number and different geometrical configurations on thermo-hydraulic performance of microchannels with *LVGs*. They validated their numerical results with experimental data from the literature and achieved a deviation of less than 10%. In their study, five different configurations of the microchannel with varying angles of attack of the *LVGs* have been investigated for Reynolds numbers between 100 and 1100. They reported that the Nusselt number for microchannels has improved by 2 – 25% with 4 – 30% increase in the friction factor. Moreover, they concluded that introducing the *LVGs* increases the required pumping power. They also noticed that increasing Reynolds number leads to an increase in the heat transfer and friction factor.

Another investigation has been conducted by Al-Asadi *et al.* (2016) to analyse numerically a three-dimensional conjugate heat transfer problem under laminar flow conditions within a microchannel equipped with vortex generators at its base.

They explored the effect of spanwise gaps of cylindrical vortex generators (*CVGs*) having half-circle and quarter-circle cross-sections on the thermal-hydraulic performance of the microchannel heat sink in their study. This heat sink has a length (L) of 25 mm and height (H_t) of 0.9 mm. The radius of the vortex generators was varied up to 400 μm , and the distance between the vortex generators (x_{in}) was 4 mm. Three different configurations of the cylindrical vortex generators have been used in their investigation, namely, full-span, centred and split. The *CVG* covers the full width of the microchannel in the full-span while it is shorter for the other two designs with gaps. Their results showed that the best model among those being studied was the centred *CVG* which demonstrated a significant reduction in the thermal resistance and a smaller increase in the pressure drop penalty in comparison to the full-span *CVG* design. On the other hand, the split *CVG* design has a similar performance like the full-spanned design.

Continuing with their work, Al-Asadi *et al.* (2018) carried out recently a numerical simulation for two different models of a microchannels heat sink to examine the impact of geometry and type of coolant on the heat and flow characteristics. They employed perforated pinned heat sink (*PPHS*) in the first model. In contrast, in the second model, they suggested different shapes, i.e. circular, triangular and rectangular, of vortex generators and distributed them along the microchannel base with a specified distance between them. The flow was laminar with a range of Reynolds number between 50 to 2300. They used air and water as a working fluid. The results revealed that no significant augmentation in heat transfer could be achieved by using water in *PPFHS*. Nevertheless, the proposed *VGs* showed a potential enhancement in heat transfer which could help in tackling the challenges of cooling the electronics. They also noticed that all the suggested *VGs* had provided a substantial improvement in heat transfer performance but at the expense of a higher pressure drop.

Another numerical study has been performed by Al-Asadi *et al.* (2018) to investigate the gaps in cylindrical vortex generators (*CVG*) on the heat transfer enhancement in plate-fin heat sink microchannels. Their results demonstrated that the gaps between each end of the vortex generators and walls of the channel help improve the heat transfer and mitigate the pressure drop as compared to full-span

CVG. They also concluded that the end-gap arrangement is superior to the other arrangements in their study.

More recently, Hosseinirad *et al.* (2019) performed numerical simulations for water flow through a minichannel provided with various non-uniform transverse vortex-generators (*TVGs*). They conducted experimental measurement to validate their numerical results. They concluded that the presence of *TVGs* in minichannels improves the thermal performance in comparison to the smooth channel. They attributed that improvement to the increase in cooling area, interruption of the thermal boundary layer and chaotic mixing. Furthermore, they observed that employing *TVGs* with non-uniform heights affects heat transfer and pressure drop characteristics. The best heat transfer can be achieved by arranging the *TVGs* in the long-to-short order.

The literature is rich with the studies that investigated the use of vortex generators in microchannels system such as Hsiao *et al.* (2014), Kim *et al.* (2011), Datta *et al.* (2016), Al-Asadi *et al.* (2016), Li *et al.* (2016), Zhang *et al.* (2019) and Datta *et al.* (2017). Recently, Chai and Tassou (2018) presented a comprehensive review of the experimental and numerical studies that addressed vortex generators (*VGs*) of variant types to enhance the thermal performance of the airside surface of heat exchangers.

2.5 Serpentine Microchannel Heat Sinks

Serpentine microchannel heat sinks have received considerable attention as they have demonstrated an attractive performance of low thermal resistance and pressure drop due to periodical interruption of the flow at the bends of the channels. This interruption causes a periodic break of the thermal boundary layer, and as a consequence, the heat transfer performance is enhanced in serpentine channels (Hao *et al.*, 2014). This configuration has been employed in different thermal system applications such as flow batteries (Gundlapalli and Jayanti, 2019 and Lee *et al.*, 2019), battery cell (Deng *et al.*, 2018), compact heat exchangers (Southall *et al.*, 2008), underfloor heating/cooling systems, turbine blade/vane internal cooling, on-chip cooling (Liou *et al.*, 2018), solar thermal collector (Joy *et al.*, 2016; Moss *et al.*, 2017 and Singh *et al.*, 2019), and proton exchange membrane fuel cells (Neto *et al.*, 2019).

Li *et al.* (2013) presented an optimisation study for the channel configuration of a serpentine channel heat sink with 180° bends, Fig. 2-6, through employing a multi-objective genetic algorithm based on NSGA-II to produce a Pareto front. The geometrical parameters were the aspect ratio of the cross-section of channels ($a = H/W_{ch}$) and the ratio of fin width to channel width ($b = W_b/W_{ch}$). They considered laminar flow, i.e. Reynolds number in the range ($1000 < Re < 2300$), to avoid any influence of Re on loss coefficient (i.e. to ensure that the loss coefficient is independent of Re).

To explore the hydrothermal performance of the heat sink in their investigation, they developed analytical models to obtain the overall thermal resistance and the total pressure drop. They formulated the total thermal resistance using a thermal resistance network model which is based on the equivalent thermal circuit method and determined the pressure drop by considering a straight channel along with the bend loss. Their proposed correlation of pressure loss coefficient for sharp bends was valid for ($1 < a < 6$) and ($0.25 < b < 2$).

The objective functions of the optimisation problem were the pressure drop (ΔP) and the thermal resistance (R_{th}), while the design parameters to be optimised were the number of channels ($4 < N < 20$), channel width in mm ($1 < W_{ch} < 4$), channel height in mm ($2 < H_{ch} < 5$) and the inlet velocity in m/s ($0 < V < 2$). The optimisation problem was subjected to constraints of fixing length ($L = 32\text{ mm}$), width ($W = 32\text{ mm}$) of the heat sink and the thickness of base plate ($t_b = 1\text{ mm}$).

The study showed that optimizing the channel parameters and the inlet velocity could minimise simultaneously thermal resistance and pressure drop. They validated the optimisation results for five representative solutions using CFD simulations. It is found that the relative error between the objective functions extracted from the Pareto front and those from the CFD simulations are in good agreement with maximum error less than 7.1% except for one design ($N = 10$, $W_{ch} = 2.8\text{ mm}$, $H = 5$ and $V = 0.389\text{ m/s}$) where the difference was 12%. They attributed that discrepancy to the fact that the value of the ratio of the width of the fin and width of the channel (≈ 0.13) occurred out of the range of bend loss coefficient correlation.

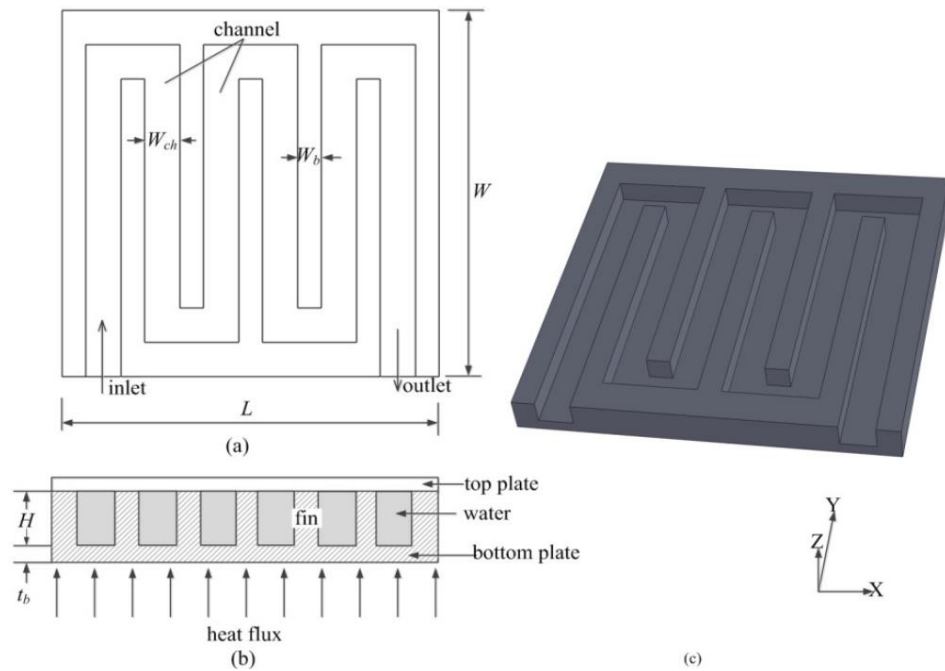


Fig. 2-6 Schematic of the heat sink with serpentine channel: (a) top view, (b) side view, and (c) isometric view (Reproduced from Li et al., 2013 with permission).

In another study, Hao *et al.* (2014) investigated the same heat sink configuration of Li *et al.* (2013) work. They also developed analytical models for the overall thermal resistance and the pressure drop to explore the hydrothermal performance of the serpentine channel heat sinks with 180° bends. They formulated the total thermal resistance using a thermal resistance network model which is based on the equivalent thermal circuit method. They also determined the pressure drop by considering a straight channel along with the bend loss as the bends break the hydrodynamic boundary periodically. The validation of the numerical results has been performed experimentally by measuring temperature and pressure characteristics of heat sinks with Reynolds number in the range (1000 – 2200) and eight heat sink configurations with different geometric parameters. These studied geometric parameters were the aspect ratio of the cross-section of channels ($1 < a < 6$) and ratio of fin width to channel width ($0.25 < b < 2$). The authors have demonstrated that the bend loss coefficient is highly dependent on the geometric parameters of the channel, i.e. a and b , while it is independent of Reynolds number. In contrast, they have illustrated that the thermal resistance and pressure losses are strong functions of the Reynolds number but less sensitive to the geometric parameters. They found that the total pressure drop penalty increased from 13 kPa to 60 kPa when Re raised from 500 to 1500.

Another investigation has been implemented by Al-Neama *et al.* (2017) where they studied numerically and experimentally the effect of four different designs, Fig. 2-7, for the *MCHS* on its hydrothermal performance. The first design had an array of straight rectangular microchannels (*SRMs*), Fig. 2-7 (a), while the rest had single (*SPSMs*), double (*DPSMs*) and triple path multi-serpentine rectangular microchannels (*TSPSMs*), Fig. 2-7 (b). They employed the conjugate heat transfer model for the laminar and turbulent flows for each design in their study. They were successful in achieving an enhancement in the average Nusselt number up to 35% and a reduction in total thermal resistance of 19% at a volumetric flow rate of 8.333 *ml/s* for the *SPSM* in comparison to the straight rectangular microchannel. This improvement, nonetheless, was accompanied by a high pressure drop.

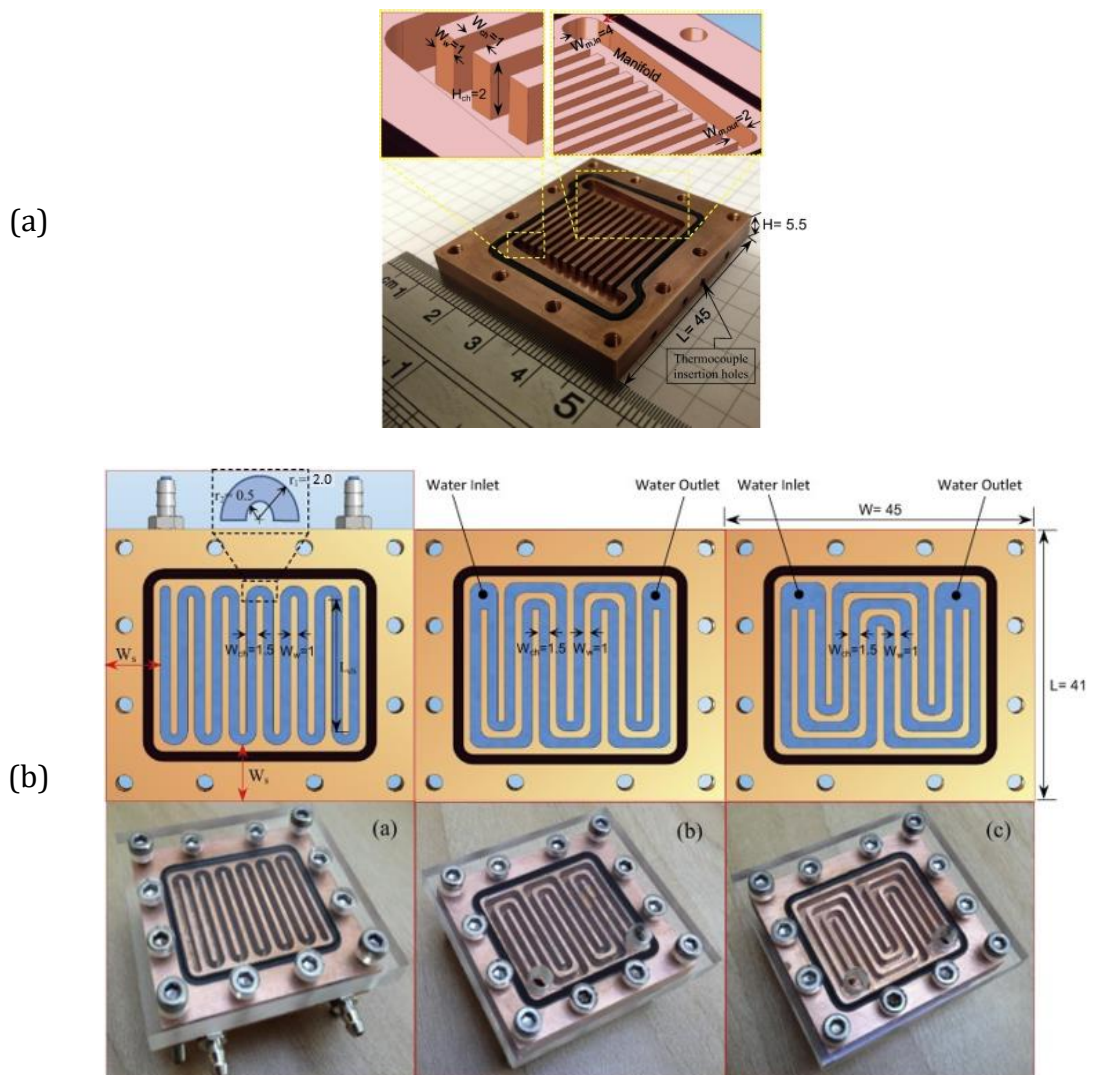


Fig. 2-7 Different minichannel heat sinks studied by Al-Neama *et al.* (2017): (a) *SRMs* and (b) *SPSMs*, *DPSMs* and *TSPSMs* (Reproduced with permission).

In another study of Al-Neema *et al.* (2018) they modified their previous work by introducing chevron fins to the serpentine microchannel heat sink design to provide a secondary path that aimed at improving the performance of the *MCHS*, Fig. 2-8. They tested the effect of the channel width (W_{ch}), number of main channels (N_c) and chevron fin's oblique angle (θ) on the hydrothermal characteristics of the water-cooled minichannel heat sinks. They demonstrated that providing fins structures reduces the thermal resistance and the pressure drop by 10% and 60%, respectively.

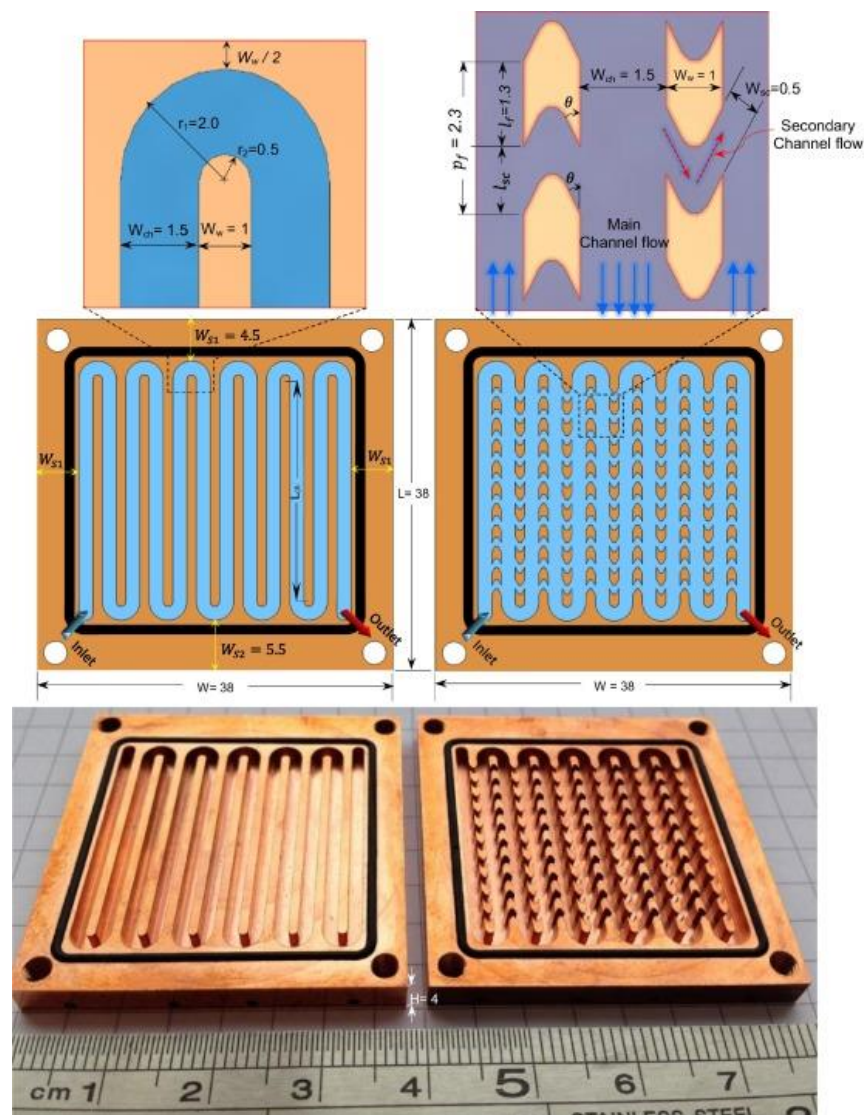


Fig. 2-8 Geometries investigated by Al-Neema *et al.* (2018): serpentine rectangular with plate fins, *SMCHS – PF* (left), and serpentine rectangular with chevron fins, *SMCHS – CF* (Right) (Reproduced with permission).

Imran *et al.* (2018) carried out a numerical and experimental investigation of the heat transfer and fluid flow of serpentine minichannel heat sink (*SMCHS*) with four

configurations, Fig. 2-9. The heat sink was made of copper and water was employed as a coolant. In their numerical part, they used the finite volume technique to simulate laminar single-phase flow through the *SMCHS*. Their numerical results were validated against the experimental measurements and they were in good agreement. They conducted the experimental study under the conditions of flow rate in the range of $0.1 - 0.6 \text{ l/m}$, the heat load between $40 - 400 \text{ W}$ and inlet temperature of 300 K . The length, width and base height of the heat sink were 150 mm , 100 mm and 10 mm , respectively, whereas the channel width was 4 mm and the height was 5 mm . All the heat sinks models were manufactured having the same channel total length of 0.9 m . The study revealed that Nusselt number increases significantly with increasing the mass flow rate while it slightly rises with increasing heat flux and this behaviour agrees with the findings of Al-Neama *et al.* (2017). The pressure drop for all the configurations was increased as the mass flow rate increased. They concluded that the proposed heat sinks, i.e. configurations B, C, and D offered better performance than the conventional serpentine one, i.e. configuration A. Comparing the performance of studied configurations, design B offered a maximum heat transfer enhancement of 136% while Design C showed the best pressure drop enhancement of 50%.

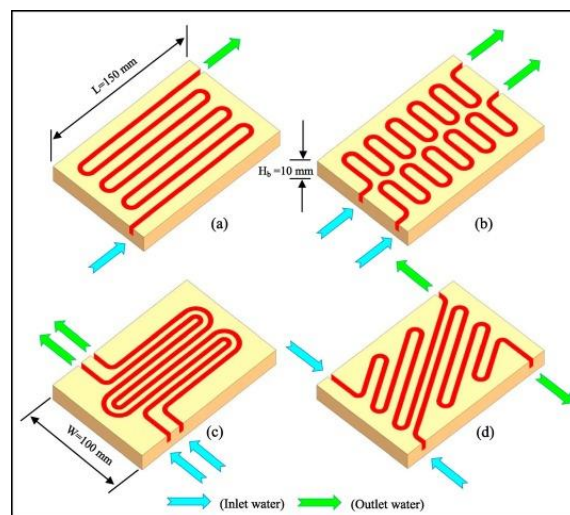


Fig. 2-9 The four configurations of the serpentine microchannel heat sinks studied by Imran *et al.* (2018) (Reproduced with permission).

The serpentine-channel design has also been employed in battery thermal management systems (BTMS) to maintain battery temperature stability. For example, Jiaqiang *et al.* (2018) conducted a numerical study to improve the designs

of the serpentine-channel cold plate for cooling high-energy battery cells utilised in electric vehicles. They developed models for the thermal resistance and pressure loss to characterise the hydrothermal performance of the cold plate in their investigation. For the optimisation procedure, they considered the thermal resistance and the pressure loss as objective functions and defined the width of channel l_w and the radius of the channel's bend r_i as design variables. They recommended selecting large values for l_w and r_i to help in producing an optimum structure for a serpentine-channel cold plate design with the best cooling effect and the minimum pressure loss.

More recently, Al-Neama (Al-Neama *et al.*, 2018) explored the suitability of water-cooled serpentine rectangular minichannel heat sinks (*MCHS*) for cooling gallium nitride (GaN) high-electron-mobility transistors (HEMTs) devices. They developed a CFD model to simulate the laminar flow conjugate heat transfer problem and then validated the computational results against their experimental measurements. Their research aimed at investigating the effect of volumetric flow rate, heat spreaders and heat spreader materials on the temperature of the chip.

Different materials have been used in their study, namely graphene, diamond, silicon carbide (SiC) and silicon (Si). The size of the copper heat sink block was $10\text{ mm} \times 10\text{ mm} \times 2\text{ mm}$ while the minichannel width (W_{ch}), the minichannel height (H_{ch}) and wall width (W_w) are respectively 0.75 mm , 1.5 mm and 0.594 mm . The heat flux dissipated from the GaN HEMT was 1823 W/cm^2 (The total power dissipated from the GaN HEMT was 70 W).

To mitigate the hot spots, the authors used a nanocrystalline diamond (NCD) layer with a thickness of $2\text{ }\mu\text{m}$ mounted on the top surface of the GaN HEMT. They found that using a graphene heat spreader with $25\text{ }\mu\text{m}$ thick along with NCD layer can lower the maximum chip temperature from $124.7\text{ }^\circ\text{C}$ to $96.7\text{ }^\circ\text{C}$ in comparison with a serpentine *MCHS* without these heat spreaders. Also, the simulation results demonstrated that the effect of the heat spreader thickness for the studied materials differs from one material to another. For example, moderate benefits were gained from increasing the heat spreader thickness for diamond while there were no remarkable benefits from increasing the thickness of the SiC heat spreaders more than $300\text{ }\mu\text{m}$. On the other hand, increasing the thickness from $100\text{ }\mu\text{m}$ to $600\text{ }\mu\text{m}$

for Si heat spreader, which has a relatively low thermal conductivity, causes the maximum chip temperature to jump from 207 °C to 253 °C.

2.6 Optimisation of Microchannel Heat Sinks

2.6.1 Deterministic Optimisation of Microchannel Heat Sinks

In order to get the best performance for the heat sink, a noticeable effort has been dedicated to optimizing the shape of the heat sink. Husain and Kim (2008) investigated numerically the optimisation of a silicon microchannel heat sink. In their study, they had exploited surrogate modelling to save time and reduce the cost of numerical computational resources. They selected three geometric variables, i.e. the microchannel width (W_c), depth (H_c) and fin width (W_w) and combined them in two design variables by normalizing with the channel depth, i.e. $\theta (= W_c/H_c)$ and $\phi (= W_w/H_c)$. They optimised the heat sink performance by formulating the multi-optimisation for the thermal resistance and pressure drop. They employed water as a coolant and took into consideration the dependency of the thermal properties on temperature following the proposal of Li *et al.* (2007). They constructed a polynomial surrogate model using the design of experiment (DoE) points of the design variables and values of the objective functions which had been evaluated numerically at each DoE point. This model has been employed to conduct the optimisation process for the objective functions and produce global Pareto optimal solutions using the evolutionary algorithm (NSGA-II). They concluded that the effect of the two design variables was significant on the thermal resistance and the pumping power for the microchannel heat sink. They found that the Pareto optimal solutions have a good spread over the range of the design variables which gives more flexibility in handling the design and manufacturing constraints.

Another optimisation investigation has been performed by Chen *et al.* (2014) to explore the optimum designs for the serpentine-channel heat sink which was studied by Li *et al.* (2013). They defined the height and width of the channel, width of the fin, and the inlet velocity as the design variables with the total thermal resistance (R_{th}) and the pressure drop (ΔP) as the objectives of the optimisation problem subjected to the constraints of constant width and length of the heat sink. In their work, the artificial swarm fish algorithm with a variable population size was

used to obtain Pareto optimal solutions and they had validated these results by conducting experiments. The results were presented pictorially as a Pareto-front, which is a trade-off between total thermal resistance and pressure drop.

Reddy *et al.* (2017) carried out a numerical analysis for the three-dimensional conjugate heat transfer problem of a heat sink with pin-fins (shaped as circles, symmetric airfoils, and symmetric convex lenses) used in cooling an integrated circuit. A uniform heat flux of 500 W/cm^2 was applied over the entire footprint, with size of $4 \times 3 \text{ mm}$, and a centrally located, $0.5 \times 0.5 \text{ mm}$, hot spot with uniform heat flux of 2000 W/cm^2 . The goal was to find the optimum sizes of the pin-fins in addition to the average speed and inlet pressure for the cooling fluid that minimise simultaneously the pumping power and maximum substrate temperature while constraining the maximum temperature to be below 85°C . The optimisation strategy was based on a surrogate model multi-objective optimisation and employed the genetic algorithm as the optimiser to obtain the best trade-off solutions, i.e. the Pareto front. The study found that the pin-fin with symmetric convex lens shapes produce the lowest pressure drop, followed by the symmetric airfoil and circular cross-section pin-fins.

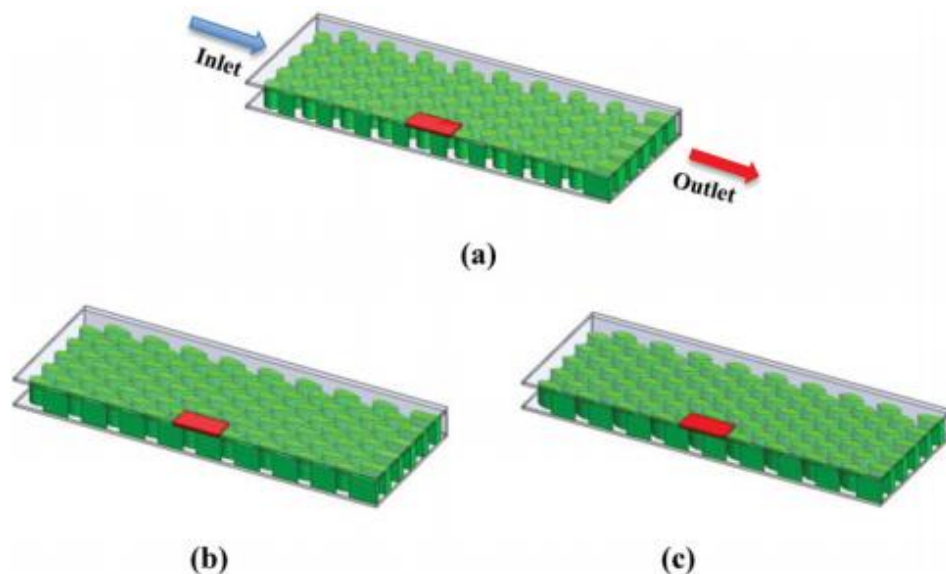


Fig. 2-10 Half domain of the micro pin-fins heat sink with: (a) circular, (b) symmetric airfoil, and (c) symmetric convex cross sections (Reproduced from Reddy *et al.* (2017) with permission).

Later on, Al-Neama *et al.* (2017) performed the structural design and optimisation of thermal performance of the serpentine minichannel heat sink for cooling the

electronic equipments. The goal was to find the channel's width (W_{ch}) and the number of channel (N_{ch}) that minimise the two conflicting objectives, i.e. the total thermal resistance (R_{th}) and the pressure drop (ΔP). They used the Optimal Latin Hypercube (OLHC) approach to generate the DoE points that were utilised in generating the surrogate model. The surrogate model type was Moving Least Squares (MLS) approximation with a second order base polynomial. They employed the multi-objective genetic algorithm (*moga*) method to find the global minimum of the surrogate models and their results were presented graphically as a Pareto front for the two objective functions. In another study of Al-Neama (2018), they modified their previous work by introducing chevron fins to the serpentine minichannel heat sink design to provide secondary paths that aimed at improving the performance of the *MCHS*, Fig. 2-8. They performed an optimisation process for the water-cooled minichannel heat sinks in terms of the channel's width (W_{ch}), number of channels (N_{ch}) and chevron's oblique angle (θ). They used the OLHC to sample the design space and MLS to generate the surrogate models. They performed the surrogate-based optimisation utilising the multi-objective genetic algorithm. Their optimisation results have been summarised in the Pareto front curve that helps designers in selecting appropriate compromises between the conflicting performance parameters of *MCHS* – *CF*, i.e. the pressure drop and the thermal resistance.

Recently, Shi *et al.* (2019) conducted a multi-objective optimisation for the geometrical parameters of an *MCHS* with the secondary flow, Fig. 2-11, to minimise the thermal resistance and pumping power of the heat sink under constant water mass flow rate. They selected the ratio of secondary channel width to microchannel width (α), the ratio of half pitch of secondary channel to microchannel width (β), and the tangent value of secondary channel angle (γ) as the design variable for the optimisation problem. They concluded that the design variable (α) has the greatest influence on the performance of the *MCHS* in comparison to the other design variable, i.e. (β) and (γ). According to the authors, the thermal resistance and pumping power can be reduced by 28.7% and 22.9%, respectively, by optimizing the structure parameters.

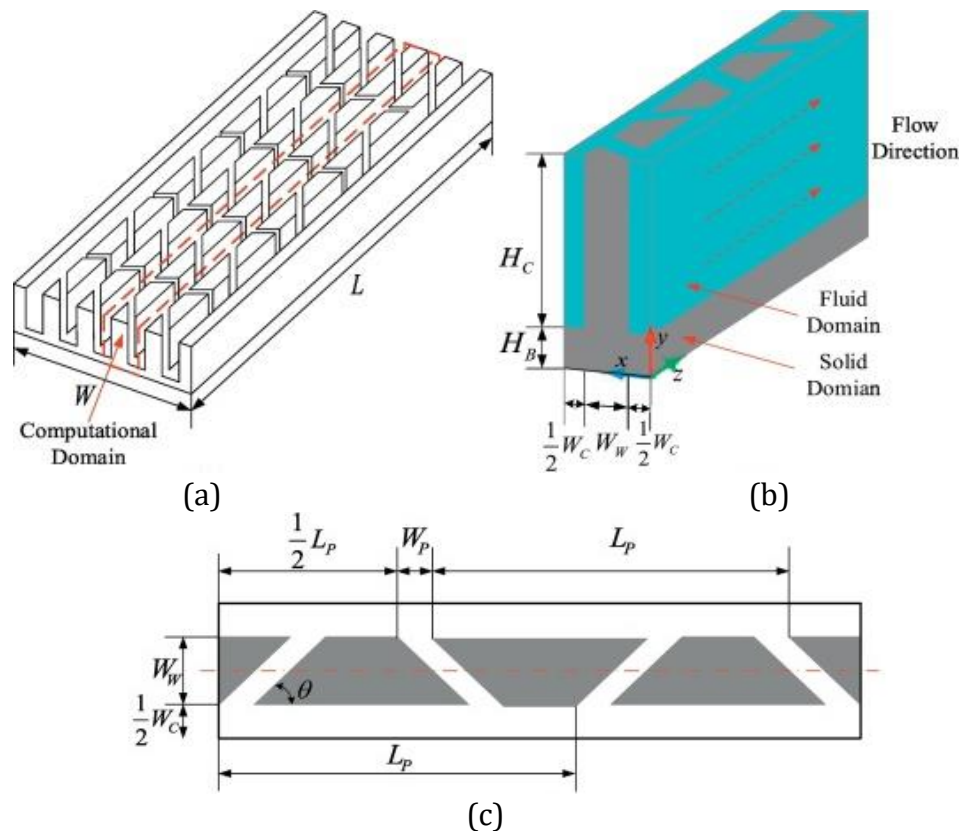


Fig. 2-11 Schematic diagram of the microchannel heat sink (a) 3D full geometry (b) computational domain and (c) top view of the computational domain (Reproduced from Shi *et al.* (2019)) with permission).

There are other studies that dealt with the optimisation of the *MCHS* such as the investigation of Knight *et al.* (1992), Hung *et al.* (2012) and Alfaryjat *et al.* (2014). Besides, optimisation of the microchannel heat sinks by varying the geometric dimensions has also been carried out in order to improve the hydrothermal performance of the heat sink, like the studies of Ahmed and Ahmed (2015) and Fan *et al.* (2014). A recent review for optimisation of the thermal design of heat sinks has been conducted by Ahmed *et al.* (2018) and they did not mention any work that considered the uncertainty in the input parameters for optimisation microchannels heat sinks, e.g. variations in geometrical shape due to manufacturing errors or in operating conditions, and their effect on hydrothermal performance. Producing robust designs which are insensitive to the variations of the input parameters is vital for some applications like safety-critical applications, e.g. the aerospace industry.

2.6.2 Robust Design

There are numerous sources uncertainty in the heat sink and in the modelling context the uncertainties have been classified as either aleatory or epistemic. The

root of the word aleatory is Latin '*alea*' which means the rolling of dice. Therefore, aleatory uncertainty (which is also known as type (A), stochastic uncertainty, or irreducible uncertainty) represents an inherent randomness of the system or process such as the variability in geometric parameters due to manufacturing processes, the uncertainty in material property constants and uncertainty in weather conditions. This type of uncertainty is physical in nature and probability theory can be used to mathematically model this kind of uncertainty due to its probabilistic nature. On the other hand, the root of the word epistemic is Greek '*επιστημη*' (episteme) which means knowledge. So epistemic uncertainty (which is also known as type (B) or reducible uncertainty) refers to a lack of information or data about the appropriate value to use for a quantity at the time of decision. Imperfect understanding of physical phenomena or physical coupling, and inadequate experimental data to accurately describe a probability distribution are both examples of epistemic uncertainty (Romero *et al.*, 2004; Sahinidis, 2004; Oberkampf and Ferson, 2007; Der Kiureghian and Ditlevsen, 2009; Bodla *et al.* 2013 and Shahbaz *et al.*, 2016). Including the uncertainties within the optimisation helps in obtaining robust and reliable designs. This type of optimisation is called the non-deterministic optimisation, probabilistic optimisation or optimisation under uncertainty (OUU).

Non-deterministic optimization has attracted increasing attention during the last two decades. This type of optimization has two different design formulations that consider the probability in the response of the system, namely Reliability-Based Design Optimization (RBDO) and Robust Design Optimization (RDO), Fig. 2-12. The former seeks a safe design in the presence of parameters' variability, while the goal of the second kind is to produce a design insensitive to the uncertainty associated with design variables (Doltsinis and Kang, 2004 and Papadrakakis *et al.* 2005). The start of robust design dated back to the early 1920s when Fisher was working on developing the statistical design of experiments (DoE) method to increase the yield of agricultural crops. During the 1950s, the Japanese engineer Dr. Genichi Taguchi, which is known as the "father of robust design", set up the basics of the robust design, (Shahbaz *et al.*, 2016).

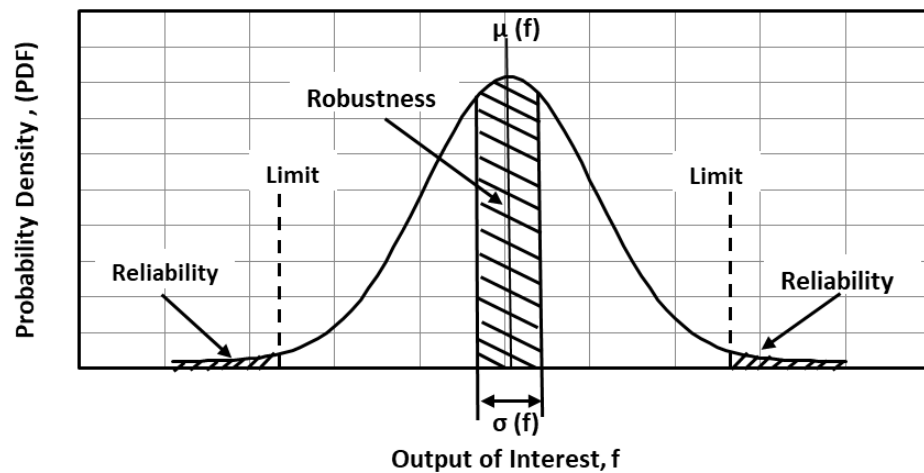


Fig. 2-12: Comparison between robust and reliable design concepts in terms of PDF.

In previous works, robust optimization in structural design have been widely studied. For example, Doltsinis and Kang (2004) proposed a new method to investigate numerically the robust design of structures with stochastic parameters. In their proposed approach, they evaluated the sensitivity of the mean and variance of structural response based on the perturbed equations for stochastic analysis. They also formulated the robust design optimization of structures as a multi-objective optimization problem aimed at minimizing the expected value and the standard deviation of performance. Thereafter, the multi-criteria optimization problem has been converted into a scalar optimization problem and solved using a gradient based optimization algorithm. Later on, Marano *et al.* (2010) conducted a comparison between conventional deterministic and robust optimum design methods used in structural optimization. They employed the problem of the optimum design for mechanical characteristics of a single tuned mass damper (TMD) device as a case of study. To perform the robust design strategy, they included not only the absolute performance of the system but took into account its sensitivity to the uncertain parameters. The comparison revealed the importance of conducting a robust design as it provided solutions which differed from the deterministic one.

Robust Design in other Disciplines

As the literature shows, robust design has been widely utilised by researchers in aerodynamic design optimization with the aim of minimizing the statistical moments, i.e. mean and variance, of the objective function over alterations of

uncertain design parameters. For example, Zaho *et al.* (2014) studied numerically the design robustness of a transonic, high Reynolds number laminar flow supercritical airfoil. They used $\gamma - \theta$ transition model along with the shear stress transport (SST) $k - w$ turbulence model to predict the transition region for a laminar-turbulent boundary layer. They employed a surrogate model based on Kriging models to reduce the cost of evaluating the objective functions and used the non-dominated sorting genetic algorithm-II (NSGA-II) to search for the optimum solutions of the multi-objective problem. The type of the airfoil was NASA0412, and the uncertain variable for the robust design was the Mach number. They analysed and compared their results of the optimised design with original airfoil and found that natural laminar flow can be achieved on a transonic supercritical airfoil leading to considerably decrease in the drag coefficient. They noticed the importance of introducing robust design to achieve a compromise between the drag and the drag divergence characteristics of the airfoil. They also achieved a trade-off between the mean value and the variance by employing a multi-object evolution strategy.

Shahbaz *et al.* (2016) have implemented a robust aerodynamic design optimization for a RAE 2822 airfoil to reduce the statistical mean and variance of drag coefficient (C_d) over two uncertain input variables, namely the Mach number and angle of attack. An in-house code, PMNS2D, has been employed to calculate the CFD model response for the airfoil design. The statistical parameters and probability density functions of the design response quantities have been extracted using an inexpensive Monte Carlo (IMC) approach with a kriging surrogate model to assess the robustness of a candidate design. To judge the accuracy of the surrogate model in their study, they compared the CFD outputs for the aerodynamic coefficients with predicted values using the surrogate model and found them accurate. They achieved a reduction in the objective function, drag coefficient (C_d), around 37.48% and 39.19% for the combination of the angle of attack and Mach number uncertainties under normal and LHS distributions respectively.

Recently, Chakraborty *et al.* (2017) have suggested two new methods to solve robust design optimization (RDO) problems. The first one is the low-fidelity (LF) polynomial correlated function expansion (PCFE) based differential evolution algorithm (DEA), and the second is the high-fidelity (HF) PCFE based DEA. In each one, they combined polynomial correlated function expansion (PCFE) with

differential evaluation algorithm (DEA) in which the first was to calculate the statistical moment properties of performance functions while the second was employed to solve the optimization problem. In order to assess the performance of the proposed approaches, they have been applied to three benchmark RDO problems, and the accuracy and efficiency of their results were outperforming the popular techniques, i.e. Kriging, Taylor's series and tensor product quadrature. They stated that the low fidelity PCFE based DEA could be used to obtain an initial estimate for the RDO problems as it is highly efficient. Furthermore, they demonstrated the capability of the suggested methods in solving large scale problems like the RDO of a hydroelectric dam.

Uncertainty analysis for building energy assessment, according to Tian *et al.* (2018) in their review, is now considered one of the active field researches. This trend is because the thermal performance of buildings is affected by several variables which are inherently uncertain like weather conditions, residents' behaviour and thermal properties of the building envelope. Different areas of building energy analysis have been extensively studied using uncertainty analysis such as life cycle analysis, impact and adaptation to climate change, sensitivity analysis and optimization, to name of few. The two main methods of uncertainty analysis, i.e. forward (uncertainty propagation) and inverse (model calibration) uncertainty quantification have been employed in building energy assessment. The focus of the first type is to quantify the uncertainty in the system outputs (e.g. energy use or carbon emissions) propagated from uncertain input variables through mathematical models (building energy models) while the second type of the uncertainty quantification aimed at predicting the unknown variables through mathematical models from measurement data. On one hand, the literature is showing that the most widely used methods for the forward uncertainty analysis are the Monte Carlo sampling-based, non-sampling, and non-probabilistic. On the other hand, the frequentist and Bayesian approaches have been employed extensively in the inverse uncertainty analysis (Tian *et al.*, 2018).

Huang *et al.* (2017) proposed a new strategy for optimal sizing of the heating, ventilating, and air-conditioning (HVAC) systems under uncertainty in both load-demand and capacity-supply side from a life-cycle point of view. At the design stage, the uncertainty in HVAC system sizing comes from different sources such as

inaccurate prediction of system operating cost and energy performance due to the lack of information about the operational data and building's peak load demand. With the classical method of HVAC system sizing procedure, the designers are dealing implicitly with uncertainty by choosing a safety factor to minimise professional risk, which produces an oversizing system. In the suggested method, however, the authors studied the uncertainty on the cooling supply side and demonstrated its importance for proper HVAC system sizing. In their investigation, they employed Monte-Carlo simulation to produce the statistical distribution of the predicted peak cooling load while they used an open source software called EnergyPlus to generate the life-cycle performance data for the HVAC system.

In order to reduce the number of the Monte Carlo simulations for producing a robust system sizing of nearly/net zero energy buildings (ZEBs), Zhang *et al.* (2018) proposed a response-surface-model-based system sizing method. Three design criteria namely, the annual energy match ratio (AEMR), self-consumption ratio (SCR) and initial investment have been selected for their study. These criteria depended on three design points: annual energy demand, photovoltaic (PV) energy generation ratio and daily energy demand. The energy performance evaluation of the system has been performed using a popular building simulation tool called *TRNSYS*. The authors have constructed the response surface model, polynomial regression model, for the overall performance, i.e. the weighted performance of the design criteria, based on Monte Carlo simulations for 29 specific design points. These points have been determined by the design of experiments, Box-Behnken design. The predicted value of AEMR and SCR were in good agreement with actual values, and the percentage of errors were, respectively, 0.6 and 1.2. Exploiting the established response surface models, the performance has been evaluated, and the optimal design has been chosen. Their results showed that the proposed methodology had mitigated the computational load required to identify the optimal design.

Robust Optimization of Microchannel Heat Sinks

In the literature, two studies on the importance and applying the optimization under uncertainty (OUU) for microchannels heat sink have been conducted by Bodla *et al.*(2013) and Sarangi *et al.*(2014). The study of Bodla *et al.*(2013) performed

optimization under uncertainty (OUU) for both heater block and pin-fin heat sink with the impinging flow. They used Ansys Fluent for the numerical analysis and Dakota, an open-source software, to implement the optimization. To mitigate the cost of the CFD simulations, they utilised surrogate models obtained from generalised polynomial chaos (gPC). Besides, they used the nested approach within Dakota to perform the uncertainty quantification (UQ) for the optimization loop. They concluded that this methodology, i.e. optimization under uncertainty, is a powerful tool to produce a robust and reliable design if the input parameters are uncertain. The robust design aimed at minimizing the fluctuation in system performance resulting from the variation of the system input, while the aim of the reliable design is producing a design with low probability of failure under uncertainties.

Later, Sarangi *et al.* (2014) studied the geometric parameters of the manifold microchannel heat sink. In their study, two different computational analysis methods, a simple unit-cell model and porous-medium model, were employed. Furthermore, they conducted conventional deterministic optimization along with probabilistic optimization to determine the optimal parameters of the heat sink geometry that maximise heat transfer performance while minimizing pumping power. They utilised the same framework of the OUU used in the study of Bodla *et al.*(2013). They quantified the conservative nature of the probabilistic design method by comparing the deterministic and probabilistic optimization methodologies. They concluded that the maximum heat transfer occurs when the ratio of the inlet to outlet length is 3.

2.7 Gaps in knowledge and the aims of the current research

Based on the published literature reviewed in this chapter and to the best of the author knowledge, no previous study has examined the influence of adding half-cylindrical vortex generators to the sidewalls or the channel's base for the serpentine minichannel heat sink. Furthermore, there are some aspects such as the number of fins (F_n), the fin length to the secondary channel length (R_{FS}) and the fins offset (F_o) in the study of Al-Neama *et al.* (2018) that need to be covered. Besides, a simpler design, such as the hybrid rectangular-elliptical shaped fin for replacing the

chevron fins, need to be explored. The literature also showed that no study applied the OUU for the serpentine minichannel heat sinks. Therefore, this PhD study will try to bridge these gaps. Before addressing these, some heat transfer and fluid flow fundamentals related to the current research will be presented in the next chapter.

Chapter 3 Heat Transfer and Fluid Flow

Fundamentals

3.1 Introduction

In this chapter, an overview of the basic concepts of heat transfer and fluid flow for the microchannel heat sinks are given. These concepts represent the basis of the work that will be carried out in the following chapters. Firstly, a review of some heat transfer and fluid flow basics will be provided in sections 3.2 and 3.3. In section 3.4, the hydrodynamic and thermal boundary layer concepts will be explained. Furthermore, sections 3.5 and 3.6 present a brief description of the flow entrance region characteristics and the conjugate heat transfer problems. After that, sections 3.7 and 3.8 provide the governing equations for the modelling of microchannel heat sinks beside the assumptions and boundary conditions for the problem under study. A summary of this chapter will be given in section 3.9.

To study the hydro-thermal performance of microchannel heat sinks numerically or experimentally, there are several characteristics that need to be evaluated including Reynolds number, Prandtl number, Nusselt number, the average temperature for the base of the heat sink substrate, overall thermal resistance, fluid velocity distribution, fluid pressure drop and the pumping power of the fluid. Therefore, it is worth reviewing some of the heat transfer and fluid flow fundamentals in the following sections.

3.2 Heat Transfer Basics

Heat transfer is the process of transferring energy from one region to another when a temperature gradient exists. There are three modes of heat transfer: conduction, convection and radiation. Basically, conduction heat transfer takes place across a solid (or a stationary fluid) due to the presence of temperature difference in the medium. While the heat transfer by convection occurs between a solid and fluid, in contact, at different temperature which it can be free convection (buoyancy force causes fluid motion) or forced convection (external source forces the fluid to move). Finally, the heat transfer by thermal radiation is the process in which two solid

bodies or more (not in direct physical contact) at different temperature exchange thermal energy. The space between the bodies could be a vacuum or could be filled with gas or liquid (Sachdeva, 2009 and Cengel, 2014).

Microchannel heat sinks mainly dissipate the generated heat in electronics through two modes of heat transfer, i.e. conduction and convection. With the presence of temperature differences across the heat sink, heat is transferred from the source to the fluid in the microchannels. The fluid that flows inside the channels, in turn, takes the heat by convection and rejects it to the ambient. The rate of heat transfer by conduction is expressed by Fourier's law as:

$$\dot{Q}_{cond} = k A \frac{(T_{s1} - T_{s2})}{L} \quad \text{Equ. 3-1}$$

where \dot{Q}_{cond} , k , A and T_s , L respectively represent the rate of heat transfer by conduction, the thermal conductivity, the heat transfer area, the temperatures on solid sides and wall thickness. According to the thermal resistance concept that has been used in heat transfer analysis, the conductive thermal resistance is:

$$R_{cond} = \frac{L}{k A} \quad \text{Equ. 3-2}$$

Heat sinks are usually manufactured from a high thermal conductivity material with a large surface area to reduce the conductive thermal resistance and hence improve the thermal performance of the heat sinks.

On the other hand, the rate of heat transfer by convection is governed by Newton's law of cooling:

$$\dot{Q}_{conv} = h A (T_s - T_{\infty}) \quad \text{Equ. 3-3}$$

where \dot{Q}_{conv} , h , A , T_s and T_{∞} are the rate of heat transfer by convection, heat transfer coefficient, the heat transfer area, surface temperature and fluid temperature, respectively (Bergman *et al.*, 2011 and Çengel *et al.*, 2012). The convective thermal resistance can be written as:

$$R_{conv} = \frac{1}{h A} \quad \text{Equ. 3-4}$$

In convective heat transfer studies, a commonly used nondimensional parameter is the Nusselt number which is the nondimensional form of heat transfer coefficient.

This parameter is defined as the ratio of convective heat transfer to conductive heat transfer:

$$Nu = \frac{\text{Convective heat transfer}}{\text{Conductive heat transfer}} = \frac{h L}{k} \quad \text{Equ. 3-5}$$

Nusselt number is used to assess the enhancement of heat transfer caused by convection relative to conduction heat transfer.

3.3 Fluid Flow Basics

Fluid mechanics plays a vital role in analysis of convective heat transfer; therefore, it is worth presenting the basic concept briefly here. In fluid mechanics applications, there are generally two kinds of flow namely the external flow and internal flow. The external flow refers to the flow of unconfined fluid such as flow over a surface of a plate, pipe and ball. In contrast, the internal flow represents the flow of a bounded fluid like the flow in ducts and pipes. In microchannel heat sink, since the cooling fluid is bounded by channel walls, it is classified as internal flow.

The flow, furthermore, can be laminar, transient or turbulent depending on its flow velocity. When fluid flows smoothly and its layers do not interact with each other, the flow is called laminar. On the contrary, if the flow is highly disordered and characterised by velocity fluctuation then it is termed as turbulent flow. The transient flow represents the intermediate flow state between the laminar and turbulent flow. Osborne Reynolds in the 1880s performed an experimental investigation to study the flow regime in pipes and found that the ratio of inertial forces to viscous forces in the fluid affects broadly the flow regime. This ratio, then, is termed the Reynolds number (Re) and it is used to identify the flow type and determine the transition from laminar flow to turbulent flow (Çengel, 2010, Bergman *et al.*, 2011 and Çengel *et al.*, 2012). Reynolds number (Re) is expressed as follows:

$$Re = \frac{\text{Inertial forces}}{\text{Viscous forces}} = \frac{\rho U_{avg} D}{\mu} \quad \text{Equ. 3-6}$$

here ρ is the density of the fluid, U_{avg} is the average flow velocity, D is the characteristic length of the geometry and μ is the dynamic viscosity.

For internal flow in a circular pipe, the characteristics length of the geometry used in Reynolds number (Re) is the diameter of the pipe whereas it is the hydraulic diameter D_h for noncircular pipes. The hydraulic diameter is defined as:

$$D_h = \frac{4 A_c}{P} \quad \text{Equ. 3-7}$$

where A_c and P are respectively the cross-sectional area of the pipe and its wetted perimeter.

Different factors affect the value of the critical Reynolds number (Re_c), at which the flow transits from laminar to turbulent, such as fluid velocity, surface geometry, surface roughness, the temperature of the surface, and the type of fluid, among other things. For external flow over a smooth flat plate, the critical Reynolds number for the different regimes are as follow (Çengel, 2010, Bergman *et al.*, 2011 and Çengel *et al.*, 2012):

Laminar flow regime	:	$Re_c \leq 10^5$
Transitional flow regime	:	$10^5 \leq Re_c \leq 3 \times 10^6$
Turbulent flow regime	:	$Re_c \geq 3 \times 10^6$

while for internal flow in circular pipes, the values of the critical Reynolds number are listed here (Çengel, 2010 and Bergman *et al.*, 2011):

Laminar flow regime	:	$Re_c \leq 2300$
Transitional flow regime	:	$2300 \leq Re_c \leq 4000$
Turbulent flow regime	:	$Re_c \geq 4000$

3.4 Boundary layer concept

In order to understand the convective heat transfer between a moving fluid and a surface in contact, it is necessary to understand the concept of boundary layers which was introduced by Ludwig Prandtl in 1904 (Sachdeva, 2009 and O'Malley, 2014). There are two kinds of boundary layers which are encountered in convective heat transfer: hydrodynamic boundary layer and thermal boundary layer. Some details about these boundary layers and the related concepts are given below:

3.4.1 Hydrodynamic boundary layer

The concept of the boundary layer is applied in internal and external flows. The boundary layer is a thin layer which can be defined as the flow region in the vicinity of the contact surface where the viscosity effects are significant. Within the boundary layer, the fluid velocity is slowing down in the contact surface vicinity and becomes zero at the surface itself (the no-slip boundary conditions). Outside the boundary layer, there is no velocity gradient. For the external flow, Fig. 3-1(a), the boundary layer over the surface is freely growing because the fluid has a free surface (Çengel, 2010 and Bergman *et al.*, 2011).

Similarly, for internal flows such as the flow of liquid entering a circular pipe, Fig. 3-1(b), it can be seen that the flow is divided into two regions: the hydrodynamic entrance region and the hydraulically fully developed region. The first covers the region from the pipe inlet to a point at which the velocity profile becomes fully developed and its length is termed the hydrodynamic entry length L_h . At the entrance of the pipe, fluid enters with uniform velocity and its particles within the layer that is in contact with the pipe's wall become stationary as a result of the no-slip conditions. As Fig. 3-1 (b) depicts, the boundary layer thickness grows continuously in the flow direction until it meets the centre line and fills the entire pipe. A little farther downstream, the flow becomes fully developed, i.e. the velocity becomes fully developed and remains unchanged; therefore, this region is known as hydrodynamically fully developed. In this region, the velocity profile has a parabolic shape in the laminar flow while it is somewhat flatter in the turbulent flow. This difference in velocity profile can be attributed to the fact that the wall shear stress effect is not as large in the turbulent flow as in the laminar flow, Fig. 3-1 (b), (Çengel, 2010 and Bergman *et al.*, 2011).

3.4.2 Thermal boundary layers

In a similar manner of developing the hydrodynamic boundary layer as a result of fluid flowing over a surface, a thermal boundary layer evolves due to the temperature difference between the flowing fluid and the surface in contact with it, Fig. 3-2 (a). Within the thermal boundary layer, there is a temperature gradient, and the fluid particles in the adjacent layer to the surface are in thermal equilibrium with the solid body (Çengel, 2010 and Bergman *et al.*, 2011).

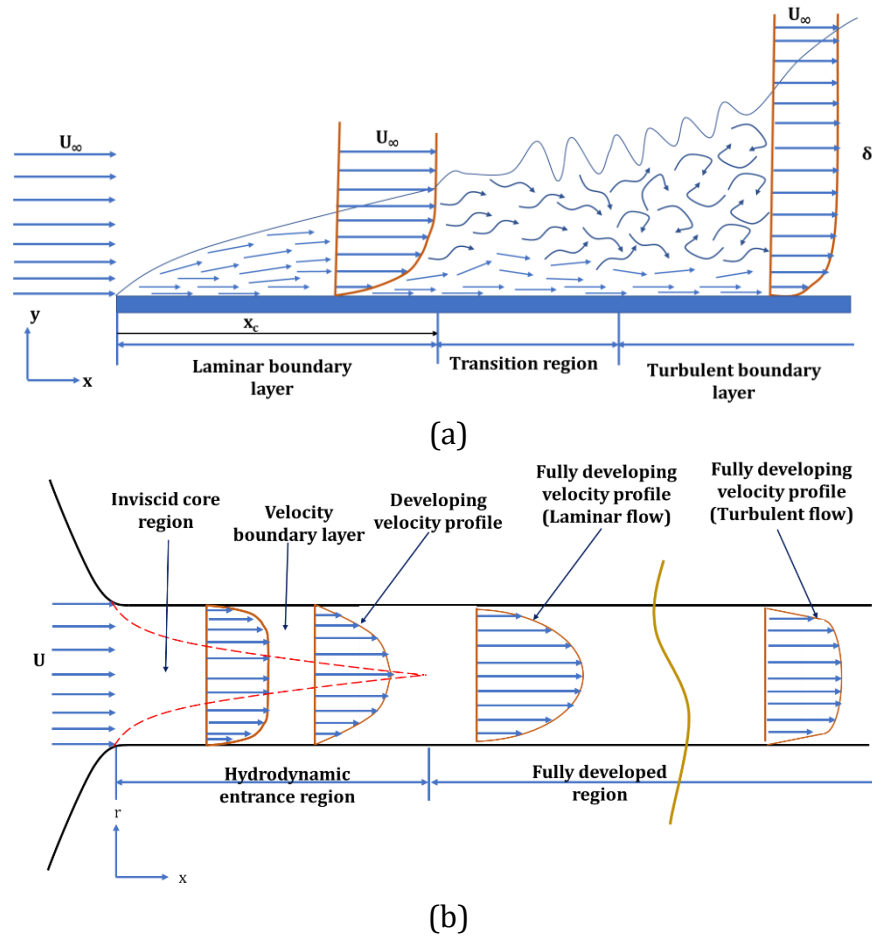


Fig. 3-1. Schematic of typical boundary layer (a) external flow and (b) internal flow.

In the same way, the thermal boundary layer also exists in internal flow if there is a difference in temperatures between the fluid and the bounding surfaces. Furthermore, two regions can be distinguished for this confined flow, i.e. thermal entrance region and thermally fully developed region, Fig. 3-2 (b). The shape of the fully developed temperature profile is fixed, however, it takes a certain pattern based on the imposed wall conditions, i.e. constant temperature or constant heat flux, Fig. 3-2 (b).

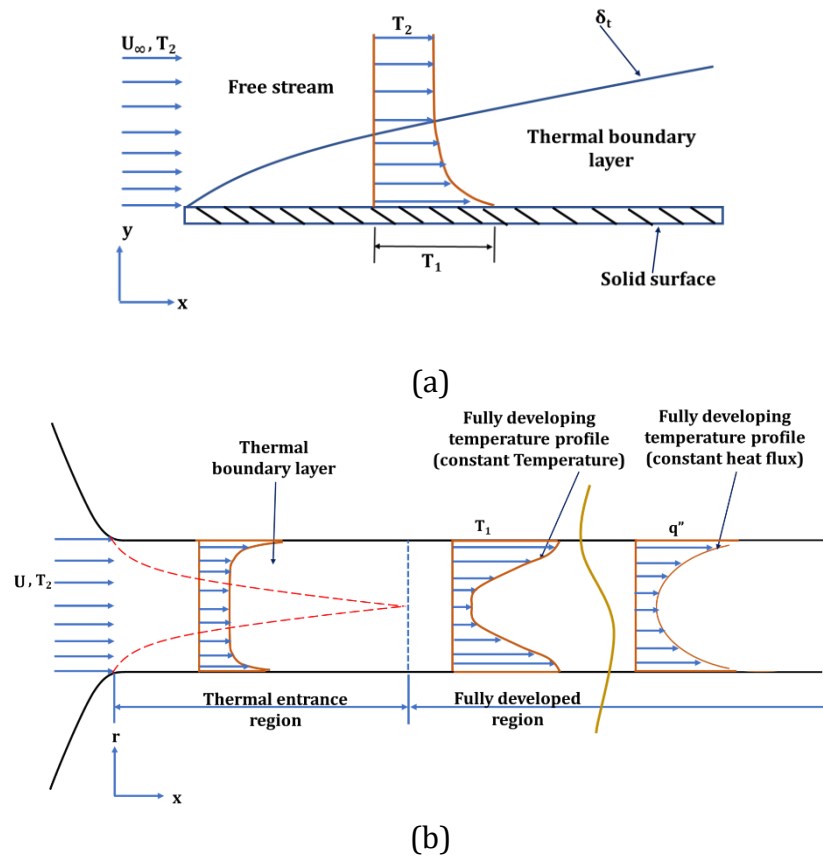


Fig. 3-2. Thermal boundary layer of cold flow: (a) over flat plate and (b) inside pipe.

3.4.3 Significance of the Prandtl Number

Prandtl number (Pr) is a nondimensional parameter which describes the relative thickness of the velocity and the thermal boundary layers (Çengel, 2010) and can be expressed as:

$$Pr = \frac{\text{Molecular diffusivity of momentum}}{\text{Molecular diffusivity of heat}} = \frac{\nu}{\alpha} = \frac{\frac{\mu}{\rho}}{\frac{k}{\rho C_p}} = \frac{\mu C_p}{k} \quad \text{Equ. 3-8}$$

here ν , α , μ , ρ , k and C_p are respectively kinematic viscosity, thermal diffusivity, coefficient of dynamic viscosity, mass density, thermal conductivity and specific heat at constant pressure of the fluid. The kinematic viscosity describes the ability of a fluid to transport momentum by diffusion whereas thermal diffusivity describes the ability of a fluid to transport energy by diffusion (Nellis *et al.*, 2009). From the definition of Prandtl number, it is clear that it is a function of the properties of the fluid itself and does not depend on the state of flow condition of the fluid (i.e. whether the flow is laminar or turbulent flow).

The Prandtl number for fluid changes with temperature and its values range from than 10^{-2} for liquid metals (like Mercury) to more than 10^4 for heavy oils (such as engine oil) (Nellis *et al.*, 2009). All gases have Prandtl number (Pr) values between 0.7 - 1 which implies that the velocity boundary layer thickness (δ) is equal to the thermal boundary layer thickness (δ_t) and this indicates that both momentum and heat dissipate through the fluid at about the same rate. However, if $Pr \ll 1$, like in liquid metals, it indicates that the thermal boundary layer thickness (δ_t) is larger than the velocity boundary layer thickness (δ) and hence heat diffuses very quickly. In contrast, when $Pr \gg 1$, as in engine oils, the thermal boundary layer thickness (δ_t) is thinner than the velocity boundary layer thickness (δ) and as a result, the heat diffusion will be very slow relative to the momentum.

For laminar boundary layers, the relationship between the Prandtl number, thickness of the velocity (δ) and the thermal (δ_t) boundary layers can be expressed mathematically as (Bergman *et al.*, 2011):

$$\frac{\delta}{\delta_t} \approx Pr^n \quad \text{Equ. 3-9}$$

here the exponents (n) is a positive number. According to (Equ. (3-9)), it can be illustrated that for gases that have $Pr \approx 1$ then $\delta_t \approx \delta$, for liquid metals with $Pr \ll 1$ then $\delta_t \gg \delta$ and for oils with $Pr \gg 1$ then $\delta_t \ll \delta$.

3.5 Flow Entrance Region Characteristics

When fluid flow is accompanied with heat transfer in internal flow, the state of the hydrodynamic and thermal boundary layers affects directly the calculations of pressure drop (ΔP) and heat transfer coefficient (h) inside conduits. For laminar flow in ducts, four types of flow based on boundary layers developments have been distinguished, these are the fully (hydrodynamically and thermally) developed, hydrodynamically developing, thermally developing, or simultaneously developing. The same types of flow exist in turbulent duct flow, but their thermal and hydrodynamic entrance lengths are much shorter than their corresponding lengths in laminar duct flow (Rohsenow *et al.*, 1998).

Table 3-1 Types of hydrodynamic and thermal boundary layers developments in duct flow (Rohsenow *et al.*, 1998).

<i>Flow type</i>	<i>Hydrodynamic Boundary layer</i>	<i>Velocity distribution in the flow direction</i>	<i>Friction factor</i>	<i>Thermal boundary layer</i>	<i>Dimensionless Temperature distribution in the flow</i>	<i>Nusselt number</i>
<i>Fully developed flow</i>	Developed	Invariant	Constant	Developed	Invariant	Constant
<i>Hydrodynamically developing flow</i>	Developing	Variant	Variant	-----	-----	-----
<i>Thermally developing flow</i>	Developed	Invariant	Constant	Developing	Variant	Variant
<i>Simultaneously developing flow</i>	Developing	Variant	Variant	Developing	Variant	Variant

Shah and London (2014) proposed two formulae to estimate the hydrodynamic entry length (L_h) and thermal entry length (L_{th}). These are:

$$L_h = L_h^+ \cdot D_h \cdot Re \quad \text{Equ. 3-10}$$

$$L_{th} = L_{th}^* \cdot D_h \cdot Pe \quad \text{Equ. 3-11}$$

where L_h^+ and L_{th}^* are the nondimensional hydrodynamic and thermal entrance lengths and they are both 0.05 (Kandlikar et al., 2014 and Lee et al., 2005). While $Pe (= Re \cdot Pr)$ a dimensionless number termed Peclet number which represents the advective transport rate to mass diffusion rate ($u/(D/L)$).

3.6 Conjugate Heat Transfer Problems

Whenever a domain consists of more than one sub-domain and its heat transfer problem is governed by different differential equations, the conjugate heat transfer becomes an essential tool to solve this kind of problems. In the current study, the fluid comes into contact with solid walls of the heat sink channels and exchange heat; therefore, the conjugate boundary condition should be applied at the fluid-solid interface to solve this heat transfer problem numerically. Accordingly, the continuities of temperature and heat flux at the interface between the solid walls and the fluid are applied, Fig. 3-3, which can be expressed as follow:

Temperature:
$$T_{f,\Gamma} = T_{s,\Gamma} \quad \text{Equ. 3-12}$$

Heat flux (Fourier's law):
$$-k_f \frac{\partial T_f}{\partial n} \Big|_{\Gamma} = -k_s \frac{\partial T_s}{\partial n} \Big|_{\Gamma} \quad \text{Equ. 3-13}$$

Velocities (No slip conditions):
$$u = v = w = 0 \quad \text{Equ. 3-14}$$

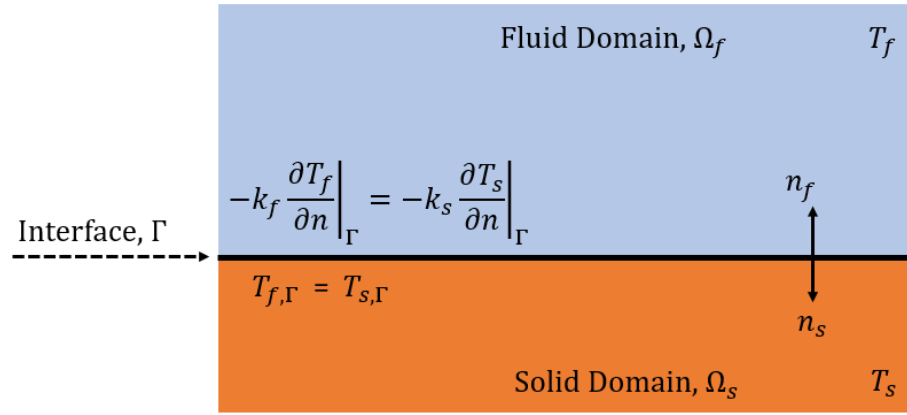


Fig. 3-3. Conjugate boundary conditions between the solid and fluid.

3.7 Governing Equations for microchannel heat sinks

In the current study, the CFD techniques will be employed to solve the convective heat transfer problem in minichannel heat sinks. The generalised form of the governing equations which are used to represent the conjugate heat transfer and fluid flow problem are given below (*COMSOL*):

Continuity equation:

$$\frac{\partial \rho}{\partial t} + \nabla \cdot (\rho \vec{V}) = 0 \quad \text{Equ. 3-15}$$

Momentum equation:

$$\rho \frac{\partial (\vec{V})}{\partial t} + \vec{V} \cdot \nabla (\vec{V}) = -\nabla P + \nabla \cdot (\mu_f (\nabla \vec{V} + (\nabla \vec{V})^T)) - \frac{2}{3} \mu_f (\nabla \vec{V}) I + F_b \quad \text{Equ. 3-16}$$

The energy equation for the fluid:

$$\rho C_p \left(\frac{\partial T}{\partial t} + \vec{V} \cdot \nabla T \right) = \nabla \cdot (k_f \nabla T) + Q \quad \text{Equ. 3-17}$$

The energy equation for the fin:

$$\rho C_p \frac{\partial T}{\partial t} = \nabla \cdot (k_s \nabla T_s) + Q \quad \text{Equ. 3-18}$$

where \vec{V} , ρ , μ_f , C_p , P , T and k are respectively the velocity vector, the density, the viscosity, the specific heat, the fluid pressure, the temperature and thermal

conductivity. The subscript f and s refer to the fluid and solid respectively. The F_b and Q are respectively the body force and the heat source/sink per unit volume and time.

For steady state laminar flow with no heat generation, the above equations can be re-written as:

Continuity equation:

$$\nabla \cdot (\rho \vec{V}) = 0 \quad \text{Equ. 3-19}$$

Momentum equation:

$$\vec{V} \cdot \nabla (\rho \vec{V}) = -\nabla P + \nabla \cdot (\mu_f \nabla \vec{V}) \quad \text{Equ. 3-20}$$

The energy equation for the fluid:

$$\vec{V} \cdot (\rho C_p \nabla T) = \nabla \cdot (k_f \nabla T) \quad \text{Equ. 3-21}$$

The energy equation for the fin:

$$\nabla \cdot (k_s \nabla T_s) = 0 \quad \text{Equ. 3-22}$$

3.8 Assumptions and Boundary Conditions

To simplify the numerical simulations of the current investigation, some assumptions were made following previous works such as Qu and Mudawar (2002a and 2002b), Lee *et al.* (2012), Lee *et al.* (2013), Kuppusamy *et al.* (2014), Al-Neama (2018) and others. These assumptions are as follows:

1. The flow is single-phase, incompressible, and laminar.
2. The heat transfer and fluid flow were assumed to be steady state.
3. No radiation effects.
4. The internal channel walls were assumed smooth.
5. All the external walls of the heat sink were assumed to be insulated ($-n \cdot (-k \nabla T) = 0$) except for the part supplying the heat flux, underneath the minichannel heat sink, i.e. $-n \cdot (-k \nabla T) = q$. For easy comparing with

experimental and numerical work of Al-Neama (2018), the q is set to be 31 W/cm^2 in this work unless stated otherwise.

6. The fluid temperature at the inlet is 20°C .
7. The no-slip conditions are applied.
8. The outlet boundary conditions are set as $P = P_o = 0$.
9. The thermo-physical properties of the fluid such as, μ_f , C_p , and k were assumed to be temperature-dependent and the *COMSOL* build-in equations of these properties have been used.

3.9 Chapter Summary

This chapter has been devoted to reviewing some of the concepts and fundamentals related to the microchannel heat sinks such as the heat transfer modes, fluid flow basics, the boundary layer concepts. Besides, in this chapter, the governing equations that control the heat transfer and fluid flow have been stated. All the above represent the bases for the current investigation including the numerical simulation which will be illustrated and implemented in the following chapters.

Chapter 4 Computational and Optimisation Methodologies

4.1 Introduction

This chapter presents the computational methodology to perform the numerical analysis and the optimisation procedure for exploring the performance of different designs of the serpentine microchannel heat sinks, i.e. the smooth serpentine heat sink and the serpentine heat sink with secondary channels. In section 4.2, an overview for the main stages of performing a CFD numerical analysis will be presented. Then, sections 4.3 to 4.5 provide a brief description for the optimisation strategy which includes the types of optimisation, software used, the surrogate-based optimisation approach and the validation of surrogate model. After that, the robust design employed to conduct in this investigation is introduced in section 4.6. Finally, section 4.7 provides a summary of the chapter.

4.2 Computational Fluid Dynamics (CFD) Methods

During the last decades and as a result of the considerable developments in the computer industry, many computer-aided engineering (CAE) software have emerged to become a popular research tool to investigate complex engineering systems by solving different differential equations associated with engineering problems. The engineering problems that involve flow phenomena are simulated using a group of software programs known collectively as computational fluid dynamics (CFD). The CFD can be defined as a branch of fluid mechanics which employs numerical techniques to obtain approximate solutions of problems involving fluid flow and heat transfer (Zikanov, O., 2019). Example of commercial CFD software include *COMSOL Multiphysics*®, *ANSYS-CFX*, *ANSYS-FLUENT* and *STAR-CCM+*, whereas the other are free and open source software like *OpenFOAM*® and *Palabos*. In the present work, *COMSOL Multiphysics*® has been selected to solve the current problem because it has a strong capability to model multi-physics problems and has also been successfully employed by researchers in other relevant studies such as the studies of Han *et al.*, (2014), Al-Neama (2018), and Turgay and

Yazıcıoğlu (2018). CFD studies are less expensive, timesaving and more flexible than real physical experimental testing, but sometimes they are not as accurate as experiments. Using the CFD techniques, designers can model, simulate and predict system performance before manufacture (Joseph, 2016 and Versteeg and Malalasekera, 2007). In CFD simulations, the set of governing mathematical equations in the form of partial differential equations (PDEs), such as conservation of mass, momentum, energy and species, for the physical problems are first discretised. Then, they are solved numerically to predict approximate solutions of the studied governing equations (Versteeg and Malalasekera, 2007 and Joseph, 2016).

In general, a typical CFD simulation study is divided into three main stages, namely, pre-processing, processing and post-processing. An overview of these stages is given below:

4.2.1 Pre- processing

Before starting a numerical study, it is essential to define the modelling goal and identify the domain of the problem. Furthermore, a CFD software that is capable of solving the considered problem should be chosen. Then, the investigator needs to specify what to solve and how to solve it. The first question can be answered through:

- Creating the geometry that provides the computational domain for the problem,
- Specifying the governing equations, that represent the physical problem, in this study (Equ. 3-15 to Equ.3-18).
- Imposing the boundary conditions and materials properties.

Whereas answering the second question needs to illustrate the solution strategies, which include:

- Discretisation of the computational domain into small elements (Meshing), and
- Specifying acceptable error tolerances for monitoring the convergence of the calculated solution of the problem.

All the above steps are called pre-processing.

Creating the geometry can be accomplished either using a geometry builder included within the software or using external computer-aided design (CAD) software such as *Solidworks*® and then export it to the CFD software.

Meshing is the process of generating a collection of non-overlapping sub-domains by partitioning the original solution domain. Accordingly, various discretisation methods are available to mesh the computational space, and the most commonly used are the finite difference method (FDM), finite element method (FEM) and finite volume method (FVM). The finite-difference is considered as the oldest one which is used for numerical analysis, and it is suitable for obtaining solutions on structured meshes, i.e. simple geometry. This approach is based on the differential form of the governing equations, and its numerical calculations occur at each node of the discretised domain.

In contrast, the finite volume and the finite element methods deal with an integral form of the governing equations and they can be used to generate the grid for complex geometries. The finite volume approach decomposes the computational domain into a discrete number of cells, each of which is treated as individual control volume. The conservation equations are applied to each control volume, and the calculations are accomplished at a node located at the centroid of each control volume (Maneeratana, 2000).

In the finite element approach, the model body is sub-divided into many smaller regions called finite elements which are interconnected at nodes common to two or more elements and/or boundaries (Lewis *et al.*, 2004). This technique utilises the “shape function” to interpolate and represent the value of the dependent variable throughout each element. The calculations are performed within the generated elements at points called “*Gauss points*”.

Studies showed that the finite element technique needs longer computational time and more memory storage than the finite volume (Jeong and Seong, 2014; and Turgay and Yazıcıoğlu, 2018); however, the finite element technique is well-suited to solve multiphysics problems (Pryor, 2011).

4.2.2 Processing

In the processing stage, the CFD software follows a set of steps to solve the problem which is defined in the pre-processing step. Solving multiphysics problems with *COMSOL* is accomplished using either fully coupled or segregated solution approaches. In the former, a single large system of equations containing the unknown and the coupling between them is formed and then solved at once within

each iteration. In contrast, when employing the segregated solver, the problem is subdivided into two or more segregated steps in which each step represents a single physical process. Then the segregated steps are solved iteratively and within a single iteration, the solution of the segregated steps is performed sequentially. In *COMSOL*, the default setting for a 2D model is the fully coupled one while for 3D models it is the segregated approach. The segregated approach is faster than the fully coupled (Tabatabaian, 2015 and *COMSOL* Manual, 2018).

4.2.3 Post-processing

In the final stage of the numerical solution, i.e. post-processing, the results are prepared for the analysis and physical interpretation by presenting them as tables, graphs, contour, animations and plots.

Before starting to acquire data, it is necessary to check whether the predicted numerical results are reliable or not. This can be implemented through the validation and verification processes. Therefore, the goal of these processes is to assess the accuracy and reliability of the CFD simulation solution. Measuring how accurate the computational outputs are in comparison with the experimental results is called validation. Whereas comparing the accuracy of computational results against highly accurate numerical and analytical solutions is called verification (Oberkampf and Trucano, 2002). If there is a discrepancy between the results of the developed CFD simulation from one side and the previous works on the other side, then a number of steps should be followed to tackle this issue such as improving mesh quality, inspecting the solution method, checking the boundary conditions and fluid properties.

4.3 Formulation of Optimisation Problems

Optimisation can be defined as the procedure or methodology of finding the optimum results under certain circumstances or constraints for an engineering or economic system (Rao, 2019 and Merriam-Webster, 2020). In different engineering aspects, i.e. design, construction and maintenance, many managerial and technological decisions need to be taken by engineers to achieve the maximum benefit or/and require the minimum effort (Arora, 2004 and Rao, 2019).

An optimisation problem consists of three main parts: objective function, variables, and constraints. The first essential part, the objective function, represents the quantity that needs to be maximised or minimised, and this may be one quantity (single objective function problem) or be more than one (multi-objective function problem). In the second category, the different objectives are usually conflicted, which means that the variables that maximise one of the objectives minimise the other objectives. The second crucial part of the optimisation problem is the variables, also called design variables, which are a set of unknowns used to define the objective function and constraints. The selection of these variables depends mainly on problem specifications and other functional requirements. These variables could be continuous or discrete. The third important part of the optimisation statement is the constraints of the problem which are a set of conditions that allow the unknowns to take specific values but exclude others. These constraints must be satisfied to make the design feasible (Arora, 2004; Parkinson *et al.*, 2013 and Rao, 2019).

Mathematically, a typical optimisation statement can be written as follows:

$$\text{Find (Design Variables):} \quad \mathbf{x} = [x_1, x_2, x_3, \dots, x_n] \quad \text{Equ. 4-1}$$

$$\text{which minimise (Objective Function):} \quad f(\mathbf{x}) \quad \text{Equ. 4-2}$$

subject to (Equality constraints, Inequality constraints, Variable bounds):

$$h_i(\mathbf{x}) = 0, \quad i = 0, 1, 2, \dots, k \quad \text{Equ. 4-3}$$

$$g_i(\mathbf{x}) \leq 0, \quad i = 0, 1, 2, \dots, p \quad \text{Equ. 4-4}$$

$$x_i^l \leq x_i \leq x_i^u \quad \text{Equ. 4-5}$$

4.4 Classification of Optimisation Problems

Optimisation problems can be categorised in different ways. Based on the variables' nature, for example, the problems could be divided into deterministic optimisation and stochastic optimisation or optimisation under uncertainty (NEOS, 2020). The deterministic optimisation for a single objective function can be grouped into two main branches, according to the type of the design variables, continuous and discrete. The assumption in the deterministic optimisation is that the data for a

given problem is known precisely. In reality, these data cannot be known with certainty; therefore, the optimisation under uncertainty can be used to find a feasible solution for almost all of the data and optimal in some sense. Besides, there are two important categories for the optimisation under uncertainty: robust optimisation and the reliability-based optimisation (NEOS, 2020). The optimisation problem could also be constrained or unconstrained based on the existence of constraints on design variables (Arora, 2004; Coello 2006; Kumar, 2009 and Muthu, 2010).

Besides, they could be global or local optimisation strategies based on the nature of the optimisation problem. Most engineering problems are considered as non-linear, constrained and multi-objective optimisation problems (Arora 2004; Coello 2006; Kumar, 2009 and Muthu, 2010).

4.5 Optimisation Algorithms

No single efficient approach exists to solve all optimisation problems (Arora 2004). Therefore, many methods have been developed to solve specific optimisation problems. The appropriate choice of the optimisation technique depends mainly on the kind of the optimisation problem itself (Parkinson *et al.*, 2013 and Rao, 2019). An overview of the most popular optimisation techniques is given below.

4.5.1 Derivative Based Optimisation Methods

Derivative based optimisation methods employ differential calculus techniques to locate the optimum points. Therefore, these methods are very beneficial in determining the optimum solutions for smooth functions, continuous and differentiable functions. Several methods can be found under this category such as Newton-Raphson method, Levenberg-Marquardt, and steepest-descent method (Fröhlich and Hasenauer, 2019). They are good for local search in the vicinity of the optimum solution. However, the derivative based classical techniques have limited application for the practical problems due to the discontinuity and/or non-differentiability of the objective functions involved in real-life problems (Arora, 2004, Kumar, 2009, Rhinehart, 2018 and Rao 2019).

4.5.2 Derivative Free Based Optimisation Methods

During the last four decades, scientists have developed derivative free based optimisation methods that have been used extensively to find the optimal solution of complex engineering problems such as design and operation engineering problems (Rhinehart, 2018). Most of these modern techniques are inspired by nature and biological systems and they use stochastic approaches to explore the entire design space. Among the non-traditional methods of optimisation are particle swarm optimisation (PSO), simulated annealing (SA), ant colony optimisation (ACO), neural network-based methods (NN) and genetic algorithms (GAs) which only rely on function evaluations in performing the optimisation. The simulated annealing (SA) and the genetic algorithms (GAs) can find the global optimum solution very efficiently (Arora, 2004 and Rao, 2019); however, they are not effective in finding the optimum solution for large numbers of design variables of more than 100 (Haftka *et al.*, 2016). For the current investigation, the number of design variables is less than five; therefore, the GAs has been selected in the present study to implement the optimisation procedure. A brief description of this method is given below.

Genetic Algorithms

Due to its robustness, efficiency, and flexibility, besides avoiding getting trapped in local minima, the genetic algorithm (GA) is regarded as one of the most useful optimisation techniques (Khan *et al.*, 2013). The GAs, invented by John Holland in the early 1970s, is a search-based optimisation technique. This algorithm is inspired by the mechanics of biological evolution. The GA mimics the survival of the fittest among individuals over consecutive generations to find a solution to the problem. The implementation of the GA can be described as follow (Arora, 2004; Coello, 2006; Kumar, 2009 and Deb, 2012):

- The algorithm is started by selecting a population of individuals so that each one of the individuals represents a feasible solution to the problem.
- Then, use these individuals to find the fitness function. The higher the fitness the better the solution.
- Parents are selected to reproduce offspring for a new generation. The selection process of individuals depends on their fitness function values from the

previous step. The fitter individuals have more opportunity to reproduce. The reproduced generation has a combination of properties of two parents. It should be noted that old generation dies, and the new generation has the same size as the older one.

4.5.3 Optimisation software Used

An open-source toolkit called DAKOTA (Design Analysis Kit for Optimization and Terascale Applications) has been selected to conduct the optimisation process in this study because it is a useful software for optimisation and uncertainty quantification (UQ). DAKOTA toolkit is provided by Sandia laboratory to do a parametric analysis for design exploration, model calibration, risk analysis, optimisation, uncertainty quantification and other facilities (DAKOTA, 2020). All the instructions and commands of doing a specific investigation, writing the output to a specified file or declaring the variables can be usually set in Dakota input file. For more details about the use of this toolkit, the reader is recommended to consult the manuals and the official website of DAKOTA (<https://dakota.sandia.gov/>).

4.5.4 Surrogate-Based Optimisation

For realistic engineering optimisation problems, the evaluation of the response function could be computationally very expensive or complicated and takes hours or days to implement one simulation. These barriers could make the coupling of the simulation model with an optimiser prohibitively time-consuming and require tremendous computational resources. To tackle this issue, researchers have employed an alternative optimisation methodology which is called surrogate-based optimisation (Joseph, 2016 and Dakota, 2020). Surrogate models, which are also known as metamodels, or response surface models (RSM), represent inexpensive approximation models which are used to explore the variations in response quantities over the regions of the input variables space. Consequently, the surrogate-based optimisation approach relies on replacing the actual computationally expensive functions with approximate surrogate models and the search for the optimum solution is made directly on the approximated model. As a result, implementing optimisation problems which require hundreds, or thousands of function evaluations will be less expensive.

The optimisation toolkit used in this work, Dakota software, supports three categories of surrogate models: data fits, multifidelity and reduced-order model surrogates (Dakota, 2020). For the data fits, there are two types of approximation surrogate models: interpolation techniques like Kriging (KG) or Gaussian process model, and radial basis functions (RBF) and regression approaches such as polynomial regression (PR), multivariate adaptive regression splines (MARS) and artificial neural networks (ANN)(Forrester *et al.*, 2008; Ahmed and Qin, 2009 and Ben Salem *et al.*, 2017). For each fitting technique in Dakota, a different numerical method is utilised to compute its internal coefficients. For instance, the kriging surrogate model employs maximum likelihood estimation (MLE) to determine its correlation coefficients, while the polynomial surrogate model utilises the least-squares method that uses a singular value decomposition to calculate the polynomial coefficients (Dakota, 2020).

To generate a surrogate model, samples of the design space should be extracted using one of the design of experiments (DoE) methods such full factorial design, Monte Carlo design or Latin Hypercube. Then, the response values at these selected points can be produced by performing the CFD simulations. The combination of the DoE points and their corresponding response values is called a training set or build points. Employing these training points, the surrogate model can be constructed using surrogate model techniques like linear models or artificial neural networks. The accuracy of a generated surrogate model could be verified by comparing the response values from the surrogate model against the actual values produced by computer simulation (cross-validation). The following subsections give an overview of the design of the experiment and the approximation surrogate model techniques employed in this study.

4.5.5 Design of Experiments (DoE):

Sampling is the process of selecting individuals from a population under study so that the results from the sample can be employed to make a conclusion about the population. The need for sampling emerges from the fact that testing every member of the population of interest is usually impossible as it is very expensive and time-consuming. To obtain reasonable results, the sample should be well selected and evenly distributed. Therefore, the design of experiments (DoE) techniques can help

the designers explore the parameter space and identify the significant factors that affect a system's performance. Consequently, this can give the decision-makers a full insight into the interaction between design variables and the product's performance and help improve the design before manufacturing (Cavazzuti, 2012 and Montgomery, 2017). Studies have recommended that the minimum number of samples should be no less than ten times the number of variables (Swiler and Giunta, 2007).

4.5.6 Monte Carlo Sampling Method

Monte Carlo method can be used as DoE technique to generate random sampling for the design variables domain. In this approach, generating a new sample point in the design space does not consider the previously created sample points. Therefore, it could generate samples very close to each other, or concentrated in a specific region, while leaving another part of the design space unsampled (Cavazzuti, 2012 and Dakota, 2020). Therefore, it could be inefficient.

4.5.7 Latin Hypercube Sampling Method

The Latin Hypercube design sampling is one of the space-filling DoE techniques in which the design space is filled uniformly and randomly. In general, space-filling approaches are considered as a good selection for generating surrogate models (Montgomery, 2017). For sampling two variables, the Latin square design technique is used to generate random samples so that each row and column has only a single sample, Fig. 4-1.

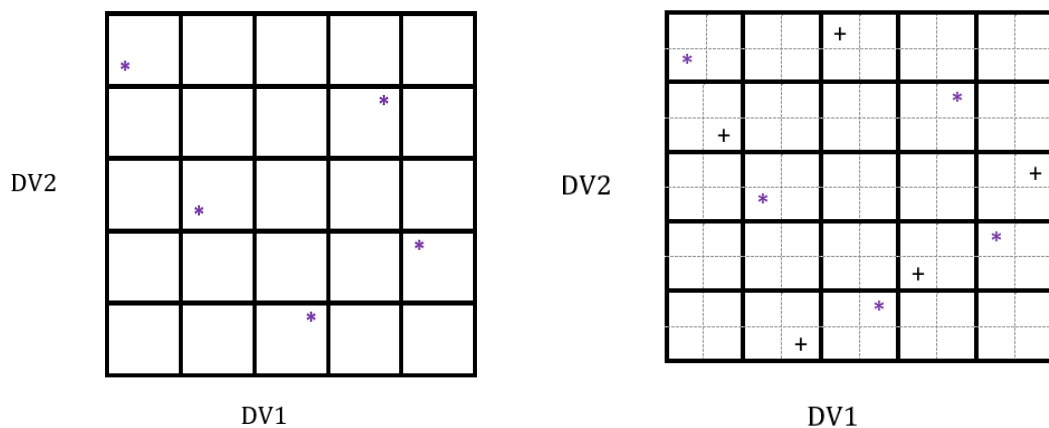


Fig. 4-1 Latin hypercube sampling (a) Five samples (b) Ten samples.

For more than two of variables, the Latin Hypercube sampling (LHS) technique, an extended version of the Latin square design which can sample from multiple dimensions and multiple hyperplanes rather than two parameters and a single plane, is employed (Cavazzuti, 2012; Montgomery, 2017 and Dakota, 2020).

In this investigation, the Latin Hypercube design approach has been exploited to generate the required sample for producing the surrogate model used in the optimisation process.

4.5.8 Surrogate Model: Gaussian Process (GP)

As stated above, several types of approximation models are available as a cheap alternative to replace expensive numerical simulations. In this thesis, the Kriging model, also termed as Gaussian process (GP) (Dakota, 2020), has been used to generate an approximation for the expensive simulator. This model has been named after the South African geologist engineer Danie Krige who proposed it in the 1950s as a tool to predict the distribution of minerals. Matheron established the mathematical formulation for the Kriging surrogate model in the 1960s (Matheron, 1963). Although the Kriging model has developed in spatial statistics and geostatistics communities, it has been widely employed in engineering applications as a fitting surrogate for expensive computer simulations during the 21st century. Kriging surrogate model has emerged in reliability studies by combining it, for example, with the importance sampling method (Echard *et al.*, 2013) or Monte-Carlo simulation (Echard *et al.*, 2011). It has also been employed in global optimisation (Husain and Kim, 2010), uncertainty propagation problems (Romero *et al.*, 2004 and Janusevskis and Riche, 2010) and robust design optimisation (Shahbaz *et al.*, 2016)

To clarify the relationship between the high-fidelity expensive computer experiments and a cheaper surrogate model, let us suppose that the outputs of the numerical analysis code can be expressed as:

$$y = f(\mathbf{x}) \tag{Equ. 4-6}$$

here y represents the quantity of interest, and the vector \mathbf{x} stands for the inputs design parameters.

An approximation model, on the other side, can be formulated as:

$$\tilde{y} = \tilde{f}(\mathbf{x}, \boldsymbol{\alpha}) \cong f(\mathbf{x}) \tag{Equ. 4-7}$$

where α denotes a vector of unknown parameters which are estimated using the build points employed in constructing the approximation model (\tilde{y}) (Echard *et al.*, 2011; Echard *et al.*, 2013 and Dakota , 2020).

In Kriging, the approximation model consists of a combination of two parts as given in Equ. 4.8. The first is the trend function (also known as global model), usually low order polynomials, that interpolates all training points; and the second is the local deviation (a Gaussian process error model) that is used to capture the deviation from the trend function (Ahmed and Qin, 2009; Kim *et al.*, 2009; Mohammadi, 2016 and Dakota , 2020).

$$\tilde{y}(x) = \sum_{i=1}^k \alpha_i g_i(x) + Z(x) \quad \text{Equ. 4-8}$$

here α_i represents the coefficients of basis function $g_i(x)$ and $Z(x)$ is a normal distribution with mean and variance of 0 and σ^2 , respectively (Kim *et al.*, 2009). The correlation of the deviation at each point of the sample can be defined as:

$$\text{Cov}[Z(x^i), Z(x^j)] = \sigma^2 \mathbf{R} [R(x^i, x^j)], \quad \text{Equ. 4-9}$$

$$i, j = 1, 2, 3, \dots, n$$

$$R(x^i, x^j) = \exp \left[- \sum_{l=1}^m \theta_l |x_l^i - x_l^j|^2 \right], \quad \text{Equ. 4-10}$$

here n represents the number of sampling points and m denotes the number of design variables. Accordingly, the design variable at the i^{th} sampling point and the l^{th} design variable is written as x_l^i . In Equ. 4.9, $R(x^i, x^j)$ refers to a correlation function between any two sampling points which is usually described by a Gaussian correlation function. This correlation function can be formulated as in Equ. 4.10, and its correlation coefficients, θ_l , can be estimated using the maximum likelihood approach (Li and Sudjianto, 2005; Ahmed and Qin, 2009, Kim *et al.*, 2009 and Dakota, 2020).

4.5.9 Surrogate Model Validation: Efficiency and Accuracy

Accepting or rejecting a surrogate model depends on its efficiency and accuracy. The efficiency can be assessed by measuring the required time for predicting the function values; whereas the accuracy can be assessed by checking the goodness of

these predictions (Hamad, 2006). In the present work, the efficiency of the constructed surrogate model was excellent as it gives the evaluations for the input design value within a few minutes while the CFD simulation model takes hours to generate the results for the same inputs.

On the other hand, the accuracy of the generated surrogate models has been checked by comparing the extracted function values from the surrogate model at unknown design variables against those obtained using CFD simulation software.

4.6 Robust Optimisation

Optimisation under uncertainty (OUU) can be defined as the design process that considers the uncertainty in design variables to produce a design less sensitive to these uncertainties, i.e. robust design. To illustrate this idea, suppose that the optimisation process results in two designs with a response of $A > B$, Fig. 4-2. By taking into consideration the uncertainty in design variables, the global optimal design (A) shows great sensitivity to the variations in input variables while the local optimal design (B) displays less sensitivity to such variations in design variables. As a result, design (B) could be better than design (A) if the worst-case performance is the target rather than the optimal performance (McClarren, 2018). Consequently, to produce a robust design, an optimisation under uncertainty (OUU) procedure should be implemented which includes propagating uncertainties from the input parameters to the quantity of interest. Before proceeding with the description of the optimisation under uncertainty procedure, it is useful to give a brief overview of some related statistical concepts.

4.6.1 Random Variables

Random variables can be defined as a variable whose value is obtained by a random experiment. These variables are associated with cumulative distribution function (CDF) and probability density function (PDF) that provide key pieces of information about such variables. The cumulative distribution function (CDF) is the probability that a random variable X is less than or equal to a given value, x , and can be written as:

$$F_X(x) = P(X \leq x) \quad \text{Equ. 4-11}$$

On the other hand, the probability density function (PDF), $f(x)$, also known as density of continuous random variable, describes the relative likelihood of a random variable X to have a specific value x (Kiran, 2017). For example, the probability of random variable x to fall within the limits of a and b can be expressed as:

$$P(a < x < b) = \int_a^b f(x)dx \quad \text{Equ. 4-12}$$

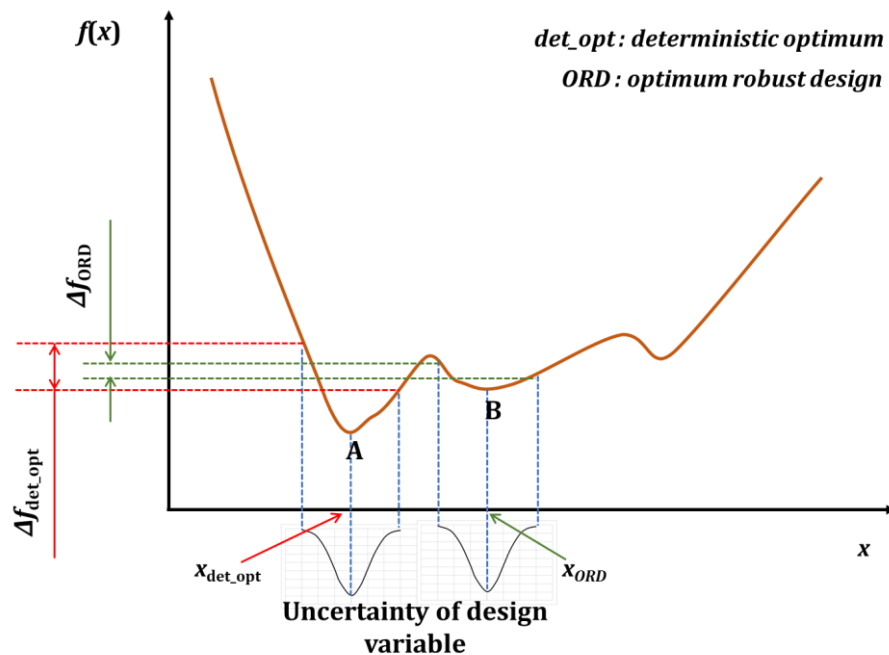


Fig. 4-2 Schematic for the concept of the: global optimal design (point A) and robust design (point B).

4.6.2 Uncertainty Quantification

Optimisation under uncertainty aims to quantify the uncertainties of a given system's response function resulting from the uncertainties in its inputs. These uncertainties of the inputs could be due to the geometrical discrepancies resulting from manufacturing tolerances, the variation in materials' properties, or insufficient knowledge of the ambient conditions. The uncertainty quantification techniques determine statistical information for outputs such as mean, standard deviation and probability distribution function. Different approaches have been used to quantify the uncertainty like Monte Carlo methods, reliability methods and polynomial chaos expansions.

4.6.3 Monte Carlo Simulations (MCS)

Monte Carlo simulation has been used extensively for quantifying uncertainty in numerous fields, like finance and business, applied statistics and engineering, due to its simplicity and ability to accommodate large number of variables. Furthermore, the convergence of the MCS is independent of the number of uncertainties, i.e. the dimensionality of the problem (Cook, 2018). The main disadvantage of this approach is that it is very slow; however, this can be overcome by using the surrogate model to implement it as has been done by the study of Shahbaz *et al.* (2016). Therefore, it has been adopted in this work to quantify the uncertainties in the output parameters. Using this approach, the mean and standard deviation of a quantity of interest (QoI), f , over K samples can be estimated as follow:

$$\mu_f \approx \frac{1}{K} \sum_{i=1}^K f(\xi_i) \quad \text{Equ. 4-13}$$

$$\sigma_f^2 \approx \frac{1}{K-1} \sum_{i=1}^K (f(\xi_i) - \mu_f)^2 \quad \text{Equ. 4-14}$$

where ξ_i represents the i^{th} sample from design space.

To perform the Monte Carlo simulation technique, the following procedure can be followed:

- Creating large number of random samples using appropriate sampling method such as the Monte Carlo sampling and the Latin Hypercube design sampling.
- Performing the simulation code, the original numerical simulation or the fit of the simulation data (surrogate model), for each random sample. In the current work, the surrogate model has been used.
- Computing the statistics of output distribution, i.e. the mean and the standard deviation, from the simulation results.

4.6.4 Optimisation under uncertainty

In section 4.3, the formulation of deterministic optimisation is presented. In real life, the variation of the operating conditions and minor manufacturing errors for engineering systems are not avoidable. Therefore, the need for performing design under uncertainty has become a necessity for critical engineering designs

(Chen *et al.*, 2012). Besides optimizing the quantity of interest, the optimisation under uncertainty is aimed at minimizing its variance. Considering the uncertainty in design variables and boundary conditions, the OUU problem could be formulated as a sum combination of mean and standard deviation (Jin *et al.*, 2003 ; Shahbaz *et al.*, 2016 and Cook, 2018):

Find (Design Variables):

$$\mathbf{x} = [x_1, x_2, x_3, \dots, x_n] \quad \text{Equ. 4-15}$$

which minimise (Objective Function):

$$d = \frac{\mu_f}{\mu_f^*} + \frac{\sigma_f}{\sigma_f^*} \quad \text{Equ. 4-16}$$

Subject to (Equality constraints, Inequality constrains, Variable bounds):

$$h_i(\mathbf{x}) = 0, \quad i = 0,1,2,, \dots, k \quad \text{Equ. 4-17}$$

$$g_i(\mathbf{x}) \leq 0, \quad i = 0,1,2,, \dots, p \quad \text{Equ. 4-18}$$

$$x_i^l \leq x_i \leq x_i^u \quad \text{Equ. 4-19}$$

For more than one objective function, the optimisation problem could be formulated as:

$$\text{minimise:} \quad (d_1 \text{ and } d_2) \quad \text{Equ. 4-20}$$

where:

$$d_1 = \frac{\mu_{f1}}{\mu_{f1}^*} + \frac{\sigma_{f1}}{\sigma_{f1}^*}$$

$$d_2 = \frac{\mu_{f2}}{\mu_{f2}^*} + \frac{\sigma_{f2}}{\sigma_{f2}^*}$$

The application of this approach will be illustrated in the next chapters.

4.7 Chapter Summary

As this study is devoted mainly to exploring the CFD-based Optimisation of the serpentine minichannel heat sink, the related computational methods and optimisation strategies have been reviewed in this chapter. *COMSOL* Multiphysics® has been selected to be the simulation tool due to its ability to solve the current

problem as demonstrated in the study of Al-Waaly (2015), Al-Neama (2018) and Al-Asadi (2018).

This chapter also presented a brief overview of the steps of performing CFD the simulations which includes the pre-processing, processing, and post-processing stages. Regarding the optimisation, the surrogate-based optimisation strategy has been explained and adopted in the current investigation because it saves time and effort in obtaining results.

Chapter 5 CFD-enabled Optimisation of the Serpentine Minichannel Heat Sinks

5.1 Introduction

This chapter focuses on investigating flow and heat transfer in simple serpentine minichannel heat sinks with plate fin (*SMCHS – PF*) through studying the channel height which has not covered by the study of Al-Neama (2018) and adding cylindrical vortex generators which has not been addressed before, as shown in Chapter 2. Accordingly, the organisation of this chapter is as follows. Section 5.2 presents the CFD simulation setup, which includes a description of the geometry, the governing equations and the boundary and operating conditions for the problem under consideration. Followed by a test for the dependency of the results on mesh size as well as the validation of the numerical results are described in same section. After that, the influence of the channel width and height and the impact of introducing vortex generators on thermal resistance and pressure drop of the serpentine minichannel heat sink is addressed respectively in sections 5.3 and 5.4. In addition, this chapter includes two optimisation procedures, i.e. the deterministic optimisation and the optimisation under uncertainty which are tackled in sections 5.5 to 5.7. Finally, a summary of this chapter is given in section 5.8.

5.2 CFD Simulation Setup:

5.2.1 Geometry description and boundary Conditions

Fig. 5-1 shows a 3-D geometrical model of the serpentine minichannel heat sink with plate fins (*SMCHS – PF*) that was investigated by Al-Neama, 2018. A cooper heat sink block with a square base ($W = L = 38 \text{ mm}$) and height ($H = 4 \text{ mm}$) has been used and 12 minichannels, with width (W_c) of 1.5 mm and height (H_c) of 2 mm , have been created in the block to allow water circulation. Two heaters were attached at the base of this heat sink to mimic the heat generated by the chip processors of the electronic systems.

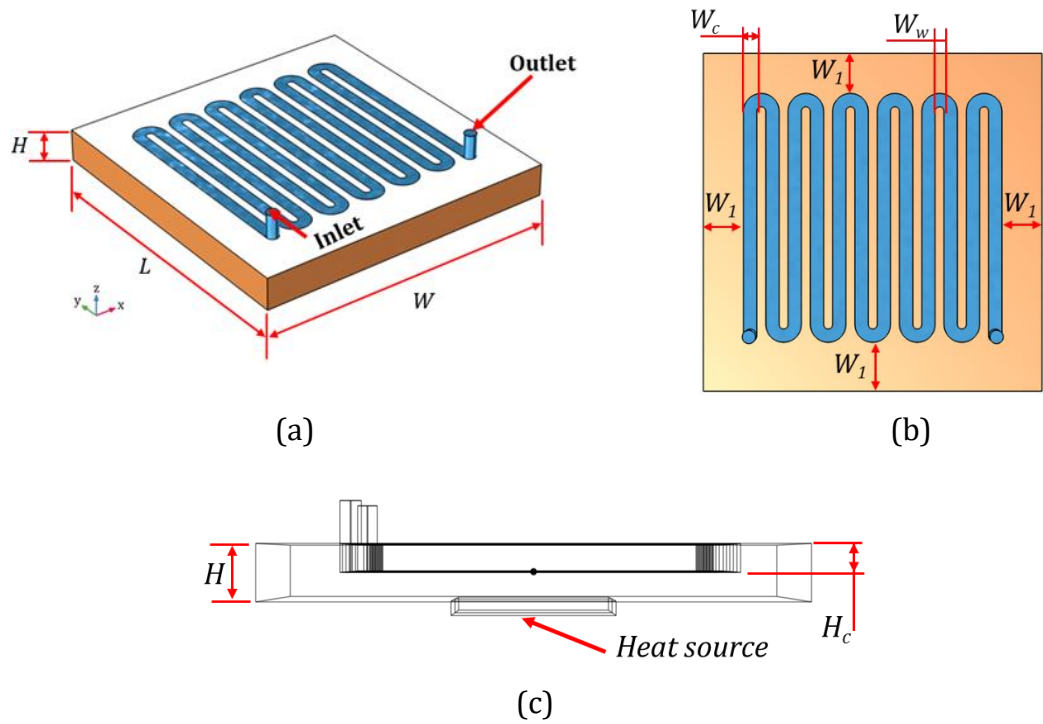


Fig. 5-1 Geometrical model: (a) 3-D geometry, (b) top view and (c) side view.

A finite element method based CFD software called *COMSOL V5.5 Multiphysics* is used to solve the fluid flow heat transfer governing equations which also implies solving the conjugate heat transfer problem, Equ. 5-1 to Equ. 5-4 (Fedorov and Viskanta, 2000 and Toh *et al.* 2002).

Continuity equation:

$$\nabla \cdot (\rho \vec{V}) = 0 \quad \text{Equ. 5-1}$$

Momentum equation:

$$\vec{V} \cdot \nabla (\rho \vec{V}) = -\nabla P + \nabla \cdot (\mu \nabla \vec{V}) \quad \text{Equ. 5-2}$$

The energy equation for the fluid:

$$\vec{V} \cdot \nabla (\rho C_p T) = \nabla \cdot (k_f \nabla T) \quad \text{Equ. 5-3}$$

The energy equation for the fin:

$$\nabla \cdot (k_s \nabla T_s) = 0 \quad \text{Equ. 5-4}$$

The numerical models were run at constant heat flux of 31 W/cm^2 provided by the attached heaters at the bottom of the heat sink. The water enters at temperature of 20°C and exits at the outlet with pressure of $P = 0 \text{ Pa}$, i.e. outflow condition.

5.2.2 Mesh Independency Test

A mesh independence study was needed to explore the effect that the mesh size has on the simulation results. Two different mesh element types, i.e. hybrid (semi-structured) and unstructured mesh, are used to accomplish this test, Fig. 5-2. For this task, the following boundary conditions have been designated for the heat sink. A power of (100 W) is applied at the bottom of the heat sink to mimic the IC chip. The fluid enters the heat sink with a temperature of (20°C) and Reynolds number of (1600). Different criteria have been used to select the appropriate element type and size and improving accuracy according to the available computational resources. These criteria are the number of elements (NOE), the average element quality (AEQ), the time required to complete a CFD simulation, the physical memory (Ph.M.), the number of degrees of freedom (DOF) and the relative difference for both the R_{th} and ΔP , calculated based on the finest mesh.

Table 5-1 summarises the key characteristics of the mesh analysis for the unstructured mesh (A) and the hybrid mesh (B). For each mesh group, four element sizes ranged from coarsest to finest meshes were applied and examined. In group (A), default meshes, generated automatically by the *COMSOL* software, named as normal, fine, finer, and extra-fine, have been tested. In contrast, meshes in group (B) were set manually and given names (Mesh-01) for the coarsest one and (Mesh-04) for the finest one. For both groups, increasing the density of the grid leads to an increase in the precision of the numerical simulation outputs but at the expense of the computational resources and the time required for completing a simulation.

For group (A), it can be noticed that the relative differences in both the thermal resistance and pressure drop were respectively reduced from 5.22% and 9.96 (using “Normal” mesh) to 3.42% and 3.73 (using “Finer” mesh). However, the time consumed for obtaining the results was increased from (9 min for the coarsest mesh) to (4 hr and 05 min for the finest mesh). Similarly, for group (B), the relative differences in R_{th} and ΔP were decreased from 0.5 and 7.45 (using “Mesh-01” mesh) to 0.2 and 1.69 (using “Mesh-03” mesh), with an increase in the required time for implement the simulation from (14 min) to (1 hr and 56 min). As a compromise between the results precision and the available computational resources on one hand and time on the other hand, the “Finer” mesh (group A) and “Mesh-03” (group B) are selected for further verification and validation.

5.2.3 Validation of the Numerical Simulation Model

To validate the present CFD simulation model, the current numerical results have been compared against the numerical and experimental study of Al-Neama (2018), Fig. 5-3. The current CFD outputs were obtained using two different mesh approaches, i.e. the unstructured and hybrid meshes. It is evident that the comparison of the current CFD results obtained from both mesh designs against the previous work shows a good agreement with a difference of less than 9% in R_{th} and 12.3% in ΔP . As the unstructured mesh shows better predictions than the hybrid mesh with a difference of less than 5% in comparison with the previous experimental observations, therefore it is adopted for this investigation.

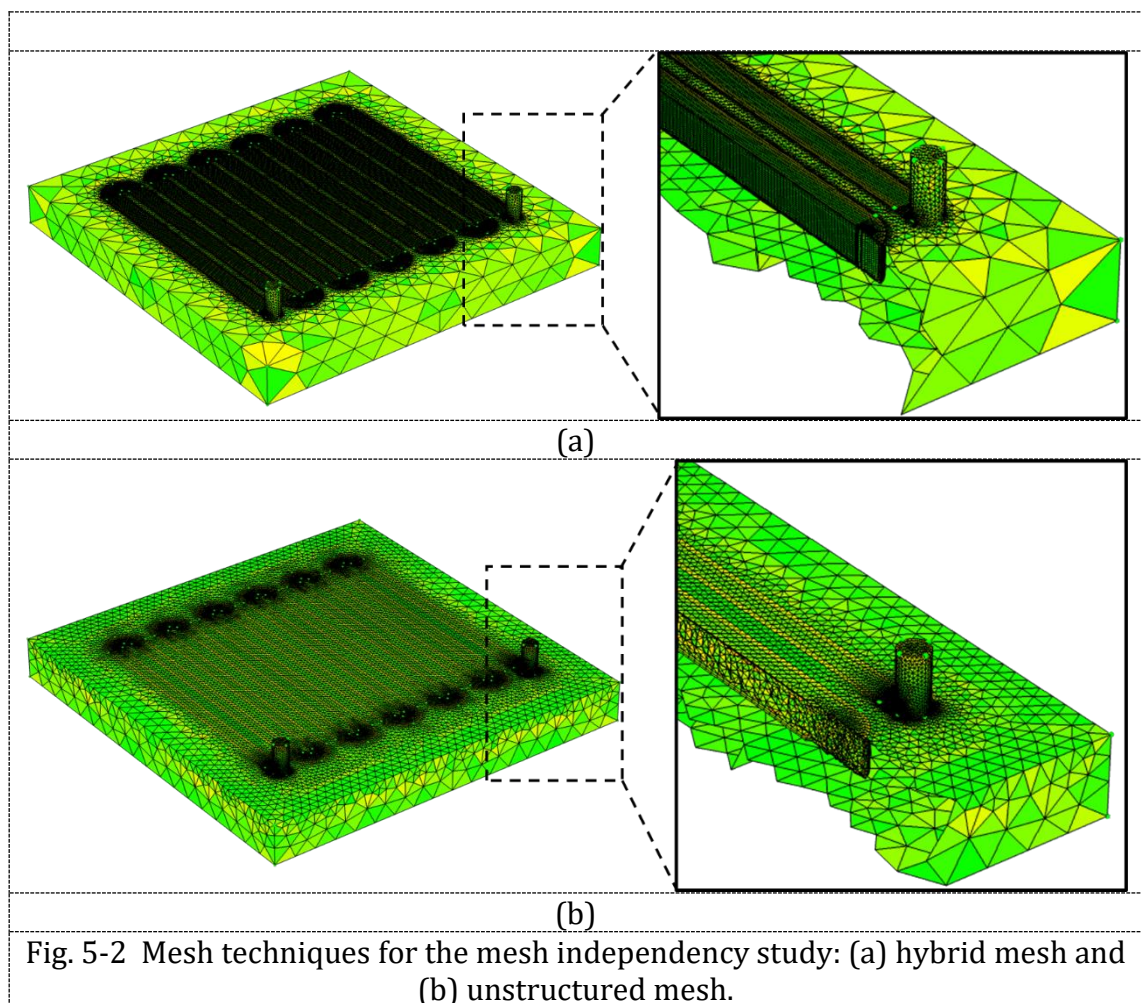


Table 5-1 Mesh dependence test for the serpentine microchannels heat sink.

No	Mesh Resolution	NOE x 10 ⁶	AEQ	time (H: min)	Ph.M. (GB)	DOF x 10 ⁶	R_{th} [K/W]	% diff. (±)	ΔP [Pa]	% diff. (±)
Group (A): Unstructured mesh										
1	Normal	0.222	0.6524	00:09	2.77	257,173	0.34587	5.22	5415	9.96
2	Fine	0.446	0.6553	00:17	3.46	469,985	0.34477	4.89	5594.4	6.97
3	Finer	1.201	0.6613	00:53	4.97	1,145,301	0.33995	3.42	5789.4	3.73
4	Extra fine	4.341	0.6653	04:05	13.1	3,725,212	0.32870	-----	6013.8	-----
Group (B): Hybrid mesh										
1	Mesh-01	0.247	0.6649	00:14	2.94	402,423	0.34048	0.50	6266.4	7.45
2	Mesh-02	0.433	0.6745	01:04	4.19	714,523	0.34064	0.45	6105.3	4.69
3	Mesh-03	0.880	0.6772	01:56	6.33	1,485,503	0.34151	0.20	5930.5	1.69
4	Mesh-04	1.225	0.6848	03:42	8.81	2,137,690	0.34218	-----	5831.8	-----

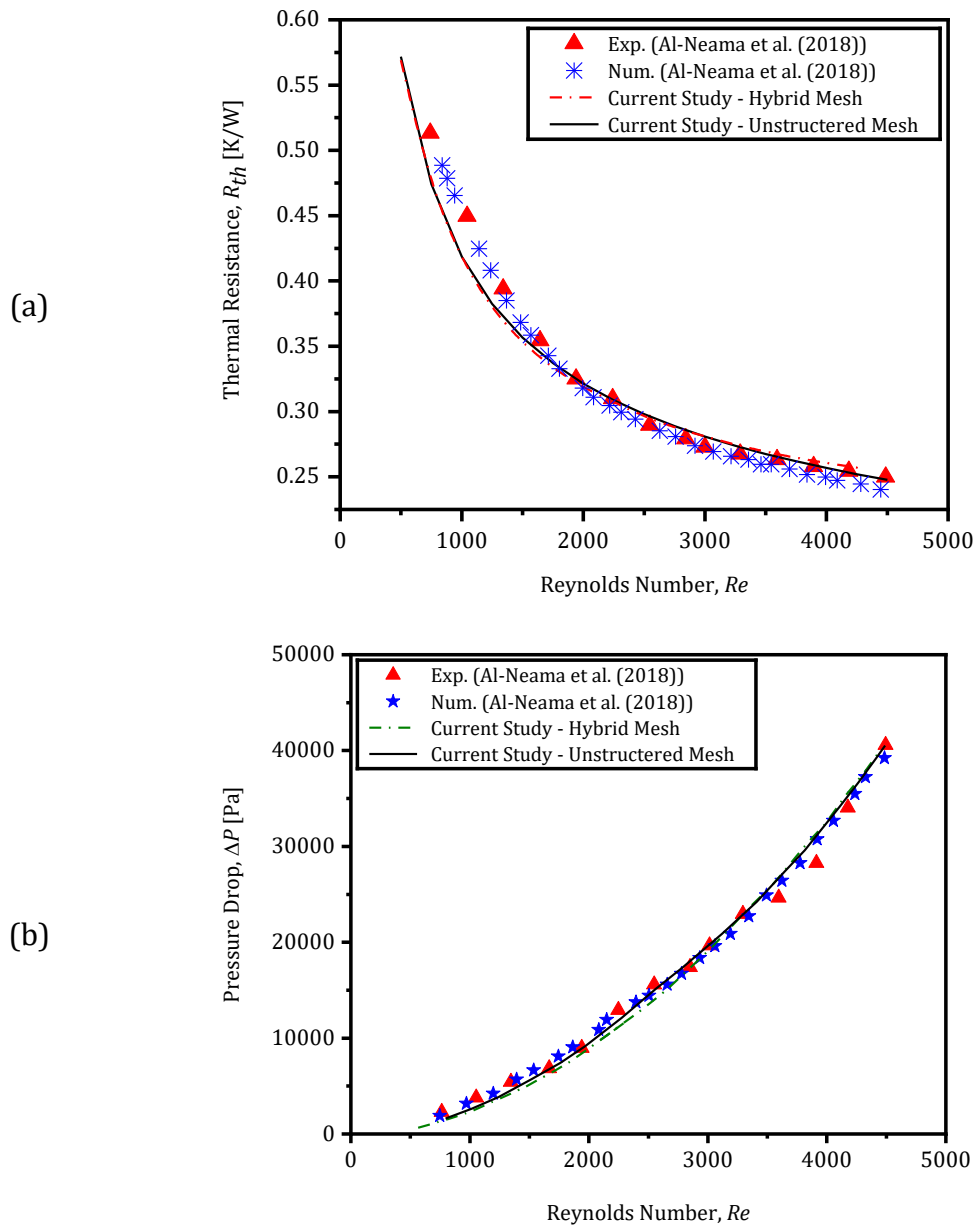


Fig. 5-3 Comparison of the present work against the work of Al-Neama (2018): (a) R_{th} and (b) ΔP .

With the CFD simulation model validated against the work of Al-Neama *et al.* (2018), the original results of the current work, i.e. the effect of channel height and adding cylindrical vortex generator, are presented in the following sections.

5.3 Effect of Channel Width and Channel Depth

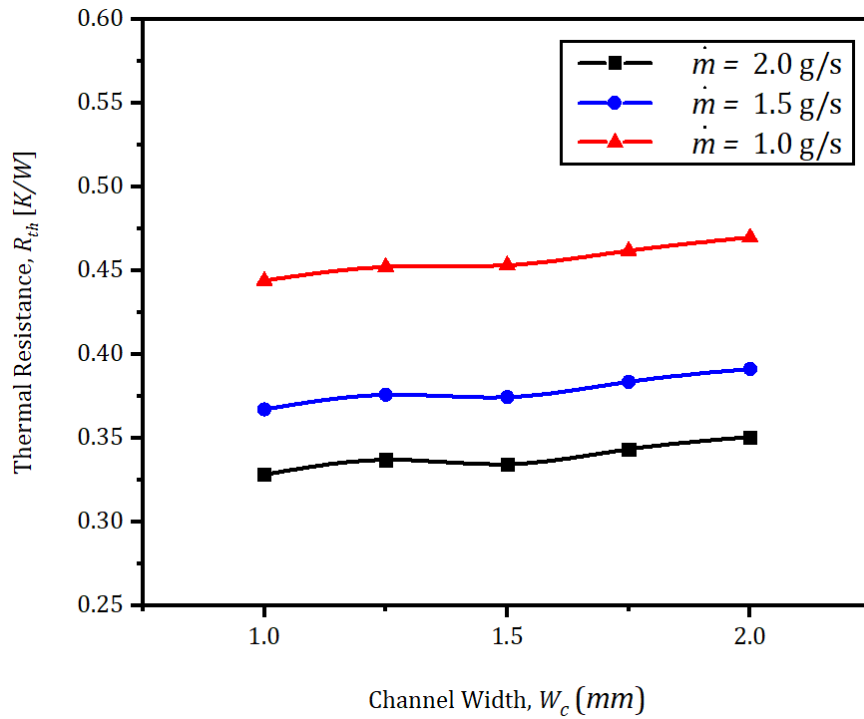
The effect of channel width (W_c) and depth (H_c) of the serpentine minichannel heat sink, Fig. 5-1, were explored to reveal their impact on the overall thermal resistance and pressure drop of the considered heat sink. To examine the channel width effect on the heat sink performance, its values were changed in the range from 1 mm to

2 mm while the channel depth was fixed at 2 mm. However, to test the influence of the channel depth, this design variable has given values from 0.5 mm to 3 mm whereas the width of the channel has been kept at 1.5 mm. The other dimensions and boundary conditions were taken as in section 5.2.1. The results are presented graphically, in Fig. 5-4 to Fig. 5-7, in terms of thermal resistance (R_{th}) and pressure drop (ΔP) in addition to the temperature, velocity and pressure distributions for selected mass flow rates (\dot{m}) which ranged from $\dot{m} = 0.75 \text{ g/s}$ to $\dot{m} = 2 \text{ g/s}$.

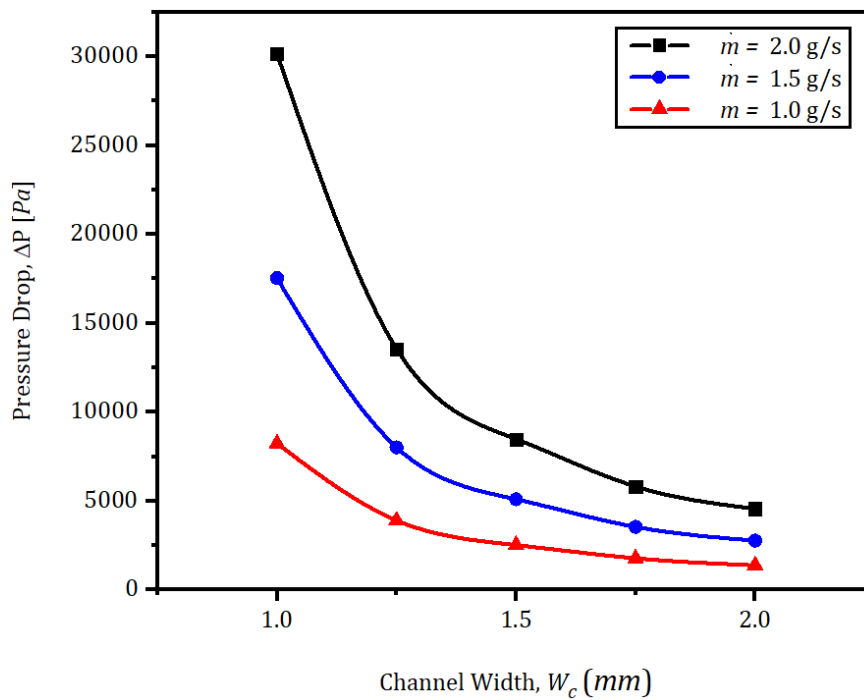
By inspecting Fig. 5-4 (a) and Fig. 5-5 (a), it can be noticed that the overall thermal resistance increases with increasing channel width and depth. It is also clear that the rate of change of the thermal resistance is affected by the flow rate magnitude, the higher the flow rate the lower the thermal resistance. At $\dot{m} = 2.0 \text{ g/s}$, for example, the R_{th} increased from 0.3285 K/W and 0.3181 K/W to 0.3509 and 0.3506 K/W by increasing respectively the W_c and H_c in their prescribed range of change. Besides, at constant channel width, it has been noticed that the maximum increase in thermal resistance due to change in channel height was 5.33% at $\dot{m} = 0.75 \text{ g/s}$ whereas it was 9.5% for the $\dot{m} = 1.75 \text{ g/s}$.

On the contrary, a decrease in pressure drop penalty with increasing the W_c and H_c is observed for all the studied flow rates, Fig. 5-4 (b) and Fig. 5-5 (b). The current investigation shows that the maximum reduction in pressure drop achieved was 94.92% for $H_c = 3 \text{ mm}$ at $W_c = 1.5 \text{ mm}$ and $\dot{m} = 2 \text{ g/s}$.

The above behaviour for the performance criteria could be attributed to the fact that the increase in the considered design variables, i.e. W_c and H_c , leads to providing additional flow section which results in lowering the Reynolds number, i.e. decreasing in cooling fluid velocity inside the minichannels, for a given flow rate. Therefore, the ability of the fluid to transfer the heat from the source underneath the heat sink and reject it out to the surrounding will reduce. This can be seen clearly by comparing the maximum magnitudes of the velocity, the pressure, and the temperature for different values of W_c and H_c , shown in Fig. 5-6 and Fig. 5-7.

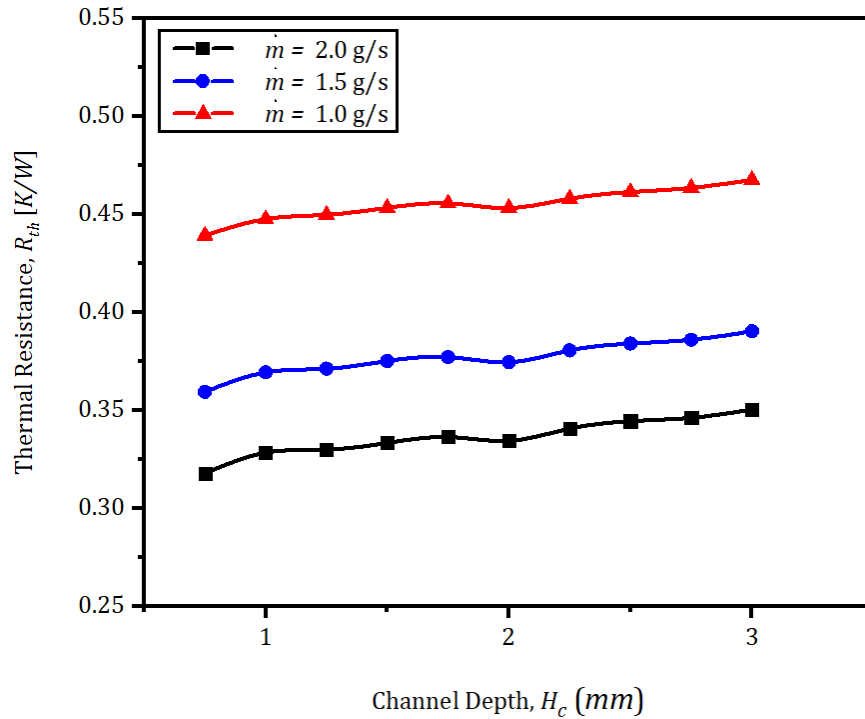


(a)

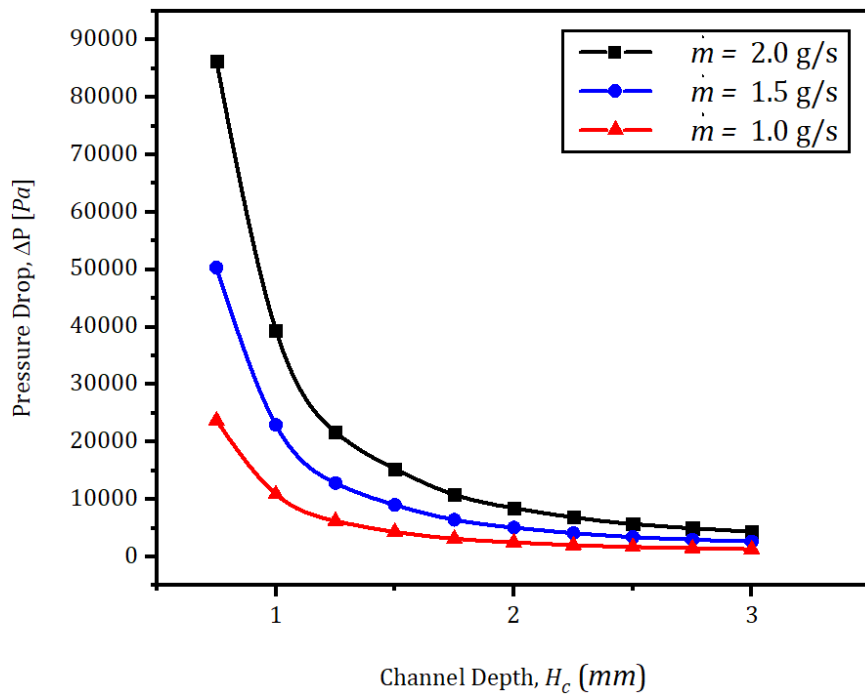


(b)

Fig. 5-4 The variation in (a) thermal resistance and (b) pressure drop due to change in channel width for different mass flow rate and $H_c = 2$ mm.



(a)



(b)

Fig. 5-5 The variation in (a) thermal resistance and (b) pressure drop due to change in channel depth for different mass flow rate and $W_c = 1.5$ mm.

From Fig. 5-6, for example, it can be noticed that the maximum velocity in the channel with depth $H_c = 1.25$ mm, Fig. 5-6 (a), is 0.88 m/s where as it is reduced to

0.37 m/s by increasing the channel depth to $H_c = 3 \text{ mm}$, Fig. 5-6 (b). This reduction in the coolant velocity affects adversely the heat transfer and results in raising the temperature of the heat sink by 2 K from 347 K to 349 K . It is worth stating that the velocity vectors are scaled and coloured with respect to the velocity components in the x-direction, i.e. u , for all the figures presenting the velocity field in this thesis. Furthermore, the results reveal that there is also a reduction in pressure drop penalty where it falls dramatically from 9.42 kPa to 2.07 kPa by increasing the channel depth from $H_c = 1.25 \text{ mm}$ to $H_c = 3.0 \text{ mm}$. It should be noted here that these results were obtained for $W_c = 1.5 \text{ mm}$ and $\dot{m} = 1.25 \text{ g/s}$.

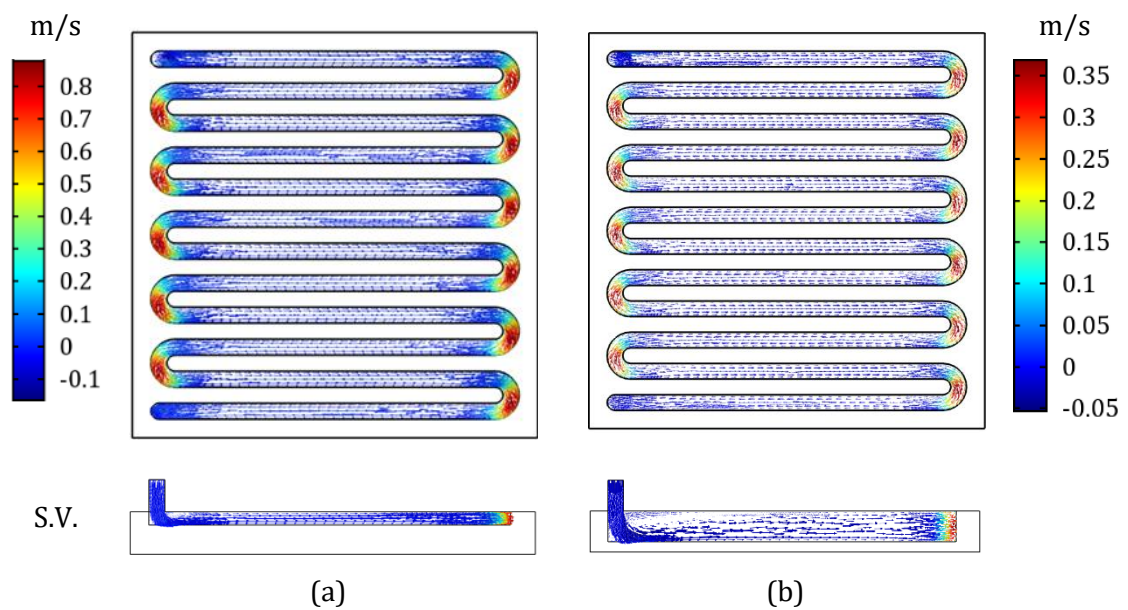


Fig. 5-6 Velocity vectors at the middle of the minichannels, i.e. $z = 0.5H_c$ and the middle of the first channel for: (a) $H_c = 1.25 \text{ mm}$ and (b) $H_c = 3.0 \text{ mm}$ both at $W_c = 1.5 \text{ mm}$ and $\dot{m} = 1.25 \text{ g/s}$.

In the same way, the channel width, Fig. 5-7, had similar effects to those of the channel depth. As a result of increasing the channel width from 1 mm to 2 mm , for instance, the fluid velocity and pressure drop were respectively reduced from 0.86 m/s and 13 kPa to 0.46 m/s and 2.07 kPa , while the temperature was increased from 347 K to 349 K .

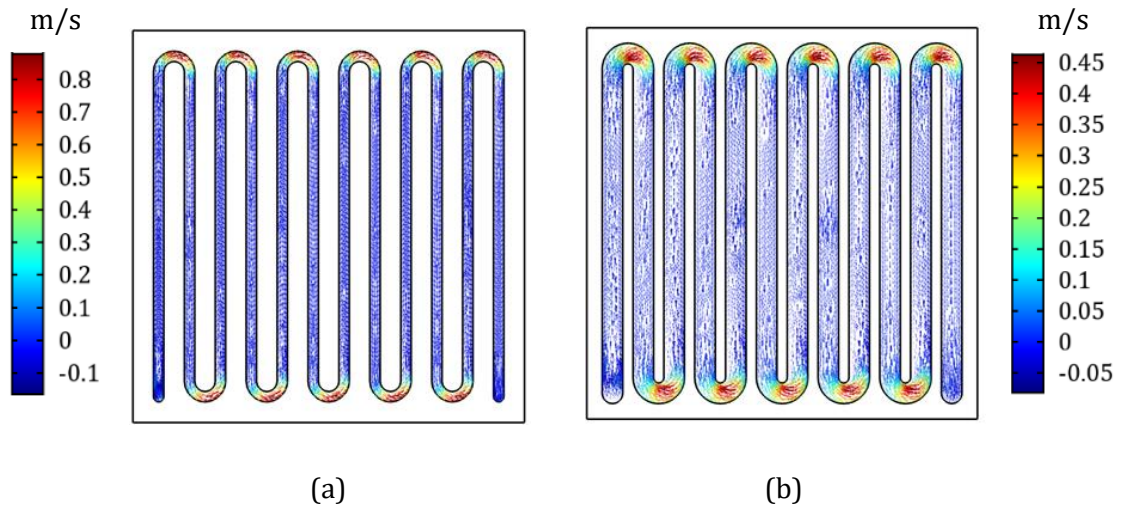


Fig. 5-7 Velocity vectors at the middle of the minichannels, i.e. $z = 0.5H_c$ for:
(a) $W_c = 1.0 \text{ mm}$ and (b) $W_c = 2.0 \text{ mm}$ both at $H_c = 2.0 \text{ mm}$ and $\dot{m} = 1.25 \text{ g/s}$.

5.4 Effect of Vortex Generators

As has been stated in the literature review section 2.4.6, several studies, such as Liu *et al.* (2011); Al-Asadi (2018), Hosseini-rad *et al.* (2019) and Cheng, 2020, have employed vortex generators within the microchannel heat sinks to improve their heat transfer performance, however, it has not been used with the serpentine minichannel heat sink. Therefore, the effect of the transverse semi-cylindrical vortex generators on the thermal-hydraulic performance of the serpentine minichannel heat sink with plate fins (*SMCHS – PF*) is investigated in the current study. Two designs have been tested; in the first one, the vortex generators were attached to the sidewalls, whereas they were added on the minichannels base in the second design. The considered flow was laminar with Reynolds number range from 500 to 2250. The results are presented in the following subsections.

To evaluate the benefit of using the *VGs*, the thermal-hydraulic performance criterion (PEC) has been employed. This criterion might be defined as the ratio of the heat transfer enhancement to the pressure drop penalty of the new design in comparison to the smooth serpentine (Manca *et al.*, 2012; Ahmed *et al.*, 2014; Zhao *et al.*, 2016; Al-Asadi, 2018 and Al-Neama, 2018). Mathematically, it can be expressed as:

$$PEC = \frac{\overline{Nu}_{SMCHS-PF-VGs} / \overline{Nu}_{SMCHS-PF}}{(\Delta P_{SMCHS-PF-VGs} / \Delta P_{SMCHS-PF})^{1/3}} \quad \text{Equ. 5-5}$$

where \overline{Nu} and ΔP represent the average Nusselt number and the pressure drop for the compared models, i.e., the smooth serpentine (*SMCHS – PF*) and the one with *VGs* (*SMCHS – PF – VGs*). The average Nusselt number can be determined using:

$$\overline{Nu} = \frac{\overline{h} \cdot D_h}{k_f} \quad \text{Equ. 5-6}$$

The \overline{h} , D_h and k_f are the average heat transfer coefficient, the minichannel hydraulic diameter ($\frac{4 W_c \cdot H_c}{2 (W_c + H_c)}$) and the fluid thermal conductivity, respectively. The k_f is obtained at the average fluid temperature (\overline{T}_f) which is calculated based on fluid temperatures at the inlet ($T_{f,in}$) and outlet ($T_{f,out}$). The heat transfer coefficient, on the other hand, is determined by:

$$\overline{h} = \frac{Q}{A_e (\overline{T}_{base_c} - \overline{T}_f)} \quad \text{Equ. 5-7}$$

where the Q is total heat imposed over a part of the heat sink bottom, \overline{T}_{base_c} is the average minichannel base temperature and A_e is the available surface area for the heat transfer. In the current investigation, as the top surface of the serpentine channel has been assumed to be insulated, the heat is transferred through the other three surfaces of the channel to the cooling fluid. Consequently, the effective heat transfer area (A_e) can be calculated using the following equation:

$$A_e = \eta_f A_{fin} + A_{base} \quad \text{Equ. 5-8}$$

here, η_f and A_{fin} are the efficiency and the area of the fins whereas A_{base} denotes the minichannel base. The efficiency can be calculated as follows:

$$\eta_f = \frac{\tanh(m \cdot H_c)}{m \cdot H_c}$$

$$m = \sqrt{\frac{2\overline{h}}{W_c \cdot k_s}}$$

where k_s is thermal conductivity of the solid.

The areas in (Equ. 5-8) can be determined as:

$$C1 = (L_c - R_{inlet}) W_c \cdot N_c$$

$$L_c = L - 2(W_1 + R_o)$$

$$C2 = \frac{\pi}{2} (R_o^2 - R_i^2)(N_c - 1)$$

$$C3 = 2 \left[\frac{\pi}{2} R_{inlet}^2 + W_c (R_o - R_{inlet}) \right]$$

$$A_{base_{SMCHS-PF}} = C1 + C2 + C3$$

$$C4 = 2(L_c - R_{inlet}) H_c \cdot N_c$$

$$C5 = \pi (R_o + R_i)(N_c - 1) H_c$$

$$C6 = (4(R_o - R_{inlet}) + 2\pi R_{inlet}) H_c$$

$$C7 = (R_o - R_{inlet}) H_c$$

$$A_{fin_{SMCHS-PF}} = C4 + C5 + C6 + C7$$

$$A_{e_{SMCHS-PF}} = \eta_f A_{fin_{SMCHS-PF}} + A_{base_{SMCHS-PF}}$$

Equ. 5-9

For vertical vortex generators:

$$K8 = (2r_{VG} \cdot H_{VVG}) N_{VVG} \cdot N_c + (2r_{VG} \cdot H_{VVG})(N_c - 1)$$

$$K9 = (\pi r_{VG} \cdot H_{VVG}) N_{VVG} \cdot N_c + (\pi r_{VG} \cdot H_{VVG})(N_c - 1)$$

$$A_{base_{SMCHS-PF-VVGs}} = A_{base_{SMCHS-PF}}$$

$$A_{fin_{SMCHS-PF-VVGs}} = A_{fin_{SMCHS-PF}} - K8 + K9$$

$$A_{e_{SMCHS-PF-VVGs}} = \eta_f A_{fin_{SMCHS-PF-VVGs}} + A_{base_{SMCHS-PF-VVGs}}$$

Equ. 5-10

For horizontal vortex generators:

$$K10 = (2r_{VG} \cdot H_{HVG}) N_{HVG} \cdot N_c + (2r_{VG} \cdot H_{HVG})(N_c - 1)$$

$$K11 = (\pi r_{VG} \cdot H_{HVG}) N_{HVG} \cdot N_c + (\pi r_{VG} \cdot H_{HVG})(N_c - 1)$$

$$A_{base_{SMCHS-PF-HVGs}} = A_{base_{SMCHS-PF}} - K10 + K11$$

$$A_{fin_{SMCHS-PF-HVGs}} = A_{fin_{SMCHS-PF}}$$

$$A_{e_{SMCHS-PF-HVGs}} = \eta_f A_{fin_{SMCHS-PF-HVGs}} + A_{base_{SMCHS-PF-HVGs}}$$

Equ. 5-11

5.4.1 Vertical Transverse Vortex Generators Attached to the Sidewalls

Fig. 5-8 shows a serpentine minichannel heat sink equipped with vertical semi-cylindrical vortex generators (*SMCHS - PF - VVGs*), with a radius of r_{VG} (0.1, 0.15, 0.2, 0.25 and 0.3 mm) and height of $H_{VG} = 2$ mm, attached to its sidewalls. These *VVGs* were distributed on both sides of the channel in two

arrangements: (1) staggered (*SMCHS – PF – VSVGs*), Fig. 5-8(b), and (2) in-lined (*SMCHS – PF – VIVGs*), Fig. 5-8(c).

For the staggered pattern, the number of *VVGs* was 5 on one side and 4 on the other side. The distance between any *VVGs* on the same side was $l_{VG} = 2.5 H_{VG}$ while the distance between *VVGs* on one side and another on the opposite side was $d_{VG} = 0.5 l_{VG}$. Moreover, for the in-lined configuration, the number of *VVGs* in each channel was 5 with a distance of l_{VG} between any two of them. The other dimensions are as stated in section 5.2.

For the two studied cases of the *VVGs*, the influence of Reynolds number on thermal resistance, pressure drop and PEC is illustrated in Fig. 5-9 and Fig. 5-10. As expected, increasing Reynolds number (Re) leads to a decrease in thermal resistance, Fig. 5-9(a) and Fig. 5-10(a), which can be attributed to the decrease in the surface temperature of the minichannel heat sink. In contrast, the pressure drop, Fig. 5-9(b) and Fig. 5-10(b), increases with increasing Re and this is consistent with the internal flow theory, which states that:

$$\Delta P = f \frac{L}{D} \frac{\rho V^2}{2} \quad \text{Equ. 5-12}$$

Furthermore, this investigation reveals that adding vertical vortex generators (*VVGs*) to the serpentine minichannels (*SMCHS – PF*) leads to a decrease in the overall thermal resistance, R_{th} . Depending on Re , r_{VG} and the arrangement of the *VVGs*, the achieved improvement in R_{th} was in the range of 4% to 11% in comparison to that without vortex generators, serpentine smooth minichannels. This enhancement can be mainly assigned to the contribution of the additional surface area (2.8%) provided by the *VVGs* to heat transfer. However, this advantage is accompanied by a remarkable increase in pressure penalty ranging from 30% to 200% due to the contraction in the flow passage at the locations of the *VVGs*.

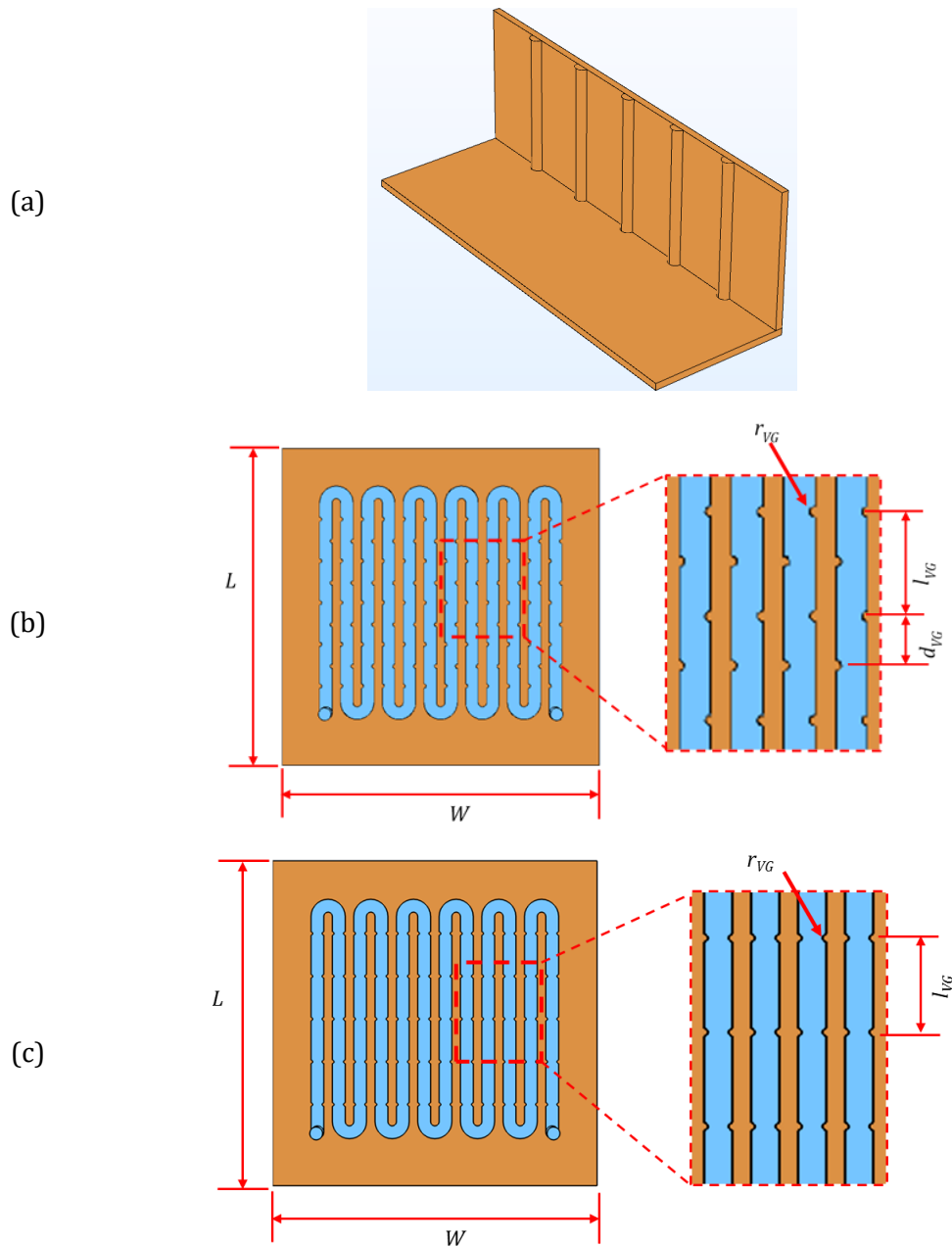


Fig. 5-8 Serpentine minichannel heat sink equipped with vertical traverse vortex generators: (a) 3D view showing the VGs , (b) top view with an enlarged view $SMCHS - PF - VSVGs$ and (c) top view with an enlarged view for $SMCHS - PF - VIVGs$.

On one hand, for example, the in-lined $VVGs$ arrangement uncover that the reduction in R_{th} at $Re = 2250$ and for $r_{VG} = 0.1, 0.2$ and 0.3 was respectively 9.3%, 9.4 and 11.1% accompanied with an increase in pressure penalty of 45%, 88% and 208%. On the other hand, the staggered $VVGs$ configuration shows that the reduction in R_{th} for the same conditions, i.e., $Re = 2250$ and for $r_{VG} = 0.1, 0.2$ and 0.3 , was respectively 9.1%, 9.2% and 10.7% with increasing in pressure drop (ΔP)

of 37%, 63% and 115%. All the above percentages have been calculated with respect to the smooth serpentine minichannel heat sink, i.e. without VGs .

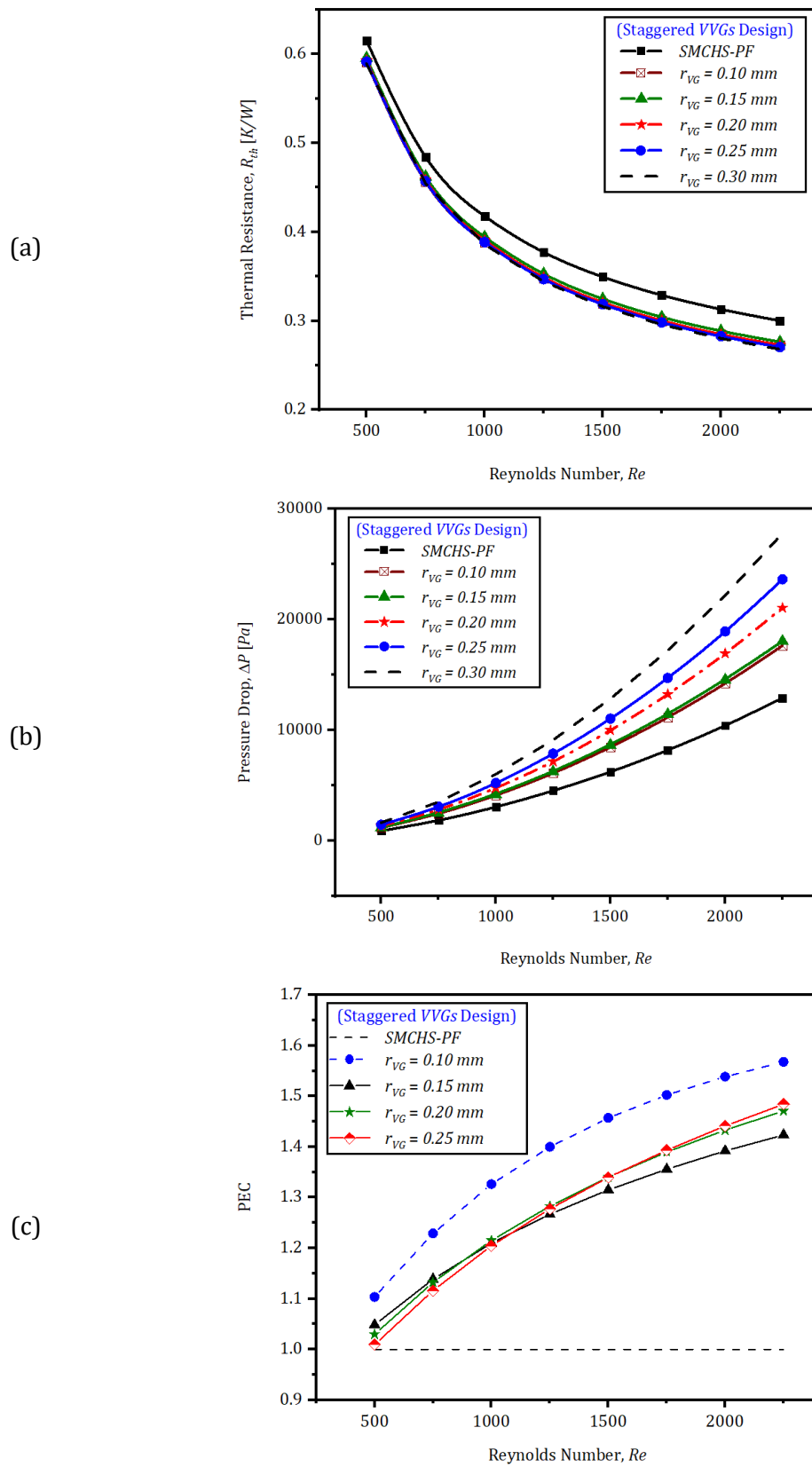


Fig. 5-9 Effect of Reynolds number on: (a) R_{th} , (b) ΔP and (c) PEC for $SMCHS - PF - VSVGs$.

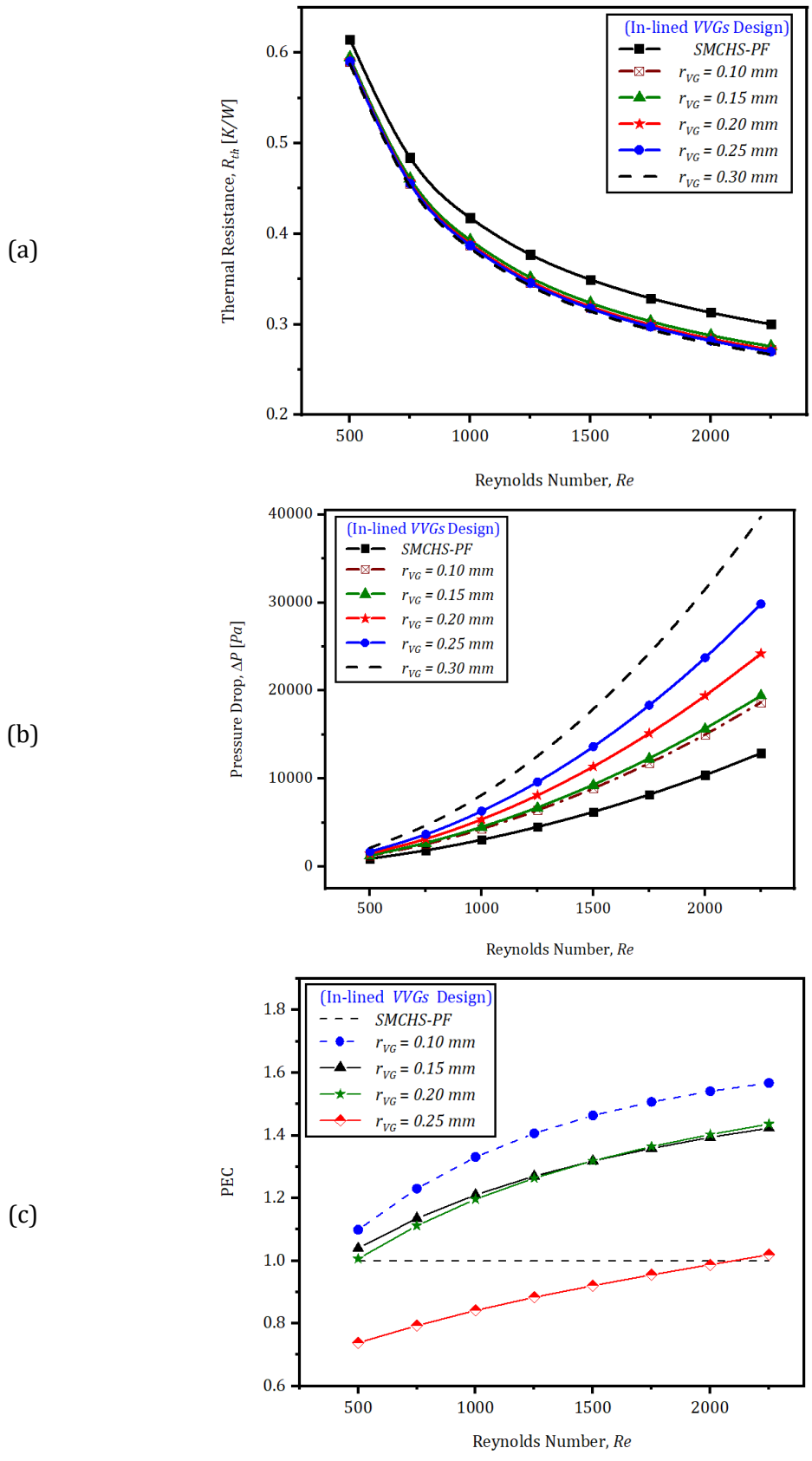


Fig. 5-10 Effect of Reynolds number on: (a) thermal resistance, (b) pressure drop and (c) PEC for SMCHS – PF – VIVGs.

To assess the benefit of adding the *VVGs*, the performance evaluation criteria (PEC) index was used, and the results are presented in Fig. 5-9 (c) and Fig. 5-10 (c). For the staggered *VVGs* arrangement, Fig. 5-9 (c), it can be noticed that the PEC are greater than 1 for all studied ranges of r_{VG} and Re and the maximum PEC reached to 1.57 for $r_{VG} = 0.1 \text{ mm}$ and $Re = 2250$. These results mean that the presence of the *VVGs* arranged in staggered is beneficial for improving the hydrothermal performance of the considered heat sink. However, for the in-lined *VVGs* arrangement, the findings show that they can offer good enhancement except for the design with $r_{VG} = 0.25 \text{ mm}$ where the PEC was less than 1 for $Re \leq 2000$. Therefore, the best design among the studied cases for the two arrangements is the one with $r_{VG} = 0.1 \text{ mm}$.

Fig. 5-11 and Fig. 5-12 present the velocity vectors in the xy - plane at $z = 3 \text{ mm}$ for the staggered and the in-lined *VVGs* arrangements with $r_{VG} = 0.15$ and 0.3 mm , respectively. It is found that the presence of the *VVGs* disturbs the flow, reduces the boundary layers thickness, and helps in mixing the fluid which results in promoting the heat transfer efficiency from the solid walls to water and, consequently, reduce the maximum temperature of the heat sink.

Fig. 5-11 shows the velocity vector in the channels without and with vertical vortex generators. For the smooth straight minichannel, Fig. 5-11(a), the fluid particles following in smooth paths layers and these layers slide smoothly on each other with no mixing. Introducing the *VVGs* on the sidewalls of the serpentine minichannel with the staggered arrangement, Fig. 5-11(b and c), interrupts the flow at the locations of the *VVGs*. For this arrangement, an increase in maximum fluid velocity from 0.96 m/s for the smooth channels to 1.04 m/s for the channels with *VVGs* of $r_{VG} = 0.3 \text{ mm}$ is observed. This increase in velocity reflects on the heat sink maximum temperature (T_{max}) and the pressure penalty of the coolant where the T_{max} falls from 346 K to 342 K , while the pressure raises from 8.6 kPa to 17.6 kPa for the same minichannel conditions.

Using the in-lined configuration in distributing the *VVGs* on the sidewalls of the channel has a clear impact on velocity, Fig. 5-12, and pressure loss. For the same boundary conditions and comparing to the smooth serpentine minichannel heat sink, the fluid pressure penalty increases to 24.2 kPa (i.e., by 196%) for in-lined *VVGs* whereas it was 17.6 kPa (i.e. by 110%) for staggered *VVGs* $r_{VG} = 0.3 \text{ mm}$.

The reason behind that is the large periodic contraction in channel width at the locations of in-lined VVGs in comparison to the staggered VVGs.

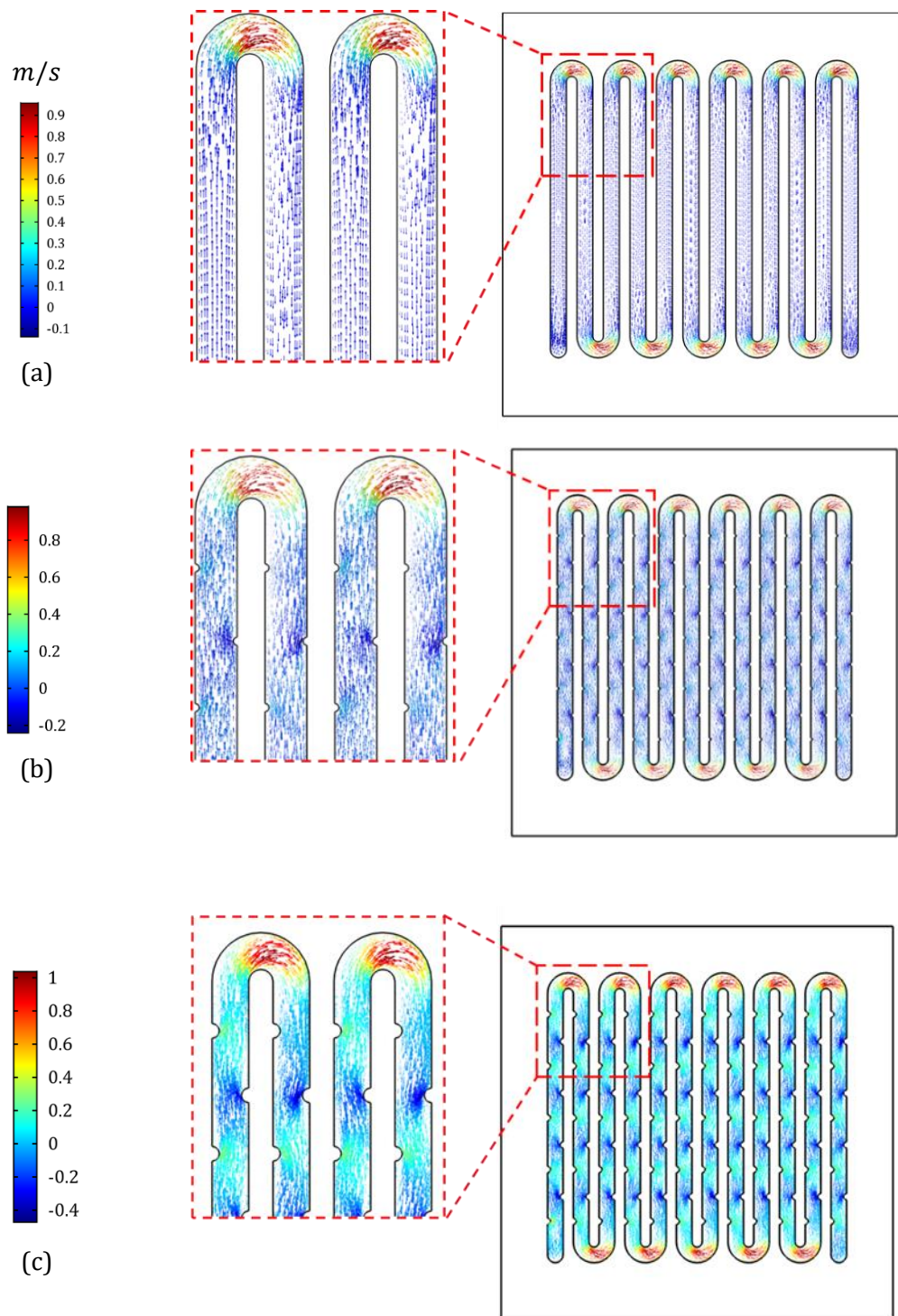


Fig. 5-11 Velocity vectors in the xy – plane at $z = 3 \text{ mm}$, for staggered VVGs at $Re = 1750$ with: (a) smooth channel (b) $r_{VG} = 1.5 \text{ mm}$ and (c) $r_{VG} = 3.0 \text{ mm}$.

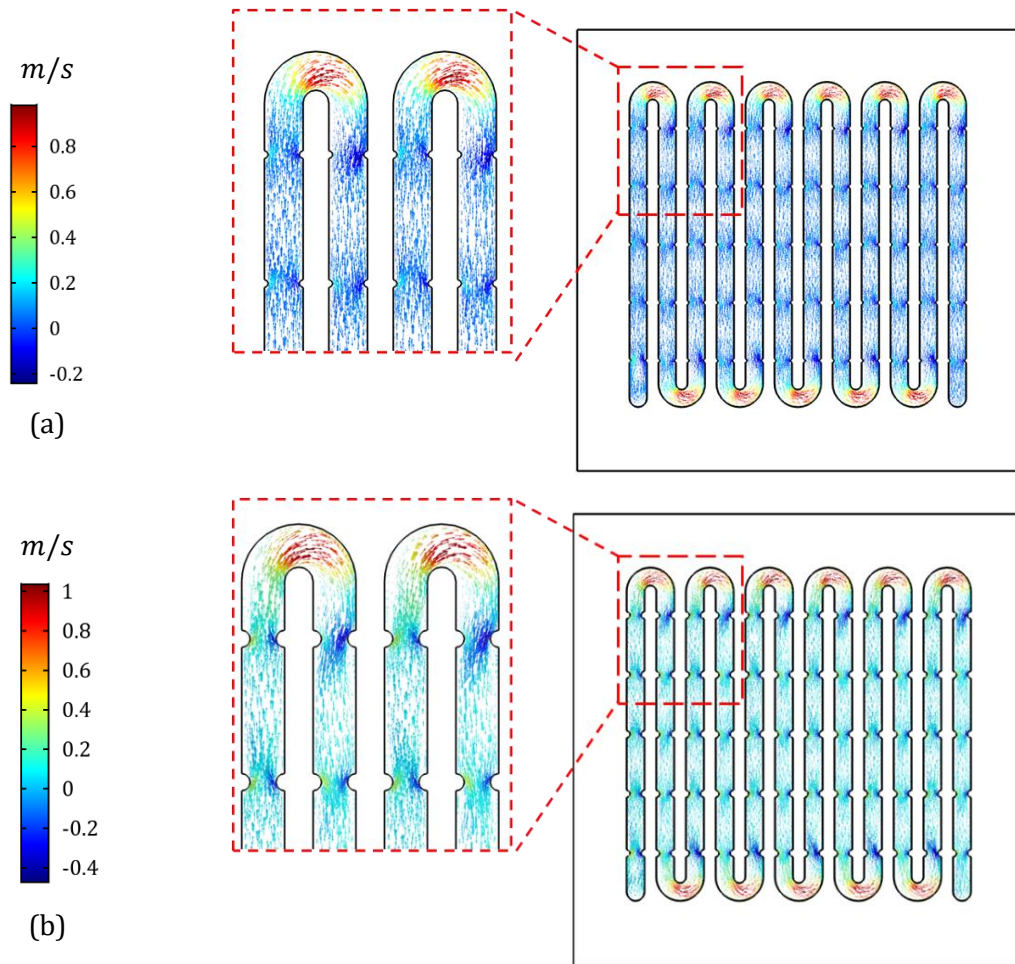


Fig. 5-12 Velocity field in the yz – plane at $z = 3.75 \text{ mm}$, for in-lined $VVGs$ at $Re = 1750$ with: (a) $r_{VG} = 1.5 \text{ mm}$ and (b) $r_{VG} = 3.0 \text{ mm}$.

5.4.2 Horizontal Transverse Vortex Generators Attached to the Channel Base

For further exploration of the effect of the VGs on the performance of the $SMCHS - PF$, horizontal transverse vortex generators ($HVGs$) at the bottom of the minichannel instead of the sidewalls have been employed, $SMCHS - PF - HVG$, Fig. 5-13. The investigated radius of the semi-cylindrical vortex generators, r_{VG} , was in the range from 0.1 mm to 0.3 mm with a height of $H_{VG} = 0.5 W_c$. The Reynolds number of the coolant was less than or equal to 2250 to maintain laminar flow and its inlet temperature was 20°C . The heat flux applied underneath the heat sink was 31 W/cm^2 .

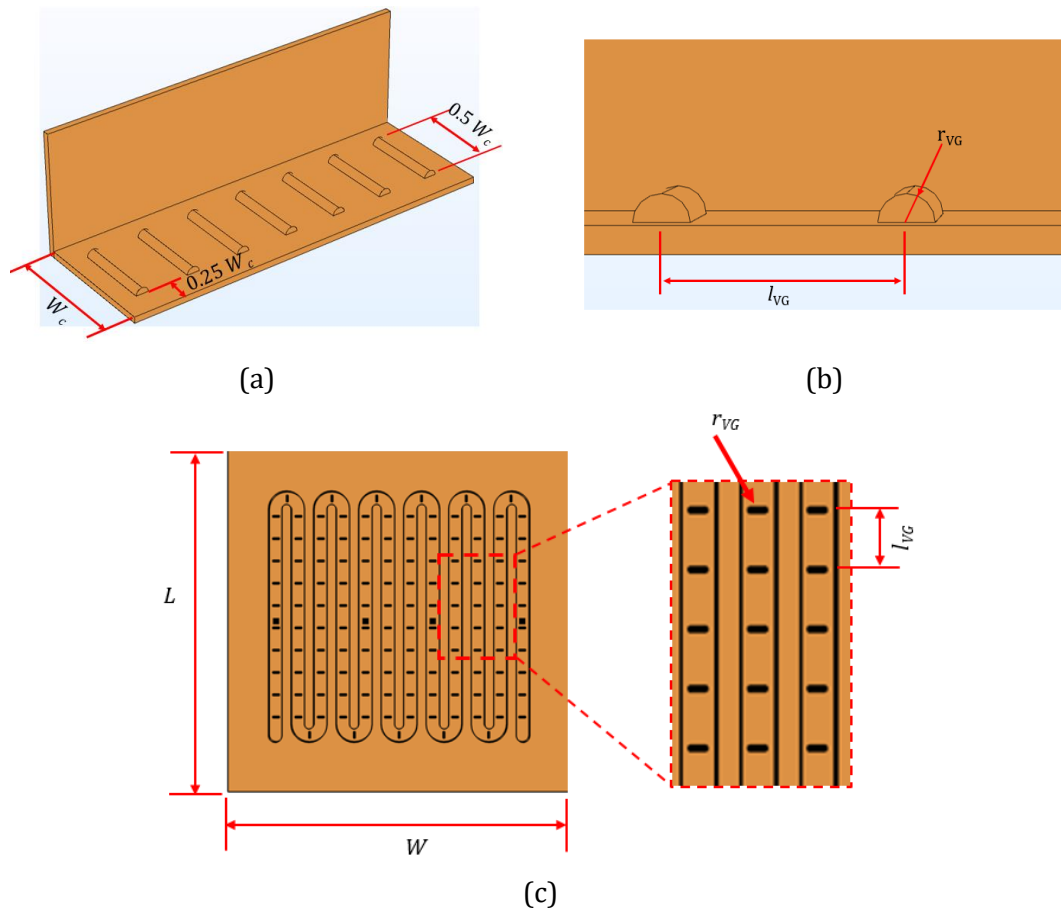


Fig. 5-13 Serpentine minichannel heat sink equipped with horizontal traverse vortex generators at the base of the minichannels (*SMCHS – PF – HVG*): (a) 3D view showing the channel base with *HVGs*, (b) side view of the channel and (c) top view with an enlarged view for the *HVGs*.

The impact of the *HVGs* on the thermal-hydraulic characteristics of the studied heat sink is presented in terms of R_{th} , ΔP and PEC , Fig. 5-14. It can be noticed that there is a significant reduction in overall thermal resistance (R_{th}) in comparison to that of the *SMCHS – PF* without *HVGs* but this reduction is offset by a noticeable increase in pressure drop penalty. At $Re = 1250$ and $r_{VG} = 0.1 \text{ mm}$, for instance, the thermal resistance was lowered by 48% while the pressure was raised by 19%. Besides, the increase in the radius of the vortex generator (r_{VG}) results in a slight increase in thermal resistance with a remarkable rise in pressure penalty. The study has exhibited, for example, that the improvement in thermal performance (R_{th}) was shifted from 52% to 54% by increasing the r_{VG} from 0.1 mm to 0.3 mm, whereas the pressure penalty elevated from 18% to 48% under the same conditions.

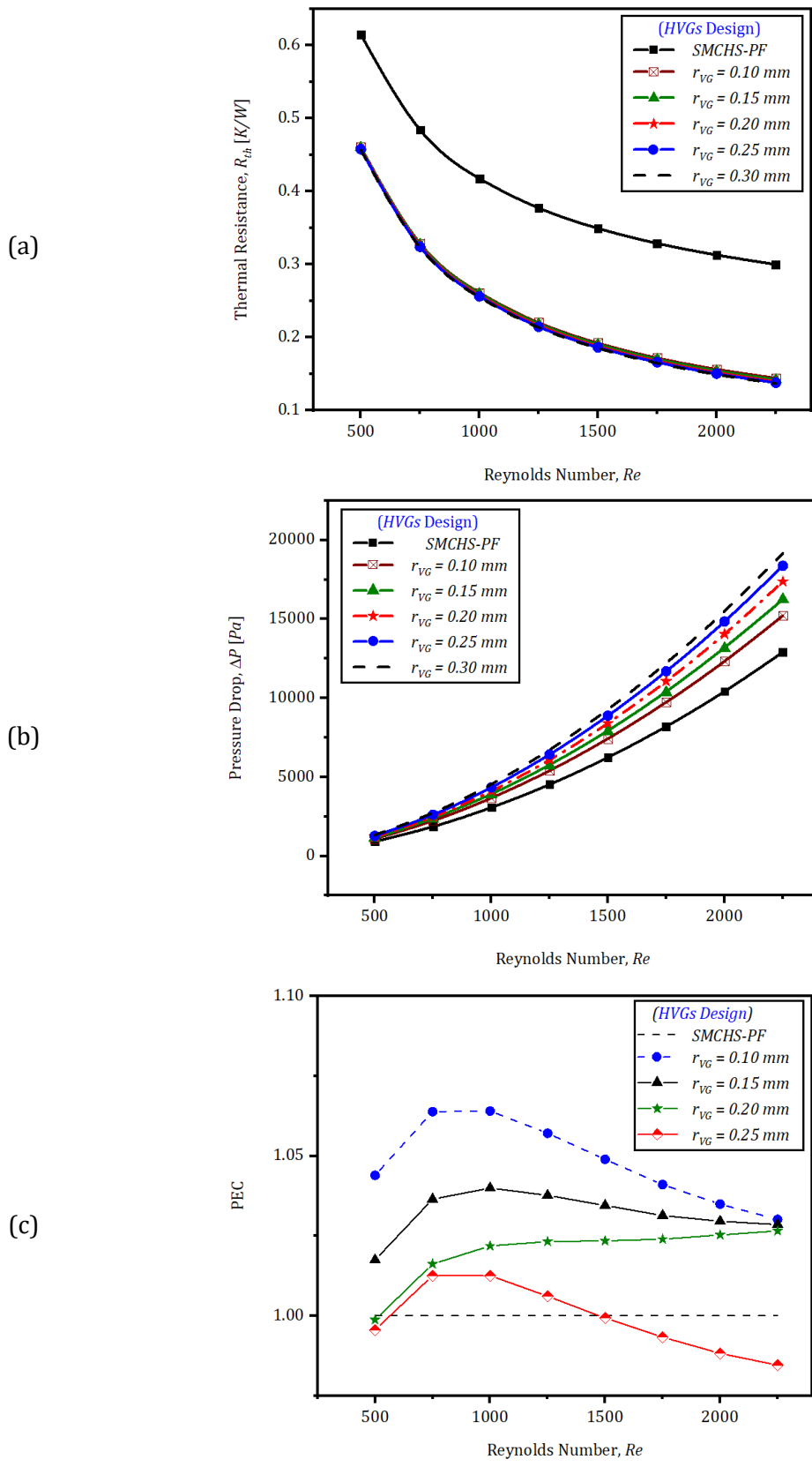


Fig. 5-14 Effect of Reynolds number on: (a) thermal resistance, (b) pressure drop and (c) PEC for SMCHS – PF – HVG.

Furthermore, the reduction in R_{th} due to introducing the *HVGs* reduces the heat sink's maximum temperature from 353 K (for the *MCHS – PF*) to 313 K (for the *SMCHS – PF – HVG* with $r_{VG} = 0.25 \text{ mm}$), i.e., 11.33%, as shown in Fig. 5-15.

Similar to the case of the *VVGs*, the above improvement in thermal performance can be attributed to the disturbance caused by introducing the *HVGs* which break the boundary layers and augment fluid mixing near the solid walls, Fig. 5-16. This influence is increased by increasing the r_{VG} as depicted in Fig. 5-16(b). However, as stated above, there is an increase in the pressure penalty by including the *HVGs* and increasing its radius, r_{VG} , Fig. 5-14(b).

Moreover, the *HVGs* generate longitudinal vortices which in turn push the fluid from the bottom toward the centre of the channel with the flow direction, helping in transferring the heat from the solid walls to the cooling fluid. This behaviour can be identified easily by comparing the centre of the fluid vortices for the smooth serpentine heat sink (Fig. 5-17 a) with those containing *HVGs* where it can be noticed how the vortices centre shift upward as shown in Fig. 5-17 b and c. However, the regions behind the *HVGs* have stagnant zones which generate hot spots as illustrated in Fig. 5-18.

Assessing the benefits of employing the *HVGs*, has been implemented through the PEC, shown in Fig. 5-14(c). The PEC values are, for all designs, above 1 except for the one which has $r_{VG} = 0.25 \text{ mm}$ with $Re > 1500$. It has also been noticed that PEC for the studied designs increased to a maximum point then decreased, and the best performance can be achieved using $r_{VG} = 0.1 \text{ mm}$ with $750 < Re < 1000$.

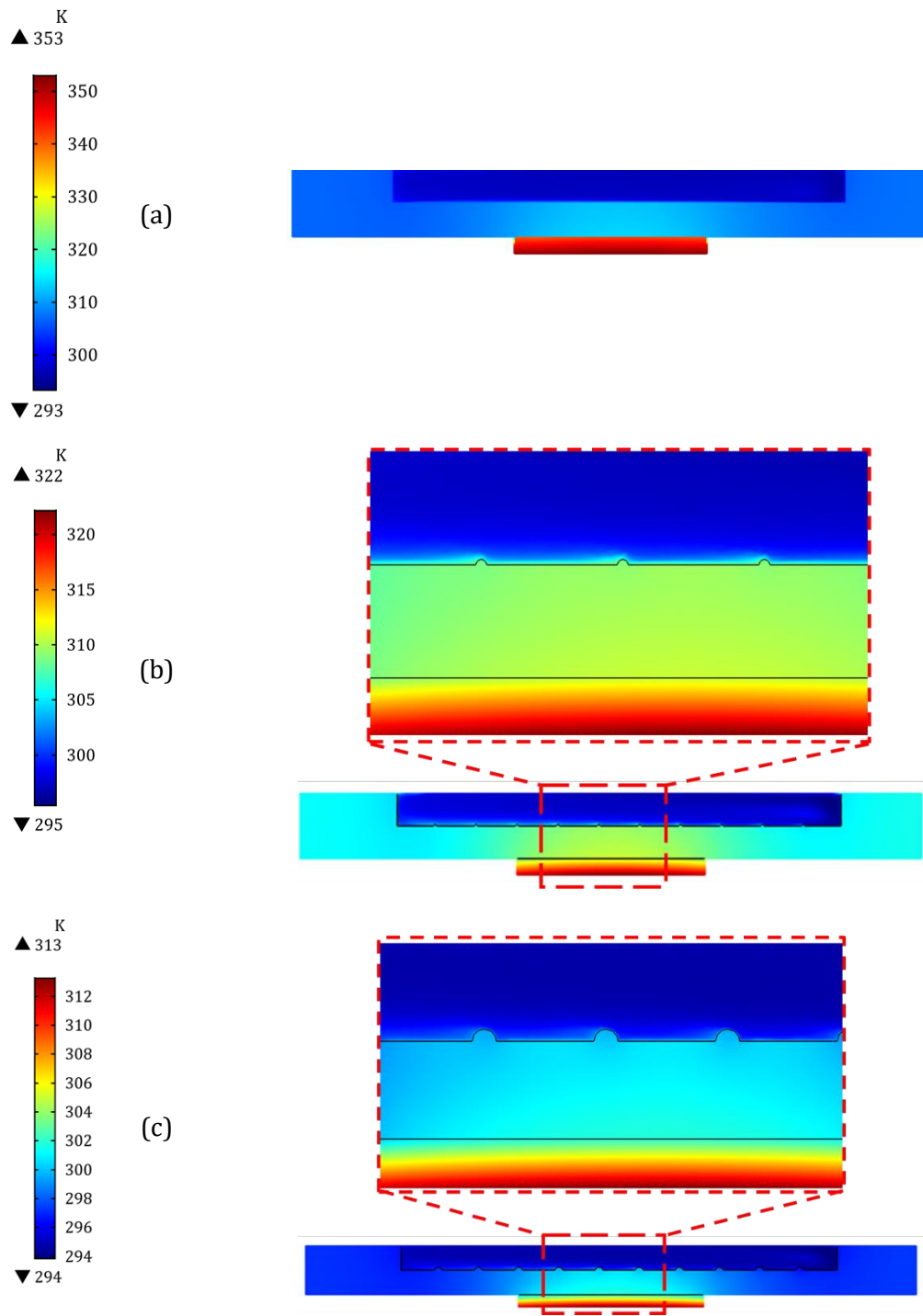


Fig. 5-15 Temperature distribution in the yz – plane at $x = 7.75 \text{ mm}$ and at $Re = 1000$ for: (a) smooth serpentine and HVGs with (b) $r_{VG} = 0.1 \text{ mm}$ and (c) $r_{VG} = 0.25 \text{ mm}$.

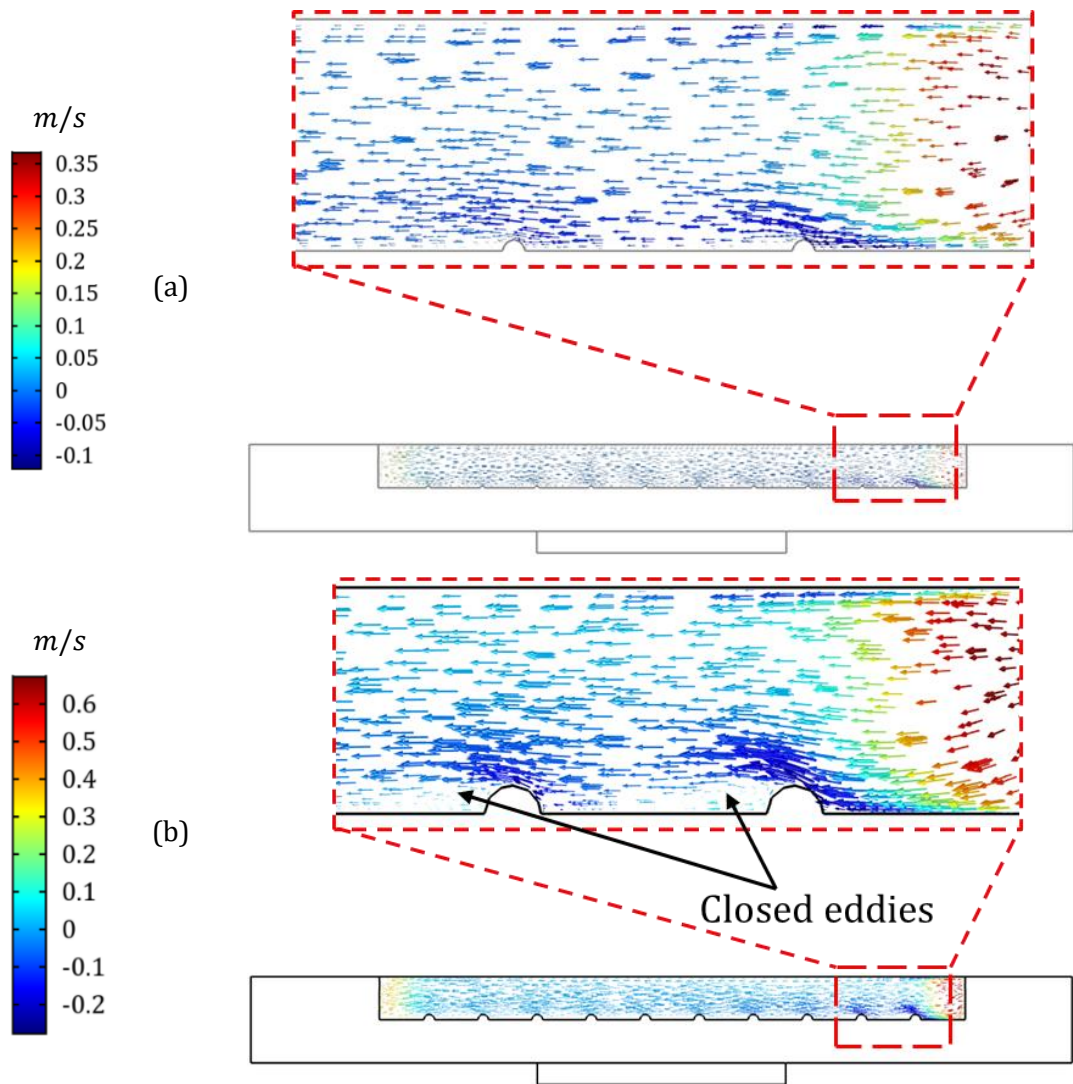


Fig. 5-16 Velocity vectors in the yz – plane at $x = 7.75 \text{ mm}$ and at $Re = 1000$ for: (a) smooth serpentine and $HVGs$ with (b) $r_{VG} = 0.1 \text{ mm}$ and (c) $r_{VG} = 0.25 \text{ mm}$.

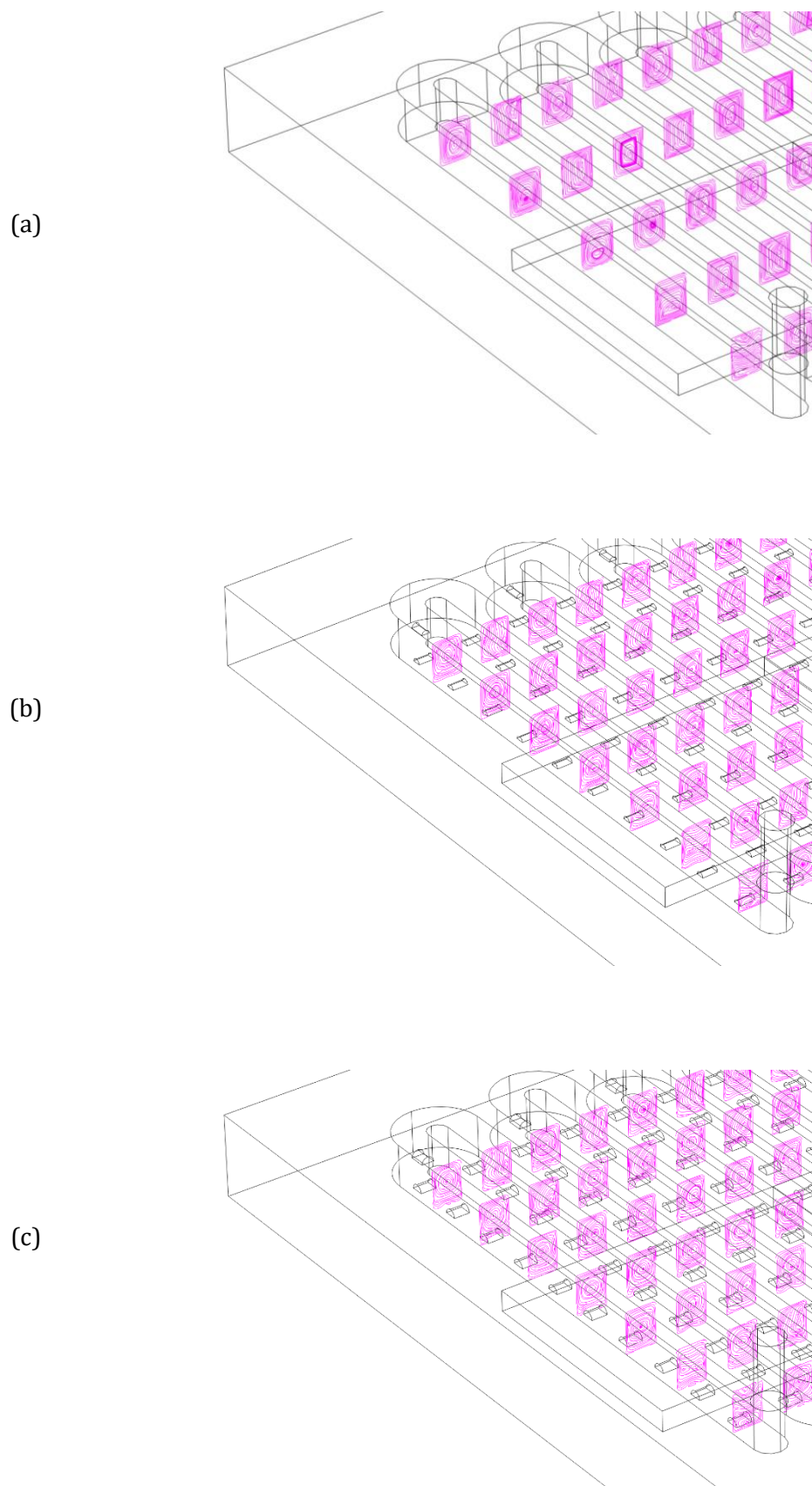


Fig. 5-17 Vortical structures in the xz – plane at different y values and at $Re = 1000$ for: (a) smooth serpentine and $HVGs$ with (b) $r_{VG} = 0.2 \text{ mm}$ and (c) $r_{VG} = 0.3 \text{ mm}$.

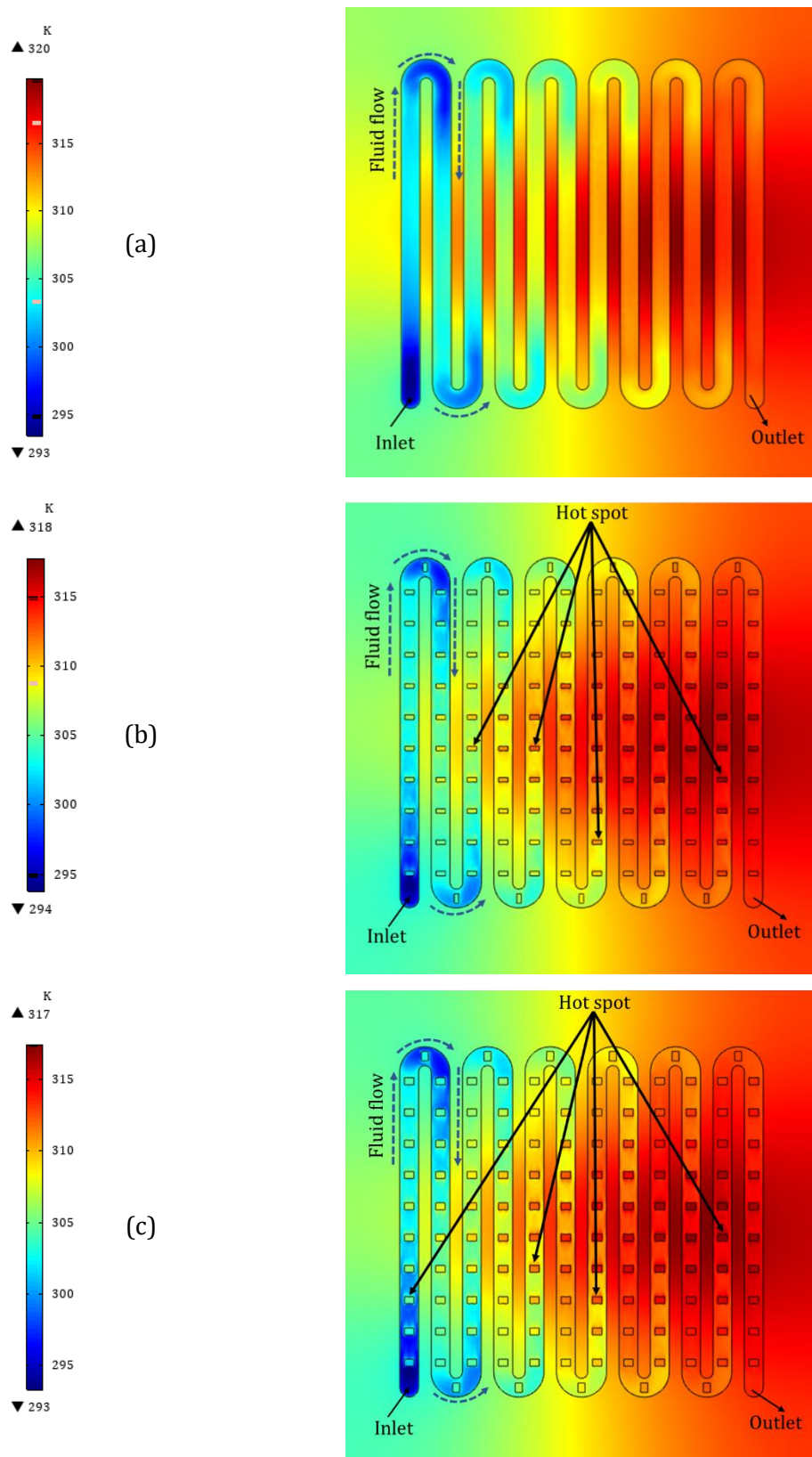


Fig. 5-18 Temperature distribution in the xy – plane at $z = 2.05 \text{ mm}$, and at $Re = 1000$ for: (a) smooth serpentine and HVGs with (b) $r_{VG} = 0.2 \text{ mm}$ and (c) $r_{VG} = 0.3 \text{ mm}$.

5.5 Deterministic Optimisation of the Serpentine Minichannel Heat Sinks

This section addresses the optimisation of the hydrothermal performance of the serpentine minichannel heat sink with plate fin (*SMCHS – PF*). Consequently, both single- and multi-objective optimisation will be formulated and explored in the following subsections.

5.5.1 Single-Objective Deterministic Optimisation

In the study of Al-Neama *et al.* (2017), they did not address the height of the channel in their optimisation study, therefore, it is considered in this investigation. In the first stage, a single-objective function deterministic optimisation for each quantity of interest for the *SMCHS – PF*, i.e. R_{th} and ΔP , has been performed. The design variables were chosen to be the width W_c and the height H_c of the minichannel. It is assumed that $W_c + W_w = 3.0[mm]$. The optimisation problem for the R_{th} has been formulated as:

$$\begin{array}{ll} \textit{Find} & W_c \textit{ and } H_c \\ \textit{To minimise} & R_{th}(W_c, H_c) \end{array} \quad \text{Equ. 5-13}$$

whereas, the one for the ΔP has been written as:

$$\begin{array}{ll} \textit{Find} & W_c \textit{ and } H_c \\ \textit{To minimise} & \Delta P(W_c, H_c) \end{array} \quad \text{Equ. 5-14}$$

Both optimisation problems are subjected to:

$$1.0 \leq W_c \leq 2.0 \quad \text{Equ. 5-15}$$

$$1.0 \leq H_c \leq 3.0 \quad \text{Equ. 5-16}$$

As the optimisation strategy is a surrogate-based optimisation methodology, the design space has been sampled using the Latin-hypercube sampling method to obtain space-filling points that represent the whole space with relatively few sample points (50 points), Fig. 5-19.

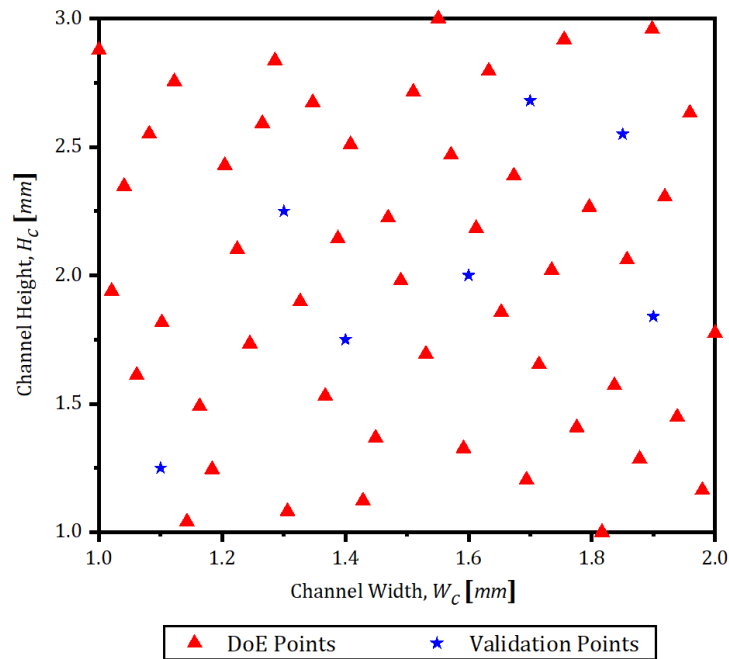
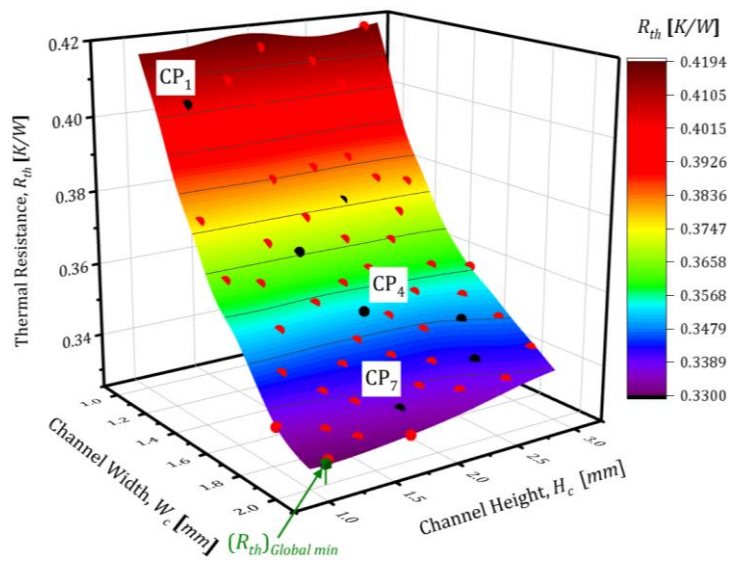
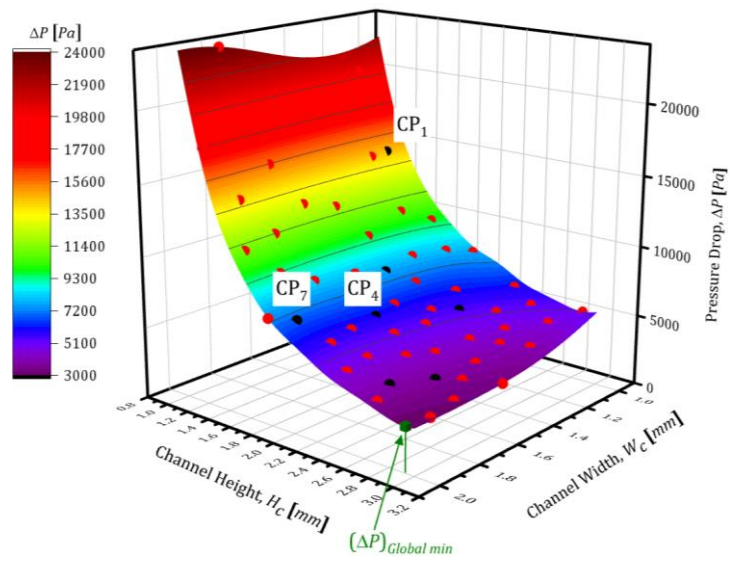


Fig. 5-19 Design of experiments and validation points used to build the surrogate model for the *SMCHS – PF* design.

Then, the CFD *COMSOL* model for *SMCHS – PF* (with $Re = 1500$, $q'' = 31 \text{ W/cm}^2$ and $T_{in} = 20 \text{ }^\circ\text{C}$) was run at each point of the DoEs to generate the response of the model. After that, the metamodel (Gaussian Process model) for each of R_{th} and ΔP was constructed, Fig. 5-20, based on these DoEs points and their corresponding response. In these figures, the black points are heat sink's performance at the DoE points while the green points represent the minimum values of these responses. The accuracy of those surrogate models was assessed by the cross-validation method, i.e. comparing their responses against those of the CFD model at new design variables, the blue stars in Fig. 5-19. The results, Table 5-2, demonstrate a very good agreement with a maximum difference of 1.93%. Based on this assessment, the constructed surrogate models can be considered as excellent candidates to replace the expensive CFD model to predict the R_{th} and ΔP of the heat sink under study. Then, the optimisation procedure for each function, i.e. the thermal resistance and pressure drop, has been run using the genetic algorithms (*soga*) to find the design variable values that minimises these objectives and the results are shown in Fig. 5-20 and Table 5-3.



(a)



(b)

Fig. 5-20 Surrogate model for the performance criteria of *SMCHS – PF* design: (a) R_{th} and (b) ΔP . The red points are the training points, while the black (Labeled as CP_i) points are the validation points.

Table 5-2 Comparison of the responses evaluated by the CFD simulation and the approximation surrogate model (cross-validation).

Point	Design Variables		CFD-Predictions		Surrogate model		% diff. (\pm)	
	W_c	H_c	R_{th}	ΔP	R_{th}	ΔP	R_{th}	ΔP
			[K/W]	[Pa]	[K/W]	[Pa]		
CP ₁	1.10	1.25	0.40363	14471.0	0.40325	14452.0	0.09	0.13
CP ₂	1.30	2.25	0.37590	5393.9	0.37644	5405.1	0.14	0.21
CP ₃	1.40	1.75	0.36662	7657.1	0.36582	7703.0	0.22	0.60
CP ₄	1.60	2.00	0.35295	5950.7	0.35134	5995.9	0.46	0.76
CP ₅	1.70	2.68	0.34811	3726.2	0.34778	3710.8	0.10	0.41
CP ₆	1.85	2.55	0.34139	3923.9	0.34112	3902.5	0.08	0.55
CP ₇	1.90	1.84	0.33527	6869.2	0.33526	6736.9	0.00	1.93

Table 5-3 Global surrogate-based single-objective optimisation results for the thermal resistance and pressure drop.

Case	Objective function	Global Opt.	W_c [mm]	H_c [mm]
1	Thermal resistance, R_{th} [K/W]	0.330	1.994	1.127
2	Pressure drop, ΔP [Pa]	3061.289	1.997	2.925

5.5.2 Multi-Objective Functions Deterministic Optimisation

In this subsection, a surrogate-based multi-objective deterministic optimisation for the R_{th} and ΔP has been conducted to examine the effect of the channel width and channel height on these outputs of interest. The optimisation problem could be written as:

Find W_c and H_c

To minimise $R_{th}(W_c, H_c)$ & $\Delta P(W_c, H_c)$ Equ. 5-17

Subjected to $1.0 \leq W_c \leq 2.0$ Equ. 5-18

$1.0 \leq H_c \leq 3.0$ Equ. 5-19

As in the previous subsection, the genetic algorithm (*moga*) has been employed in the surrogate-based optimisation process and the results are presented graphically in the form of Pareto front along with their DoE points, Fig. 5-21.

The points on the Pareto front are non-dominated in the sense it is impossible to decrease the R_{th} without increasing the ΔP and vice versa. Therefore, these points represent a compromise between the optimised objective functions. Accordingly, the designers can use the Pareto front to choose the appropriate design in which the goal of their design is satisfied.

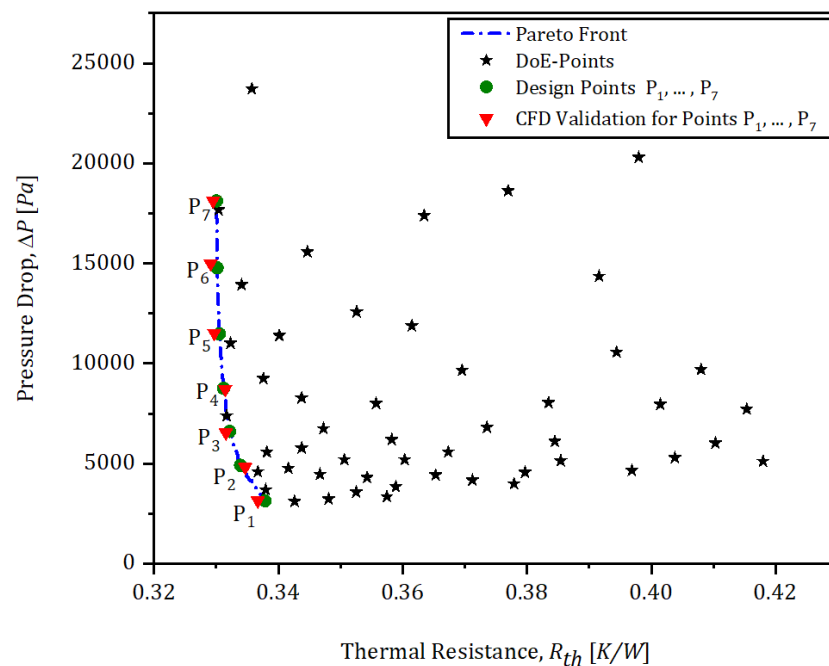


Fig. 5-21 Pareto front for the pressure drop and thermal resistance of the *SMCHS – PF*.

Seven design points (P_1 - P_7), Fig. 5-21, were selected randomly on the Pareto front as representatives for the purpose of demonstrating the accuracy of the metamodelling method. The channel width and height with their corresponding responses have been tabulated in Table 5-4. The numerical solutions have been obtained at the design variables of these points and presented in the same table. It is obvious that there is a good agreement between the results of the surrogate model with those of the CFD simulation with a relative difference less than 3.1% for both two objective functions in the present case. It can be noticed that all the selected optimum points occur with $W_c \cong 2 \text{ mm}$ while the H_c varies from 1.15 mm to 2.84 mm . To minimise the thermal resistance, channel height should be chosen near the lower limit of the

studied range of the channel height, but this will at the expense of the raise in ΔP , and vice versa.

Table 5-4 Validation of the metamodeling method for the *SMCHS – PF*.

Point	Design Variables		Surrogate model		CFD-Predictions		% diff. (\pm)	
	W_c	H_c	R_{th} [K/W]	ΔP [Pa]	R_{th} [K/W]	ΔP [Pa]	R_{th}	ΔP
P ₁	1.999	2.837	0.338	3141.4	0.337	3241.4	0.34	3.1
P ₂	1.999	2.237	0.334	4909.7	0.335	4819.9	0.22	1.86
P ₃	1.999	1.896	0.332	6603.3	0.332	6535.8	0.18	1.03
P ₄	1.999	1.632	0.331	8754.8	0.332	8715.7	0.08	0.45
P ₅	1.999	1.261	0.330	14778.3	0.329	14825.0	0.46	0.31
P ₆	1.999	1.423	0.331	11479.2	0.330	11511.0	0.25	0.28
P ₇	1.999	1.151	0.330	18122.4	0.329	18128.0	0.17	0.03

5.6 Deterministic Optimisation of *SMCHS – PF – VGs*

The single- and multi-objective optimisation on the serpentine minichannel heat sink's hydrothermal performance equipped with vortex generators has been applied in this section. The *SMCHS – PF – VSVGs* and *SMCHS – PF – HVGs* designs have been selected to implement this optimisation strategy.

5.6.1 Single-objective Optimisation for *SMHS – PF – VSVGs* and *SMHS – PF – HVGs*

For the serpentine minichannel heat sinks equipped with staggered vertical vortex generators (*SMCHS – PF – VSVGs*) and horizontal vortex generators (*SMCHS – PF – HVGs*), the single-objective optimisation has been performed for the R_{th} , ΔP and PEC. The design variables were the radius of the vortex generator (r_{VG}) and the distance between vortex generators (l_{VG}), Fig. 5-8(b) and Fig. 5-13(b). It is also assumed that $d_{VG} = 0.5 l_{VG}$. Accordingly, the three optimisation problems were formulated as:

$$\begin{array}{ll}
 \textit{Find} & r_{VG} \textit{ and } l_{VG} \\
 \\
 \textit{To minimise} & R_{th}(r_{VG}, l_{VG}) \qquad \qquad \text{Equ. 5-20}
 \end{array}$$

$$\text{To minimise} \quad \Delta P (r_{VG}, l_{VG}) \quad \text{Equ. 5-21}$$

$$\text{To minimise} \quad \text{PEC} (r_{VG}, l_{VG}) \quad \text{Equ. 5-22}$$

Based on the design configuration, these optimisation problems were subjected to two different design variables ranges which are written as:

$$\text{For } SMCHS - PF - VSVGs \text{ design:} \quad 0.1 \leq r_{VG} \leq 0.3 \quad \text{Equ. 5-23}$$

$$1 \leq l_{VG} \leq 10 \quad \text{Equ. 5-24}$$

$$\text{For } SMCHS - PF - HVGs \text{ design:} \quad 0.1 \leq r_{VG} \leq 0.5 \quad \text{Equ. 5-25}$$

$$1.5 \leq l_{VG} \leq 4.5 \quad \text{Equ. 5-26}$$

As in the previous optimisation section, the Latin-hypercube sampling technique has been utilised to generate 50 points in the design space for each studied design, the red triangles in Fig. 5-22. Following that, the quantities of interest, i.e. R_{th} , ΔP and PEC were obtained using the CFD simulation model for the *SMCHS - PF - VSVGs* and *SMCHS - PF - HVGs*, with $Re = 1500$, $q'' = 31 \text{ W/cm}^2$ and $T_{in} = 20 \text{ }^\circ\text{C}$, at each of these DoE points. Then, the DoE points and their corresponding simulation outputs (training points) were used to construct the surrogate model (Gaussian Process model) for each objective function, Fig. 5-23. The validation of these surrogate models was implemented by comparing their results against the CFD predictions at new design points, the blue stars in Fig. 5-22. The comparison showed that the obtained data from the two methods, Table 5-5, were in good agreement and the maximum difference was less than 4.1%, which validated the constructed surrogate models.

After that, the single-objective optimisation with genetic algorithms (*soga*) has been employed to find the design parameters that produce optimum performance for *SMCHS - PF - VSVGs* and *SMCHS - PF - HVGs* designs. The results are presented in Fig. 5-23, Fig. 5-24, Table 5-7 and Table 5-8; and validated against the numerical predictions with a maximum difference of 5% for the pressure penalty.

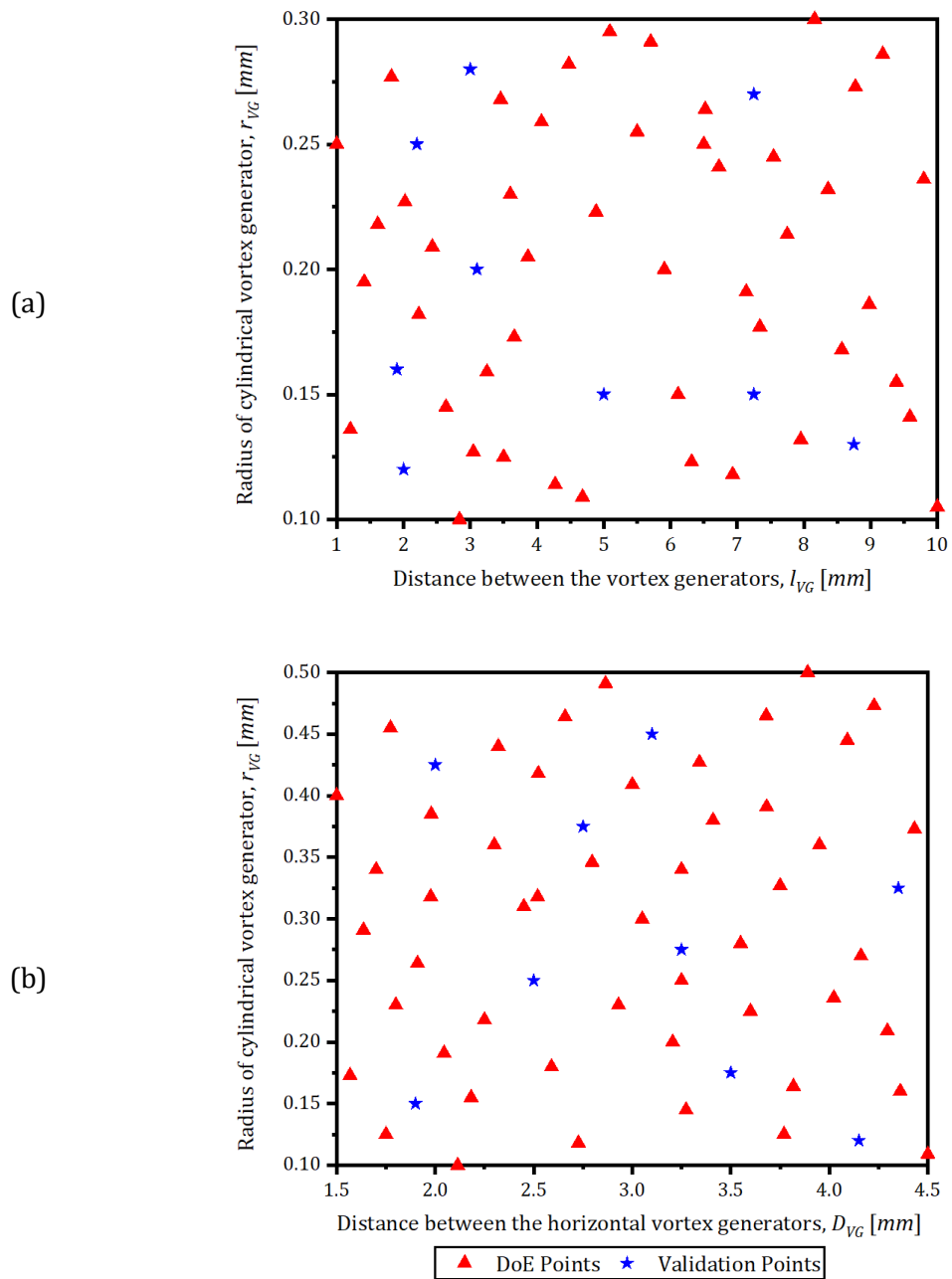


Fig. 5-22 Design of experiments and validation points used to build the surrogate model for the: (a) *SMCHS – PF – VSVGs* and (b) *SMCHS – PF – HVGs* designs.

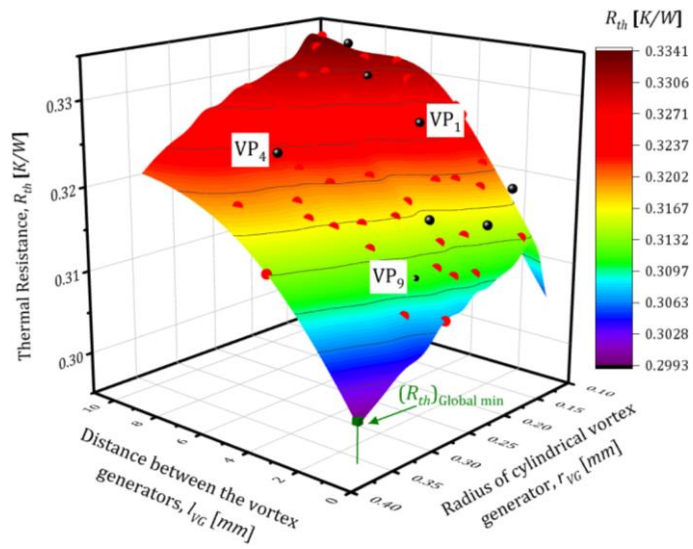
Table 5-5 Surrogate model validation for the *SMCHS – PF – VSVGs* design.

No	DVs		Surrogate Evaluations			CFD-Predictions			% diff. (\pm)		
	l_{VG}	r_{VG}	R_{th}	ΔP	PEC	R_{th}	ΔP	PEC	R_{th}	ΔP	PEC
VP ₁	5	0.15	0.325	8680.3	1.22	0.325	8691.5	1.21	0.04	0.13	0.36
VP ₂	3	0.28	0.312	16482.4	1.26	0.311	16699	1.27	0.38	1.30	1.19
VP ₃	2	0.12	0.317	9728.6	1.36	0.318	9400.2	1.33	0.41	3.49	2.21
VP ₄	7.25	0.27	0.323	10519.6	1.20	0.323	10729	1.17	0.15	1.95	1.92
VP ₅	7.25	0.15	0.330	8116.9	1.16	0.330	8317.3	1.15	0.05	2.41	0.31
VP ₆	8.75	0.13	0.333	7693.0	1.15	0.333	7535.3	1.13	0.13	2.09	1.34
VP ₇	3.1	0.2	0.316	12076.8	1.28	0.316	12169	1.28	0.12	0.76	0.24
VP ₈	2.2	0.25	0.312	16055.8	1.27	0.311	16739	1.25	0.20	4.08	1.18
VP ₉	1.9	0.16	0.314	11506.6	1.34	0.315	11448	1.32	0.18	0.51	1.36

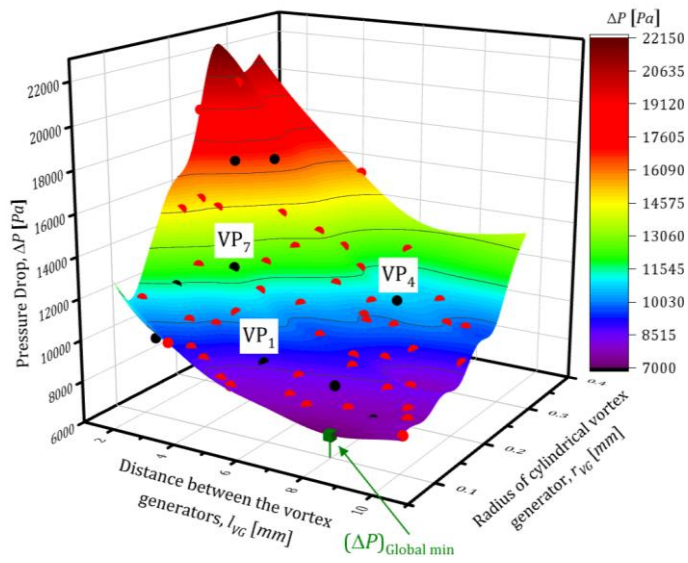
Table 5-6 Surrogate model validation for the *SMCHS – PF – HVGs* design.

No	DVs		Surrogate Evaluations			CFD-Predictions			% diff. (\pm)		
	D_{VG}	r_{VG}	R_{th}	ΔP	PEC	R_{th}	ΔP	PEC	R_{th}	ΔP	PEC
HP ₁	4.15	0.12	0.334	7265	1.16	0.334	7411	1.17	0.23	1.97	0.72
HP ₂	1.9	0.15	0.33	7967	1.228	0.33	7917	1.21	0.03	0.63	1.16
HP ₃	3.5	0.175	0.331	7835	1.192	0.331	7936	1.19	0.11	1.27	0.22
HP ₄	2.5	0.25	0.327	8669	1.238	0.327	8837	1.25	0.02	1.9	0.6
HP ₅	3.25	0.275	0.327	8622	1.242	0.327	8717	1.25	0.12	1.1	0.35
HP ₆	4.35	0.325	0.327	9181	1.252	0.326	9255	1.26	0.13	0.8	0.37
HP ₇	2.75	0.375	0.323	10059	1.289	0.323	10107	1.29	0.04	0.48	0.4
HP ₈	2	0.425	0.321	11026	1.337	0.321	10890	1.31	0.09	1.25	1.98
HP ₉	3.1	0.45	0.321	10929	1.328	0.322	10970	1.32	0.02	0.37	0.65

(a)



(b)



(c)

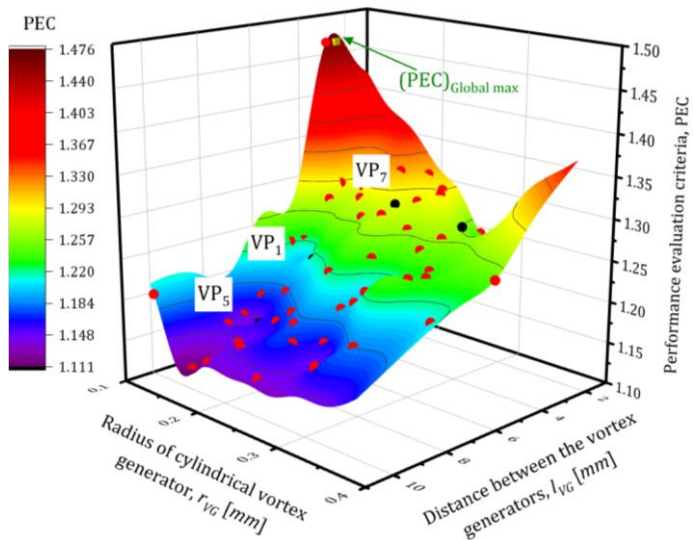


Fig. 5-23 Surrogate model for the performance criteria of *SMCHS – PF – VSVGs* design: (a) R_{th} , (b) ΔP and (c) PEC.

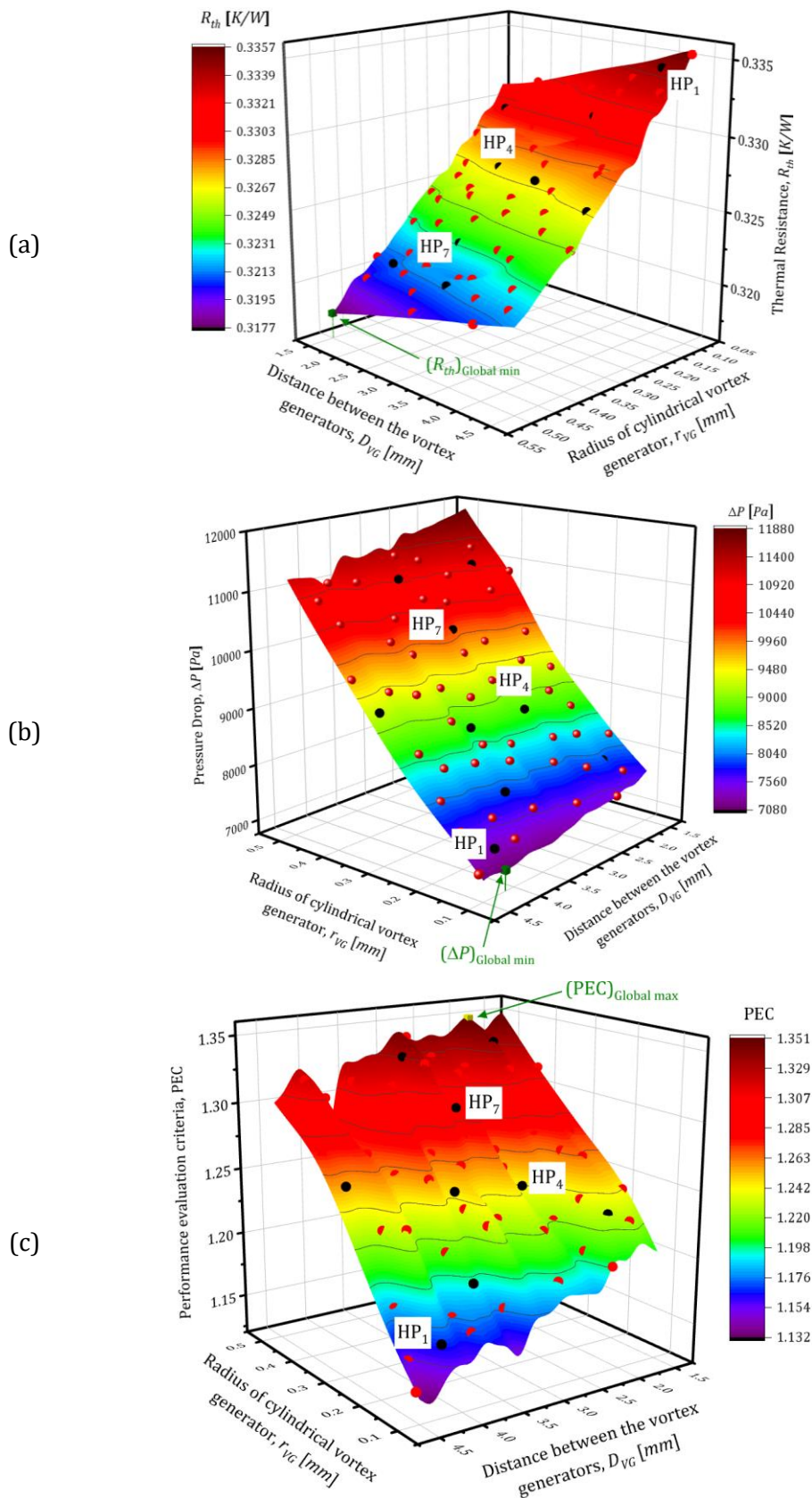


Fig. 5-24 Surrogate model for the performance criteria *SMCHS – PF – HVGs* design: (a) R_{th} , (b) ΔP and (c) PEC.

Table 5-7 Global surrogate-based single-objective optimisation results for R_{th} , ΔP and PEC of the *SMCHS – PF – VSVGs* design.

Case	Objective function	Global Opt.	l_{VG} [mm]	r_{VG} [mm]	CFD-Predictions	% diff. (\pm)
1	R_{th} [K/W]	0.299	1.077	0.358	0.302	1
2	ΔP [Pa]	7051	7.952	0.1	7427	5
3	PEC	1.112	9.937	0.145	1.110	0.2

Table 5-8 Global surrogate-based single-objective optimisation results for R_{th} , ΔP and PEC of the *SMCHS – PF – HVGs* design.

Case	Objective function	Global Opt.	l_{VG} [mm]	r_{VG} [mm]	CDF-Predictions	% diff. (\pm)
1	R_{th} [K/W]	0.318	1.502	0.499	0.3176	0.1
2	ΔP [Pa]	7102	4.137	0.1	7235.7	1.8
3	PEC	1.35	1.998	0.496	1.34	0.8

It has been noticed that R_{th} and ΔP are conflicting objectives, for example, to obtain a design with minimum R_{th} (0.299 K/W), Table 5-7, was accompanied by a high pressure penalty of 36.637 kPa and vice versa. This behaviour can be attributed to the fact that the design with minimum R_{th} in this study had 41 vortex generators in each channel with a radius (r_{VG}) of 0.36 mm and the distance between any two of them (l_{VG}) was 1.077 mm which increased the effective heat transfer area to be 2149 mm² (increased by 16% with respect to *SMCHS – PF*). This helped in reducing the thermal resistance by 13.5% and hence augmenting the heat transfer between the solid wall of the heat sink and coolant. However, this affected the pressure drop adversely where it was raised by 482% in comparison to that of the *SMCHS – PF*.

In contrast, the design with minimum pressure penalty had only 5 vortex generators for each channel with $r_{VG} = 0.1$ mm and $l_{VG} = 7.95$ mm. Therefore, the increase in pressure drop was about 22% compared to the pressure drop for the *SMCHS – PF*, but the reduction in R_{th} was only 6.3%.

The PEC which combines the effect of R_{th} and ΔP in one parameter has also been optimised. It has been concluded that the maximum PEC, as shown in Table 5-7 and Table 5-8, occurs with $r_{VG} = 0.145 \text{ mm}$ and $l_{VG} = 9.937 \text{ mm}$ for *SMCHS – PF – VSVG* design whereas they were $r_{VG} = 0.496 \text{ mm}$ and $l_{VG} = 1.998 \text{ mm}$ for *SMCHS – PF – HVGs* design. This design is considered the best one in the studied ranges, which offers the optimal use of introducing the vertical vortex generators.

5.6.2 Multi-objective optimisation for *SMHS – PF – VSVGs* and *SMHS – PF – HVGs*

Following the same procedure in the previous sections, the surrogate-based multi-objective optimisation for the R_{th} and ΔP using the genetic algorithm (*moga*) has been performed to look for the optimum design. The optimisation problems for the *SMCHS – PF – VSVGs* and *SMCHS – PF – HVGs* have been formulated as:

Find r_{VG} and l_{VG}

To minimise $R_{th}(r_{VG}, l_{VG})$ & $\Delta P(r_{VG}, l_{VG})$ Equ. 5-27

Depending upon the design type, these optimisation problems were subjected to two different design variables ranges which are written as:

For *SMCHS – PF – VSVGs* design: $0.1 \leq r_{VG} \leq 0.3$ Equ. 5-28

$1 \leq l_{VG} \leq 10$ Equ. 5-29

For *SMCHS – PF – HVGs* design: $0.1 \leq r_{VG} \leq 0.5$ Equ. 5-30

$1.5 \leq l_{VG} \leq 4.5$ Equ. 5-31

By utilising the surrogated models generated in the previous section, Fig. 5-23 and Fig. 5-24, the optimisation process was implemented and the results are depicted in Fig. 5-25.

Five points from Pareto front curves, P_1 to P_5 (Fig. 5-25(a)) and HP_1 to HP_5 (Fig. 5-25(b)), have been selected as optimum design candidates. These points have also been validated by comparing them against the CFD predictions and they

showed a good agreement with maximum difference less than 2.6%, Table 5-9 and Table 5-10.

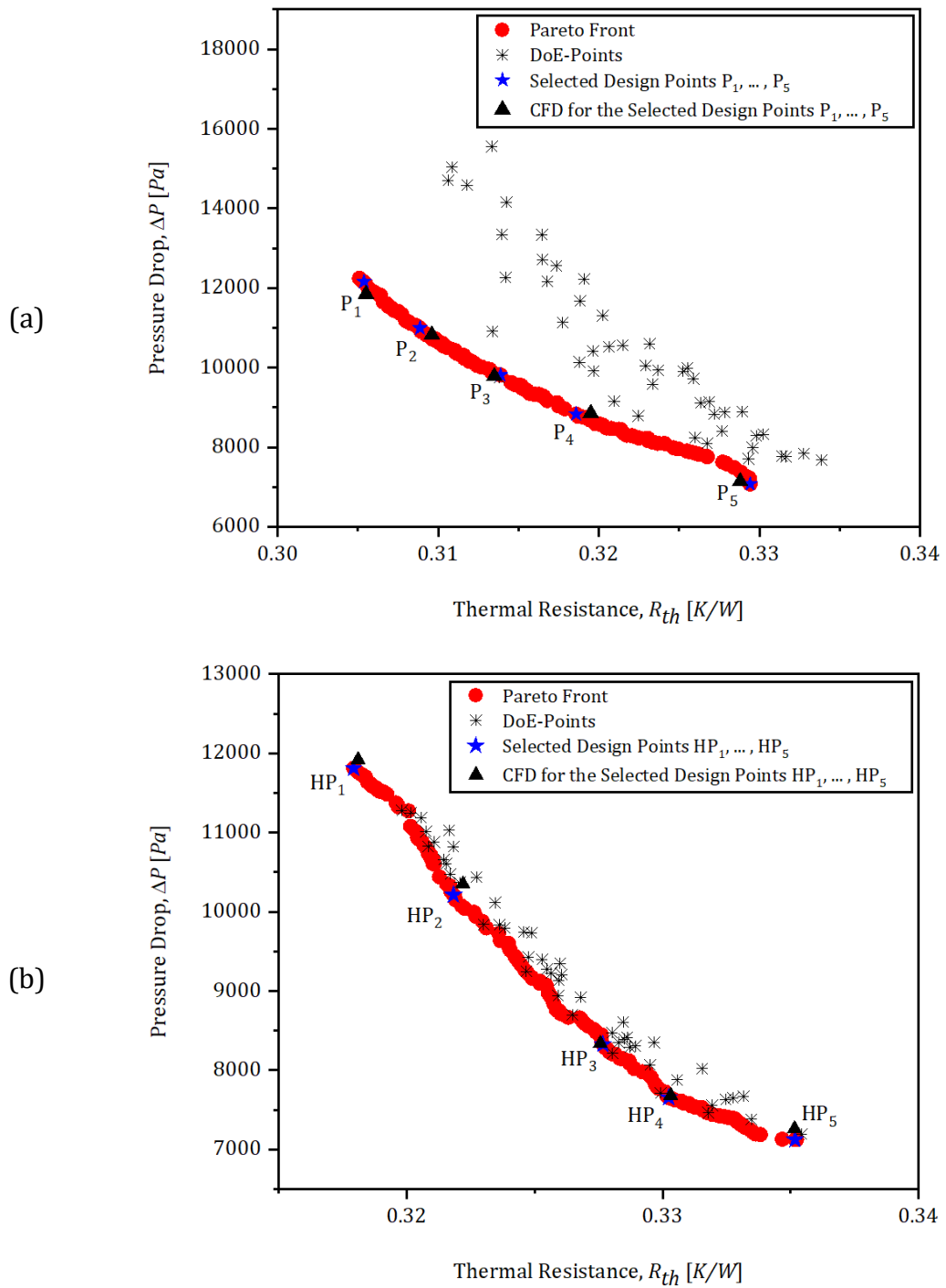


Fig. 5-25 Pareto front for the pressure drop and thermal resistance: (a) *SMCHS – PF – VSVGs* and (b) *SMCHS – PF – HVGs*.

Table 5-9 Performance of the *SMCHS – PF – VSVGs* for the selected optimum designs located on the Pareto front, P₁ to P₅ as shown in Fig. 5-22.

Point	Design Variables		Surrogate model		CFD-Predictions		% diff. (\pm)	
	l_{VG} [mm]	r_{VG} [mm]	R_{th} [K/W]	ΔP [Pa]	R_{th} [K/W]	ΔP [Pa]	R_{th}	ΔP
P ₁	1.030	0.101	0.305	12159	0.306	11850	0.04	2.6
P ₂	1.689	0.102	0.309	10993	0.310	10825	0.24	1.5
P ₃	2.675	0.102	0.314	9813	0.313	9787	0.12	0.3
P ₄	3.688	0.101	0.319	8834	0.320	8854	0.29	0.2
P ₅	8.245	0.100	0.329	7074	0.329	7139	0.19	0.9

Table 5-10 Performance of the *SMCHS – PF – HVGs* for the selected optimum designs located on the Pareto front, HP₁ to HP₅ as shown in Fig. 5-25.

Point	Design Variables		Surrogate model		CFD-Predictions		% diff. (\pm)	
	l_{VG} [mm]	r_{VG} [mm]	R_{th} [K/W]	ΔP [Pa]	R_{th} [K/W]	ΔP [Pa]	R_{th}	ΔP
HP ₁	0.496	1.529	0.3179	11812	0.318	11920	0.03	0.91
HP ₂	0.406	3.203	0.3218	10211	0.322	10352	0.06	1.36
HP ₃	0.184	1.541	0.3276	8326	0.328	8339	0.12	0.16
HP ₄	0.118	1.771	0.3302	7656	0.330	7683	0.06	0.35
HP ₅	0.102	4.218	0.3352	7123	0.335	7264	0.06	1.95

From Table 5-9, all the optimum designs of the *SMCHS – PF – VSVGs* can be achieved by setting r_{VG} to 0.1 mm. However, changing the distance between the *VGs* affects the hydrothermal performance criteria. For example, l_{VG} can be selected to be 1.03 mm to minimise the R_{th} to 0.305 K/W, but a high pressure drop of 12159 Pa accompanies it. On the other hand, to obtain a minimum pressure drop, l_{VG} should be set to 8.245 mm.

Regarding the *SMCHS – PF – HVGs* design, changing r_{VG} and l_{VG} affect the heat sink's optimum performance under consideration. Therefore, the minimum R_{th} can be achieved by adjusting l_{VG} and r_{VG} to 0.496 mm and 1.529 mm, respectively. However, to obtain a *SMCHS – PF – HVGs* design with minimum ΔP , l_{VG} and r_{VG} should be set respectively to 0.102 mm and 4.218 mm.

5.7 Optimisation under Uncertainty for *SMCHS – PF*

5.7.1 Uncertainty Quantification for the Performance of *SMCHS – PF*

As mentioned in section 4.6, the main difference between the optimisation under uncertainty procedure and that of the deterministic optimisation is the uncertainty analysis task. This step aimed at characterising the uncertainties of the output response, in our case the thermal resistance (R_{th}) and pressure drop (ΔP) of the *SMCHS – PF*, caused by the uncertainties of the inputs such as the design variables and boundary conditions. The probabilistic characteristics used in robust design are the mean μ and standard deviation σ (Wang and Yu, 2006). As in the study of (Bodla *et al.*, 2013), the channel width (W_c) and the channel height (H_c) were treated as uncertain inputs in the current investigation and had the probability distributions defined in terms of μ and σ , as illustrated in Table 5-11. The i in the table represents the i^{th} DoE point.

Table 5-11 The uncertainty associated with the input design variables.

Variable	Distribution	μ [mm]	σ [mm]
W_c	Normal	W_{ci}	0.025
H_c	Normal	H_{ci}	0.025

Before extracting the statistical metrics for the responses, their dependence on the number of samples used within Monte Carlo simulation (*MCS*) has been assessed, Fig. 5-26. It is clear that there is no change in the statistical moments evaluation by increasing the number of samples more than 500000, therefore this number of samples has been adopted to implement *MCS*.

Based on the distributions of the uncertain input parameters presented in Table 5-11, the Monte Carlo simulations, described in section 6.4.3, have been applied at each DoE point to quantify the corresponding statistical moments (μ and σ) for the thermal resistance and pressure drop. The mean of each response was in excellent agreement with its corresponding original CFD response with a difference less than 0.045 and 0.18 for the R_{th} and ΔP respectively. Therefore, the surrogate models for

the $\mu_{R_{th}}$ and $\mu_{\Delta P}$ are identical to the surrogate models shown in Fig. 5-20; however, Fig. 5-27 shows the standard deviation for each response.

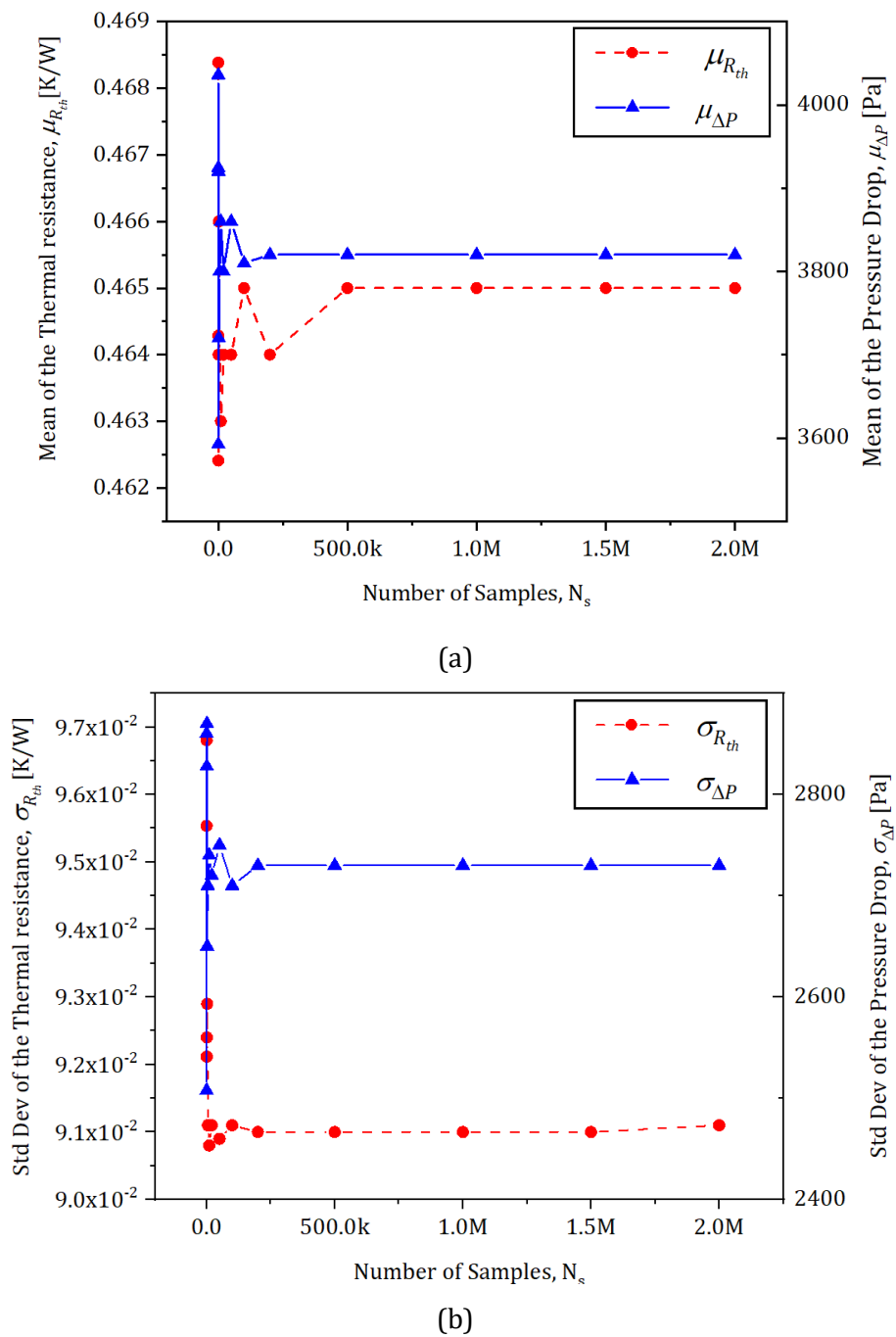
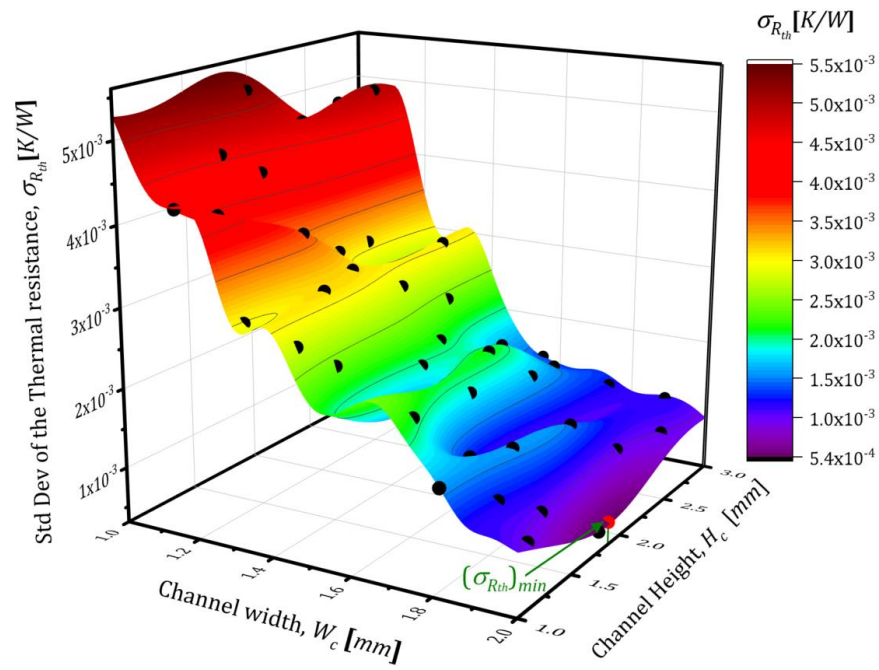
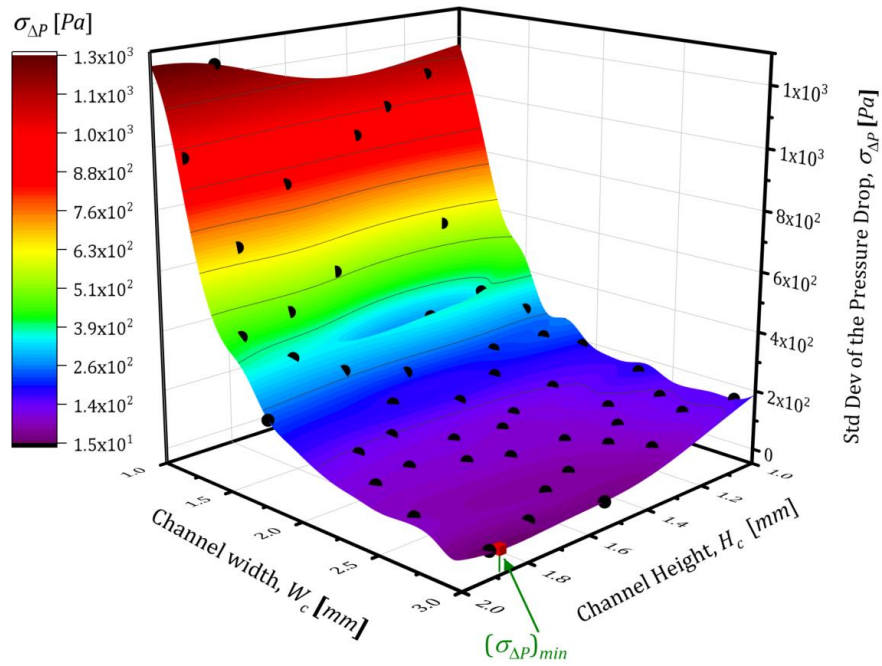


Fig. 5-26 (a) the mean and (b) the Std Dev of R_{th} and ΔP as a function of the number of samples N_s .



(a)



(b)

Fig. 5-27 Surrogate model for the Std Dev of (a) the thermal resistance ($\sigma_{R_{th}}$) and (b) the pressure drop ($\sigma_{\Delta P}$) with the DoE points and the optimum at min σ as a function of the two design variables, W_c and H_c .

5.7.2 Single-Objective Optimisation for $\sigma_{R_{th}}$ and $\sigma_{\Delta P}$

After obtaining the statistical moments for the R_{th} and ΔP at each of the 50 sample points generated previously, the single-objective optimisation for the standard deviation of each quantity of interest for the *SMCHS – PF* has been performed. The design variables were the width W_c and the height H_c of the minichannel. The optimisation problem for the $\sigma_{R_{th}}$ has been formulated as:

$$\begin{aligned} \textit{Find} & & & W_c \textit{ and } H_c \\ \\ \textit{To minimise} & & \sigma_{R_{th}}(W_c, H_c) & \text{Equ. 5-32} \end{aligned}$$

whereas, the one for the $\sigma_{\Delta P}$ has been written as:

$$\begin{aligned} \textit{To minimise} & & \sigma_{\Delta P}(W_c, H_c) & \text{Equ. 5-33} \end{aligned}$$

The above optimisation problems were subjected to:

$$1.0 \leq W_c \leq 2.0 \quad \text{Equ. 5-34}$$

$$1.0 \leq H_c \leq 3.0 \quad \text{Equ. 5-35}$$

The genetic algorithms included within the Dakota toolkit have been utilised to run the optimisation procedure for each function, stated in Equ. 5-32 to Equ. 5-35. The results are shown in Table 5-12 and Fig. 5-28. Therefore, the obtained design parameters represent the robust design for the *SMCHS – PF*. A comparison between the designs at the global optimum and the robust designs are illustrated in Table 5-13. It can be noticed that the difference in the performance of these designs is small, and this could be attributed to the low deviation applied to design variables. The scenario could differ if a larger variation were assigned to these variables.

Table 5-12 Surrogate-based single-objective optimisation results for $\sigma_{R_{th}}$ and $\sigma_{\Delta P}$.

Case	Objective function	Opt. Value	$(W_c)_{Robust}$ [mm]	$(H_c)_{Robust}$ [mm]
1	Std Dev of thermal resistance, $\sigma_{R_{th}}$ [K/W]	0.54×10^{-3}	1.995	1.898
2	Std Dev of pressure drop, $\sigma_{\Delta P}$ [Pa]	19.539	1.876	2.971

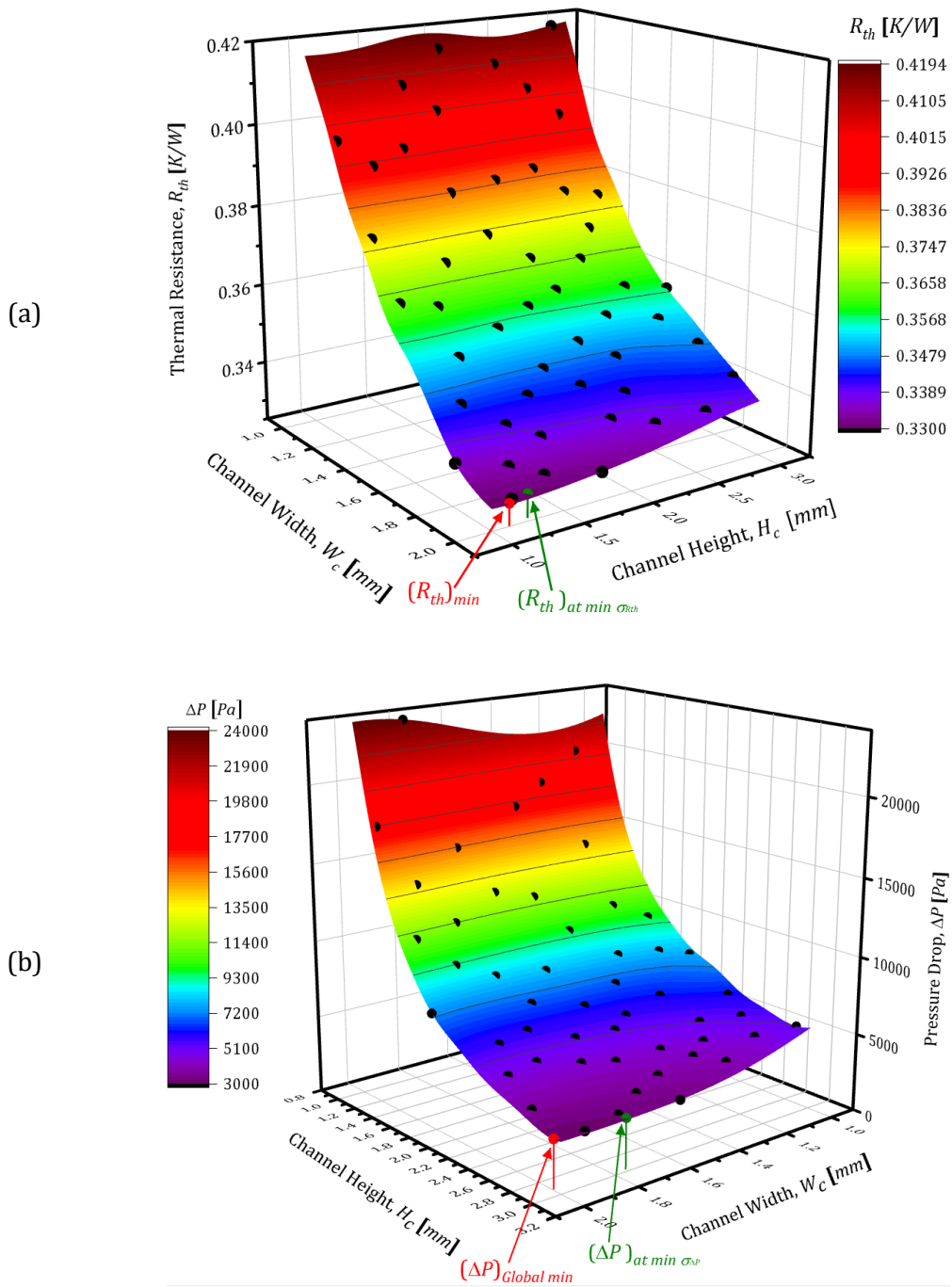


Fig. 5-28 (a) thermal resistance and (b) pressure drop surrogate model showing the global minimum (red point) and the robust design at the minimum σ (green point).

Table 5-13 Comparison between the global optimum and the robust optimum for the thermal resistance and pressure drop evaluated at $(W_c)_{Robust}$ and $(H_c)_{Robust}$.

Case	Objective function	Opt. Robust	Opt. Global	% diff. (\pm)
1	Thermal resistance, R_{th} [K/W]	0.331	0.330	0.3
2	Pressure drop, ΔP [Pa]	3186.729	3061.289	4.1

5.7.3 Multi-Objective Function Optimisation for $\mu_{R_{th}}$, $\sigma_{R_{th}}$, $\mu_{\Delta P}$ and $\sigma_{\Delta P}$

In this section, the multi-objective optimisation for the statistical metrics of each performance criterion has been implemented. To achieve this task, the multi-objective optimisation problems for the statistical mean and standard deviation of the R_{th} and ΔP have been formulated as stated below:

For the thermal resistance (R_{th}):

$$\begin{array}{lll} \textit{Find} & W_c \textit{ and } H_c & \\ \\ \textit{To minimise} & \mu_{R_{th}}(W_c, H_c) \textit{ and } \sigma_{R_{th}}(W_c, H_c) & \text{Equ. 5-36} \end{array}$$

For the pressure drop (ΔP):

$$\begin{array}{lll} \textit{To minimise} & \mu_{\Delta P}(W_c, H_c) \textit{ and } \sigma_{\Delta P}(W_c, H_c) & \text{Equ. 5-37} \end{array}$$

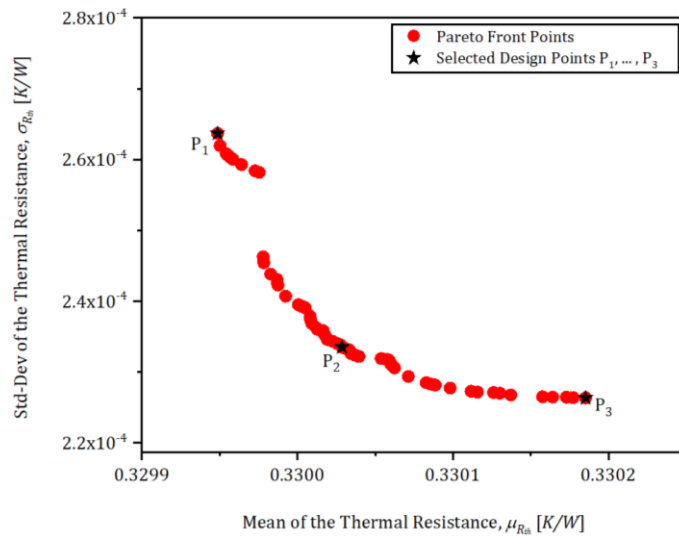
These problems were subjected to:

$$1.0 \leq W_c \leq 2.0 \quad \text{Equ. 5-38}$$

$$1.0 \leq H_c \leq 3.0 \quad \text{Equ. 5-39}$$

As in previous sections, the multi-objective optimisation process has been conducted employing the genetic algorithms embedded within the Dakota software and the results are illustrated in Fig. 5-29 and Fig. 5-30. The Pareto fronts curves of the statistical parameters considered are depicted in Fig. 5-29(a) and Fig. 5-30(a). Three different points on each Pareto curve (two on the extremes of the curve and one at its middle) have been chosen, as shown in the figures, to compare between the global optimum design and the robust designs, those obtained by taking into account the uncertainty associated with the geometric design variables. The comparisons are illustrated in Fig. 5-29(b) and Fig. 5-30(b) and it can be seen that, for the two objectives, these three points are located between the global optimisation and the robust design obtained from the single-objective optimisation previously. Like the previous results, the design points are close to each other, which means that the small deviation associated with the design variables has not strongly affected the performance.

(a)



(b)

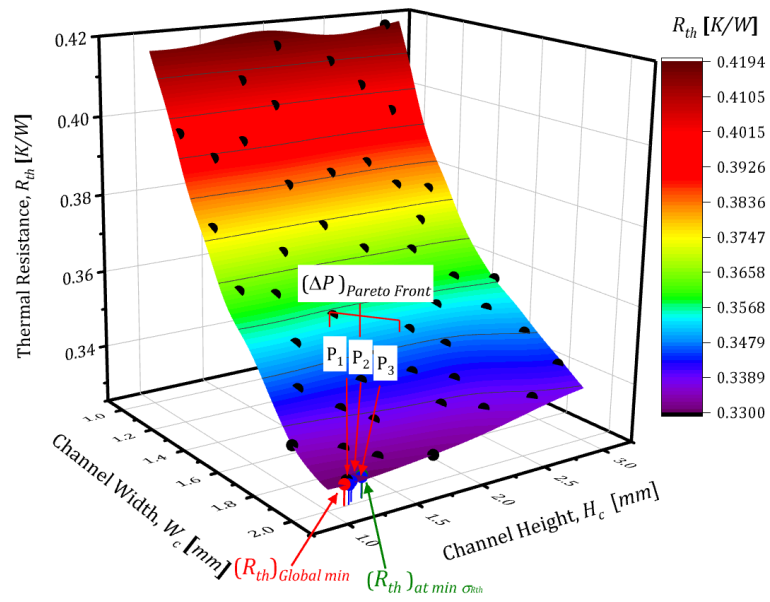
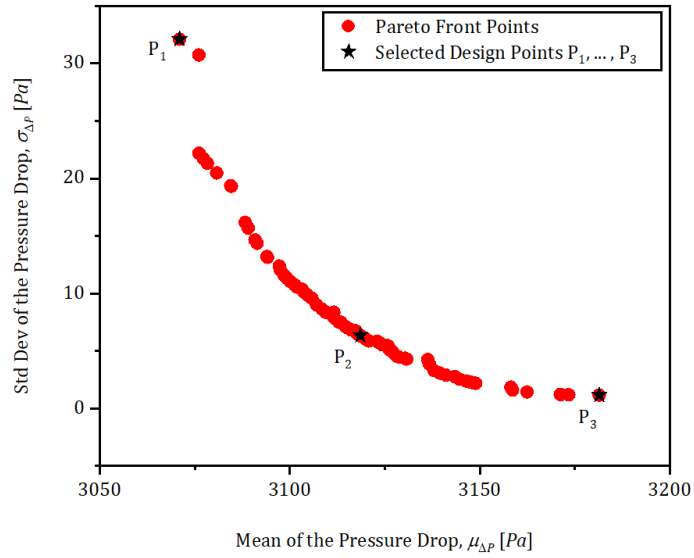
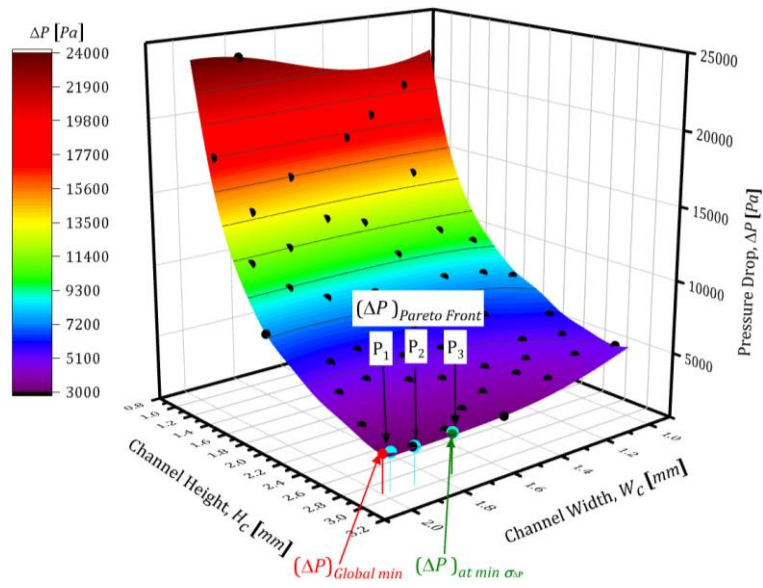


Fig. 5-29 (a) Pareto front and (b) surrogate model of R_{th} showing the global minimum (red point) and the robust design at the minimum σ (green points).



(a)



(b)

Fig. 5-30 (a) Pareto front and (b) surrogate model of ΔP showing the global minimum (red point) and the robust design at the minimum σ (green points).

To minimise all the objective together, it could be more convenient to define the optimisation problem as follow:

$$\begin{aligned} & \text{Find} && W_c \text{ and } H_c \\ & \text{To minimise} && f_{R_{th}} \text{ and } f_{\Delta P} \end{aligned} \quad \text{Equ. 5-40}$$

$$\text{where} \quad f_{R_{th}} = \frac{\mu_{R_{th}}}{(\mu_{R_{th}})_{opt.}} + \frac{\sigma_{R_{th}}}{(\sigma_{R_{th}})_{opt.}} \quad \& \quad f_{\Delta P} = \frac{\mu_{\Delta P}}{(\mu_{\Delta P})_{opt.}} + \frac{\sigma_{\Delta P}}{(\sigma_{\Delta P})_{opt.}}$$

$$\text{Subjected to} \quad 1.0 \leq W_c \leq 2.0 \quad \text{Equ. 5-41}$$

$$1.0 \leq H_c \leq 3.0 \quad \text{Equ. 5-42}$$

The optimisation result of the above problem is presented in terms of the Pareto front for the $f_{R_{th}}$ and $f_{\Delta P}$, Fig. 5-31, and three different selected designs, P_1, P_2 and P_3 are chosen to compare their performance against the global deterministic optimum design obtained previously. For example, the three points are projected on the surrogate model for thermal resistance.

The optimisation result of the above problem is presented in terms of the Pareto front for the $f_{R_{th}}$ and $f_{\Delta P}$, Fig. 5-31, which shows the nondominated optimum solutions. In addition, three different designs (P_1, P_2 and P_3) have been chosen to compare their performance against the global deterministic optimum design obtained previously. For example, the three points have projected on the surrogate models for thermal resistance, Fig. 5-32(a), and the pressure drop, Fig. 5-32 (b), which clearly show that the values of all three points are higher than the global optimum solution. However, these three designs are better than the global one since their standard deviations have been minimised to produce robust designs. Consequently, it is the decision maker's choice to select among these robust solutions depending on the design requirements. For instance, P_1 represents the robust design which has the minimum thermal resistance, higher than the global minimum by 0.1%, but at the same time, its pressure drop exceeds that of the global minimum by 345%. In contrast, P_3 design offers thermal resistance higher than the global optimum by 5.7% but with pressure drop higher than that of the global minimum by 4.3%.

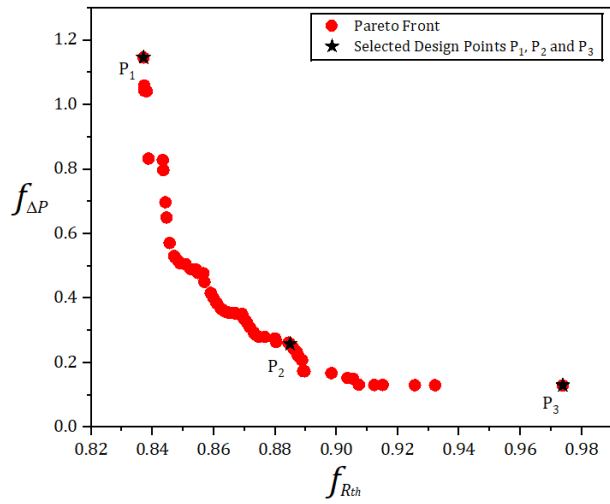
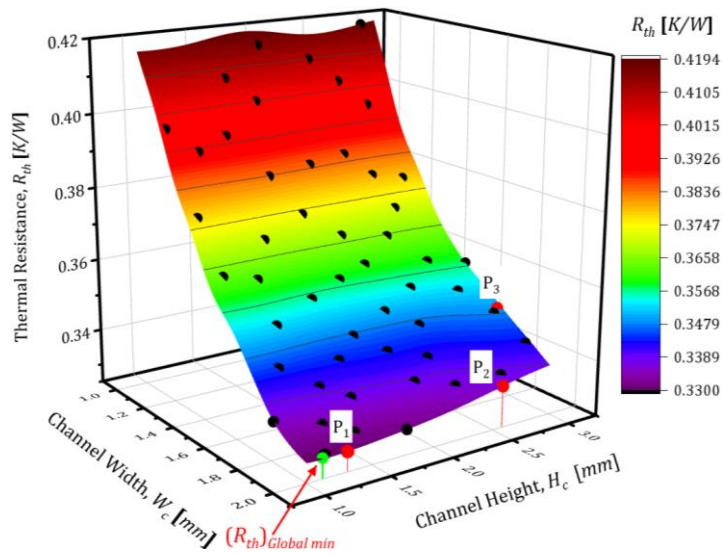


Fig. 5-31 Pareto front for the $f_{R_{th}}$ and $f_{\Delta P}$.

(a)



(b)

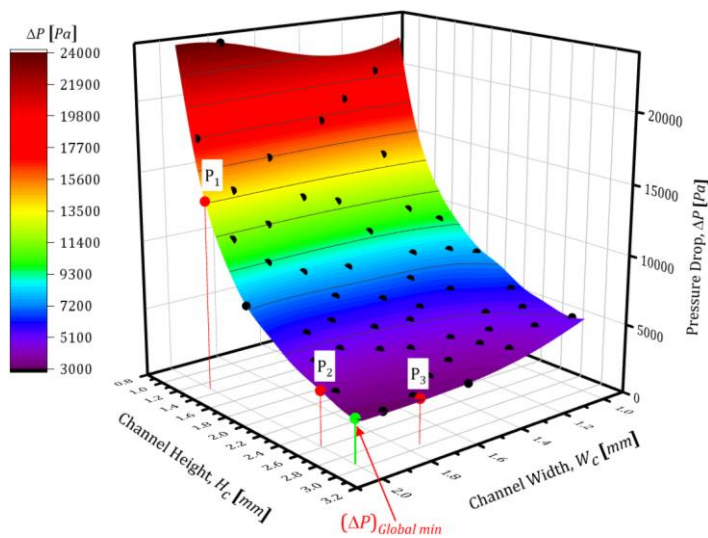


Fig. 5-32 Surrogate models for (a) thermal resistance and (b) pressure drop showing the global minimum (green point) and the three selected points from Pareto front.

5.8 Chapter Summary

This chapter has explored the effect of the change in the geometrical parameters of the minichannel and the impact of adding vortex generators on the hydrothermal performance of the heat sink under study. Furthermore, two strategies of optimisation, i.e. deterministic and probabilistic optimisation, have been performed to find the optimum design and the robust design.

The channel width (W_c) and height (H_c) have been selected to study their influence on the hydrothermal performance of the *SMCHS – PF* which is represented by the thermal resistance (R_{th}) and pressure drop (ΔP). The study exhibited that these two geometrical parameters, i.e. (W_c) and (H_c), has a significant effect on (R_{th}) and (ΔP). It has been revealed that the increase in W_c and H_c leads to an increase in thermal resistance and decrease in pressure drop. For $H_c = 3\text{ mm}$ and $W_c = 1.5\text{ mm}$ with $\dot{m} = 2\text{ g/s}$, for instance, the present exploration demonstrated that, compared to $H_c = 0.5\text{ mm}$, the achieved reduction in pressure drop was 94.9% whereas the rise in the overall thermal resistance was 10%. Similarly, the pressure drop in the minichannel was reduced by 84% while the overall thermal resistance was increased by 7% for the heat sink design of $H_c = 2\text{ mm}$, $W_c = 1.5\text{ mm}$ and operates at mass flowrate of $\dot{m} = 1.5\text{ g/s}$.

In addition, the impact of adding vortex generators, attached to the sidewalls (*VVGs*) and the base of the minichannel (*HVGs*), on the heat sink performance has also been investigated separately. The *VG* has a semi-cylindrical shape with r_{VG} ranged from 0.1 to 0.5 mm. The study exhibited that the existence of the *VGs* enhanced the heat transfer but this came at the expense of an increase in pressure losses.

Using the in-lined *VVGs* arrangement with radius r_{VG} of 0.3 at $Re = 2250$, the achieved R_{th} was 0.267 W/K and the pressure drop was 39716 Pa. This means that, in comparison to the smooth serpentine minichannel heat sink (*SMCHS – PF*), there is a reduction in thermal resistance of 11% which is accompanied by an increase in pressure drop of about 208%. This study has also shown that the penalty of pressure drop could be mitigated by about 50%, with keeping the heat transfer improvement at the same level, by re-arranging the *VVGs* to be staggered. In this manner, the pressure drop penalty will be reduced to 27774 Pa (i.e. increased by 115% compared to *SMCHS – PF*) while the $R_{th} = 0.26813\text{ W/K}$ (i.e. reduced by 11%). The *HVGs* arrangement has shown an improvement in thermal resistance by

54% (fallen to $0.1382 K/W$) while the pressure losses were risen by 48% (increased to 9160 Pa). It is worth mentioning that all the above percentages were calculated with respect to the smooth channels.

The performance evaluation criteria (PEC) has also been used to assess the benefit of adding the VGs . The study has revealed that the $SMCHS - PF - VSVGs$ design has a superior performance among the studied designs for the explored r_{VG} .

The deterministic optimisation procedure has been implemented to find the optimum solutions for the single- and multi-objective optimisation problem of the heat sink under study. As noticed throughout this chapter, the performance criteria of the heat sinks, i.e. R_{th} and ΔP , are conflicting objectives. Therefore, the optimal solutions were obtained and presented graphically in terms of Pareto front curve. This curve has a vital role in helping the designers to select suitable compromises between designs with low thermal resistance and those with low pressure losses.

Finally, the probabilistic design optimisation process has been conducted to find a robust design. In this optimisation approach, uncertainty has been imposed on the geometrical variables of the channel, i.e. the channel width (W_c) and the channel height (H_c), and this uncertainty has been propagated to the outputs of interest using Monte Carlo simulations. Accordingly, the statistical moments (μ and σ) for the R_{th} and ΔP has been determined. Then, the single-objective optimisations were conducted to minimise the standard deviations for both responses separately which produced the robust designs with responses higher than those for global optimum by 0.3% and 4.1% for R_{th} and ΔP , respectively. By employing the multi-objective to include all the statistical metrics of the responses of the considered heat sink, the results show that it is possible to obtain a robust design close to the global design with a difference of 1% R_{th} at the expense of increase ΔP by 345%. Similarly, a robust design could be produced with R_{th} and ΔP higher than those of the global design by 5.7% and 4.3%, respectively.

Chapter 6 Effect of Chevron Fins on the Performance of Serpentine Minichannel Heat Sinks

6.1 Introduction

This chapter extends investigations of minichannel heat sinks with secondary channels, Fig. 6-1, first studied by Al-Neama (2018), to cover some aspects that have not been studied, such as the effect of the number of fins (F_n), the fin offset (F_o), and the impact of the fin's secondary channel lengths ratio ($R_{FS} = \frac{F_L}{l_{sc}}$) on its thermal resistance (R_{th}) and pressure drop (ΔP). The sections of this chapter are organised as follows. Section (6.2) presents the numerical analysis setup which includes the definition of the problem, specifying the computational domain and validating the CFD model. In section (6.3) description and discussion are given for the influence of the explored parameters, i.e. F_n , F_o and R_{FS} . Then section (6.4) addresses the deterministic and probabilistic optimisation for the serpentine minichannel heat sink equipped with chevron fins. A summary of the chapter is included in section 6.5.

6.2 CFD Analysis of the *SMCHS* – *CF*

6.2.1 CFD Modelling

A minichannel heatsink with secondary flow microchannels used in the current work is provided in Fig. 6-1. This design has been proposed and studied by Al-Neama (Al-Neama, 2018) and it has been chosen here for further investigations. The simulation model consists essentially of a 4 mm thick copper block with a square base of dimension ($38\text{ mm} \times 38\text{ mm}$). A number of main and secondary channels were etched in it to allow the water to circulate and take the heat away. The width of the minichannels (W_c) was 1.5 mm while the width of the secondary channels (W_{sc}) was 0.5 mm. The depth of all channels (H_c) was 2 mm. There are nine fin structures in each wall that separates main channels. These fins have a chevron shape with length (F_l), width (F_w) and oblique angle of the fins (θ) of 1.3 mm, 1 mm

and, 30° , respectively. All the dimensions of this model are illustrated in Fig. 6-1. Furthermore, two thermal resistor heaters were attached at the base of the substrate to mimic the electronic chip. The detailed fin dimensions, Fig. 6-1(d), are useful for manufacturing the heat sink model for experimental work.

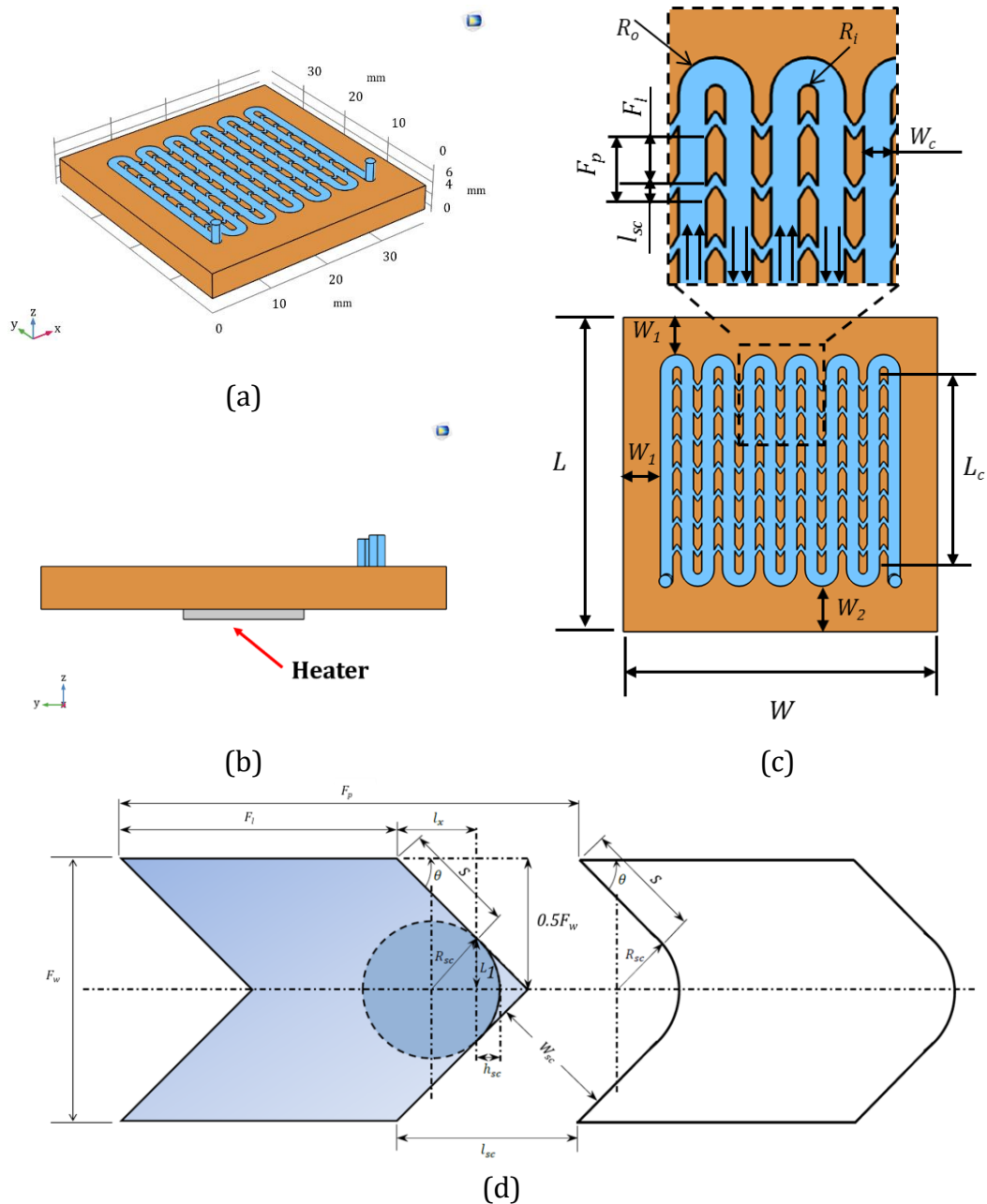


Fig. 6-1 Geometry of the serpentine microchannels heatsink with secondary channels: (a) 3D view, (b) side view, (c) top view showing the main dimensions and (d) detailed fin dimensions (Reproduced from Al-Neama *et al.* (2018) with permission).

6.2.2 Mesh Independence tests and Validation

To verify the accuracy of the CFD solutions and to keep the computational costs as low as possible, a dependency test of the numerical results on mesh density has been conducted for the serpentine microchannel heat sink model with chevron fins (*SMCHS – CF*) shown in Fig. 6-1. All the dimensions of this model are as stated in section 6.2.1, whereas the boundary and operating conditions for this test are tabulated in Table 6-1 below. Due to the complexity of the computational domain, an unstructured mesh has been used to mesh the geometry, Fig. 6-2.

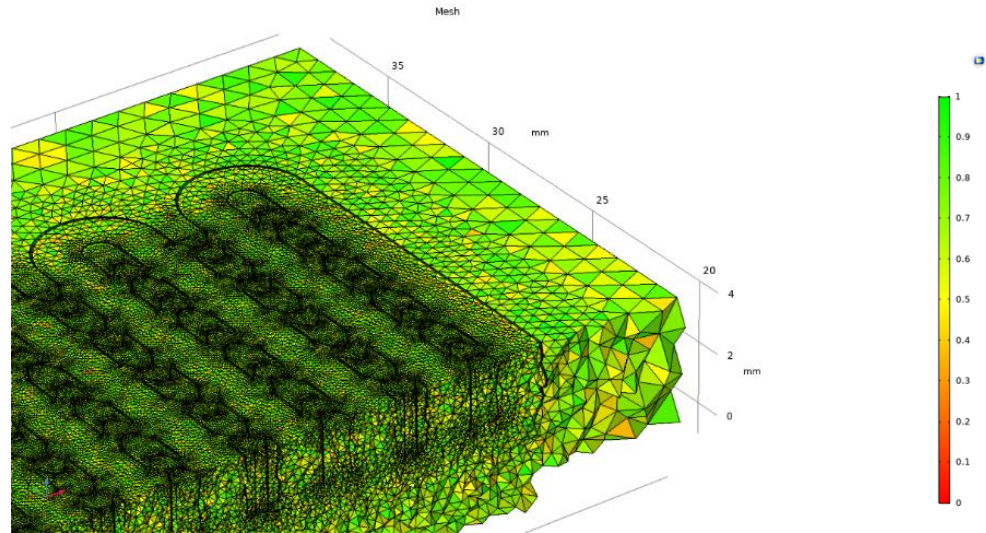
Table 6-1 Boundary and operating conditions for mesh dependence analysis.

Boundary conditions	Quantity
Heat flux, [W/cm^2]	31
Reynolds number	1000
Water inlet temperature, [$^{\circ}C$]	20

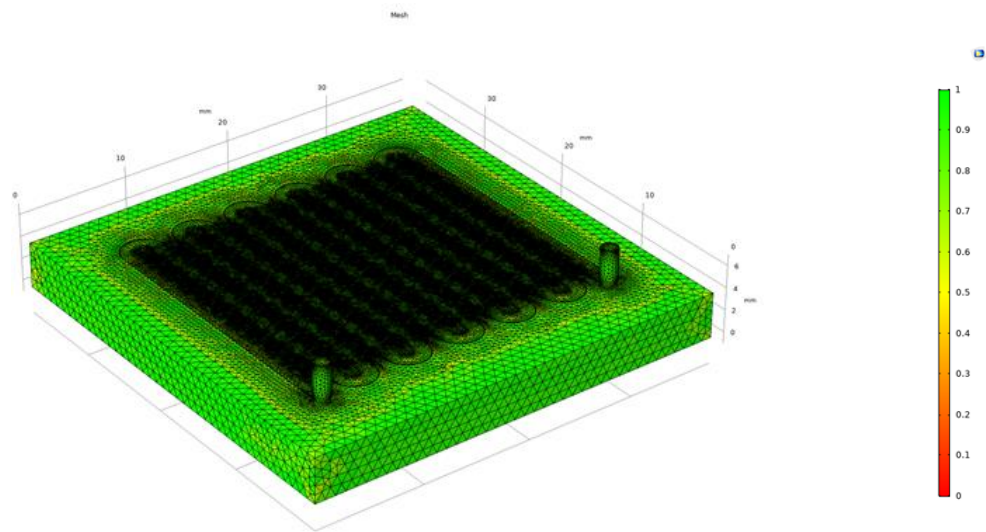
Following the procedure mentioned in section 5.2, a mesh independency test has been conducted to choose the suitable number of elements to obtain the numerical calculations of the model used in this study using the same criteria, i.e. the number of elements (NOE), the average element quality (AEQ), the time required to complete a CFD simulation, the physical memory (Ph.M.), the degree of freedom (DOF) and the relative difference for the quantity of interest which is calculated based on the finest mesh.

Different mesh sizes, ranging from 5×10^5 elements to 4×10^6 elements, have been employed to investigate how the mesh quality affects CFD simulation results. From the detailed results of the mesh independency analysis, Table 7-2, it has been found that the percentage difference of the outputs is decreasing with increasing the number of cells. However, this is at the expense of the time and the computational resource required to run the simulations. As the mesh density increased from the coarsest mesh (Mesh-01) to a finer mesh (Mesh-06), for instance, the difference in ΔP decreased from (17.17%) to (1.01%) whereas the CFD simulation time increased from (19 min) to (2 hr and 46 min). Increasing the number of elements to 4×10^6 leads to rising the time required to complete the simulation to (4 hr and 27 min). As the deviation percentage in both the thermal resistance and pressure drop is slight,

the mesh (Mesh-05) in Table 6-2 is the best regarding computational cost. The relative differences of the response of interest has been calculated with respect to the finest mesh in this test.



(b)



(a)

Fig. 6-2 Mesh quality of the *SMCHS – CF* used in the mesh sensitivity test: (a) full meshed geometry and (b) magnifying view for a part of the meshed geometry.

Table 6-2 Results of the mesh independency study.

No	Mesh Resolution	NOE x 10 ⁶	AEQ	time (hr:min)	Ph.M. (GB)	DOF x 10 ⁶	R_{th} [K/W]	% E	ΔP [Pa]	% E
1	Mesh-01	0.552	0.623	00:19	5.39	0.708	0.40441	1.257	1043.6	17.17
2	Mesh-02	0.758	0.637	00:23	5.30	0.765	0.40498	1.118	1032.7	15.95
3	Mesh-03	1.020	0.639	00:28	5.88	0.882	0.40477	1.170	994.14	11.62
4	Mesh-04	1.951	0.647	01:36	8.37	2.129	0.41064	0.264	940.74	5.62
5	Mesh-05	2.403	0.634	01:40	13.73	2.601	0.41042	0.210	901.06	1.17
6	Mesh-06	3.531	0.643	02:46	17.87	3.696	0.41035	0.193	899.70	1.01
7	Mesh-07	4.085	0.647	04:27	20.19	4.202	0.40956	----	890.67	---

As a further verification and validation of the numerical approach, the CFD predictions have been compared against the study Al-Neama (2018). The dimensions and the boundary conditions of the CFD model are as stated above in this section. The range of Reynolds number (Re) was from 750 to 2250, and the results were presented in terms of the thermal resistance (R_{th}) and pressure drop versus Reynolds number (Re), Fig. 6-3. The current results and those of Al-Neama (2018) are in a good agreement and the maximum difference between the current study and the experiment data was less than 6.1%.

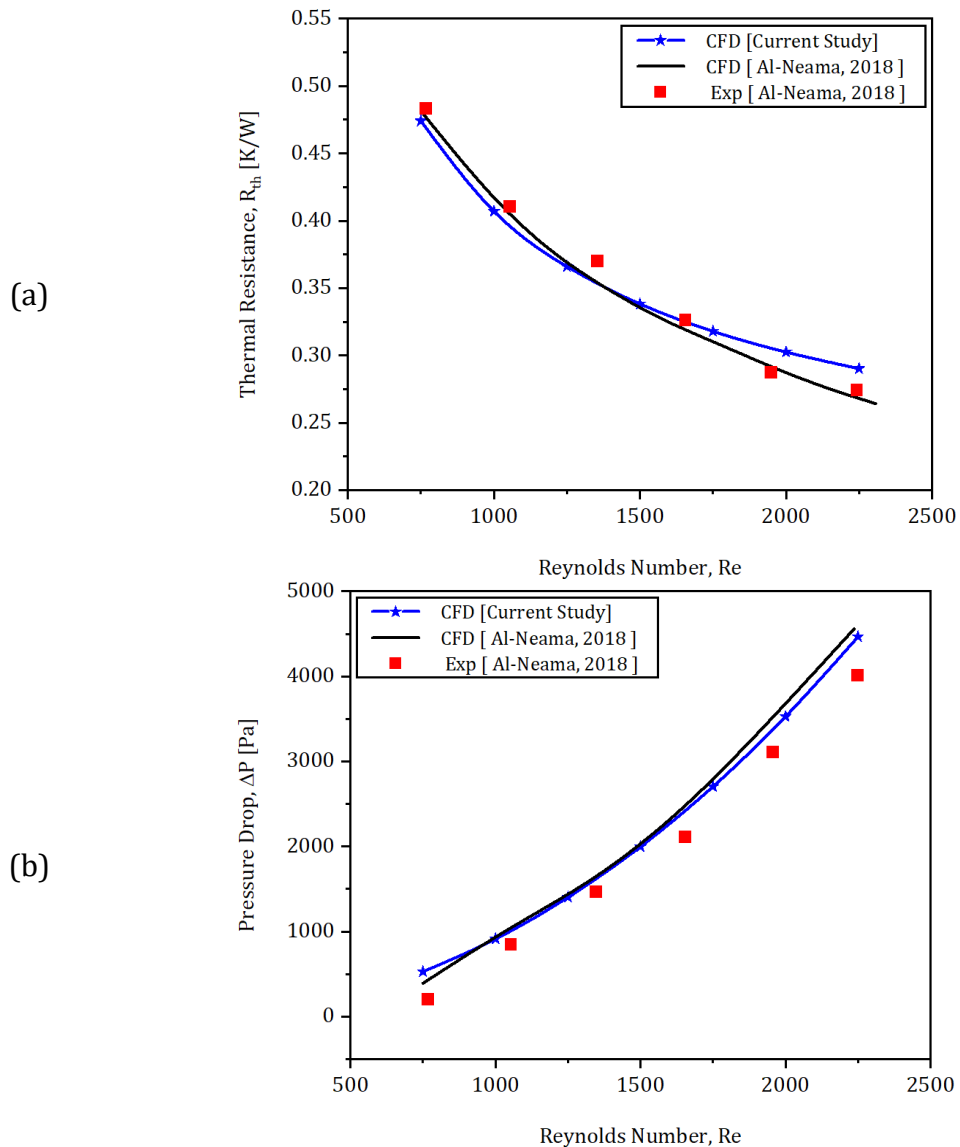


Fig. 6-3 Validation of the present work against previous study for serpentine minichannel heat sink with chevron fins, (Al-Neama , 2018).

As the validation of the CFD simulation model against the work of Al-Neama (2018) has been accomplished, the following sections of this chapter will provide the original results of the present work.

6.3 Characteristics of Fluid Flow and Heat Transfer

6.3.1 Effect of Number of Fins (F_n)

This section presents an investigation of the impact of number of fins (F_n) on performance of the serpentine minichannel heat sink equipped with chevron fins (*SMCHS – CF*). This performance, in terms of total thermal resistance and pressure drop, has been examined for four different values of the secondary channel lengths (i.e. $l_{sc} = 0.25, 0.5, 0.75$ and 1.0 mm) using a constant heat flux of 31 [W/cm^2] and single-phase laminar flow with Reynolds number in the range of 500 to 2250 .

Fig. 6-4 depicts the effect of (F_n) on hydrodynamic performance for *SMCHS – CF* for all the set out values of l_{sc} at Reynolds number (Re) of 1500 . In all the studied cases, the pressure penalty for the serpentine microchannel heat sink with chevron fins (*SMCHS – CF*) is less than that with plate fins (*SMCHS – PF*) which is consistent with the findings of Al-Neama (2018).

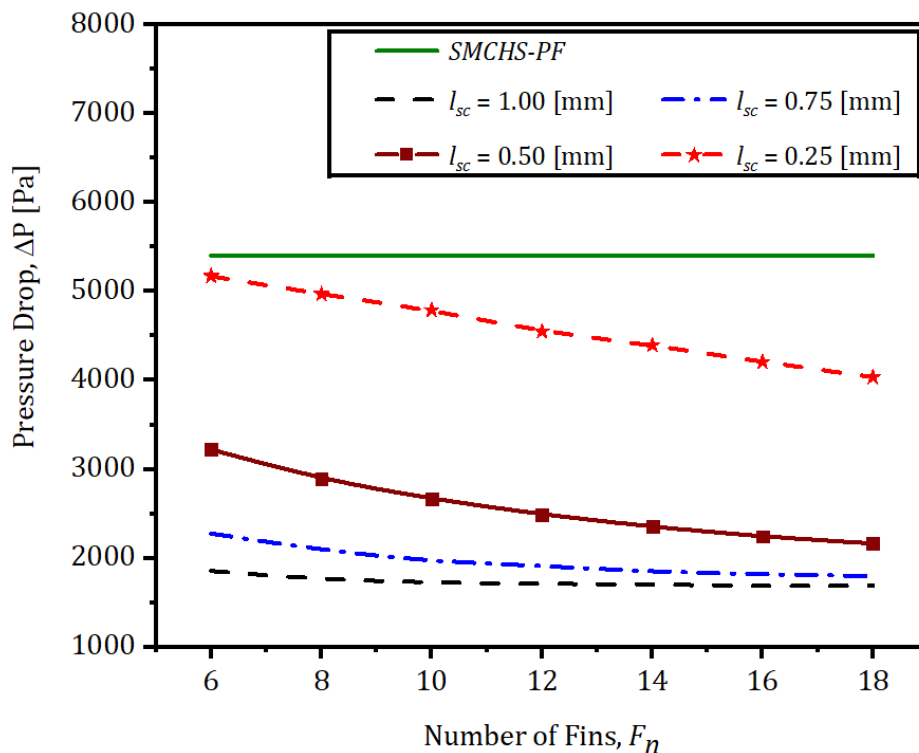


Fig. 6-4 Influence of the number of fins on Pressure drop (ΔP) at Reynolds number $Re = 1500$ for different secondary channel length.

From Fig. 6-4, it is clear that the pressure drop decreases dramatically with increasing the number of fins for $l_{sc} = 0.5$ and 0.25 mm. However, it shows less sensitivity to the number of fins for $l_{sc} = 0.75$ and 1.0 mm. By increasing F_n from 6

to 18, for example, the pressure drop falls from 5171.9 Pa to 4036 Pa, i.e. about 28.12%, for $l_{sc} = 0.25 \text{ mm}$ while it drops from 1855.6 Pa to 1691.1 Pa, i.e. 9.73%, for $l_{sc} = 1.0 \text{ mm}$. This behaviour could be attributed to the fact that the distance between any two fins for the designs which have l_{sc} less than 0.5 mm is short therefore increasing the number of fins leads to increase the number of these gaps which results in increasing the share of the flow through the secondary channels and as a consequence the pressure drop decreased remarkably.

Besides, the pressure drop decrease significantly with increasing the secondary channel length (l_{sc}). The wider the secondary channel, the lower is the pressure drop, Fig. 6-4. When $F_n = 10$, for instance, the percentage drop in pressure penalty relative to the *SMCHS – PF* is about 68% for $l_{sc} = 1.0$ while it is just around 11% for $l_{sc} = 0.25$.

The effect of the number of fins on the overall thermal resistance for the heat sink under consideration is also explored, and the results are presented in Fig. 6-5. This Figure shows, depending on the length of the secondary channel, the change in overall thermal resistance has different behaviour with the change in the number of fins. For example, the thermal resistance in [K/W], for $l_{sc} = 0.25 \text{ mm}$, is decreased from 0.331 to 0.319 at $F_n = 6$ and 18, respectively, i.e. about 3.7%. For the $l_{sc} = 1.0 \text{ mm}$, by contrast, it can be noticed that R_{th} decreases from 0.349 at $F_n = 6$ to 0.345 at 10 then it increases rapidly to reach its maximum value of 0.3662 at $F_n = 18$ which exceed the thermal resistance of *SMCHS – PF*. This can be attributed to the fact that keeping the l_{sc} is relatively large and increasing the number of fins to more than 10 leads to a decrease in the fluid velocity within the heat sinks which, in turn, causes a reduction in the heat transfer coefficient. Therefore, the overall thermal resistance will increase as a result of increasing the convective thermal resistance.

Fig. 6-6 and Fig. 6-7 presents the temperature and the velocity distributions at the mid-depth plane of the channel ($Z = 0.5 H_c$) for four selected extreme cases as indicated in these Figures. The effect of the number of fins and the secondary channel length is obvious. It can be seen that the value of the maximum temperature can be reduced by shortening the l_{sc} and increasing the number of fins. For instance, a maximum temperature of 309.35 K occurred by using a heat sink with 18 fins and length of a secondary channel of 0.25 mm, Fig. 6-6 (d), whereas the maximum temperature was 313.06 K for a heat sink with $l_{sc} = 1.0$ and $F_n = 18$, Fig. 6-6 (c). It is

also clear that the increase in the number of fins and the secondary channel length causes the fluid to be slower, Fig. 6-7(c), which has a negative effect on the heat transfer coefficient.

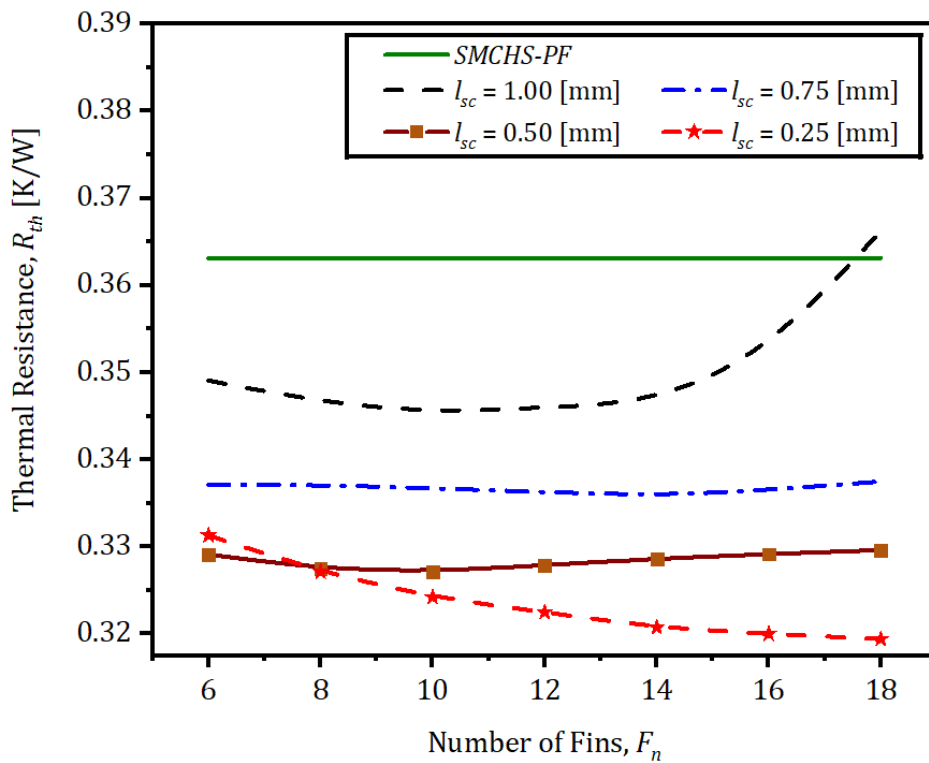


Fig. 6-5 Influence of the number of fins on thermal resistance (R_{th}) at $Re = 1500$ for different secondary channel lengths.

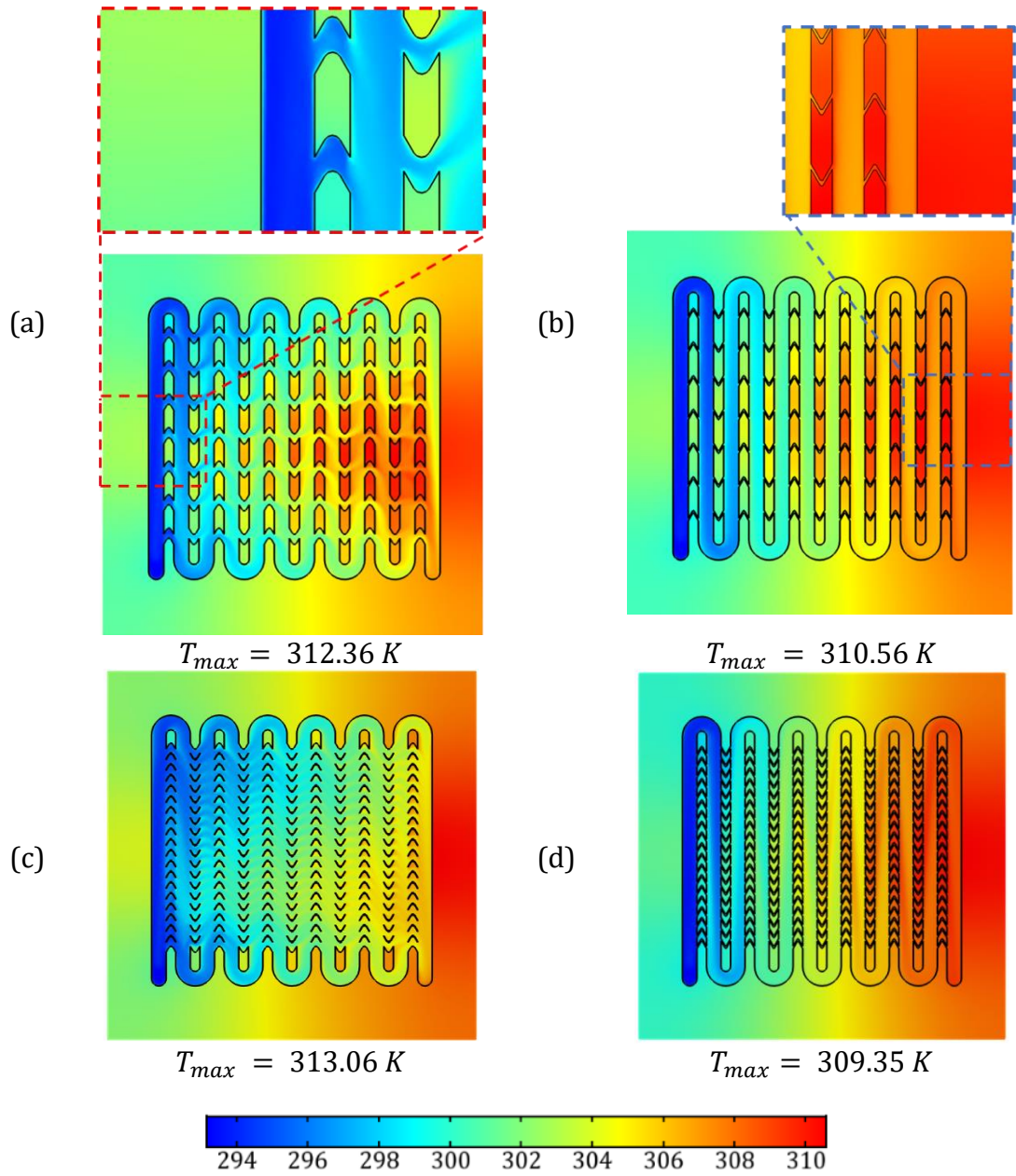


Fig. 6-6 Temperature distribution (K) at the mid-depth plane of the channel ($Z = 0.5 H_c$) for: (a) $F_n = 6$ & $l_{sc} = 1.0$ mm, (b) $F_n = 6$ & $l_{sc} = 0.25$ mm, (c) $F_n = 18$ & $l_{sc} = 1.0$ mm, and (d) $F_n = 18$ & $l_{sc} = 0.25$ mm.

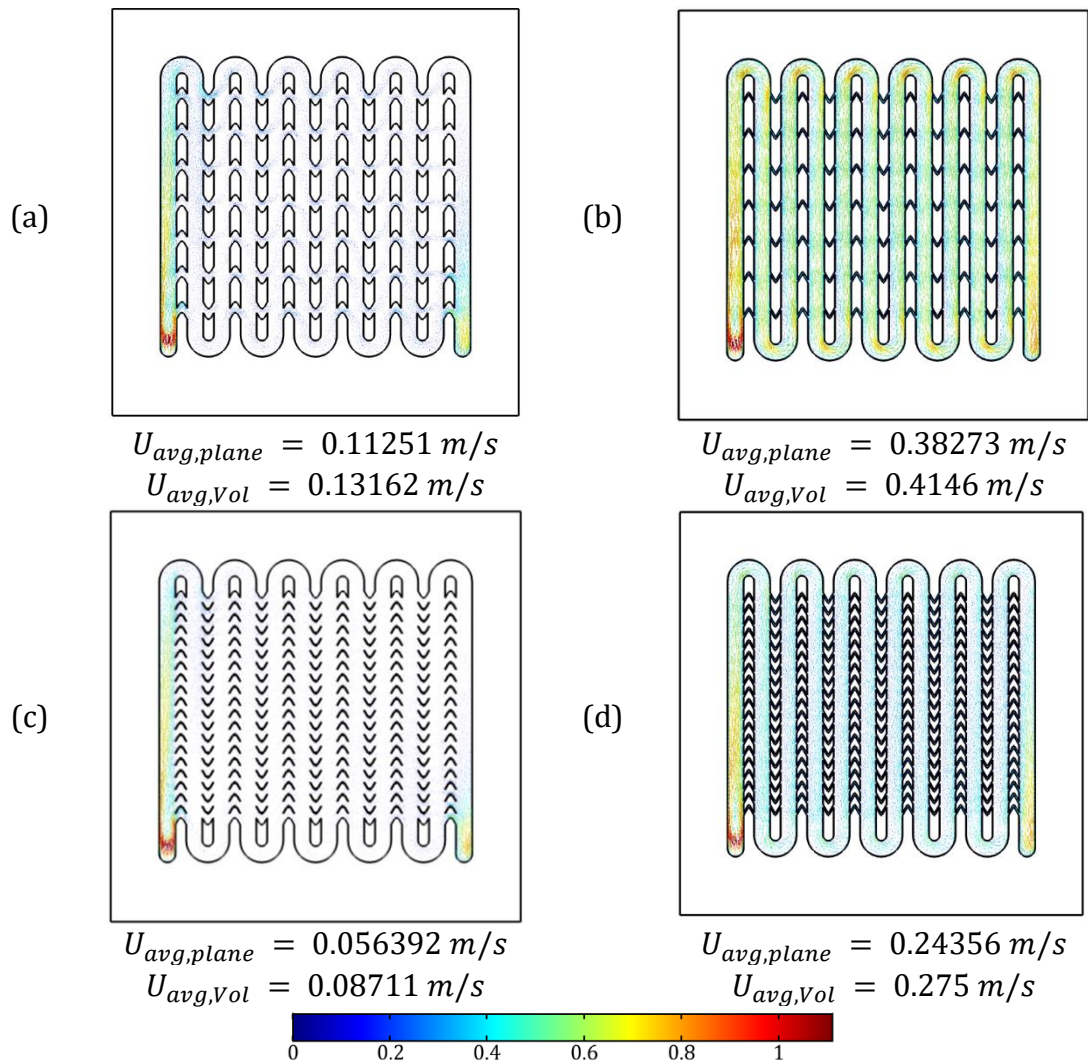


Fig. 6-7 Velocity distribution (m/s) at the mid-depth plane of the channel ($Z = 0.5 H_c$) for: (a) $F_n = 6$ & $l_{sc} = 1.0 \text{ mm}$, (b) $F_n = 6$ & $l_{sc} = 0.25 \text{ mm}$, (c) $F_n = 18$ & $l_{sc} = 1.0 \text{ mm}$, and (d) $F_n = 18$ & $l_{sc} = 0.25 \text{ mm}$.

The graph in Fig. 6-8 and Fig. 6-9 depict the two key performance indicators, R_{th} and ΔP , plotted against Reynolds number (Re), for different values of the fin number (F_n) and secondary channel length (l_{sc}). The overall thermal resistance for the serpentine minichannel heat sink with chevron fins ($SMCHS - CF$) is less than that with plate fins ($SMCHS - PF$). This behaviour which is consistent with the findings of Al-Neama (2018) could be attributed to two reasons. The first one might be attributed to the re-initialisation of both the thermal and hydrodynamic boundary layers at the leading edge of each chevron fin that reduces the thickness of the boundary layers and consequently enhances the hydrothermal performance of the heat sink. The second reason could be the increase in the effective heat transfer area (A_{eff}) for the $SMCHS - CF$ design in comparison to that of the $SMCHS - PF$ (1846.5 mm^2) which helps to decrease heat transfer. For the design $SMCHS - CF$

with $l_{sc} = 0.25 \text{ mm}$, for example, the A_{eff} increases from 2378.3 mm^2 (28.81%) to 3290.2 mm^2 (78.18%) for $F_n = 6$ and $F_n = 18$, respectively. It can also be noticed, from Fig. 6-8, that the thermal resistance decreases with increasing Reynolds number. This might be attributed to the decrease in thickness of the thermal boundary layer with increasing the fluid velocity which in turn enhances the heat transfer between the fluid and solid surface and lowering the surface temperature of the microchannel heat sink.

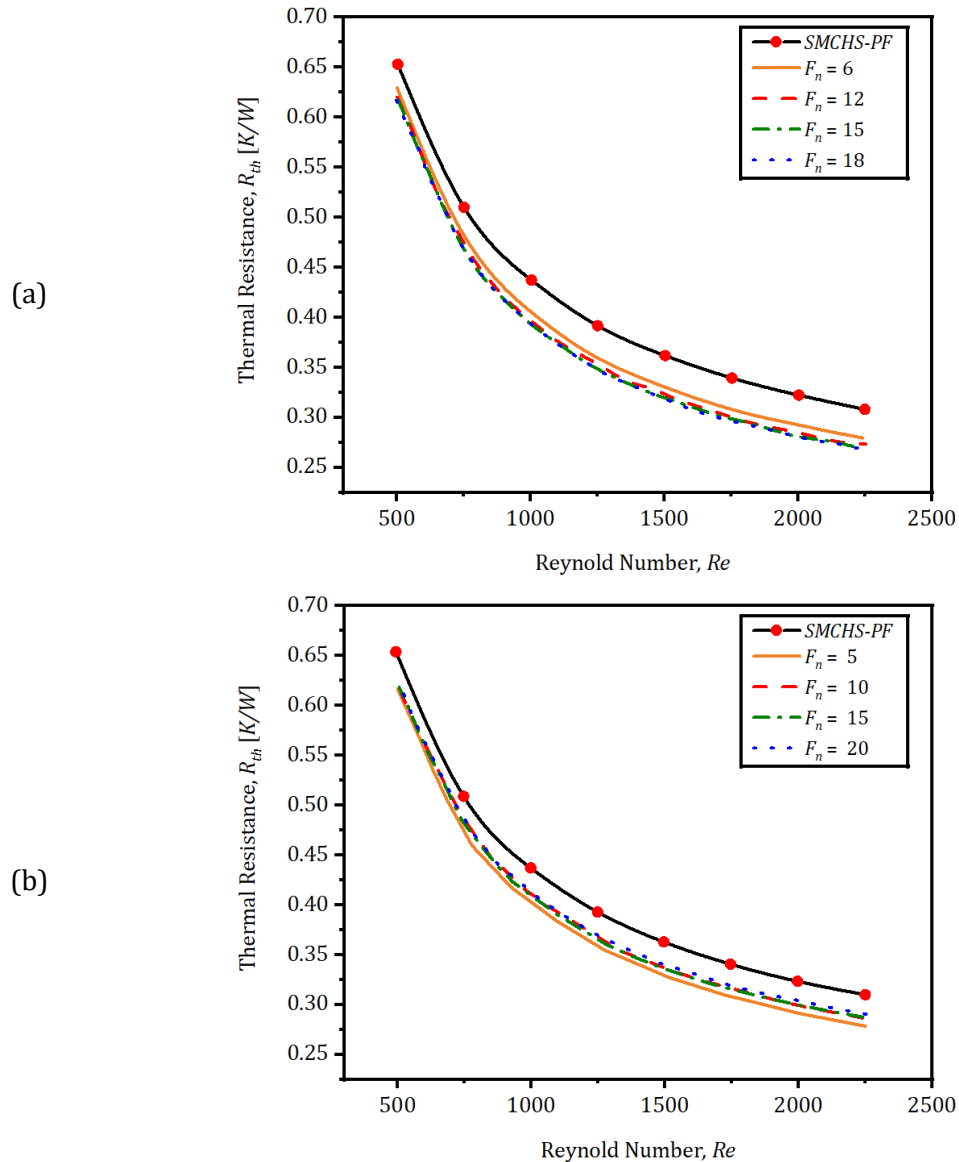


Fig. 6-8 Influence of the Reynolds number on overall thermal resistance for different numbers of fins with: (a) $l_{sc} = 0.25 \text{ mm}$, and (b) $l_{sc} = 0.75 \text{ mm}$.

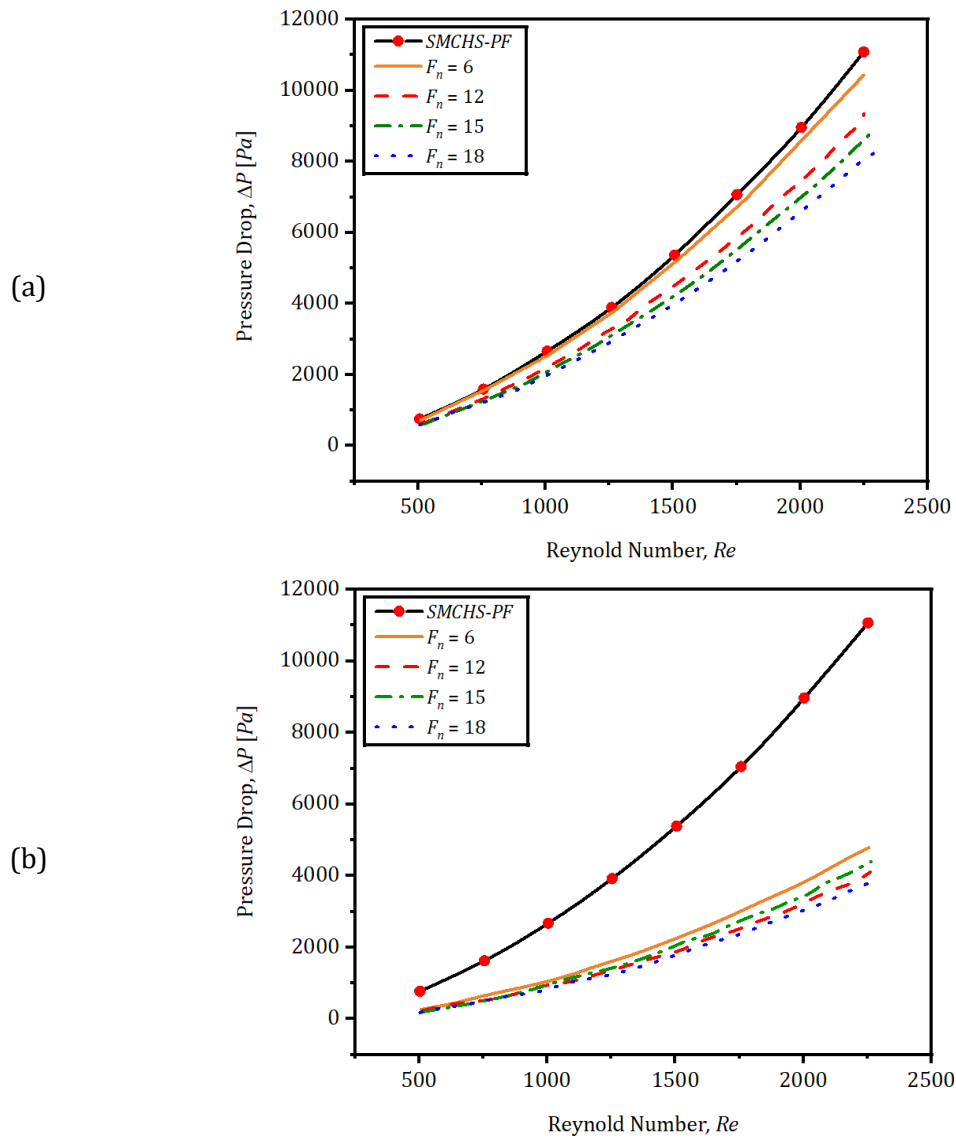


Fig. 6-9 Influence of Reynolds number on pressure losses for different numbers of fins with: (a) $l_{sc} = 0.25 \text{ mm}$, and (b) $l_{sc} = 0.75 \text{ mm}$.

Fig. 6-9 depicts the effect of Reynolds number (Re) and the number of fins (F_n) on the hydraulic performance for the $SMCHS - CF$ with $l_{sc} = 0.25 \text{ mm}$ and $l_{sc} = 0.75 \text{ mm}$. For the two displayed graphs, it can be noticed that the rise in Re leads to an increase in the pressure drop which is proportional to the square of the velocity according Equ (6-5). It is also obvious that the pressure reduced dramatically for the secondary channels with $l_{sc} = 0.75 \text{ mm}$, Fig. 6-9 (b). However, this increase in the pressure penalty can be mitigated by increasing the number of fins for each row.

To sum up, in comparison with the thermal resistance of the $SMCHS - PF$, the improvement in the thermal performance of the $SMCHS - CF$ reaches up to 12%

for $l_{sc} = 0.25$ mm with 18 fins whereas it is just around 5% for $l_{sc} = 1.0$ mm with 10 fins. Within the ranges for the design variables set out in this section, it is evident that the thermal performance of the *SMCHS – CF* is better than that of the *SMCHS – PF* except for the case of $F_n = 18$ with $l_{sc} = 1.0$. It can be concluded that the design with $F_n = 18$ with $l_{sc} = 0.25$ is recommended if a design with high heat transfer is the goal, whereas the design of $F_n = 18$ with $l_{sc} = 1.0$ is preferable if the lower pumping power is the target.

6.3.2 Effect of Fins Offset (F_o)

Since the arrangement of the chevron fins studied by Al-Neama (2018) was in-lined, the staggered configuration of the fins has been introduced here to explore the effect of the fins offset, Fig. 6-10, on the hydrothermal performance of the heat sink under study. The idea behind re-arranging the fins in staggered manner was to create more mixing and improve the heat sink performance. The fin offset (F_o) has been defined as the distance from the tip of a fin in one row to the tail of another fin in the row next to it, Fig. 6-10(b). For this investigation, the number of main minichannel and the number of the chevron fins were respectively 14 and 7, whereas the fin pitch (F_p) was 3.5 mm. Furthermore, the fin length to secondary channel length was 2 and the tested values of F_o were in the range from $0.0F_l$ to $0.9F_l$, i.e. 0.5 mm to 2.25 mm. The numerical simulation results of the effect of the fins offset on the hydrothermal performance of the *SMCHS – CF* is presented in Fig. 6-11 and Fig. 6-12. The findings have indicated a slight increase in the thermal resistance (R_{th}) by less than 1.19%, whereas it has recorded changes in pressure drop (ΔP) ranging between – 2.31% and 3.17%. For example, the results showed that, at $Re = 500$, the ΔP decreased from 266.86 Pa for $F_o = 0$ to 260.69 Pa for $F_o = 2$ mm, i.e. 2.31%, and the corresponding percentage increase in R_{th} was just 0.144%. However, the pressure drop penalty raised by 3.2%, from 3664.2 Pa to 3760.2 Pa, by changing the F_o from 0 to 0.5 mm and $Re = 2000$. The reason behind there being no noticeable changes in the thermal resistance could be attributed to the fact that the effective area of convective heat transfer is unchanged, i.e. $A_{eff} = 3011.9$ mm². However, the slight change could be imputed to the marginal variation in velocity due to the arrangement of fins. Regarding the increase in pressure drop noticed by shifting the F_o from 0 to 2 mm can be explained by inspecting Fig. 6-13. For the

highlighted flow region within the red circle, Fig. 6-13 (a), the flow exiting from the secondary channel is hitting the wall of the fins on the opposite side; however for the case of $F_o = 2 \text{ mm}$, the flow coming out from the secondary channel on one side can enter the secondary channel on the other side directly. This could be the reason for the reduction of the pressure penalty.

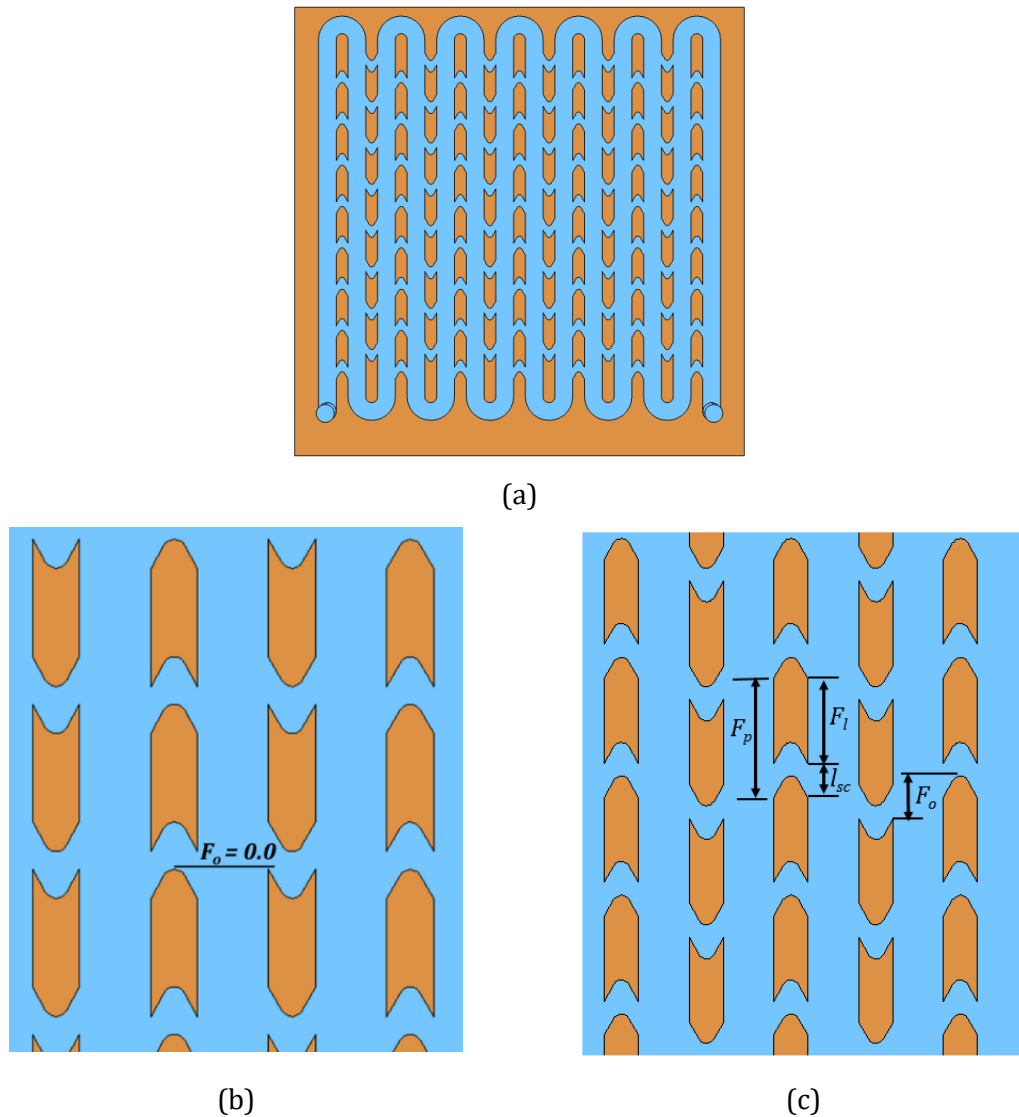


Fig. 6-10 Geometry of the CFD model: (a) Top view , (b) magnifying view for fins without offset and (c) magnifying view showing the fins offset variable, F_o [mm].

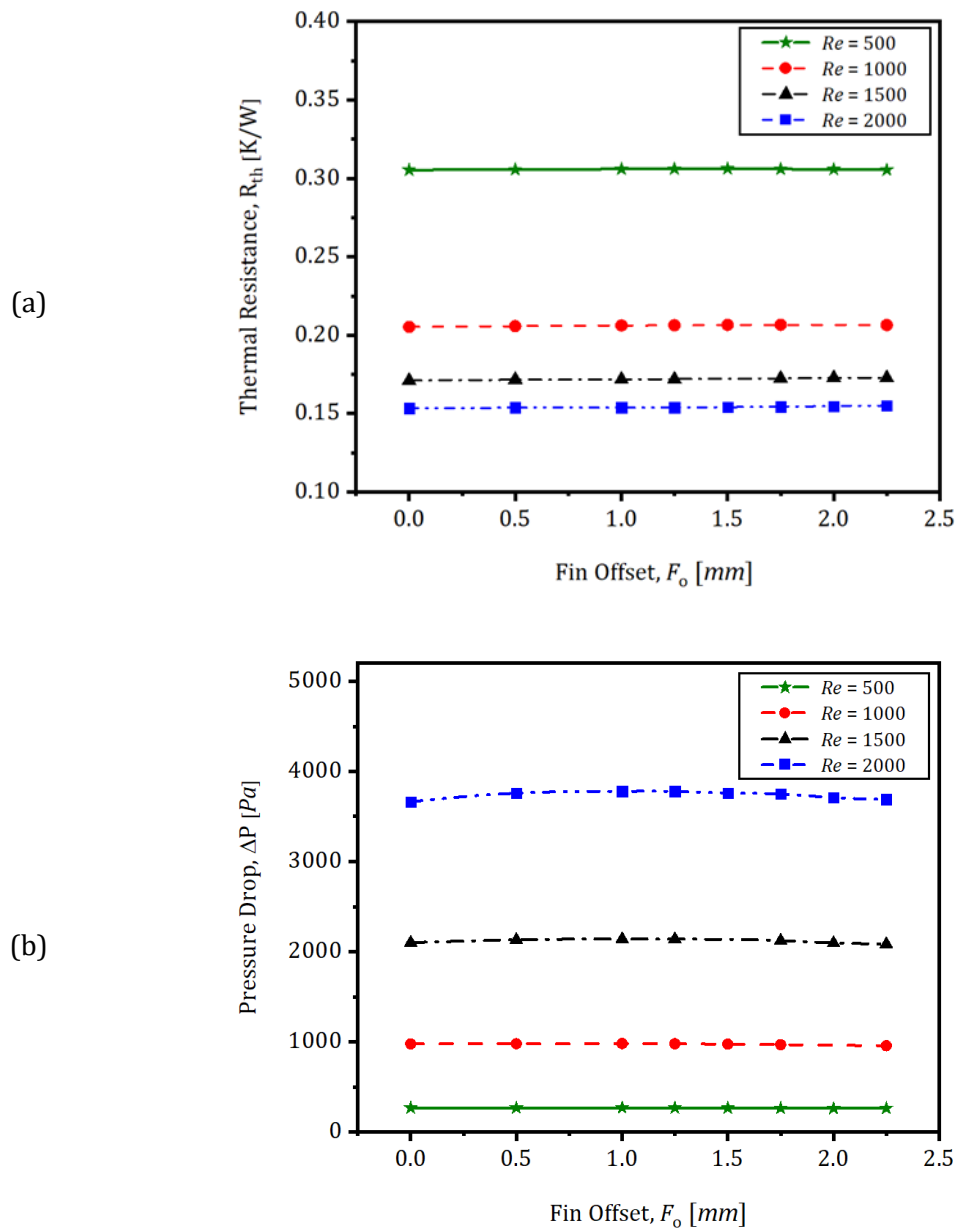


Fig. 6-11 Influence of fin offset on: (a) thermal resistance and (b) pressure losses for different values of Reynolds number.

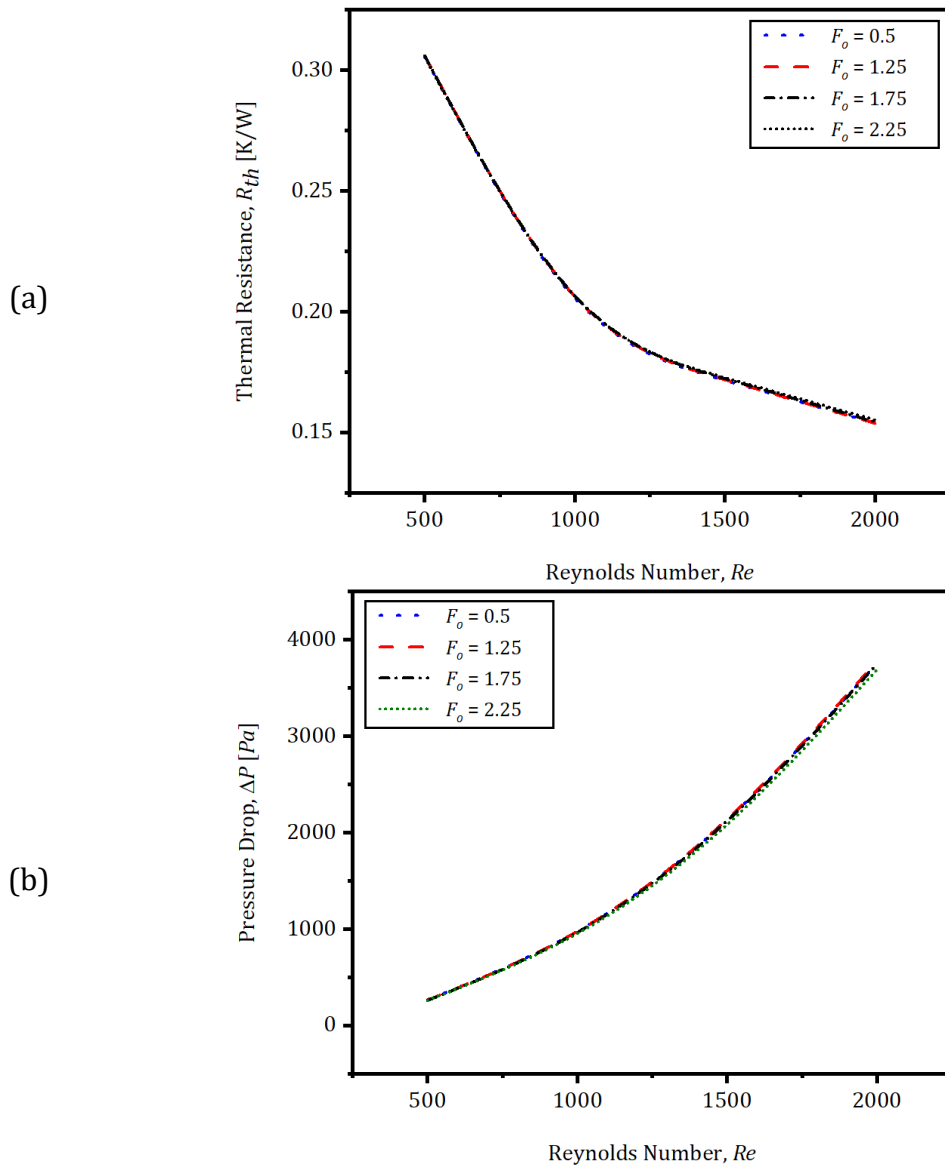


Fig. 6-12 Influence of Reynolds number on: (a) thermal resistance and (b) pressure losses for different values of fin offset.

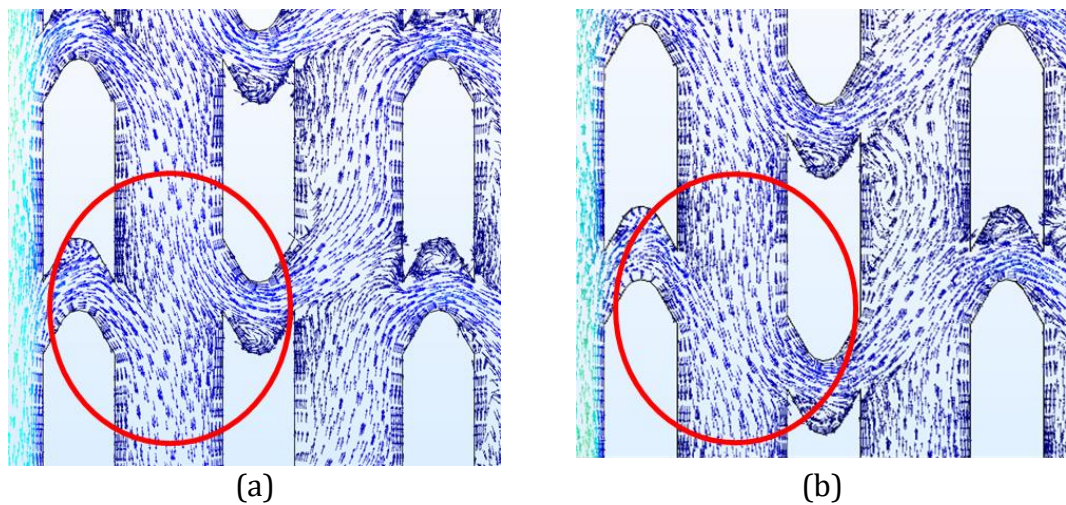


Fig. 6-13 Velocity distribution for: (a) $F_o = 0$ and (b) $F_o = 2.0$ [mm].

6.3.3 Effect of Fin Length to Secondary Channel Length Ratio (R_{FS})

Analysis of the influence of the secondary microchannel length ratio R_{FS} , the fin length (F_l) to the secondary microchannel length (l_{sc}) ratio ($R_{FS} = \frac{F_l}{l_{sc}}$), on the hydrothermal performance of the *SMCHS – CF* for a range of Reynolds number from 500 to 2250 was carried out. The analysis is based on CFD model which is described in section 6.2.1 with the exception that the number of fins F_n , the pitch of fins $F_p (= F_l + l_{sc})$ and the heat flux were 7, 3 mm and $50 W/cm^2$, respectively. Fig. 6-14 shows the related variables.

Effect of R_{FS} on Mass Flow Rate

As it has been reported by Lee *et al.* (2012) and Al-Neama (2018), the existence of the secondary microchannels allows fractions of the flow to pass through them which helps in reducing the pressure loss and thermal resistance by breaking the boundary layers and enhancing the mixing of the cooling fluid itself. Fig. 6-15 (b) illustrates the effect of varying the length ratio ($0.5 \leq R_{FS} \leq 5$) on the average mass flow rate in the main minichannel and microchannels, their locations are designated in Fig. 6-15 (a). These data were gathered for the Reynolds number of 1500. It can be noticed that 37 – 56% of the total flow rate coolant is flowing in the main minichannel and the rest is distributed unevenly among the microchannels. In addition, the amount of fluid entering each microchannel is affected by the R_{FS} ratio. For example, the share of the mass flow rate in the main minichannel increases with increasing the R_{FS} ratio whereas the shares of the secondary microchannels, i.e. SCH-2 to SCH-8, increases then decreases except channel SCH-1 where it decreases steadily with increasing the R_{FS} ratio. This could be attributed to the fact that for fixed fin pitch F_p increasing the R_{FS} leads to elongating the fins at the expense of the length of the secondary channels, as illustrated in Fig. 6-14, which results in restricting the amount of the cooling fluid that is diverted into the secondary microchannels.

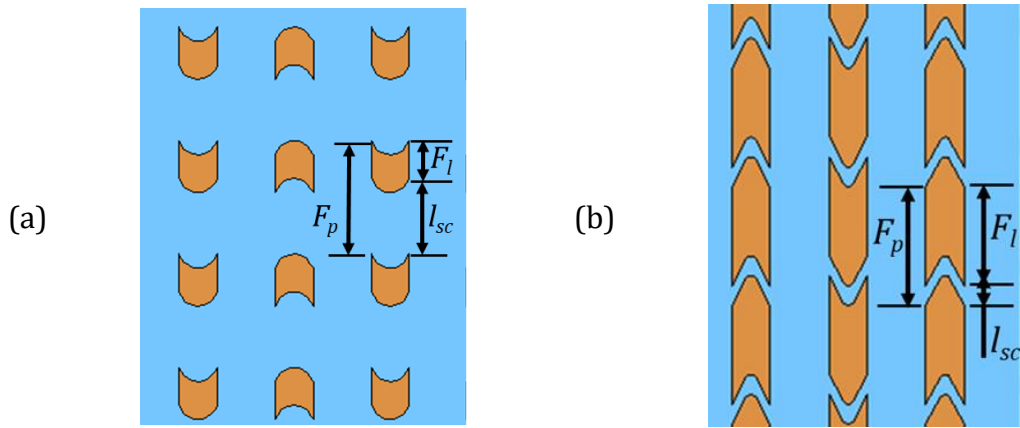
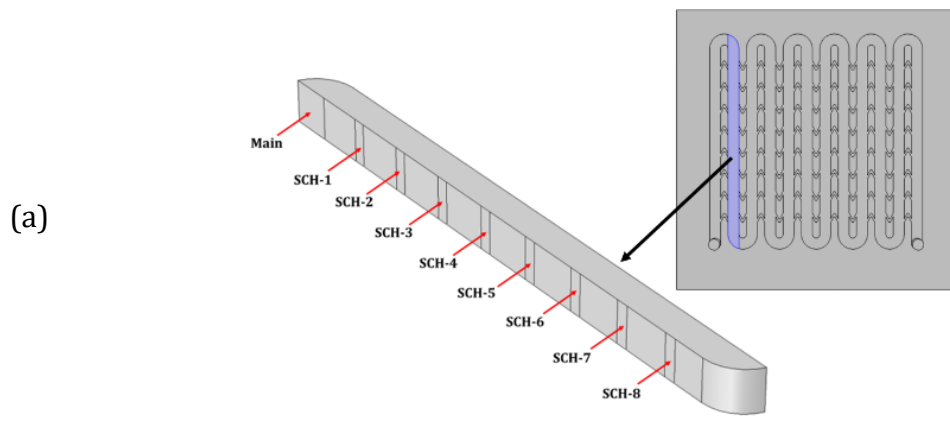


Fig. 6-14 Magnifying view illustrating the fin length to the secondary channel length ratio ($R_{FS} = \frac{F_l}{l_{sc}}$) for: (a) $R_{FS} = 0.5$ and (b) $R_{FS} = 5.0$.



(b)

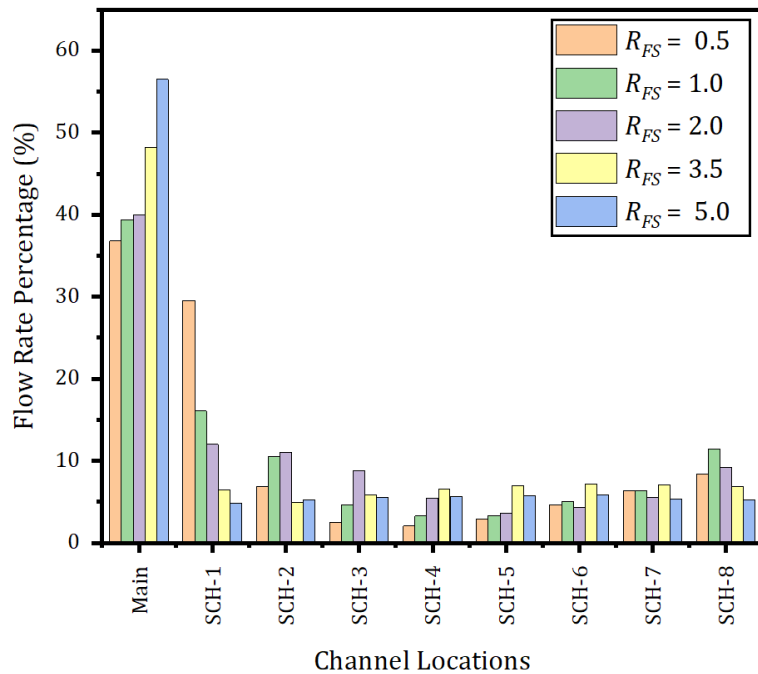


Fig. 6-15 (a) A single minichannel cell with its secondary microchannels and (b) percentage of the mass flow rate at the corresponding channels for different R_{FS} and $Re = 1500$.

Effect of Re and R_{FS} on R_{th} and ΔP

Fig. 6-16 shows the variation in the thermal resistance (R_{th}) and the pressure drop (ΔP) against Reynolds number (Re) for some R_{FS} values, i.e. 0.5, 1.0, 2.0, 3.0 and 5.0. It is evident from Fig. 6-16 (a) that there is a significant reduction in R_{th} as Re increases. This can be attributed to the fact that increasing the velocity of the fluid flow inside the channels leads to an increase in the convective heat transfer coefficient of the fluid which reduces the convective thermal resistance, R_{conv} ($= \frac{1}{h \cdot A}$). Besides, it can be noticed that the increase in the R_{FS} leads to a decrease and then to an increase in the overall thermal resistance R_{th} which could be ascribed to two reasons: (1) the increase in the surface area of the fin and (2) the enhancement of fluid mixing. For example, the effective area of heat transfer, A_{eff} , has increased from by 7.34% for $R_{FS} = 1$ to 27.86% for $R_{FS} = 5$. However, this improvement in R_{th} was moderated and it was less than 7.3% for the best case, $R_{FS} = 3$, in the explored range. The worst design in terms of the thermal resistance was the one with $R_{FS} = 0.5$ which has the highest thermal resistance among all the investigated designs.

By contrast, as depicted in Fig. 6-16 (b), it is clear that ΔP gradually increases with increasing Re which is in agreement with internal fluid flow theories, Equ. 5-5 (Cengel, 2014). Furthermore, introducing the fin structures by dividing the wall of the minichannels reduces the pressure drop (Lee *et al.*, 2012 and Al-Neama, 2018). In this section, the effect of the R_{FS} ratio on pressure drop is also presented. By careful inspection of Fig. 6-16 (b), It can be noticed that lowering the R_{FS} ratio leads to reduce the pressure drop significantly. The numerical results indicated, for instance, that using $R_{FS} = 1$ and 3 led to an improvement in the pressure drop by 72% and 58% respectively in comparison with the serpentine heat sink design without secondary channels ($SMCHS - PF$). In terms the pressure losses, the best design among the studied cases is the one with $R_{FS} = 0.5$. This reduction in pressure penalty can be credited to the increase in the secondary channel length in comparison to the fin length which in turn allows more fluid to pass through these secondary channels.

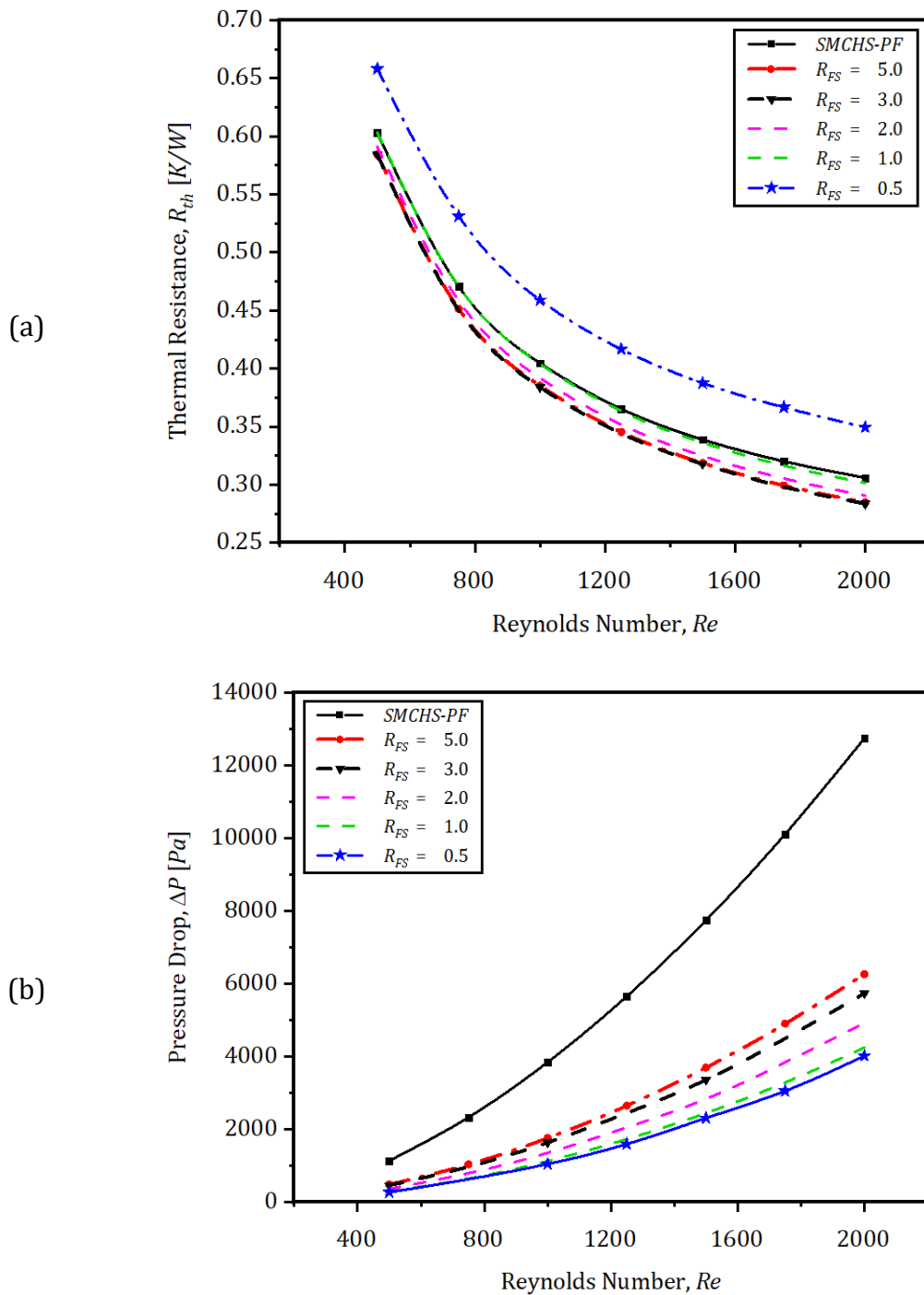


Fig. 6-16 Influence of the fin length to secondary channel length ratio on: (a) Thermal resistance, (R_{th}) and (b) Pressure drop (ΔP).

Effect of R_{FS} and F_n on R_{th} and ΔP

The effect of R_{FS} and the number of fins F_n on the hydrothermal performance of the *SMCHS – CF*, the variation of the thermal resistance and pressure drop against R_{FS} with different F_n is shown in Fig. 6-17. As stated previously, the numerical predictions have been obtained using water as the working fluid entering the

minichannels at 20°C with Reynolds number ranging from 500 to 2250, laminar flow. Besides, a heat flux of 31 W/cm^2 was applied underneath the heat sink. The same behaviour has been noticed for different Re within the ranges set out in this study, therefore, for the brevity purpose, the numerical simulation results were presented for $Re = 1500$.

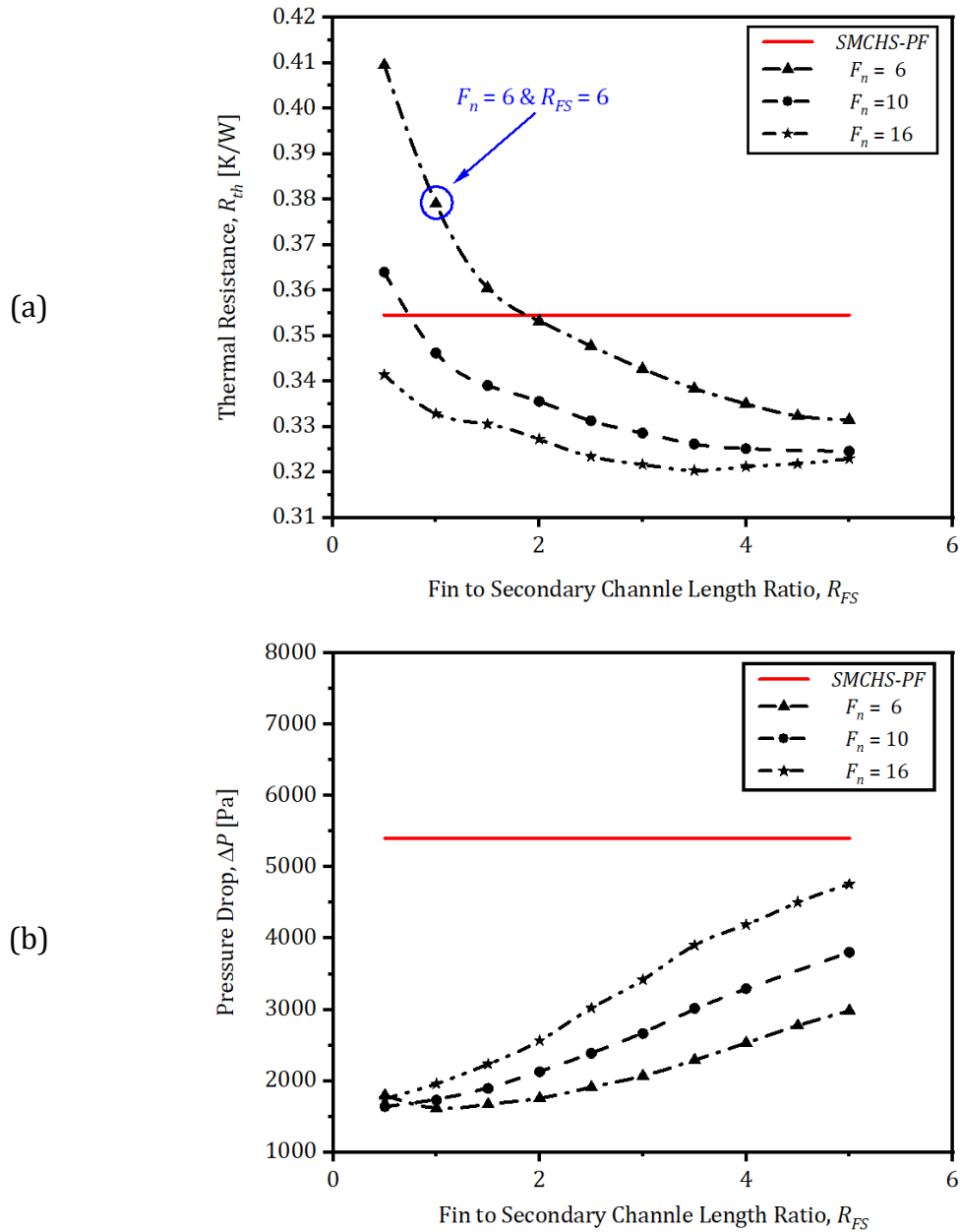


Fig. 6-17 Influence of the fin length ratio, R_{FS} , and numbers of fins F_n on: (a) the overall thermal resistance and (b) the pressure drop penalty.

As shown in Fig. 6-17 (a), it is evident that the increase in R_{FS} reduces the thermal resistance, and this reduction becomes greater by increasing the number of fins. Consequently, as a result of increasing the effective area (A_{eff}) of heat transfer, the

heat transfer between the walls of the heat sink channels and the circulated cooling fluid through it is augmented. It can also be noticed that, for some cases, the presence of the secondary passages has a reverse effect on the heat transfer in comparison to the minichannel heat sink without secondary channels (*SMCHS – PF*). The *SMCHS – CF* with $F_n = 6$ and $R_{FS} = 1$, Fig. 6-18, is an example of such cases. As depicted in Fig. 6-17 (a), this design has a thermal resistance 0.3791 [K/W] which is higher than that of the *SMCHS – PF* design (0.3546 [K/W]) by 6.9%.

The pressure drop penalty, Fig. 6-17 (b), is increased dramatically with increasing R_{FS} due to the decrease in the secondary channel width. For the design with 16 chevron fins, for example, the pressure losses raised from 1752.4 Pa at $R_{FS} = 0.5$ to 4759.5 Pa at $R_{FS} = 5$, i.e. 171.6%. Reducing the number of fins per row has led to mitigate this rate of increase which was only 81.86% for the $F_n = 6$. For all the studied designs, the ΔP was lower than that of the *SMCHS – PF* design.

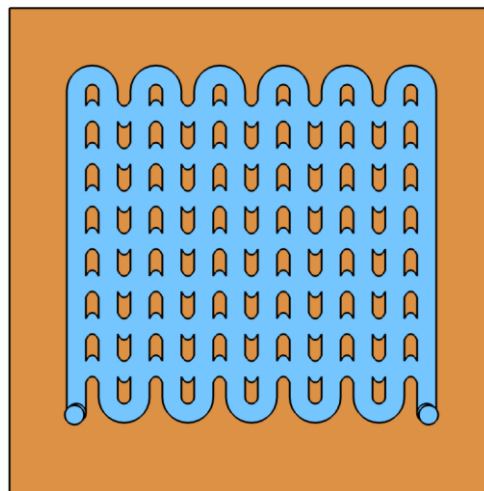


Fig. 6-18 The geometry of the *SMCHS – CF* with $F_n = 6$ and $R_{FS} = 1$.

6.4 Deterministic and Probabilistic Optimisation for MCHSs with Chevron Fins

In his study, Al-Neama (2018) optimised the performance of the minichannel heat sink provided with chevron fins (*SMCHS – CF*) in terms of three design variables which were the width of the minichannel, W_c , the number of the minichannels, N_c , and the oblique angle of the chevron fin, θ . In this investigation, on the other hand, the optimisation exploration took into consideration other design variables, i.e. l_{sc} , F_n , and R_{FS} . The employed optimisation procedure is the surrogate-based

optimisation technique, i.e. the strategy of optimisation is based on replacing the costly CFD evaluation with a cheaper mathematical model to implement the optimisation process. In the following sections, deterministic and probabilistic optimisations for the performance of the minichannel heat sink with chevron fins (*SMCHS – CF*) is presented. It is worth mentioning that the CFD results were obtained for Re_{inlet} and T_{inlet} of 1000 and 20°C and the heat flux applied underneath the substrate of the heat sink was 31 W/cm^2 .

6.4.1 Deterministic Single-Objective Optimisation

Single-Objective Optimisation with Respect to W_c , l_{sc} and θ

The effect of the design variables (W_c , l_{sc} and θ) on R_{th} and ΔP is explored by performing, firstly, a single objective deterministic optimisation for each output of interest and, then, multi-objective optimisation. The single objective deterministic optimisation problem can be formulated as:

$$\textit{Find} \quad W_c, l_{sc} \text{ and } \theta$$

For the thermal resistance (R_{th}):

$$\textit{To minimise} \quad R_{th}(W_c, l_{sc}, \theta) \quad \text{Equ. 6-1}$$

For the Pressure Drop (ΔP):

$$\textit{To minimise} \quad \Delta P(W_c, l_{sc}, \theta) \quad \text{Equ. 6-2}$$

Both optimisation problems are subjected to:

$$1.0 \leq W_c \leq 2.0 \quad \text{Equ. 6-3}$$

$$0.75 \leq l_{sc} \leq 1.25 \quad \text{Equ. 6-4}$$

$$20 \leq \theta \leq 45 \quad \text{Equ. 6-5}$$

Following the previous studies, the number of extracted samples should be at least $10 \times$ the design variables (Swiler and Giunta, 2007). Therefore, for this optimisation problem with three design variables, the number of samples should be 30 points or more—the higher the number of samples, the more accurately representing the design domain. However, increasing the number of samples will make the process of obtaining responses of interest more expensive. As a compromise, 45 samples have been selected to represent the design domain.

The surrogate models for the objective functions have been built using 45 points of the design variables, Fig. 6-19, which have been generated using the Latin-hypercube sampling (LHS) method. This number of points has been chosen to satisfy the above criterion. The type of these models was Gaussian-Process and their accuracy was checked using the cross-validation method, for each of thermal resistance (R_{th}) and pressure drop (ΔP) as shown in Table 6-3. Based on these results, the obtained surrogate models were adopted here to implement the optimisation study.

As in the previous chapter, single-objective optimisation using the genetic algorithms (*soga*) within Dakota toolkit has conducted for each objective function defined in Equ. 6-1 to Equ. 6-5 to find the design variables that give minimum (R_{th}) and (ΔP). The results are tabulated in Table 6-4.

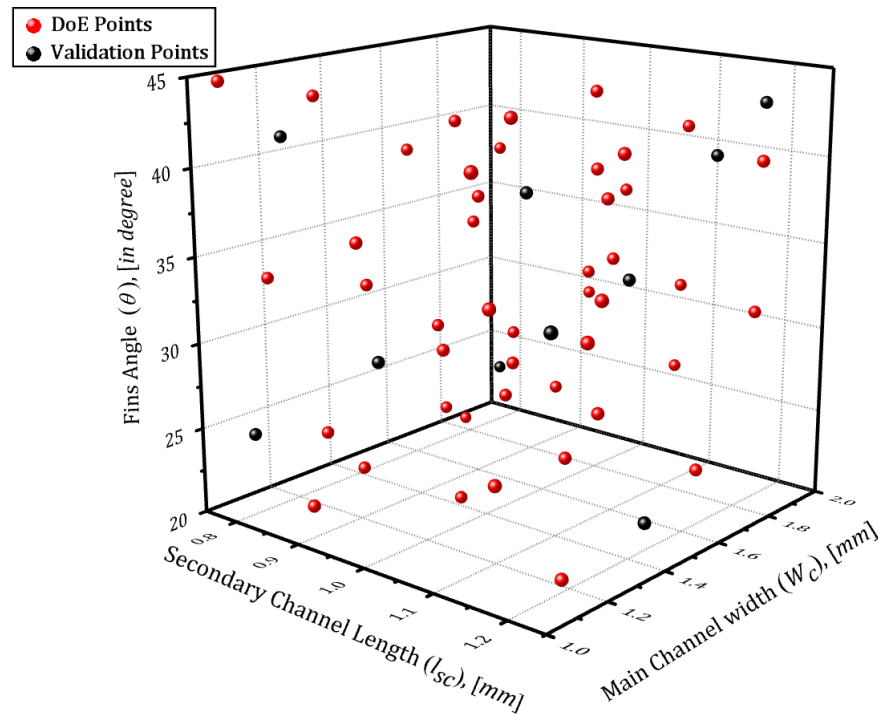


Fig. 6-19 Design of experiments points (red points) used to build the metamodel and validation points (black points) for the *SMCHS – CF* with W_c , l_{sc} and θ as design variables.

Table 6-3 Comparison of the responses evaluated by the CFD simulation and the approximation surrogate model (cross-validation).

Point	Design Variables			Surrogate Model		CFD-Predictions		% diff. (\pm)	
	l_{sc} [mm]	W_c [mm]	θ [°]	R_{th} [K/W]	ΔP [Pa]	R_{th} [K/W]	ΔP [Pa]	R_{th}	ΔP
1	1.15	1.85	40	0.388	739.253	0.392	756.551	1.2	2.34
2	1.24	1.35	23	0.446	1258.990	0.456	1274.098	2.05	1.28
3	1.05	1.42	39	0.435	1049.916	0.441	1062.515	1.5	3.15
4	1.13	1.58	34	0.413	869.974	0.416	880.414	0.9	1.68
5	1.23	1.06	35	0.528	1729.084	0.536	1749.833	1.6	2.62
6	0.77	1.23	41	0.468	1703.085	0.476	1723.522	1.75	1.24
7	0.82	1.87	24	0.354	1049.673	0.362	1062.269	2.1	0.98
8	0.81	1.05	25	0.474	1846.614	0.478	1868.773	0.75	2.87
9	0.95	1.16	30	0.472	1628.740	0.484	1648.285	2.6	1.54
10	1.19	1.92	43	0.449	1179.219	0.453	1193.370	0.85	2.14

Within the ranges set out in the definition of the optimisation problem, it is clear that the minimum performance criteria occur with the upper limit of the W_c . However, regarding the other design variables studied here, the minimum thermal resistance takes place with the lower limits of the secondary channel length ($l_{sc} = 0.751$) and the fin oblique angle ($\theta = 20.04$), Fig. 6-22(a), while the minimum pressure drop obtained with the upper limit of the ($l_{sc} = 1.217$) and at fin angle of ($\theta = 34.75$), Fig. 6-22(b).

Table 6-4 Surrogate-based single-objective optimisation results for the thermal resistance and pressure drop of the *SMCHS – CF* with W_c , l_{sc} and θ as design variables.

Case	<i>soga</i> results		Optimum Design			CFD Validation		% diff. (\pm)	
	R_{th}	ΔP	l_{sc}	W_c	θ	R_{th}	ΔP	R_{th}	ΔP
1	0.347	-----	0.750	1.996	20.04	0.345	-----	0.5	----
2	-----	775.74	1.217	1.902	34.75	-----	759.6	-----	2.2

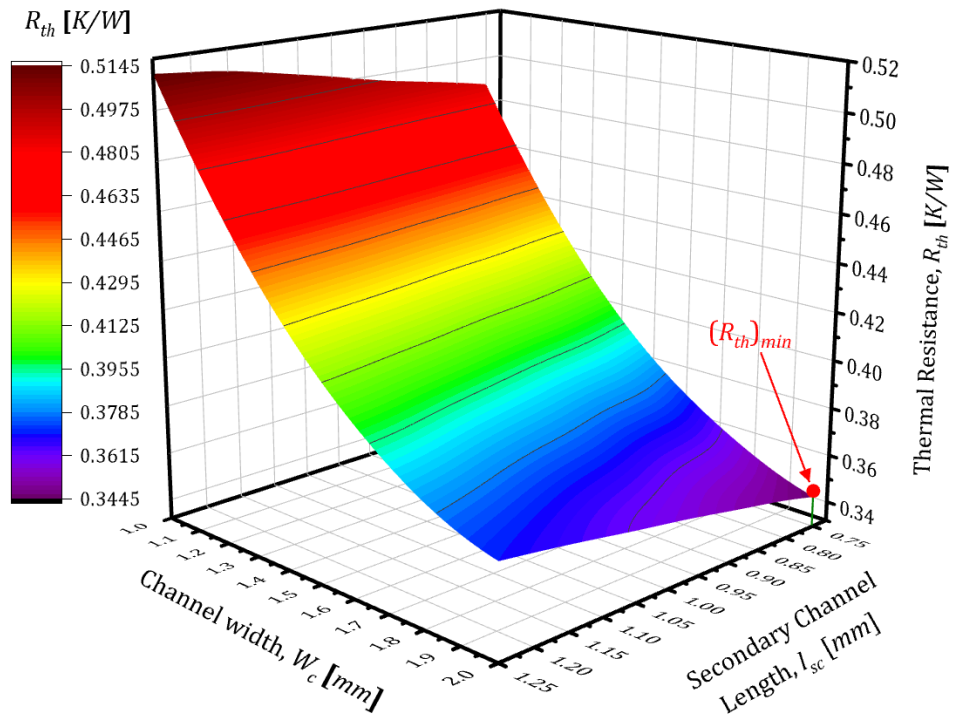


Fig. 6-20 Metamodel for the thermal resistance (R_{th}) as a function of two design variables, W_c and l_{sc} , at $\theta = 20.04$ at which the minimum thermal resistance happen.

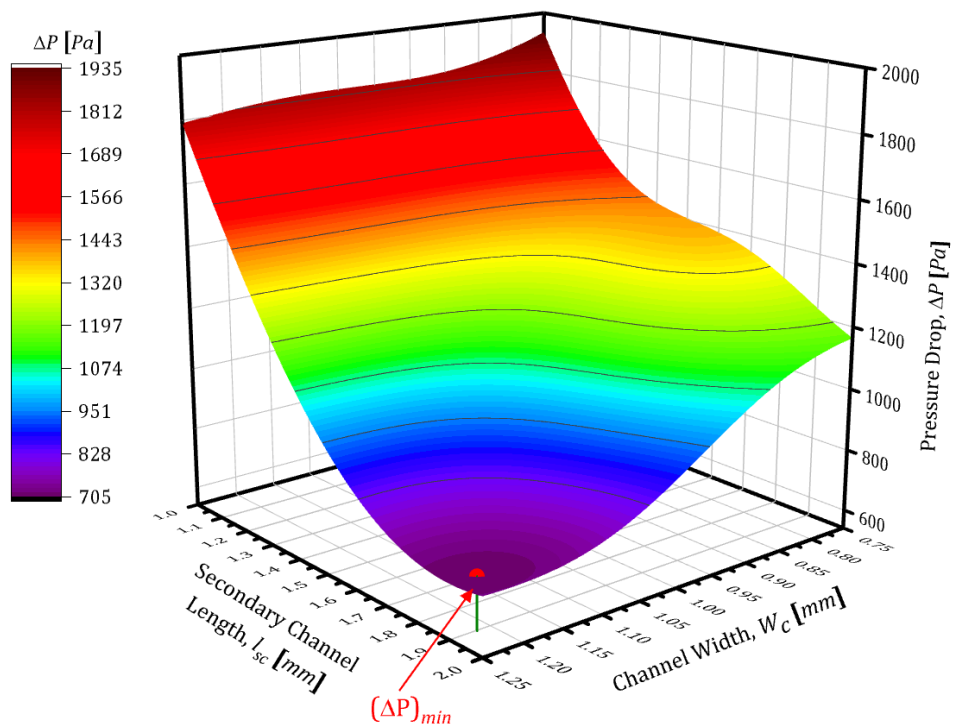


Fig. 6-21 Metamodel for the pressure drop (ΔP) as a function of two design variables, W_c and l_{sc} , at $\theta = 34.75$ at which the minimum pressure drop take place.

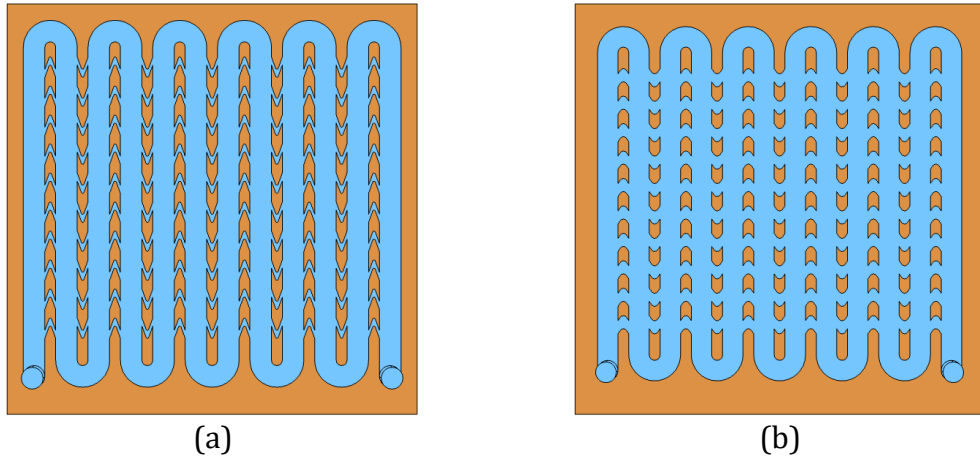


Fig. 6-22 Geometries for the optimum design of the *SMCHS – CF* with W_c , l_{sc} and θ as design variables obtained with *soga* for: (a) minimum thermal resistance and (b) minimum pressure drop.

Single-Objective Optimisation with Respect to F_n , F_o and R_{FS}

Another design variables which are the number of fins (F_n), fins offset ratio (F_o) and the fin length to secondary channel length ratio (R_{FS}) have been considered to conduct single-objective and multi-objective optimisation for R_{th} and ΔP . The fin offset ratio was defined as the ratio of the fin offset (F_{offset}) to the fin length (F_l), i.e.

$F_o = \frac{F_{offset}}{F_l}$, While the fin length ratio was expressed as the fin length to secondary channel length ratio ($R_{FS} = \frac{F_l}{l_{sc}}$).

The single-objective deterministic optimisation problem for each performance criteria with respect to F_n , F_o and R_{FS} as design variables can be defined as follow:

Find F_n, F_o and R_{FS}

For the thermal resistance (R_{th}):

To minimise $R_{th}(F_n, F_o, R_{FS})$ Equ. 6-6

For the Pressure Drop (ΔP):

To minimise $\Delta P(F_n, F_o, R_{FS})$ Equ. 6-7

Both optimisation problems are subjected to:

$$5 \leq F_n \leq 20 \quad \text{Equ. 6-8}$$

$$-1 \leq F_o \leq 1 \quad \text{Equ. 6-9}$$

$$0.25 \leq R_{FS} \leq 2.5 \quad \text{Equ. 6-10}$$

The Latin hypercube sampling (LHS) technique has been employed to generate 50 points in the design space, Fig. 6-19. These points have been used in the CFD simulation to generate the simulation predictions for the quantities of interest at $Re = 1500$. Based on these DoE points and the corresponding responses, the Gaussian-Process model has been used to construct the surrogate model that replacing the CFD simulations in the optimisation process.

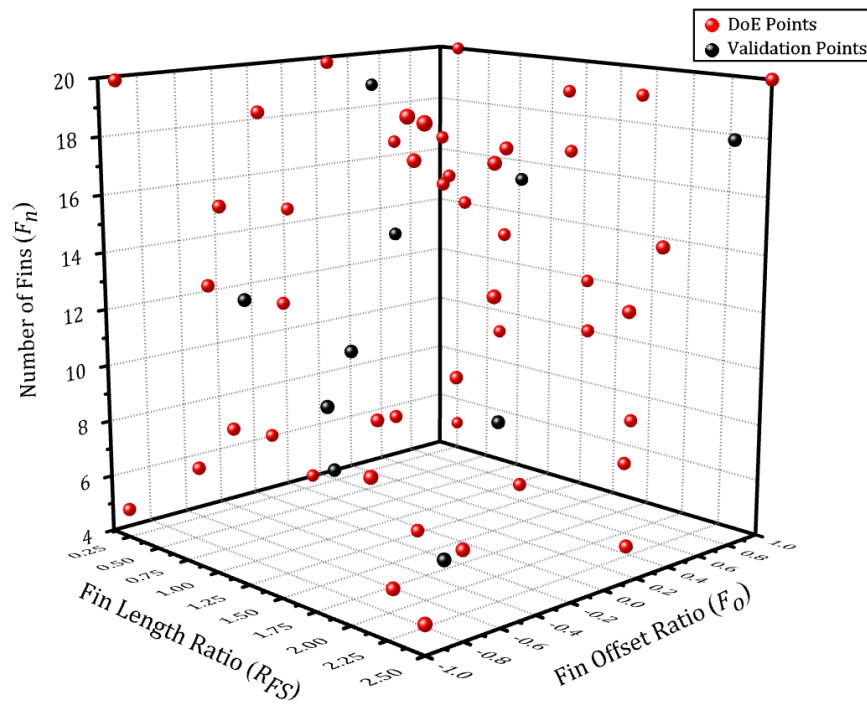


Fig. 6-23 Design of experiments points (red points) used to build the metamodel and validation points (black points) for the *SMCHS – CF* with F_n , F_o and R_{FS} as design variables.

New points, black points in Fig. 6-23, have been used to check the constructed surrogate models' accuracy by comparing their outputs against the CFD predictions at these points and the results are presented in Table 6-5. It has been noticed a good agreement between the compared data with a difference of less than 3.18% and this validates the generated surrogate models.

The Dakota toolkit's genetic algorithms (*soga*) have been utilised to perform the surrogate-based single-objective optimisation for each objective function introduced in Equ. 6-6 to Equ. 6-10. The design variables that offer minimum (R_{th}) and (ΔP) are presented in Table 6-6, and the corresponding heat sink designs are shown in Fig. 6-26. As illustrated in Table 6-6, the two objective functions are conflicting because the minimizing any one of the objective functions leads to increase the other one. For example, minimizing the R_{th} is accompanied by an

increase in the pressure drop to (3298.93 Pa), which is about double the minimum ΔP . Therefore, multi-objective optimisation will be performed in the next section.

Table 6-5 Comparison of the responses evaluated by the CFD simulation and the approximation surrogate model (cross-validation).

Point	Design Variables			Surrogate Model		CFD-Predictions		% diff. (\pm)	
	R_{FS}	F_o	F_n	R_{th} [K/W]	ΔP [Pa]	R_{th} [K/W]	ΔP [Pa]	R_{th}	ΔP
1	1.5	-	10	0.326	2050.261				
		0.75				0.393	800.966	1.73	3.01
2	1.2	-0.5	7	0.358	1838.784	0.450	1302.386	0.91	2.36
3	0.95	-0.8	13	0.330	1931.484	0.443	1080.240	2.46	1.57
4	1.2	-0.4	11	0.328	1989.518	0.418	923.095	1.68	2.67
5	1.23	0.6	16	0.320	2209.031	0.535	1748.744	2.13	0.89
6	2.4	0.87	18	0.309	3403.251	0.473	1777.616	1.75	2.19
7	1.89	-0.1	9	0.332	2008.919	0.356	1078.601	0.71	1.44
8	0.75	0.2	14	0.331	1938.714	0.479	1908.265	1.38	3.18
9	2.25	-0.7	6	0.343	2102.146	0.481	1665.318	2.78	1.74
10	0.3	0.4	19	0.329	1893.138	0.451	1231.659	0.66	2.77

Table 6-6 Surrogate-based single-objective optimisation results for the thermal resistance and pressure drop of the *SMCHS – CF* with F_n , F_o and R_{FS} as design variables.

Case	<i>soga</i> results		Optimum Design			CFD Validation		% diff. (\pm)	
	R_{th}	ΔP	F_n	F_o	R_{FS}	R_{th}	ΔP	R_{th}	ΔP
1	0.305	-----	17	-0.3	2.492	0.311	3298.93	1.93	----
2	-----	1427.34	5	0.491	0.812	0.380	1457.45	-----	2.1

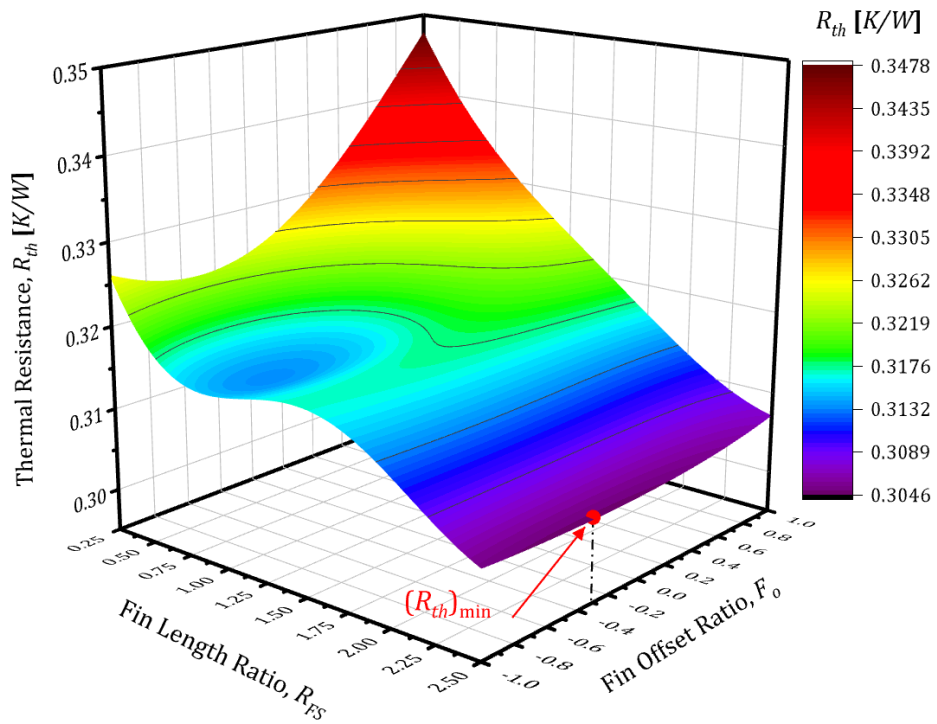


Fig. 6-24 Metamodel for the thermal resistance (R_{th}) as a function of the two design variables, F_o and R_{FS} , at $F_n = 17$ at which the minimum thermal resistance occurs.

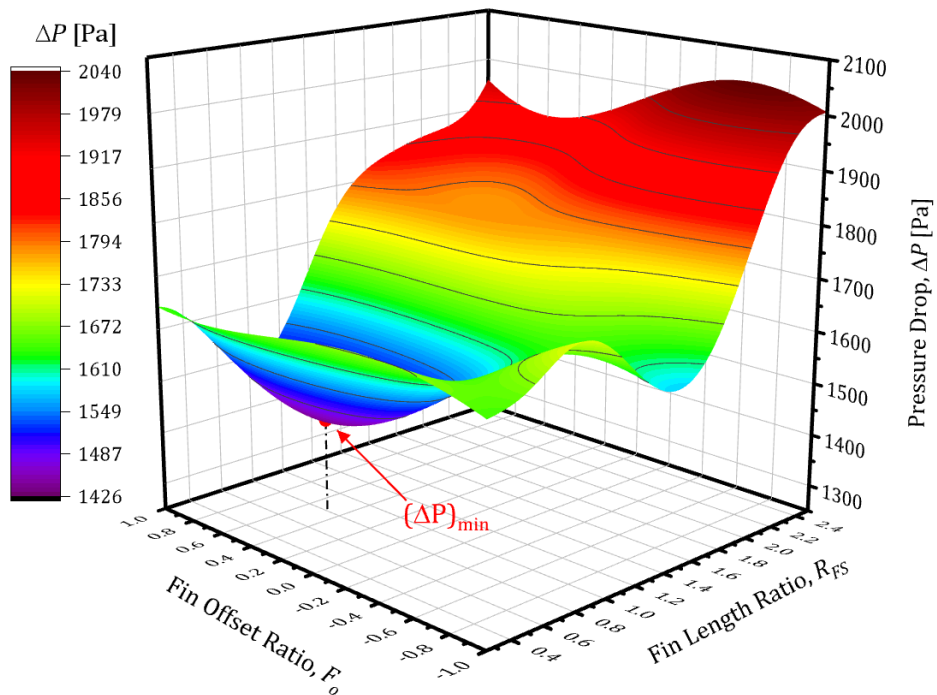


Fig. 6-25 Metamodel for the pressure drop (ΔP) as a function of the two design variables, F_o and R_{FS} , at $F_n = 5$ at which the minimum pressure drop occurs.

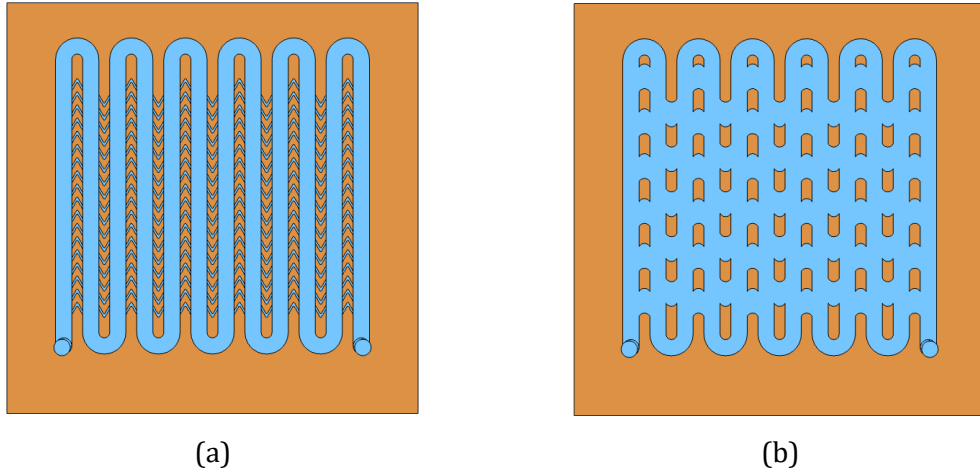


Fig. 6-26 Geometries for the optimum design of the *SMCHS – CF* with F_n, F_o and R_{FS} as design variables obtained with *soga* for: (a) minimum thermal resistance and (b) minimum pressure drop.

6.4.2 Deterministic Multi-Objective Optimisation for *SMHS – CF*

As illustrated above, the performance criteria, R_{th} and ΔP , are conflicting, therefore the following subsections address the deterministic multi-objective function optimisation for these criteria. The procedure has been performed for two cases of the minichannel heat sink with chevron fins (*SMCHS – CF*). The first one is the multi-objective optimisation for R_{th} and ΔP with respect to W_c, l_{sc} and θ , while the second has been performed in terms of F_n, F_o and R_{FS} .

Multi-Objective Optimisation with Respect to W_c, l_{sc} and θ

The multi-objective optimisation in terms of W_c, l_{sc} and θ is explored according to the following definition and constraints of the optimisation problem:

<i>Find</i>	W_c, l_{sc} and θ	
<i>To minimise</i>	$R_{th}(W_c, l_{sc}, \theta)$ & $\Delta P(W_c, l_{sc}, \theta)$	Equ. 6-11
<i>Subjected to</i>	$1.0 \leq W_c \leq 2.0$	Equ. 6-12
	$0.75 \leq l_{sc} \leq 1.25$	Equ. 6-13
	$20 \leq \theta \leq 45$	Equ. 6-14

Utilizing the same surrogate models generated previously, Fig. 6-20 and Fig. 6-21, the multi-objective optimisation using the genetic algorithms (*moga*) within Dakota

software has implemented to find the optimal solutions and the result are presented, i.e. Pareto front, Fig. 6-27. As part of the validation process for the results, five random points on this Pareto front have been selected as potential optimum design and compared against the corresponding results obtained using the CFD model, Fig. 6-27 and Table 6-7. The compared data are in an excellent agreement with maximum difference of less than 2.82%.

Table 6-7 Validation of the Pareto front results for the *SMCHS – CF*.

Points	Design Variables			Metamodel		CFD Validation		% diff. (\pm)	
	l_{sc} [mm]	W_c [mm]	θ [deg]	R_{th} [K/W]	ΔP [Pa]	R_{th} [K/W]	ΔP [Pa]	R_{th}	ΔP
P ₁	0.816	1.960	20.294	0.354	1314.52	0.352	1340	0.67	1.90
P ₂	0.774	1.960	29.129	0.365	1012.59	0.363	1008.6	0.55	0.40
P ₃	0.764	1.982	39.249	0.368	860.54	0.368	847.75	0.11	1.51
P ₄	0.988	1.960	39.249	0.375	736.84	0.376	758.21	0.48	2.82
P ₅	1.230	1.863	34.483	0.389	706.78	0.392	695.67	0.73	1.60

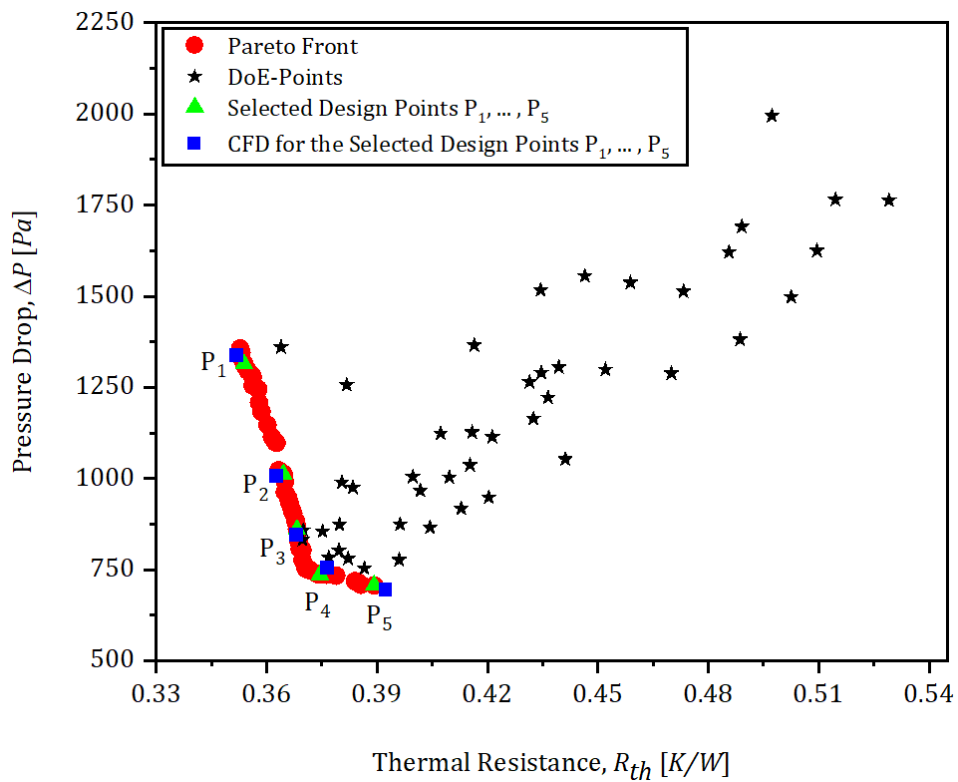


Fig. 6-27 Pareto front for the pressure drop and thermal resistance of the *SMCHS – CF* with W_c , l_{sc} and θ as design variables.

Multi-Objective Optimisation with Respect to F_n , F_o and R_{FS}

This section conducts a multi-objective optimisation for the minichannel heat sink (*SMCHS – CF*) performance with respect to the number of fins (F_n), fins offset ratio (F_o) and the fin length to secondary channel length ratio (R_{FS}) as design variables.

The optimisation problem was formulated as follow:

Find F_n, F_o and R_{FS}

To minimise $R_{th}(F_n, F_o, R_{FS})$ & $\Delta P(F_n, F_o, R_{FS})$ Equ. 6-15

Subjected to $5 \leq F_n \leq 20$ Equ. 6-16

$-1 \leq F_o \leq 1$ Equ. 6-17

$0.25 \leq R_{FS} \leq 2.5$ Equ. 6-18

Using the surrogate models generated previously to implement the single-objective optimisation problem for the same design variables (Fig. 6-24 and Fig. 6-250) which were constructed from the DoE points, Fig. 6-23, and their corresponding CFD responses, the multi-objective optimisation utilising the genetic algorithms (*moga*) has been performed to obtain the Pareto front. The results are depicted in Fig. 6-28. This figure also shows some selected points (P_1 to P_4) as optimal designs candidates. The design variables for these optimal solutions along with the CFD validation for the responses at these points are presented in Table 6-8. The CFD results are in a good agreement with those obtained from the Pareto front, and the maximum difference between them was 2.63%.

Table 6-8 Validation of the Pareto front results for the *SMCHS – CF* with R_{FS} , F_o and F_n as design variables.

Points	Design Variables			Metamodel		CFD Validation		% diff. (\pm)	
	R_{FS}	F_o	F_n	R_{th} [K/W]	ΔP [Pa]	R_{th} [K/W]	ΔP [Pa]	R_{th}	ΔP
P_1	0.888	-0.132	12	0.331	1848.735	0.328	1875.40	0.84	1.42
P_2	0.924	-0.540	17	0.316	2061.626	0.318	2096.80	0.55	1.68
P_3	2.018	-0.686	15	0.313	2602.500	0.311	2635.65	0.58	1.26
P_4	2.013	-0.121	20	0.308	3110.351	0.309	3194.30	0.49	2.63

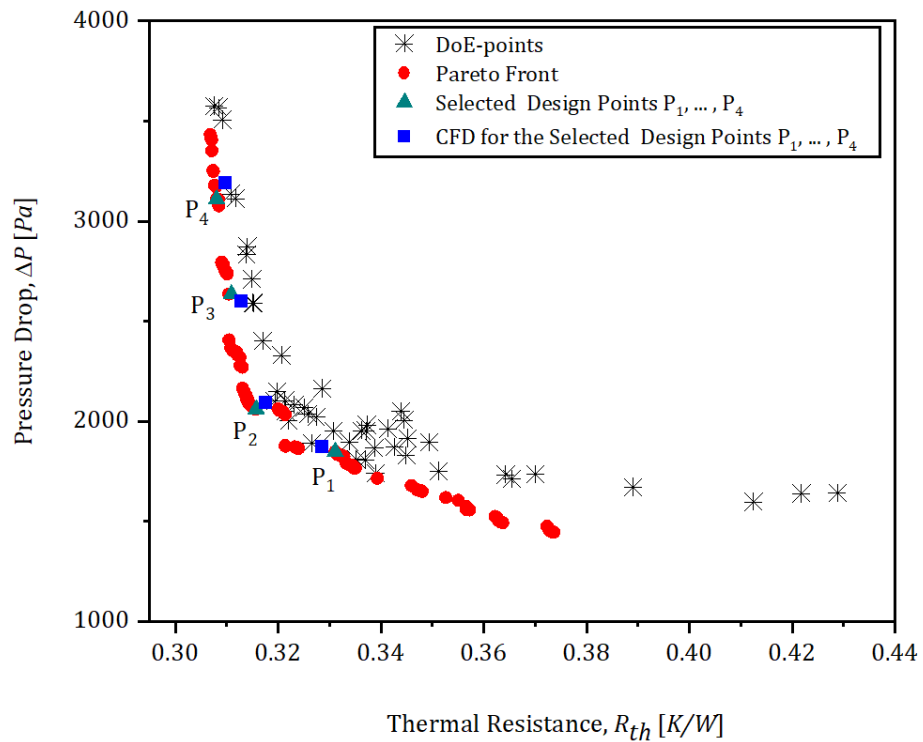


Fig. 6-28 Pareto front for the pressure drop and thermal resistance of the *SMCHS – CF* with R_{FS} , F_o and F_n as design variables.

6.4.3 Probabilistic Optimisation for Minichannels Heat sink with Chevron Fins (*SMCHS – CF*)

As stated earlier, uncertainty in dimensions due to manufacturing is unavoidable; therefore, this section is devoted to investigating the effect of these uncertainties on the performance of the microchannel heat sink with chevron fins. Consequently, this investigation requires propagating the uncertainty in design variables (W_c , l_{sc} and θ) into the quantities of interest, i.e. the thermal resistance (R_{th}) and pressure drop (ΔP) which can be accomplished using Monte Carlo simulation.

Uncertainty Quantification for the Performance of the *SMCHS – CF*

In this section, the mean (μ) and standard deviation (σ) for each response, i.e. (R_{th}) and pressure drop (ΔP), need to be estimated using Monte Carlo simulations. Therefore, as in the study of (Bodla *et al.*, 2013), variability in the dimensions of the design variables, i.e. main channels width (W_c), length of the secondary channels (l_{sc}), and the oblique angle of the chevron fins (θ), have been imposed as summarised in Table 6-9.

Table 6-9 The uncertainty associated with the input design variables.

Variable	Distribution	μ	σ
W_c [mm]	Normal	W_{ci}	0.025
l_{sc} [mm]	Normal	l_{sci}	0.025
θ [°]	Normal	θ_i	2

First of all, the dependency of these statistical moments on the number of samples was assessed as shown in Fig. 6-29. It can be concluded that there is no significant change in (μ) and (σ) values by increasing the number of samples more than 1,000,000. Therefore, this number of samples has been adopted to conduct the uncertainty quantification in the following sections.

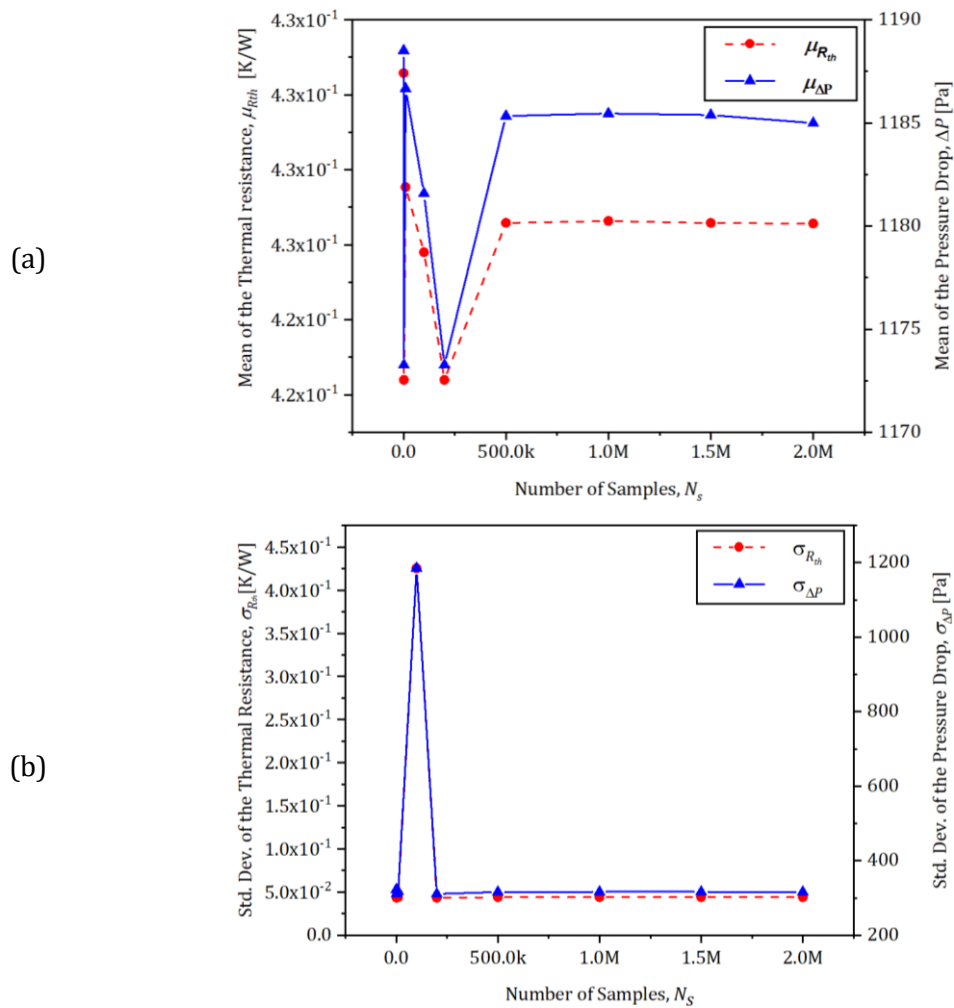


Fig. 6-29 (a) the mean μ and (b) the Std Dev σ of R_{th} and ΔP as a function of the number of samples N_s .

The *MCS* technique has been applied at each points of 45 DoE points, generated in section 6.4.1, to estimate the statistical metrics for R_{th} and ΔP and the results are shown in Fig. 6-30.

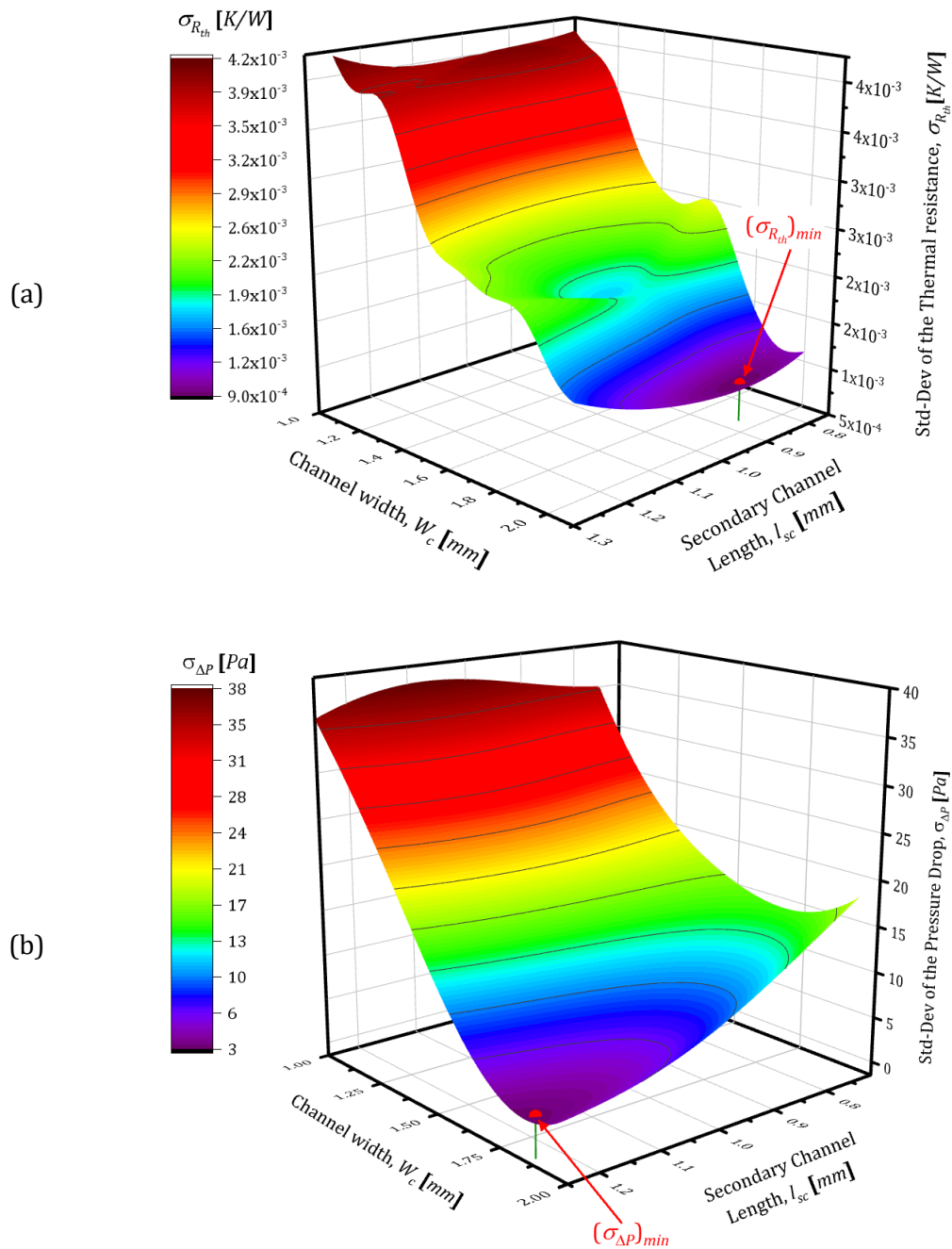


Fig. 6-30 Surrogate models for the Standard deviations as a function of W_c , l_{sc} and θ_{opt} for: (a) the thermal resistance ($\sigma_{R_{th}}$) and (b) the pressure drop ($\sigma_{\Delta P}$).

Single-Objective Optimisation for $\sigma_{R_{th}}$ and $\sigma_{\Delta P}$

Following the same procedure used in section 5.7.2, the single-objective optimisation technique for each of the standard deviation of R_{th} and ΔP as a

function of W_c , l_{sc} , and θ for the *SMCHS – CF* has been conducted. The optimisation problem for each objective function has been formulated as:

$$\textit{Find} \quad l_{sc}, W_c, \textit{ and } \theta \quad \text{Equ. 6-19}$$

$$\textit{To minimise} \quad \sigma_{R_{th}}(l_{sc}, W_c, \theta) \quad \text{Equ. 6-20}$$

$$\textit{To minimise} \quad \sigma_{\Delta P}(l_{sc}, W_c, \theta) \quad \text{Equ. 6-21}$$

The above optimisation problems were subjected to:

$$1.0 \leq W_c \leq 2.0 \quad \text{Equ. 6-22}$$

$$0.75 \leq l_{sc} \leq 1.25 \quad \text{Equ. 6-23}$$

$$20 \leq \theta \leq 45$$

The solutions to these objectives have been obtained using the genetic algorithm (*soga*) included within Dakota software. These solutions are, shown in Fig. 6-30 and summarised in Table 6-4, considered as robust designs. Since the objective functions are functions of three design variables, it is hard to represent the difference between the global optimum design and the robust design graphically, however, it is shown as difference percentage (% diff.) in Table 6-4. It is clear that the robust designs have responses higher than those of the global optimum designs by 8.65% and 12.4% for the R_{th} and ΔP , respectively. It can be noticed that the standard deviation for the global optimum performance, i.e. R_{th} and ΔP , were respectively $8.7 \times 10^{-3} K/W$ and $66.4 Pa$, which are higher than those obtained using *soga*. As the robust design (RD) is obtained at the minimum standard deviation of the responses, it is less sensitive to the variability in input design parameters.

Table 6-10 Surrogate-based single-objective optimisation results for the standard deviations of the R_{th} and ΔP for the *SMCHS – CF* with W_c , l_{sc} and θ as design variables.

<i>soga</i> results		Parameters for the Robust Design					Responses						
							Responses of the Robust Design		of the Global Optimum Design		Standard deviation for the Objective Function		% diff. (\pm)
$\sigma_{R_{th}}$	$\sigma_{\Delta P}$	l_{sc}	W_c	θ	R_{th}	ΔP	R_{th}	ΔP	$\sigma_{R_{th}}$	$\sigma_{\Delta P}$	R_{th}	ΔP	
$9.09 \times 10^{-}$	-----	0.86	1.93	39.6	0.37	-----	0.34	-----	$8.7 \times 10^{-}$	----	8.6	----	
	-	6	8	4	7	-----	7	-----		--	5	-	
-----	2.87	1.23	1.85	42.7	-----	792.2	-----	704.	-----	66.	----	12.	
	2	6	1	7	-	29	-	79	-----	4	-	4	

Multi-Objective Optimisation for $\mu_{R_{th}}$, $\sigma_{R_{th}}$, $\mu_{\Delta P}$ and $\sigma_{\Delta P}$

This section addresses the multi-objective optimisation for the statistical metrics of the *SMCHS – CF* performance, i.e. $\mu_{R_{th}}$, $\sigma_{R_{th}}$, $\mu_{\Delta P}$ and $\sigma_{\Delta P}$. For the statistical parameters of the thermal resistance, the optimisation problem was written as:

$$\text{Find} \quad l_{sc}, W_c, \text{ and } \theta$$

$$\text{To minimise} \quad \{ \mu_{R_{th}}(l_{sc}, W_c, \theta) \text{ and } \sigma_{R_{th}}(l_{sc}, W_c, \theta) \} \quad \text{Equ. 6-24}$$

whereas the optimisation problem for the pressure drop statistical measures was formulated as:

$$\text{To minimise} \quad \{ \mu_{\Delta P}(l_{sc}, W_c, \theta) \text{ and } \sigma_{\Delta P}(l_{sc}, W_c, \theta) \} \quad \text{Equ. 6-25}$$

Both optimisation problems were subjected to:

$$1.0 \leq W_c \leq 2.0 \quad \text{Equ. 6-26}$$

$$0.75 \leq l_{sc} \leq 1.25 \quad \text{Equ. 6-27}$$

$$20 \leq \theta \leq 45 \quad \text{Equ. 6-28}$$

Similar to the previous sections, the optimisation problems have been solved using Dakota toolkit by employing the genetic algorithm (*moga*). The results for the above problems are presented graphically in terms of Pareto front, Fig. 6-31 and Fig. 6-32 and compared against the global deterministic optimum designs, Table 6-11 and

Table 6-12. It is clear from these Pareto fronts that it is impossible to reduce one of the objectives without increasing the other objective. Therefore, the designer can select any point on the Pareto curve, which represent a compromise between the objectives of interest, such as those three points shown in Fig. 6-31 and Fig. 6-32. For the results of the thermal resistance, illustrated in Fig. 6-31 and summarised in Table 6-11, P_1 represents a design with minimum mean, $\mu_{R_{th}} = 0.349 K/W$ but it has high standard deviation, $0.00223 K/W$; in contrast, P_3 has minimum standard deviation of $0.00092 K/W$, with high mean of $0.376 K/W$. The overall thermal resistance at P_1 and P_3 are respectively $0.354 K/W$ and $0.369 K/W$ which are higher than the global optimum thermal resistance, $(R_{th})_{Det.Opt}$, by 2.02% and 6.34%. In spite of the high relative difference for $(R_{th})_{P_3}$ in comparison to $(R_{th})_{Det.Opt}$, it is represents the robust design among the obtained solutions because it has the lowest standard deviation. In the same manner, for the statistical metrics of the pressure drop results depicted in Fig. 6-32 and tabulated in Table 6-12, P_3 considered as the robust design among the generated solutions due to its low standard deviation ($2.923 Pa$) in comparison to other solutions. It is worth to mention here that the relative difference in response criteria of the heat sink has been defined as:

$$E_R = 100 \times \text{abs} \left(\frac{R_i - R_{Det.Opt}}{R_{Det.Opt}} \right) \quad \text{Equ. 6-29}$$

where R_i represent the response at point 1,2 or 3 on Pareto front and $R_{Det.Opt}$ is the optimum response obtained from the deterministic optimisation strategy.

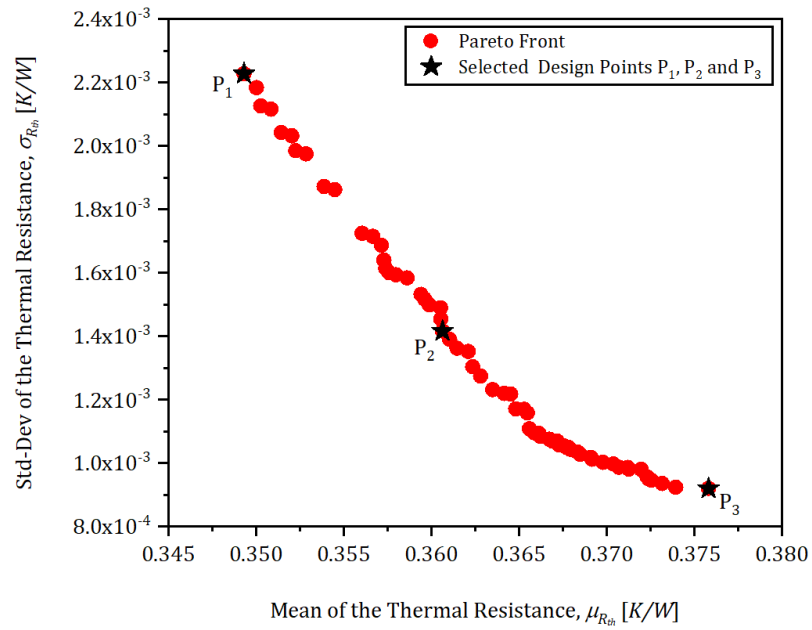


Fig. 6-31 Pareto front for the $\mu_{R_{th}}$ and $\sigma_{R_{th}}$ for the *SMCHS – CF*.

Table 6-11 Comparison between the single-objective deterministic global optimum design with the three selected point from the Pareto front results for thermal resistance of the *SMCHS – CF*.

Points	Design Variables			Surrogate model			$E_{R_{th}}$ (%)
	l_{sc} [mm]	W_c [mm]	θ [deg]	$\mu_{R_{th}}$ [K/W]	$\sigma_{R_{th}}$ [K/W]	R_{th} [K/W]	
Det. Opt.	0.751	1.999	20.04	-----	8.70 e^{-3}	0.347	-----
P ₁	0.780	1.997	20.07	0.349	2.23 e^{-3}	0.354	2.02
P ₂	0.771	1.997	30.07	0.361	1.42 e^{-3}	0.357	2.88
P ₃	0.889	1.959	39.14	0.376	9.20 e^{-4}	0.369	6.34

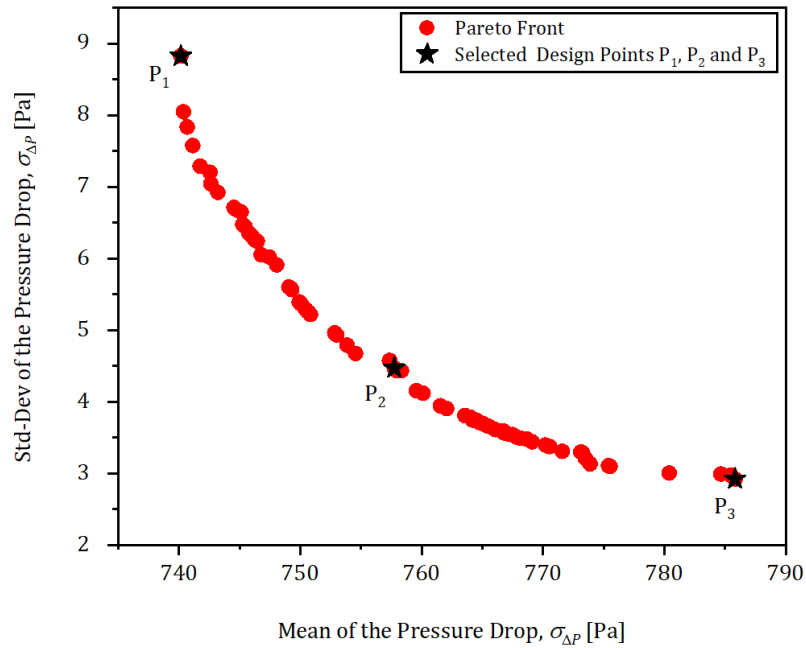


Fig. 6-32 Pareto front for $\mu_{\Delta P}$ and $\sigma_{\Delta P}$ for the *SMCHS – CF*.

Table 6-12 Comparison between the single-objective deterministic global optimum design with the three selected point from the Pareto front results for pressure drop of the *SMCHS – CF*.

Points	Design Variables			Surrogate model			$E_{\Delta P}$ (%)
	l_{sc} [mm]	W_c [mm]	θ [deg]	$\mu_{\Delta P}$ [Pa]	$\sigma_{\Delta P}$ [Pa]	ΔP [Pa]	
Det. Opt.	1.217	1.902	34.75	-----	66.4	704.79	-----
P ₁	1.086	1.999	40.9	740.169	8.826	772.425	9.59
P ₂	1.153	1.931	42.1	757.753	4.472	921.663	30.77
P ₃	1.234	1.851	42.5	785.834	2.923	1089.482	54.58

In the rest of this section, the optimisation problem has been defined in a different way to include the four statistical parameters for the two responses of interest (R_{th} and ΔP) and solve it. The formulation of the optimisation problem was defined as:

Find $l_{sc}, W_c, \text{ and } \theta$

To minimise $f_{R_{th}}$ and $f_{\Delta P}$ Equ. 6-30

where $f_{R_{th}} = \frac{\mu_{R_{th}}}{(\mu_{R_{th}})_{opt.}} + \frac{\sigma_{R_{th}}}{(\sigma_{R_{th}})_{opt.}}$ & $f_{\Delta P} = \frac{\mu_{\Delta P}}{(\mu_{\Delta P})_{opt.}} + \frac{\sigma_{\Delta P}}{(\sigma_{\Delta P})_{opt.}}$

$$\text{Subjected to} \quad 1.0 \leq W_c \leq 2.0 \quad \text{Equ. 6-31}$$

$$0.75 \leq l_{sc} \leq 1.25 \quad \text{Equ. 6-32}$$

$$20 \leq \theta \leq 45 \quad \text{Equ. 6-33}$$

Fig. 6-33 shows the results for $f_{\Delta P}$ and $f_{R_{th}}$, which are obtained using the genetic algorithm (*moga*) provided by Dakota software. Three points at different locations on Pareto front have been selected to compare the corresponding thermal resistance and pressure drop for these points against those generated using multi-objective deterministic optimisation, section 6.4.2. A summary of this comparison is presented in Table 6-13. In this table, $(P_1)_{Det.Opt.}$ represents the deterministic optimum design in terms of thermal resistance, whereas $(P_5)_{Det.Opt.}$ is the design with minimum pressure drop. On the other hand, P_1 represents the robust optimum design with minimum mean and standard deviation for the thermal resistance, whereas P_3 represents the robust optimum design with minimum mean and standard deviation for the pressure drop. Accordingly, the relative differences of the responses (E_R) have been calculated for P_1 with respect to $(P_1)_{Det.Opt.}$ and for P_3 with respect to $(P_5)_{Det.Opt.}$. For P_1 and P_3 , the results show that the relative difference $E_{R_{th}}$ are 8.2% and 2.1% and those for $E_{\Delta P}$ are 43.3% and 5.2%, respectively.

Depending upon the above results, the designer could select the design that satisfied the design requirements. For instance, if the designer is looking for a design with minimum mean and standard deviation for the R_{th} , P_1 will be recommended. In contrast, if the minimum mean and standard deviation of the ΔP is the required, then P_3 will be the right selection. Besides, any design between these two will represent a compromise between them.

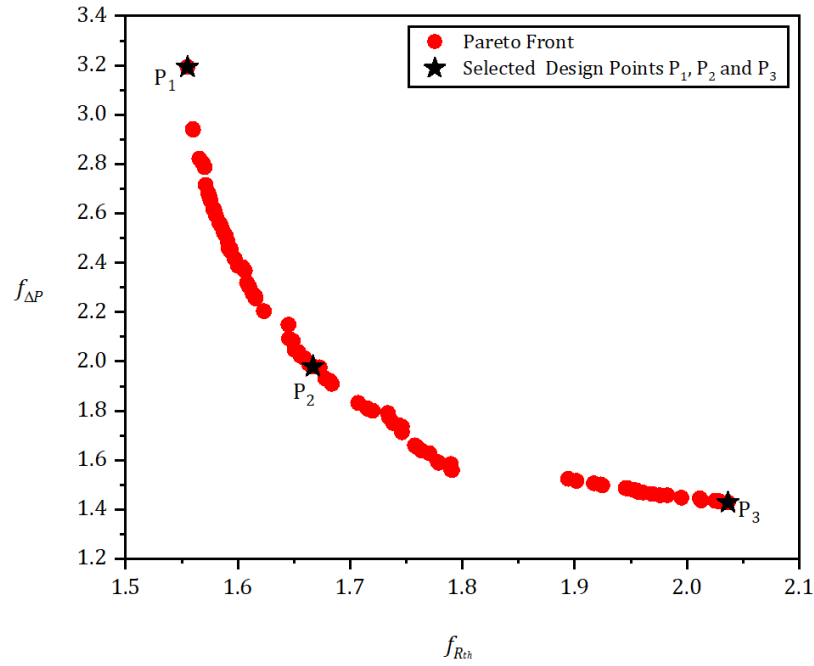


Fig. 6-33. Pareto front for $f_{\Delta P}$ and $f_{R_{th}}$ of the *SMCHS – CF*.

Table 6-13 Comparison between the multi-objective deterministic optimum designs with their corresponding designs from the Pareto front results for $f_{\Delta P}$ and $f_{R_{th}}$ of the *S – CF*.

Points	Design Variables			Surrogate model					
	l_{sc} [mm]	W_c [mm]	θ [deg]	$f_{R_{th}}$	$f_{\Delta P}$	R_{th} [K/W]	ΔP [Pa]	$E_{R_{th}}$ (%)	$E_{\Delta P}$ (%)
$(P_1)_{Det.Opt.}$	0.816	1.960	20.29	----	----	0.354	1314.52	-----	-----
P_1	1.086	1.999	40.9	1.555	3.193	0.383	745.56	8.2	43.3
$(P_5)_{Det.Opt.}$	1.217	1.902	34.75	-----	----	0.389	706.78	-----	-----
P_3	1.234	1.851	42.5	2.036	1.429	0.397	743.67	2.1	5.2
P_2	1.153	1.931	42.1	1.667	1.980	0.389	743.16		

$(P_i)_{Det.Opt.}$: from Deterministic Optimisation, Table 6-7.

6.5 Chapter Summary

In this chapter has explored the effect of the number of fins (F_n), the fin offset (F_o), the impact of the fin's secondary channel lengths ratio ($R_{FS} = \frac{F_L}{l_{sc}}$) on the thermal resistance (R_{th}) and pressure drop (ΔP) of the microchannel heat sink with chevron fins *SMCHS – CF*.

The study shows that the pressure drop and thermal resistance are affected not only by the number of fins but also by the secondary channel length (l_{sc}). For example, the pressure drop for the *SMCHS – CF* could be reduced, relative to the *SMCHS – PF*, by 28.12% by increasing F_n from 6 to 18 for $l_{sc} = 0.25 \text{ mm}$ but this reduction does not exceed 9.73% for $l_{sc} = 1.0 \text{ mm}$ for the same range of F_n .

In comparison with the thermal resistance of the *SMCHS – PF*, the reduction in thermal performance of the *SMCHS – CF* reaches upto 12% for $l_{sc} = 0.25 \text{ mm}$ with 18 fins whereas it is just around 5% for $l_{sc} = 1.0 \text{ mm}$ with 10 fins.

Regarding the fins arrangement, the results showed that the pressure drop could be reduced by 2.31% through setting the $F_o = 2 \text{ mm}$ for $Re = 500$, whereas it raised by 3.2% via fixing the $F_o = 0.5 \text{ mm}$ for $Re = 2000$. The effect of F_o on R_{th} was slight where it increased by less than 1.19% in the examined range.

Furthermore, the effect of the length ratio R_{FS} on the hydrothermal performance of the *SMCHS – CF* has also been investigated. The findings revealed that increasing the R_{FS} leads to a decrease and then to an increase in thermal resistance, R_{th} . Overall, there was an acceptable improvement, and the maximum reduction was about 7.3% for the case of $R_{FS} = 3$. The results are also indicated that lowering the R_{FS} ratio from 3 to 1 has led to an improvement in the pressure drop by 14%.

In the final section of this chapter, deterministic and probabilistic optimisation have been carried out. Furthermore, a comparison between these two optimisation strategy results has been made to show the effect of uncertainty associated geometrical parameters on optimum design. The study revealed that including the uncertainty of design variables produced designs that differ from that generated by deterministic optimisation, and they are considered robust designs.

Chapter 7 Serpentine Minichannel Heat Sink with Hybrid Elliptical-Rectangular Fins

7.1 Introduction

As shown in the literature review section 2.6.1, Reddy *et al.* (2017) used pin-fins with cross-sectional shapes of circles, symmetric airfoils, and symmetric convex lenses to reduce the pressure drop for the circulated water within the heat sink utilised to cool high heat flux electronics. Here, a hybrid elliptical-rectangular fin shape has been proposed to replace the chevron fins for the serpentine minichannel heat sink suggested by Al-Neama (2018), Fig. 6-1. This chapter is devoted to investigating this new design. In section 7.2, the definitions of the problems, the CFD simulation setup, mesh independency and validation are given. Followed by presenting the influence and the benefits of introducing the hybrid fins to the serpentine minichannel heat sink in sections 7.3 and 7.4. The influence of the hybrid fin parameters on the hydro-thermal performance of the considered heat sink is given in section 7.5. After that, the deterministic optimisation is conducted and presented in section 7.6. Finally, the chapter is concluded with a summary in section 7.7.

7.2 CFD Analysis of the *SMCHSs* with Hybrid Elliptical-Rectangular Fins

7.2.1 CFD Modelling

A minichannels heat sink equipped with hybrid elliptical-rectangular fins (*SMCHS – EF*), Fig. 6-1, has been investigated in this study. As in the previous chapters, the outer dimensions of the copper heat sink for the current CFD model were $38\text{ mm} \times 38\text{ mm} \times 4\text{ mm}$, while the applied heat flux was $31\text{ [W/cm}^2\text{]}$. The cooling fluid was water and flow was assumed to be single-phase laminar flow with Reynolds number at the entrance of less than 2250 and a temperature of 20°C . All other relevant dimensions, illustrated in Fig. 6-1(c), are given in Table 7-1.

Parameter	Value	Parameter	Value
width of the channel, W_c (mm)	1.5	Number of the small fins per row, F_n	9
Height of the channel, H_c (mm)	2	Secondary channel length, l_{sc} (mm)	0.9
Height of the substrate, H_b (mm)	2	Length of the elliptical fin, F_l (mm)	1.6
Number of the main channel, C_n	12	Fin pitch, F_p (mm)	2.5
Distance from the edge, W_{s1} & W_{s2} (mm)	4.5 & 5.5	width of the fin, W_e (mm)	1
The outer and inner radiuses of the main channel, R_o & R_i (mm)	2 & 0.5	Semi-major axis, R_f (mm)	0.5

7.2.2 Mesh Independency and Validation

Mesh dependency and validation tests have been performed to establish the numerical results' accuracy and the associated computational costs. The default meshing's tools available within *COMSOL* Multiphysics® Modelling Software were utilised to divide the computational domain of the heat sink under consideration, described in section 6.2.1, into small elements as shown in Fig. 6-2. The CFD simulations for mesh exploration have been run with $Re = 1000$ and a temperature of 20°C at the inlet and heat flux of 30 W/cm^2 . The results are presented in Table 7-2.

It is clear, from Table 7-2, that the increase in mesh density reduces the relative difference in the results for the tested performance criteria which is calculated based on the finest mesh. For example, the relative difference in R_{th} and ΔP fall, respectively, varies from 1.85% and 5.10% to 0.19% and 0.56% by increasing the number of elements from 1.565×10^6 to 6.5757×10^6 . However, this makes the numerical simulations more expensive in terms of the time and computational resources, as shown in the table. As a compromise between the required time and resources to achieve convergence on one hand and the adequate accuracy of the results on the other hand, the mesh setting with 3.03×10^6 elements, Mesh-04 in Table 7-2, has been selected to perform the CFD simulation in this chapter. The validation of the numerical approach against the work of Al-Neama (2018) has been

performed in the previous chapter as shown in section 6.2.2, Fig. 6-3. The rest of this chapter will be devoted to original investigations.

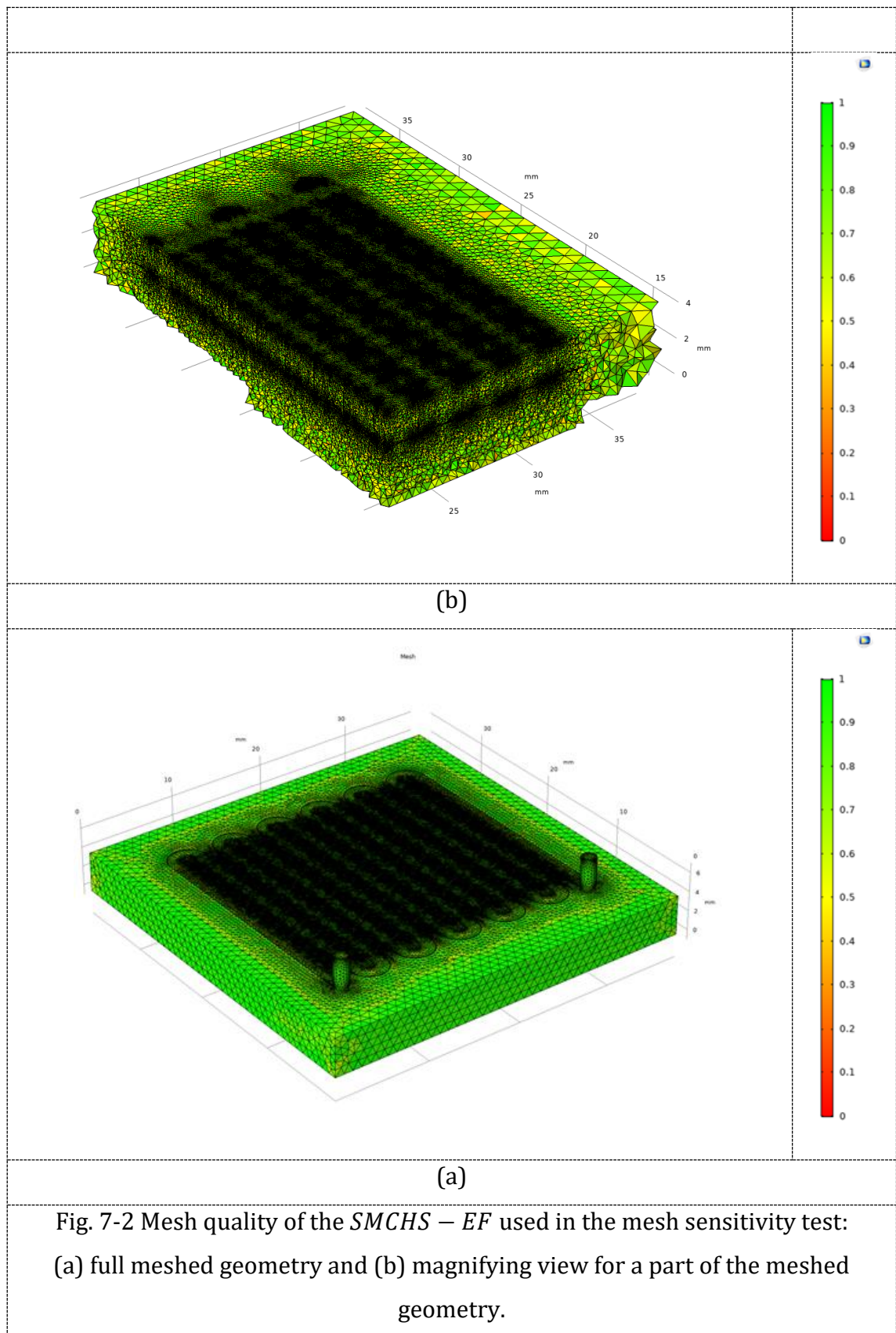


Table 7-2 Results of the mesh independency study.

No	Mesh Resolution	NOE x 10 ⁶	AEQ	time (H: min)	Ph.M. (GB)	DOF x 10 ⁶	R_{th} [K/W]	% E	ΔP [Pa]	% E
1	Mesh-01	1.565	0.6382	00:26	10.69	1.593	0.4127	1.85	835.92	5.10
2	Mesh-02	2.095	0.6496	00:42	12.68	1.991	0.4156	1.17	843.01	4.29
3	Mesh-03	2.691	0.6519	00:43	12.92	2.095	0.4163	1.00	858.29	2.56
4	Mesh-04	3.039	0.655	00: 48	13.66	2.153	0.4189	0.38	863.82	1.93
5	Mesh-05	6.576	0.6576	02:29	27.71	4.691	0.4197	0.19	875.85	0.56
6	Mesh-06	8.693	0.6572	03:09	34.31	5.993	0.4205	-----	880.82	-----

7.3 Influence of Introducing Hybrid Elliptical-Rectangular Fins in *SMCHSs*

In this section, the performance of the heat sink with hybrid elliptical-rectangular fins and secondary channels is compared against the smooth serpentine heat sink. The numerical predictions for the performance criteria were acquired with an inlet temperature of 20°C and a heat flux of $31\text{W}/\text{cm}^2$ imposed over a part of the heat sink base. Furthermore, the fluid flow was single-phase laminar flow with Reynolds number at the inlet ranging from 500 to 2250. Fig. 7-3 shows the change in R_{th} and ΔP with the Reynolds number for the compared designs.

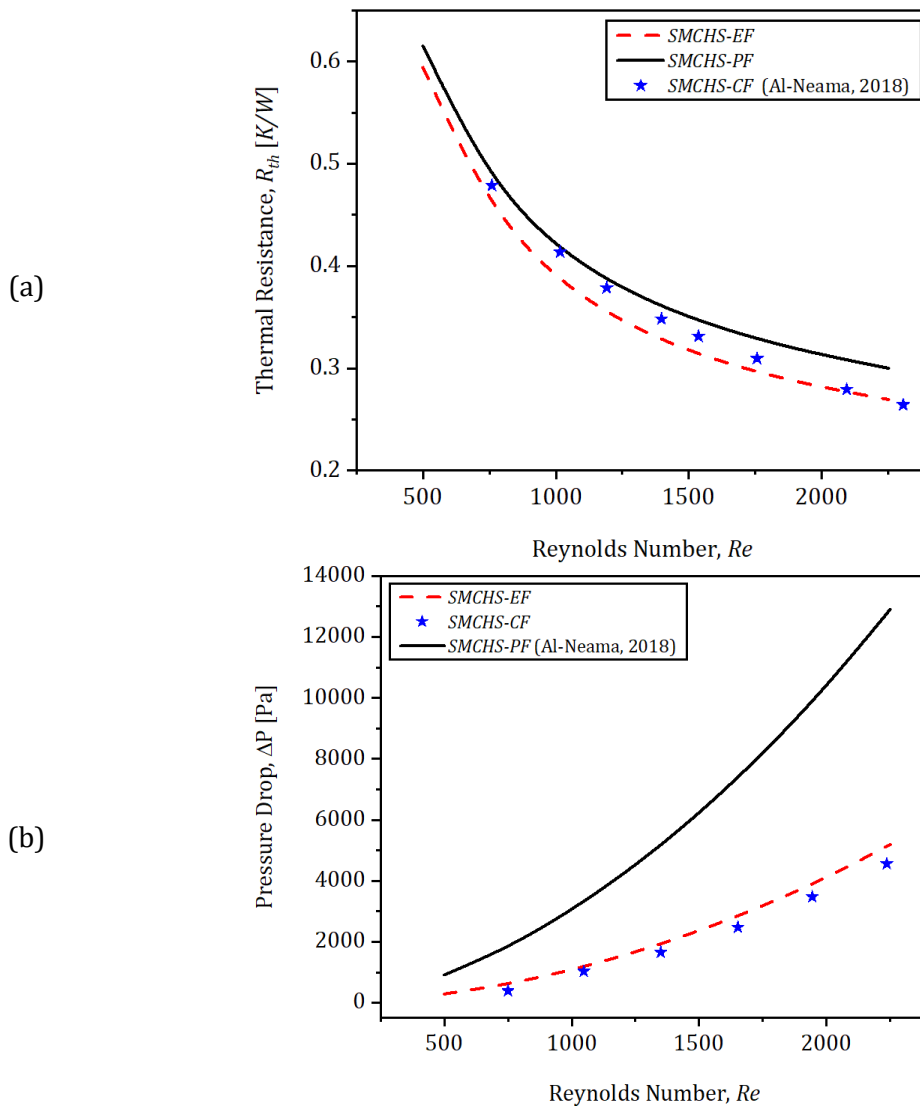


Fig. 7-3 Comparison between the serpentine minichannel heat sink with plate fin, *SMCHS – PF*, (Al-Neama, 2018) and the one with hybrid elliptical-rectangular fins, *SMCHS – EF*: (a) R_{th} and (b) ΔP .

It is obvious that increasing Re leads to a decrease in the overall thermal resistance while increasing the pressure drop penalty for the liquid-cooled heat sinks, which is consistent with results in the previous chapters of this thesis. The Figure also shows that the presence of the secondary microchannels improves the performance of the $SMCHS - EF$ in comparison to that of the $CHS - PF$. For example, the penalty of the pressure drop at $Re = 2250$ reduced from $12906 Pa$ for $SMCHS - PF$ to $5189.9 Pa$ for $SMCHS - EF$, i.e. 59.8%. Similarly, the thermal resistance reduced from $0.300 K/W$ for $SMCHS - PF$ to $0.267 K/W$ for $SMCHS - PF$, i.e. 10%; at the same Reynolds number. Furthermore, it can be noticed that the proposed design, $SMCHS - EF$, has a comparable performance to that of the $SMCHS - CF$ if not better in some cases.

7.4 The Benefit of using Hybrid Elliptical-Rectangular Shape Fins with $SMCHSs$

The thermal-hydraulic performance criterion (PEC), introduced in chapter 5, has also been used to assess the usefulness of employing the hybrid elliptical-rectangular fins with the serpentine minichannel heat sink. The effective heat transfer area for $SMCHS - EF$ design can be calculated using the following equation:

$$D1 = \left(l_{sc} \cdot W_e - \pi \cdot \frac{L_e}{2} \cdot \frac{W_e}{2} \right) (F_n + 1)(N_c - 1)$$

$$A_{base_{SMCHS-EF}} = A_{base_{SMCHS-PF}} + D1$$

$$D2 = 2 (L_c + R_o - R_{inlet}) H_c$$

$$D3 = 2 (2 W_w + 0.5 S_{ellipse}) H_c \cdot (N_c - 1)$$

$$h = \left(\left(\frac{L_e}{2} \right) - \left(\frac{W_e}{2} \right) \right)^2 / \left(\left(\frac{L_e}{2} \right) + \left(\frac{W_e}{2} \right) \right)^2$$

$$S_{ellipse} = \pi \left(\frac{L_e}{2} + \frac{W_e}{2} \right) \left(1 + \frac{h}{2^2} + \frac{h^2}{2^6} + \dots + \frac{h^3}{2^8} + \frac{25h^4}{2^{14}} + \frac{49h^5}{2^{16}} \right)$$

(Chandrupatla & Osler, 2010)

$$D4 = (2 F_l + S_{ellipse}) H_c \cdot F_n \cdot (N_c - 1)$$

$$A_{fin_{SMCHS-EF}} = C5 + C6 + D2 + D3 + D4$$

$$A_{e_{SMCHS-EF}} = \eta_f A_{fin_{SMCHS-EF}} + A_{base_{SMCHS-EF}}$$

Equ. 7-1

Based on the above equations and the numerical results obtained from the CFD simulations, the results are presented in terms of the average Nusselt number (\overline{Nu}) and the thermal-hydraulic performance criterion (PEC), Fig. 7-4.

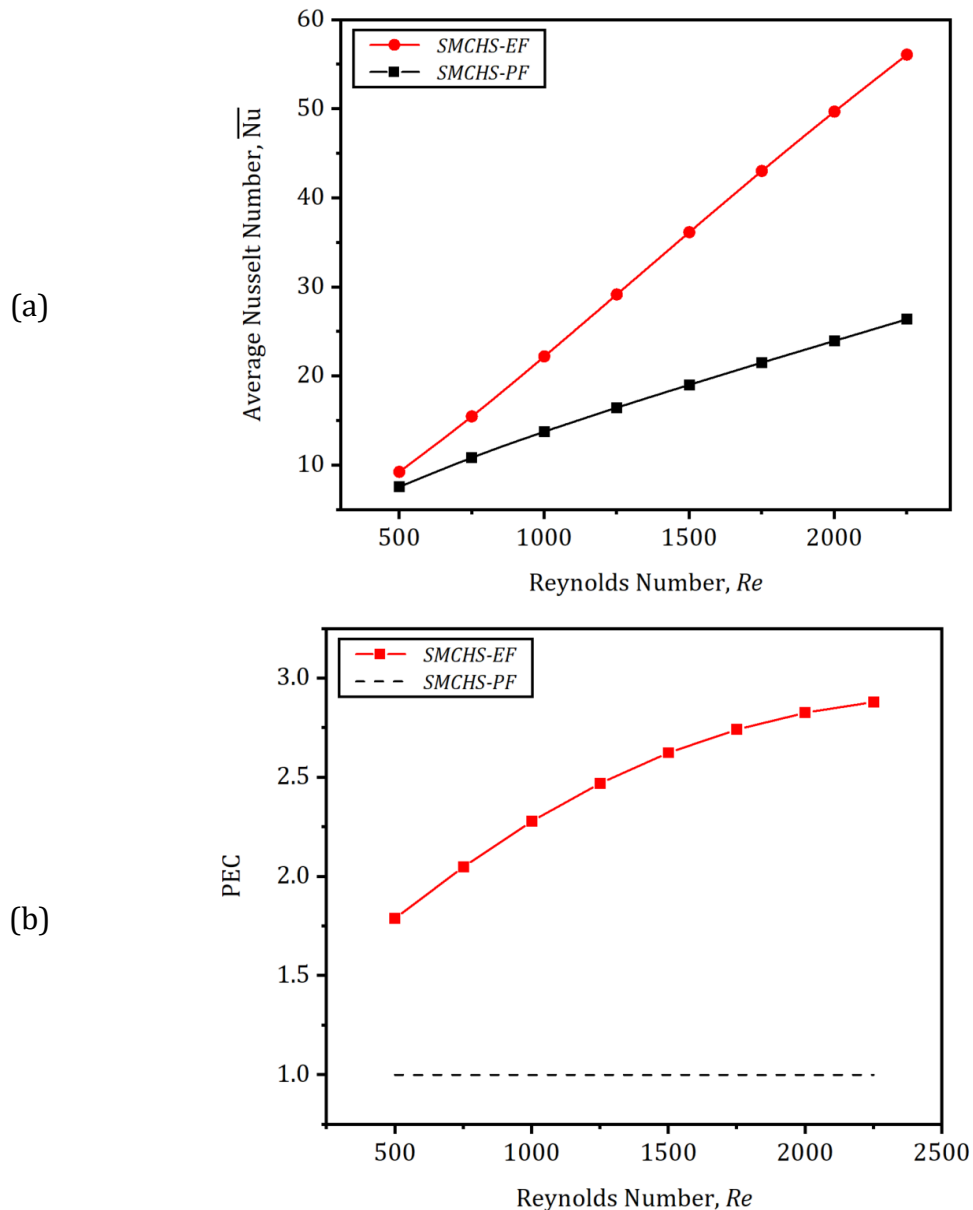


Fig. 7-4 Comparison between *SMCHS – PF* (Al-Neama , 2018) and *SMCHS – EF*:
 (a) R_{th} and (b) ΔP .

It is clear that there is a remarkable increase in heat transfer for the *SMCHS – EF* compared to that for the *SMCHS – PF* which can reach up to 53% for $Re = 2250$, Fig. 7-4 (a). Besides, as shown in Fig. 7-4 (b), the PEC has values ranging from 1.79 to 2.88 for Re from 500 to 2250, respectively. These values are all positive and greater than 1 which indicates that introducing the hybrid elliptical-rectangular fins

has a positive influence on enhancing the thermal-hydraulic performance of the studied heat sink.

7.5 Characteristics of Fluid Flow and Heat Transfer

7.5.1 Effect of the semi-minor axis (R_f) of the hybrid fin

The dependency of the overall thermal resistance (R_{th}) and pressure drop penalty (ΔP) on Reynolds number (Re) for the *SMCHS – EF* are presented in this subsection. The examined semi-minor axis (R_f) was in the range from 0.2 mm to 0.5 mm but the presented results was just for $R_f = 0.2, 0.35$ and 0.5 m, and the geometrical shape for these fins are shown in Fig. 7-5. Besides, the coolant water was entering at temperature 20°C while the heat flux applied underneath the heat sink was 31 W/cm^2 . Moreover, the number of fins (F_n) was 9 and the fin length to the secondary channel length (R_{FS}) was 10.

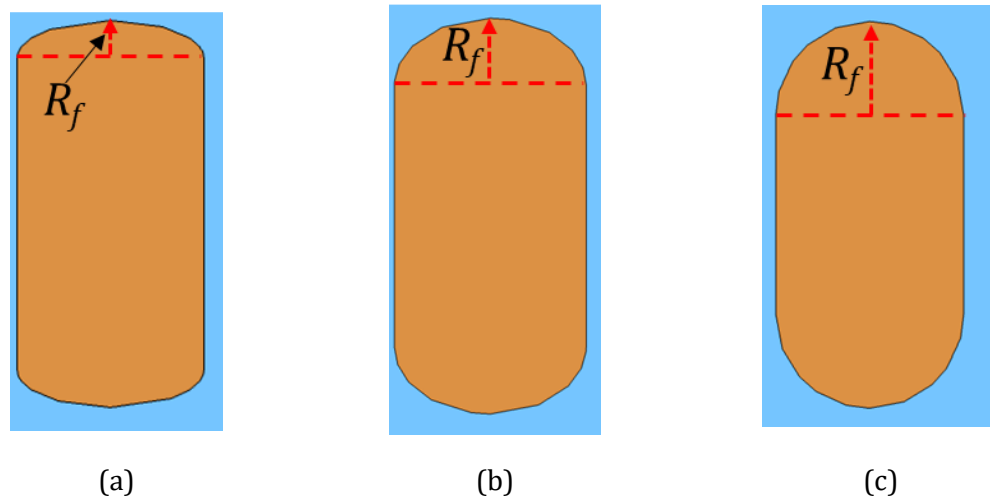


Fig. 7-5 Selected fins used with the *SMCHS – EF* showing the difference in fin tips for: (a) $R_f = 0.2 \text{ mm}$, (b) $R_f = 0.35 \text{ mm}$ and (c) $R_f = 0.5 \text{ mm}$.

As expected, the increase in Re leads to a decrease in R_{th} and an increase in ΔP . Inspecting Fig. 7-6 (a) shows that the effect of R_f on R_{th} was insignificant, and the minimum R_{th} can be obtained with $R_f = 0.5 \text{ mm}$ at $Re = 2250$ which differs from that of $R_f = 0.2 \text{ mm}$ just by 1.1%. This can be attributed to the slight change in convective thermal resistance R_{conv} where it falls from 0.245 K/W at $R_f = 0.2 \text{ mm}$ to 0.242 K/W at $R_f = 0.5 \text{ mm}$. Similarly, the effect of R_f on pressure drop,

Fig. 7-6(b), was also limited and the $R_f = 0.35 \text{ mm}$ offered the best performance in terms of the pressure drop (4.7% less) in comparison to the other investigated values of R_f . This could be imputed to the aerodynamic shape of the fin tip at this value of R_f , Fig. 7-5. It can be concluded that within the studied ranges in the current work, R_f makes very little difference to the performance criteria.

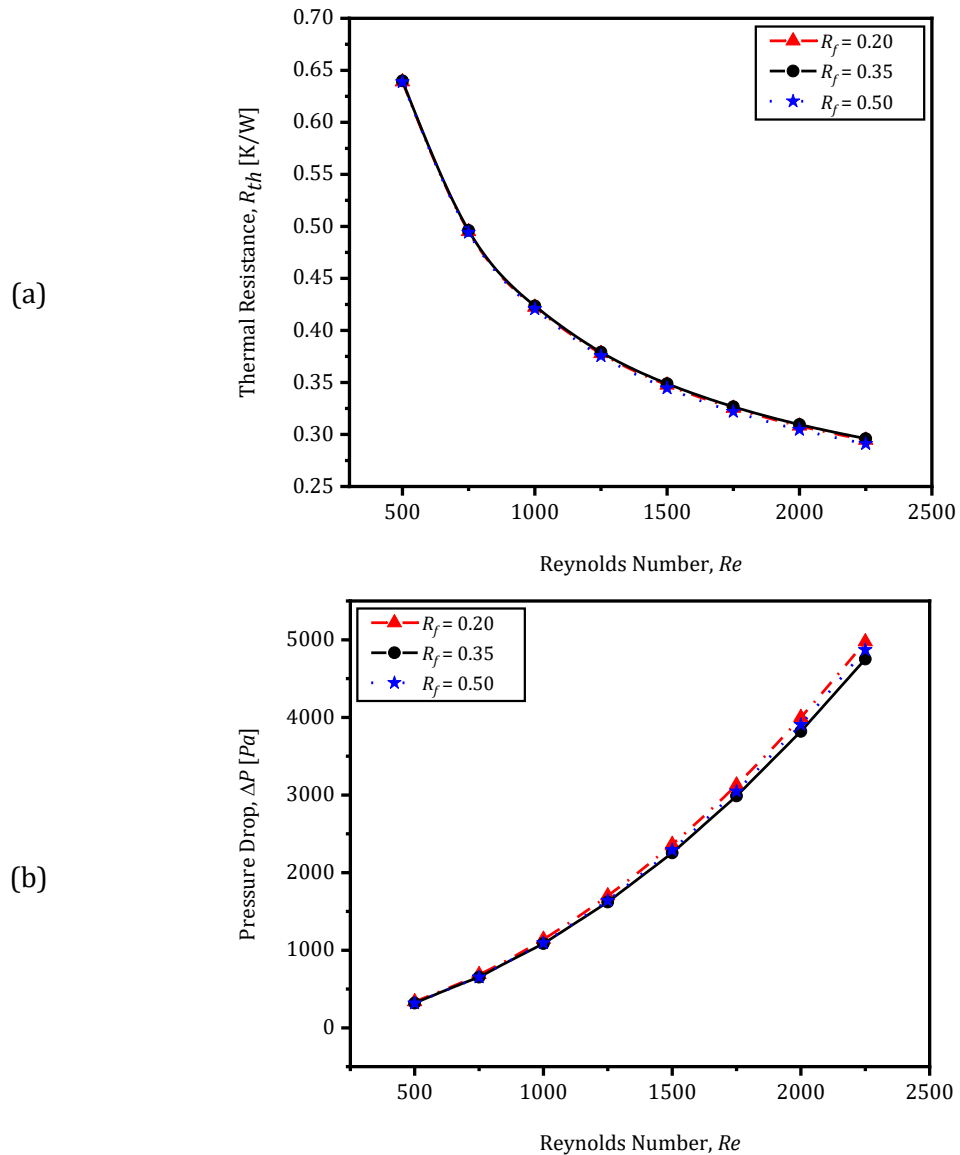


Fig. 7-6 The relationship between (a) R_{th} and (b) ΔP , and the Reynolds number (Re) for different values of the semi-minor axis, R_f , for the *SMCHS – EF*.

7.5.2 Effect of Number of Fins (F_n)

The impact of the number of fins (F_n), Fig. 7-7, on the *SMCHS – EF* performance is now discussed. The numerical simulations for this study have been implemented for the number of fins ranging from 7 to 13, Reynolds number covered a range $500 \leq Re \leq 2250$, the heat flux was 31 W/cm^2 , and the fluid inlet temperature was 20°C . In addition, the fin length to the secondary channel length (R_{FS}) was 10, and the semi-minor axis (R_f) was 0.3 mm .

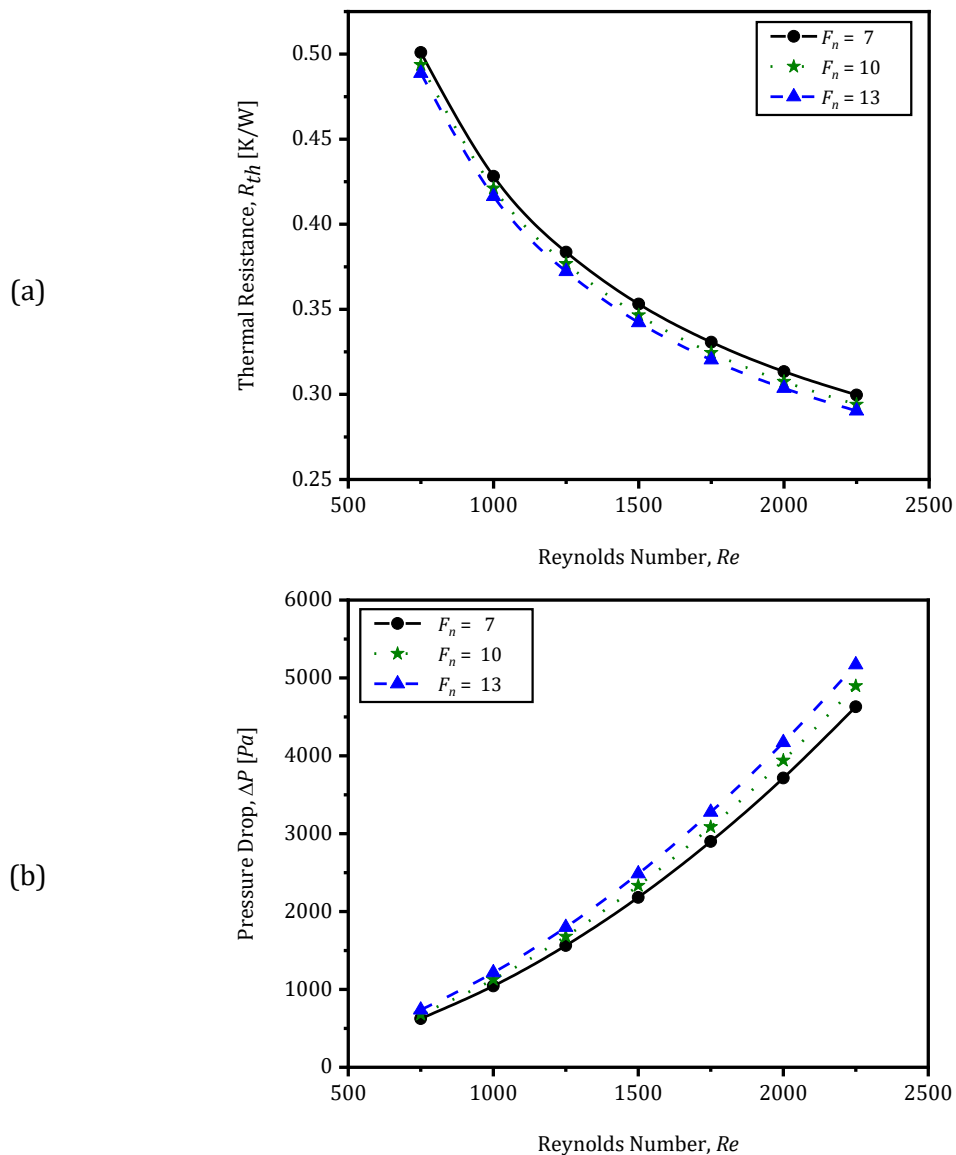


Fig. 7-7 Effect of Re and F_n on: (a) R_{th} and (b) ΔP for the *SMCHS – EF*.

Fig. 7-7 (a) shows the relationship between the thermal resistance (R_{th}) and Reynolds number (Re) for $F_n = 7, 10$ and 13 . It is clear that R_{th} decreases with

increasing Re , which is consistent with the fundamentals of heat transfer. It also decreases with increasing the number of fins due to breaking the boundary layers and enhancing the mixing of the fluid, which enhances the heat transfer. However, this increase due to the number of fins was small and not exceed 3% for $F_n = 13$ at $Re = 2250$ whereas it was 2% for $F_n = 10$ at the same Reynolds number.

On the other hand, Fig. 7-7 (b) shows the influence of Reynolds number on pressure drop for a different number of fins and, as expected, the pressure losses increase with increasing Reynolds number. Also, the study shows that the pressure penalty increases when the number of fins increases, and this could be ascribed to the shortening the length of the secondary channels which resist the fluid flow through them. For example, the pressure drop increased from 4629.9 Pa at $F_n = 7$ to 5169.4 Pa for $F_n = 13$, i.e. an increase of 12%.

7.5.3 Effect of Fin Length to Secondary Channel Length Ratio (R_{FS})

Besides the effect of the above parameters on the performance of $SMCHS - EF$, the ratio of the fin length to the secondary channel length (R_{FS}) was also studied. For this task, the other geometrical variables such as the number of fins (F_n) and semi-minor axis (R_f) have been kept constant with values of 8 and 0.4 mm , respectively. The fluid inlet temperature was set to be 21 °C, and the heat flux applied at the heat sink base was 31 W/cm^2 . Fig. 7-8 shows the influence of R_{FS} on the overall thermal resistance (R_{th}) and pressure drop penalty (ΔP) for different values of Reynolds number (Re).

As shown in Fig. 7-8 (a), for a given Re , it can be noticed that the thermal resistance is decreased with increasing the R_{FS} from 3 to 13. For $Re = 2000$, for instance, the thermal resistance decreases from 0.330 K/W for $R_{FS} = 3$ to 0.306 K/W for $R_{FS} = 13$, i.e. 7.27%. One of the reasons behind this behaviour could be the increase in the effective heat transfer area A_e which is increased from 1917.4 mm^2 to 2053.3 mm^2 by changing R_{FS} from 3 to 13. This increase in A_e leads to a decrease in the convective thermal resistance components, R_{conv} .

Fig. 7-8 (b), on the other hand, shows the impact of R_{FS} on pressure drop (ΔP) for $Re = 1000, 1500$ and 2000. It is evident that increasing the R_{FS} ratio leads to an increase in pressure losses, and the effect becomes more pronounced by increasing the Reynolds number. The results recorded, for example, an increase in ΔP from

2878.1 Pa to 4226 Pa, 46.83%, by increasing R_{FS} from 3 to 13 for $Re = 2000$. This could be attributed to the fact that increasing R_{FS} leads to decreasing secondary channel length, Fig. 7-9, which restricts the amount of flow that passes through the secondary channels and increase the pressure losses.

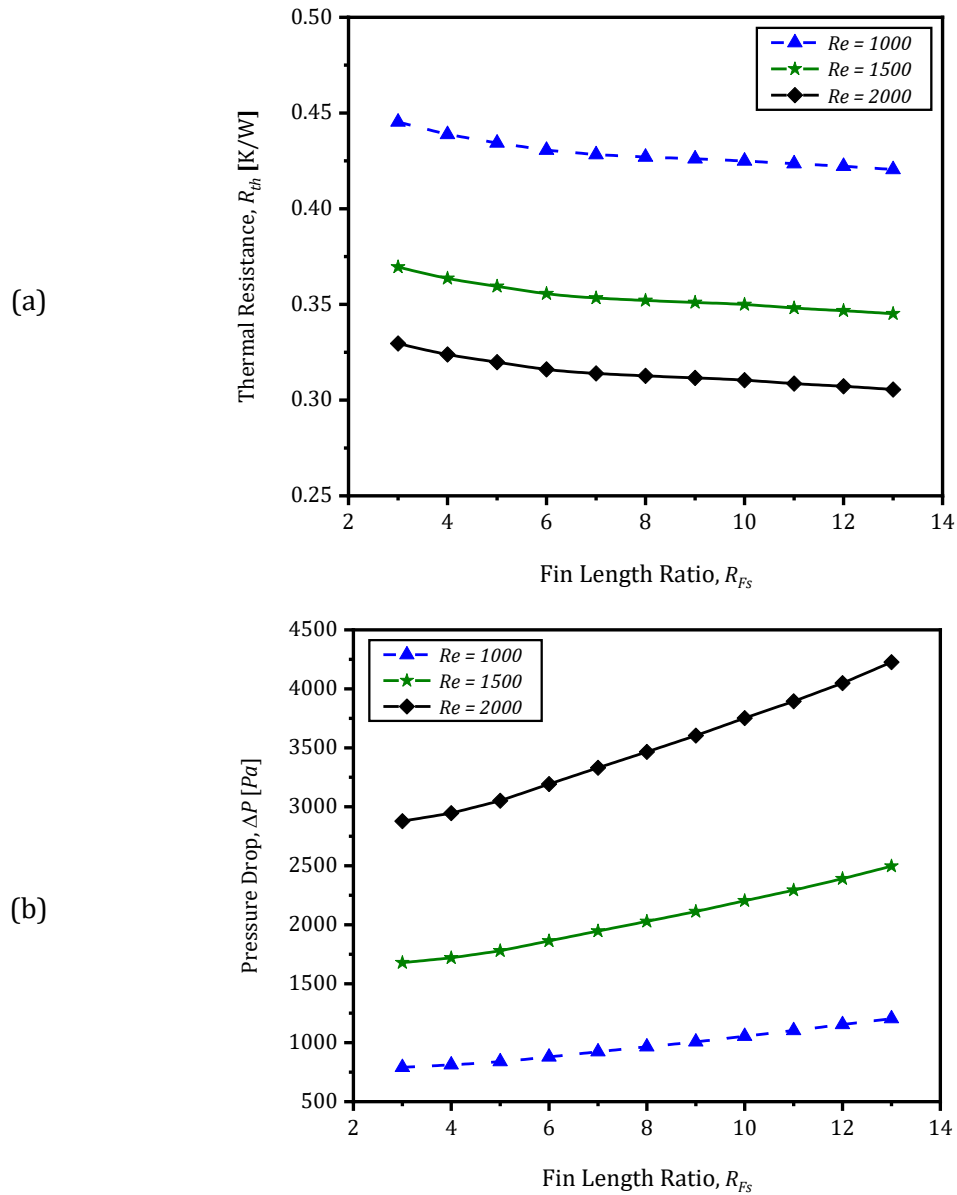


Fig. 7-8 The effect of fin length ratio (R_{FS}) on: (a) the overall thermal resistance, R_{th} and (b) pressure drop, ΔP at different values of Re for the SMCHS – EF.

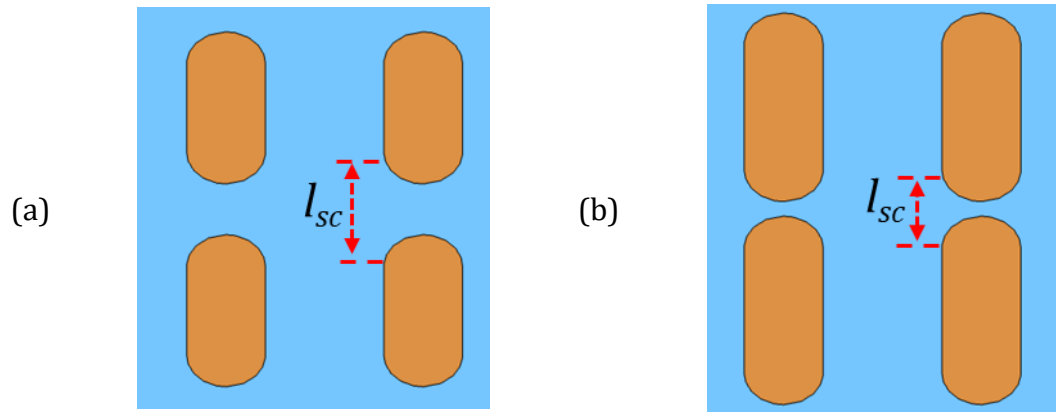


Fig. 7-9 Comparison between designs with different R_{FS} showing the secondary channel length (l_{sc}) for: (a) $R_{FS} = 3$ and (b) $R_{FS} = 13$.

7.6 Deterministic Optimisation for the *SMCHS – EF*

This part of the chapter carries out the single- and multi-objective deterministic optimisation for the serpentine heat sink with the hybrid elliptical-rectangular fin (*SMCHS – EF*). The optimisation process has considered the number of fins F_n , the Fin Length ratio R_{FS} , the fin offset F_o and the semi-minor axis (R_f) as design variables. The details will be presented in the following subsections.

7.6.1 Single-Objective Optimisation

The single-objective optimisation to minimise the thermal resistance and pressure drop of the *SMCHS – EF* has been implemented separately according to the following definitions.

<i>Find</i>	F_o, F_n, R_f and R_{FS}	
For the thermal resistance		
<i>To minimise</i>	$R_{th}(F_o, F_n, R_f, R_{FS})$	Equ. 7-2

For the pressure drop		
<i>To minimise</i>	$\Delta P(F_o, F_n, R_f, R_{FS})$	Equ. 7-3

The above optimisation problems were subjected to

$$0 \leq F_o \leq 2.0 \quad \text{Equ. 7-4}$$

$$7 \leq F_n \leq 13 \quad \text{Equ. 7-5}$$

$$0.2 \leq R_f \leq 0.4 \quad \text{Equ. 7-6}$$

$$3 \leq R_{FS} \leq 17 \quad \text{Equ. 7-7}$$

As surrogate modelling-based optimisation is used, the Latin-hypercube sampling technique has been utilised to extract an evenly distributed sample over the design space. Since four design variables have been considered for the current investigation, 92 sample points have been generated to represent the design space. For ease of visualisation, the samples are presented in two different 3D scatter plots, as shown in Fig. 7-10. The generated sample points, then, were used in the CFD simulation to obtain the corresponding responses of interest, which were all employed to construct the surrogate models for each response, Fig. 7-11 to Fig. 7-14. The type of the built surrogate model was the Gaussian process approximation, and their quality was measured using the cross-validation method. As presented in Table 7-3, the comparison between the responses evaluated by the approximation surrogate models and those predicted using the CFD simulations shows a good agreement with a difference less than 3.11% which validates these generated surrogate models.

Table 7-3 Comparison of the responses evaluated by the CFD simulation and the approximation surrogate model for cross-validation.

Point	Design Variables				Surrogate Model		CFD-Predictions		% diff. (\pm)	
	R_f	R_{FS}	F_o	F_n	R_{th} [K/W]	ΔP [Pa]	R_{th} [K/W]	ΔP [Pa]	R_{th} (%)	ΔP (%)
1	0.31	12.31	0.8	13	0.310	3955.963	0.312	4020.445	0.71	1.60
2	0.19	14.54	1.9	10	0.308	4540.742	0.311	4593.869	1.11	1.16
3	0.29	9.61	0.3	5	0.316	3436.191	0.323	3529.655	2.10	2.65
4	0.44	4.87	1.2	11	0.315	2382.578	0.319	2459.059	1.40	3.11
5	0.17	3.85	0.3	9	0.315	2601.748	0.318	2621.521	0.97	0.75
6	0.27	5.72	1.6	14	0.313	2885.380	0.319	2970.21	1.92	2.86
7	0.42	16.25	1.9	7	0.310	4303.123	0.318	4378.428	2.57	1.72
8	0.25	8.15	0.2	16	0.311	3448.556	0.316	3480.628	1.55	0.92
9	0.32	11.25	1.8	6	0.315	3694.307	0.318	3718.32	0.85	0.65
10	0.37	7.69	0.9	8	0.315	2965.69	0.317	3021.445	0.76	1.85

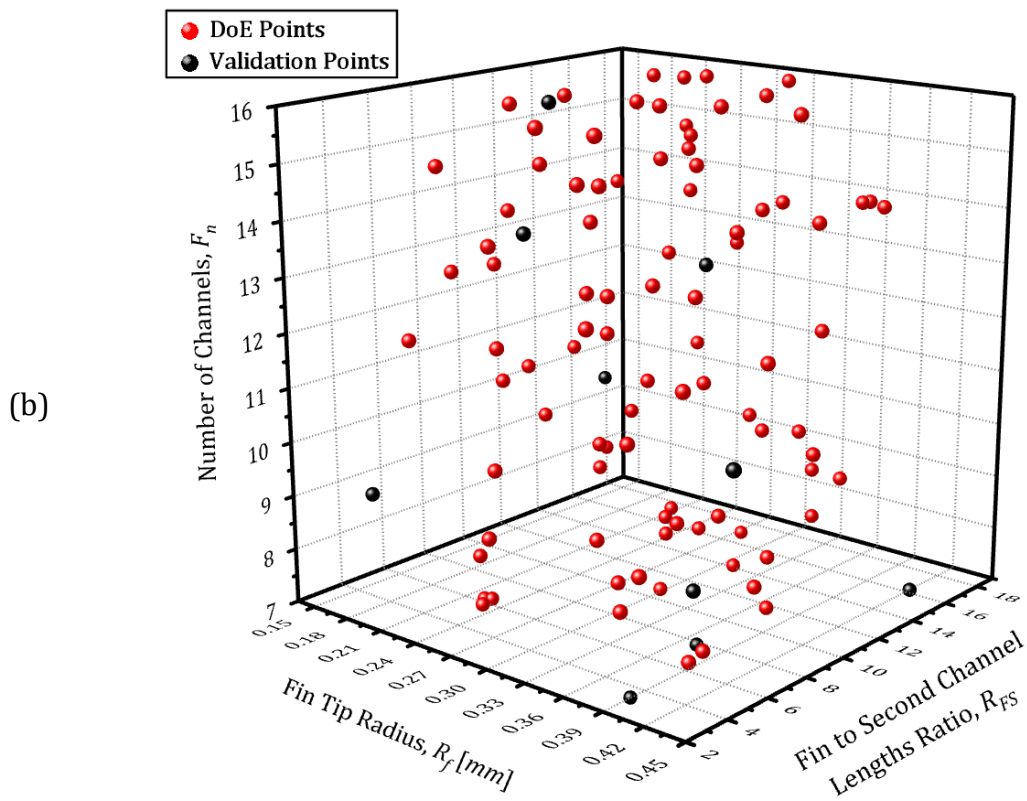
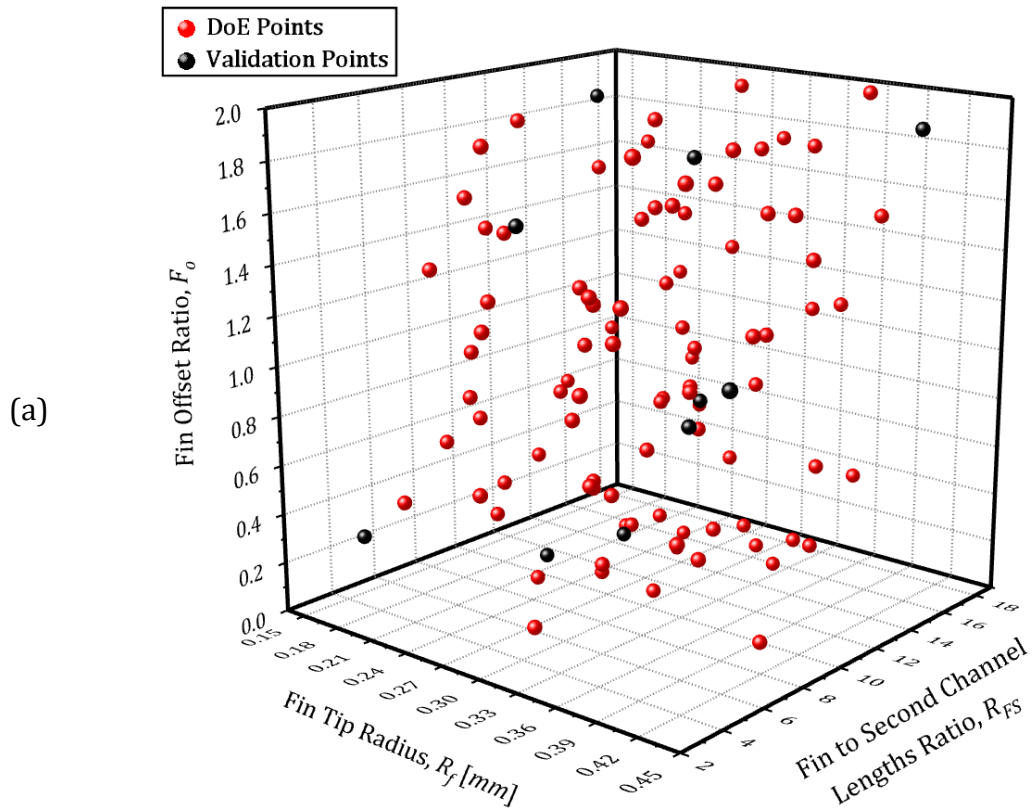


Fig. 7-10 3D scatter plots for the DoE points used to build the surrogate models for the responses of the *SMCHS – EF* with F_o , F_n , R_f and R_{FS} as design variables visualised in: (a) F_o , R_f and R_{FS} planes and (b) F_n , R_f and R_{FS} planes.

The investigation to find the global minimum for the thermal resistance and pressure drop penalty was undertaken individually to identify which geometrical shapes provide the minimum for these responses. This process has been performed using the single-objective optimisation process where the generated surrogate model along with the genetic algorithm optimiser (*soga*) have been utilised employing Dakota software toolkit. The final results for each of the metamodels are summarised in Table 7-4 and depicted in Fig. 7-11 to Fig. 7-14. The results were also validated with CFD simulation, and the validation outcomes show a good agreement. The table shows that the minimum R_{th} can be obtained by increasing the number of fins (F_n) and the (R_{FS}) ratio and reducing the fin offset (F_o) and the semi-minor axis (R_f). On the contrast, the minimum pressure penalty requires reducing the number of fins and the fin length ratio and increasing the fin offset and the semi-minor axis (R_f). This implies that these two objective functions are conflicting. The geometrical models for the optimum designs are presented in Fig. 7-15.

Table 7-4 Surrogate-based single-objective optimisation results for R_{th} and ΔP of the *SMCHS – EF* with F_o , F_n , R_f and R_{FS} as design variables.

Case	<i>soga</i> results		Optimum Design				CFD Validation		% diff. (\pm)	
	R_{th}	ΔP	F_o	F_n	R_f	R_{FS}	R_{th}	ΔP	R_{th}	ΔP
1	0.305	-----	0.659	13	0.202	16.955	0.306	-----	0.33	----
2	-----	2013.13	1.744	7	0.397	3.314	-----	2115.6	-----	4.82

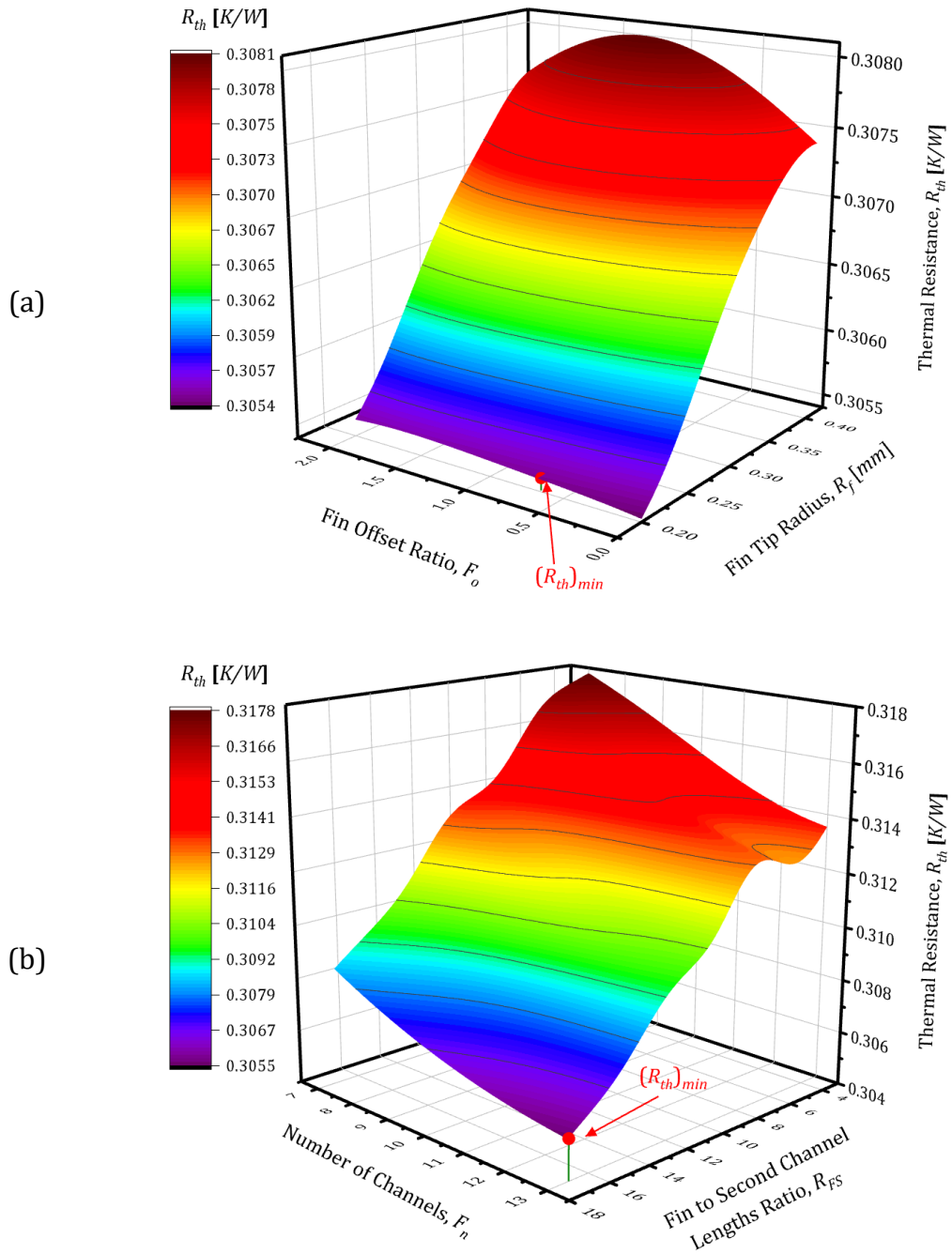


Fig. 7-11 Single-objective optimisation for R_{th} of the *SMCHS – EF* as a function of: (a) F_o and R_f and (b) F_n and R_{FS} as design variables.

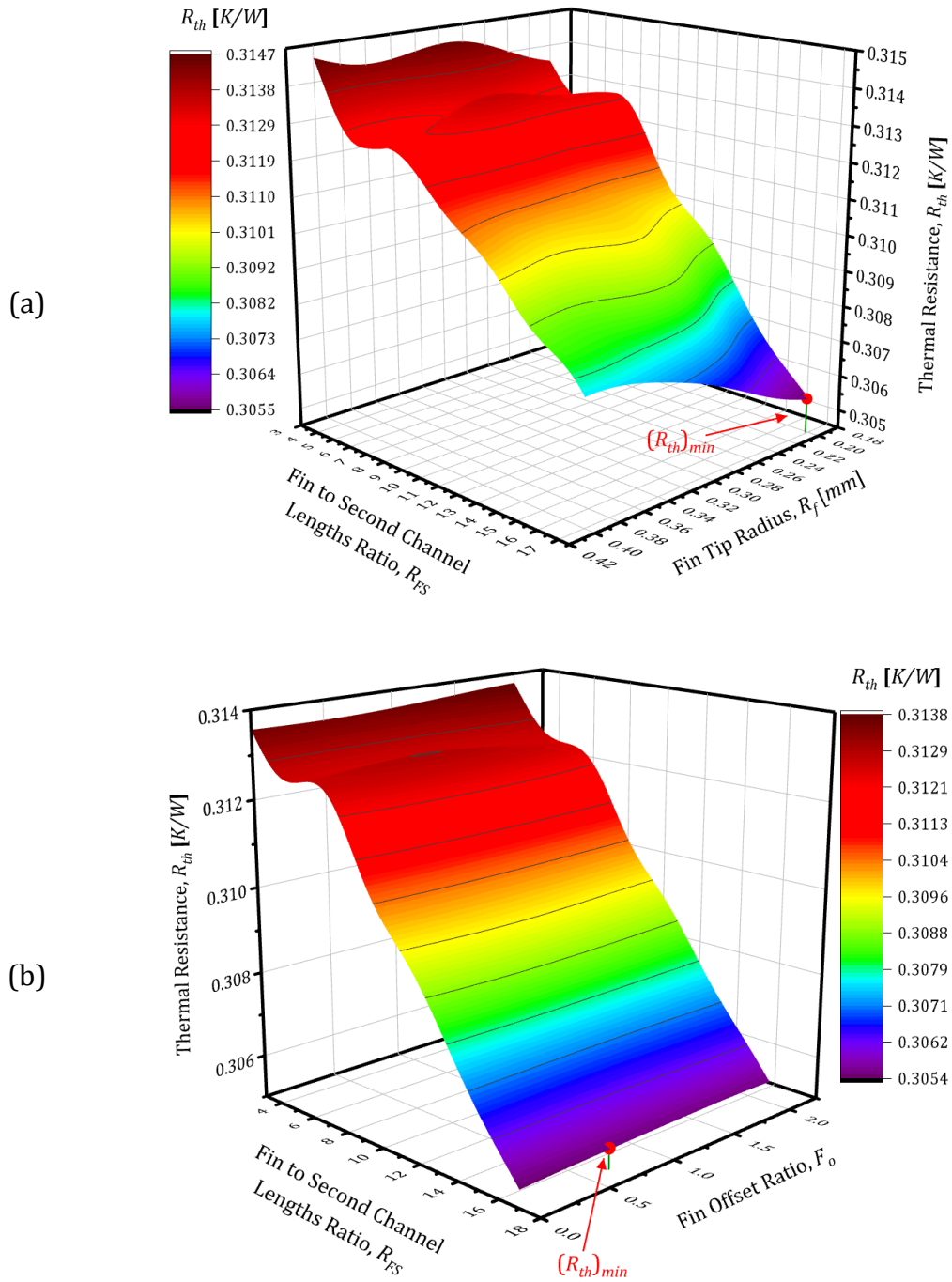


Fig. 7-12 Single-objective optimisation for R_{th} of the *SMCHS – EF* as a function of: (a) R_{FS} and R_f and (b) R_{FS} and F_o as design variables.

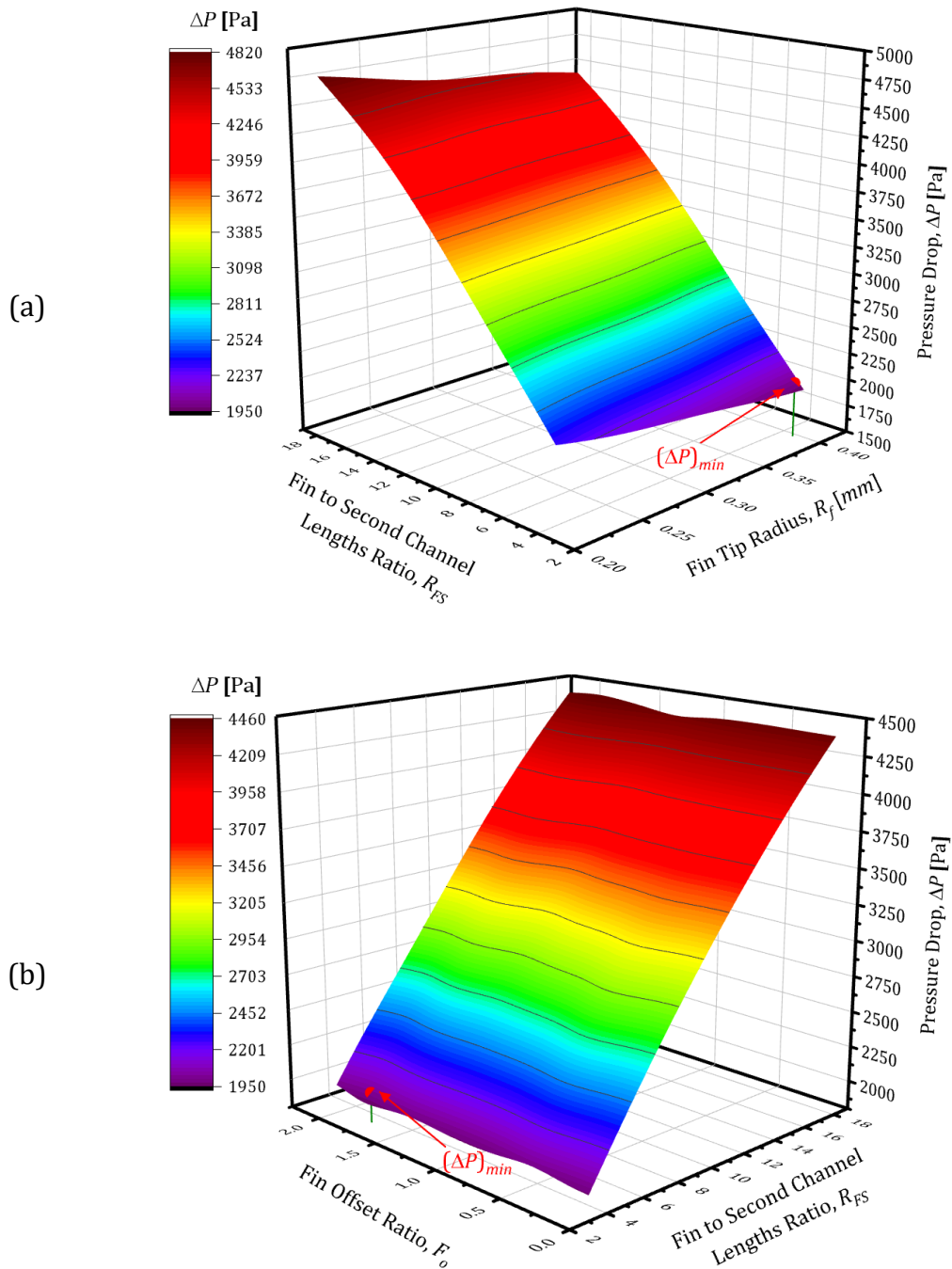


Fig. 7-13 Single-objective optimisation for ΔP of the *SMCHS – EF* as a function of: (a) R_{FS} and R_f and (b) F_o and R_{FS} as design variables.

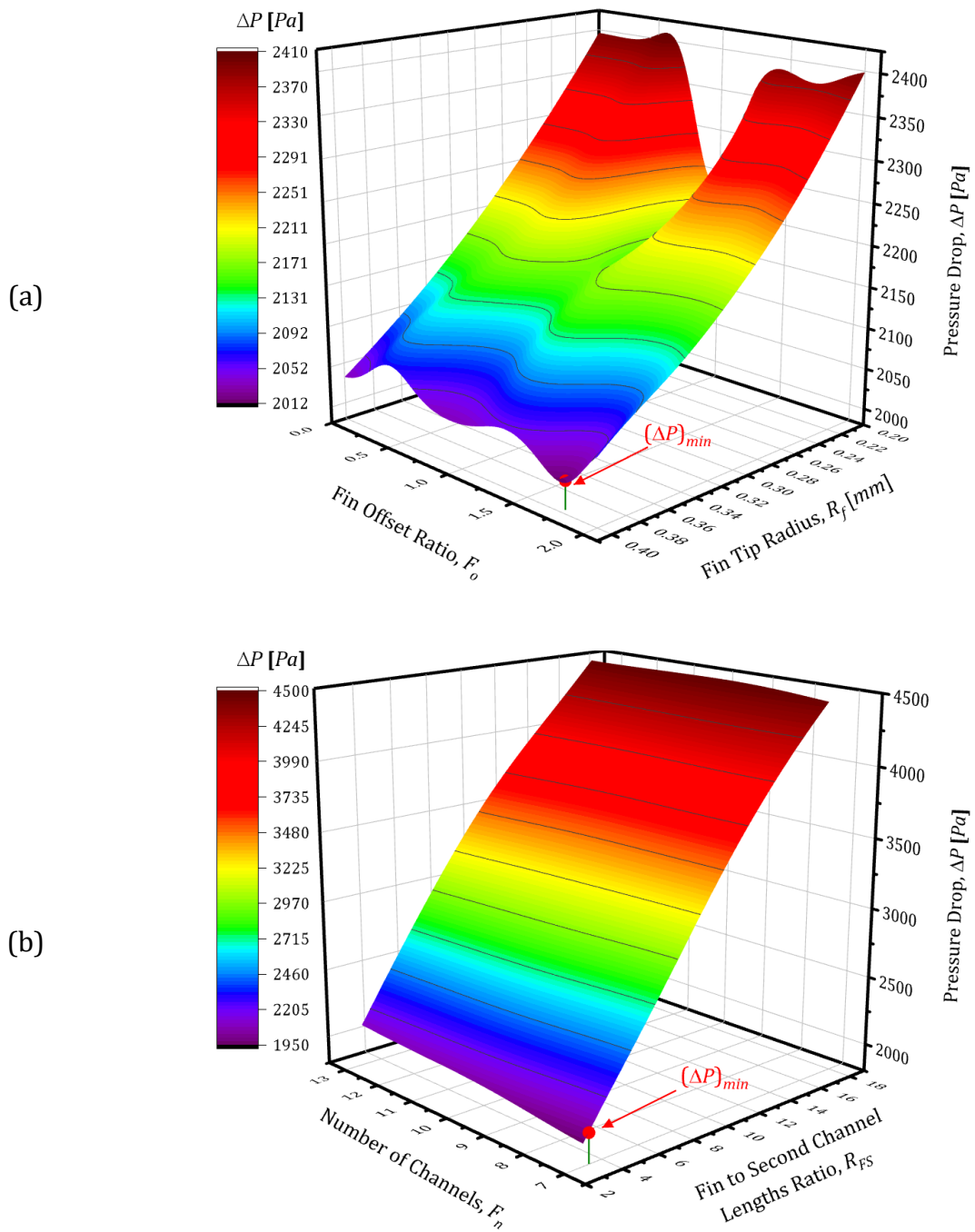
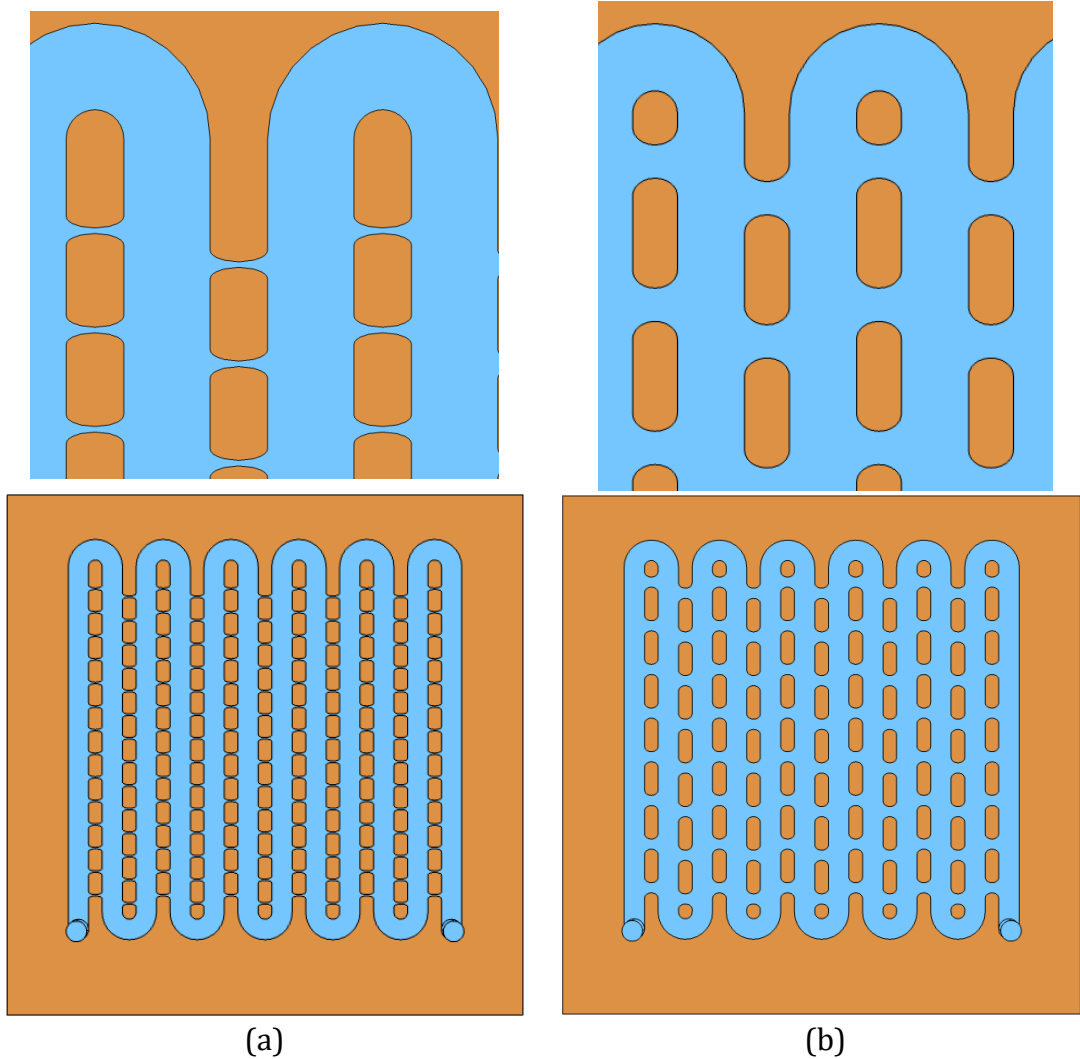


Fig. 7-14 Single-objective optimisation for ΔP of the *SMCHS – EF* as a function of:
 (a) F_o and R_f and (b) F_n and R_{FS} as design variables.



(a) (b)
 Fig. 7-15 Geometries for the optimum design of the *SMCHS – EF* with F_o , F_n , R_f and R_{FS} as design variables obtained using *soga* for: (a) minimum thermal resistance and (b) minimum pressure drop.

7.6.2 Multi-Objective Optimisation

As demonstrated in the previous section, the thermal resistance and pressure drop are conflicting function; therefore, it could be more important to implement the multi-objective optimisation technique by considering them together. Consequently, the multi-objective optimisation problem with four design variables, F_o , F_n , R_f and R_{FS} , could be expressed as follows:

$$\text{minimise } \{ R_{th} (F_o, F_n, R_f, R_{FS}) \& \Delta P (F_o, F_n, R_f, R_{FS}) \} \quad \text{Equ. 7-8}$$

$$\text{Subjected to} \quad 0 \leq F_o \leq 2.0 \quad \text{Equ. 7-9}$$

$$7 \leq F_n \leq 13 \quad \text{Equ. 7-10}$$

$$0.2 \leq R_f \leq 0.4 \quad \text{Equ. 7-11}$$

$$3 \leq R_{FS} \leq 17 \quad \text{Equ. 7-12}$$

The surrogate models constructed in section 7.6.1 have been utilised along with the genetic algorithm optimiser for the multi-objective functions (*moga*) provided by Dakota to implement the optimisation procedure for the above problem. The aim of using this technique is to identify if there is a best compromise between the two different objective functions. The results are presented in terms of Pareto front in Fig. 7-16; furthermore, five points from the Pareto optimal solutions have been selected as candidate which are a trade-off between the thermal resistance and pressure penalty. These candidates were also validated with the CFD simulation results, and they demonstrated an excellent agreement with maximum relative difference ≤ 2.3 , Table 7-5. Practically, the designer can choose any point from the Pareto optimal set based on the available pumping power to drive the fluid or the required thermal resistance.

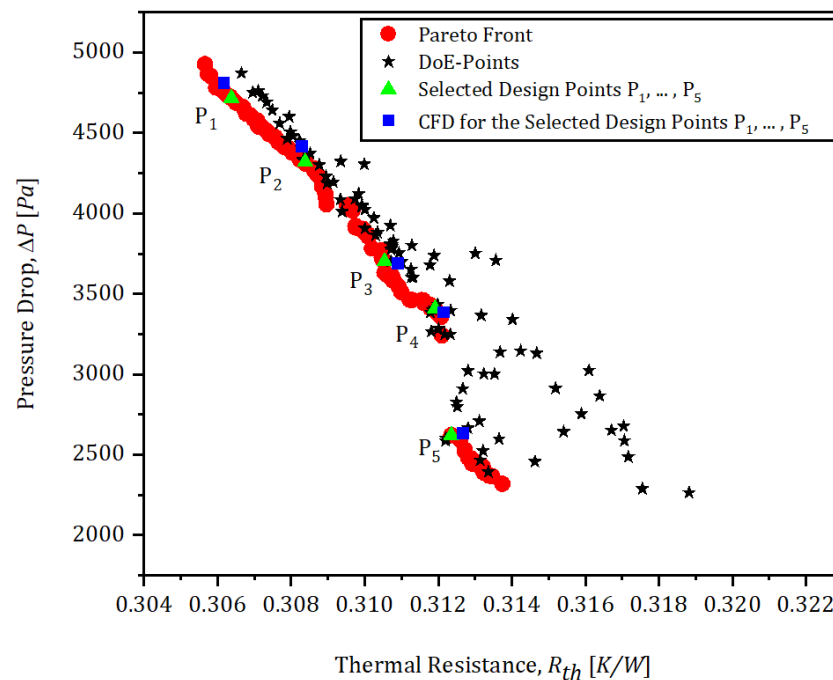


Fig. 7-16 Pareto front for the pressure drop and thermal resistance of the *SMCHS – EF* with F_o , F_n , R_f and R_{FS} as design variables.

Table 7-5 Validation of the Pareto front results for the *SMCHS – EF* with F_o , F_n , R_f and R_{FS} as design variables.

Case	moga results		Optimum Design Variables				CFD Validation		% diff. (\pm)	
	R_{th} [K/W]	ΔP [Pa]	F_o	F_n	R_f [mm]	R_{FS}	R_{th} [K/W]	ΔP [Pa]	R_{th}	ΔP
1	0.306	4716.735	0.213	16	0.148	12	0.306	4813.3	0.07	2.0
2	0.308	4321.437	0.202	13	0.427	13	0.308	4421.7	0.03	2.3
3	0.311	3702.073	0.264	10	1.261	13	0.311	3651.1	0.12	1.4
4	0.312	3408.277	0.264	9	1.261	12	0.312	3387.7	0.07	0.6
5	0.312	2622.002	0.385	5	1.120	13	0.313	2635.8	0.10	0.52

7.7 Chapter Summary

In this chapter, a new fin design of hybrid elliptical-rectangular shape has been suggested to replace the chevron fin structure for the heat sink studied in chapter 6. Accordingly, a CFD simulation investigation has been implemented for the serpentine minichannel heat sink equipped with the hybrid elliptical-rectangular fins (*SMCHS – EF*). The studied parameters were the semi-minor axis ($0.2 \leq R_f \leq 0.5 \text{ mm}$), the number of fins ($7 \leq F_n \leq 13$) and the fin length to the secondary channel length ($3 \leq R_{FS} \leq 13$). The simulations were conducted for cooling fluid with laminar flow ($500 \leq Re \leq 2250$) and inlet temperature 20°C . The applied heat flux was $31 \text{ [W/cm}^2\text{]}$.

As expected, breaking the plate fins (the walls of the minichannels) into a number of small hybrid elliptical-rectangular fins helps in improving the hydrothermal performance of the *SMCHS – EF*. The results show that the overall thermal resistance and pressure drop for the *SMCHS – EF* in comparison to that of the *SMCHS – PF* at $Re = 2250$ were respectively reduced by 10% and 59.78%. Moreover, the feasibility of employing the hybrid elliptical-rectangular fins with the serpentine minichannel heat sink has also been assessed by calculating the thermal-hydraulic performance criterion (PEC). It has been found that introducing the hybrid fins has enhanced the thermal-hydraulic performance of the studied heat sink because the PEC values were all positive and greater than 1.

Within the variable ranges set out in section 7.5.1, this study showed that the effect of the semi-minor axis (R_f) on R_{th} was insignificant and the minimum reduction can be achieved at $Re = 2250$ for $R_f = 0.5 \text{ mm}$ which is just 1.1% lower than other studied R_f . Likewise, the effect of R_f on pressure drop was also limited, and the $R_f = 0.35 \text{ mm}$ offered the best performance in terms of the pressure drop (reduced by 4.7%) in comparison to the other investigated values of R_f .

Regarding the effect of the number of fins (F_n), it was found that increasing F_n enhanced the hydrothermal performance of the *SMCHS – EF*. The results recorded a small reduction in thermal resistance reached up to 3.12% for $F_n = 13$ at $Re = 2250$. On the contrast, the reduction in pressure drop penalty was more pronounced and hit 11.65% by changing the number of fins from 7 to 13.

This study also included the exploration of the effect for R_{FS} ratio in the range $3 \leq R_{FS} \leq 13$. The results revealed that thermal resistance could be lowered by up to 7.27% by increasing R_{FS} from 3 to 13. Nevertheless, this improvement in thermal resistance comes at the expense of raising the pressure losses by 46.83%.

Finally, an optimisation process of the geometrical parameters was conducted to improve the performance of the minichannel heat sink with hybrid fins and secondary microchannel passages.

Chapter 8 Conclusions and Future Works

8.1 Introduction

One of the challenges facing the development of the electronic components is the temperature rise which could shorten the life-span and cause the failure of these electronic parts. This issue could be tackled using an effective cooling system such as the liquid-cooled heat sink. Therefore, this work has been devoted to investigating the ways of enhancing the performance of serpentine minichannel liquid-cooled heat sinks by adding vortex generators, introducing secondary channels and conducting deterministic and probabilistic optimisation. In the following section, the main conclusions of the current work will be presented.

8.2 Conclusions

8.2.1 Minichannel Geometrical Parameters of the *SMHS – PF*

- In chapter 5, the performance of the serpentine minichannel heat sink with plate fins (*SMCHS – PF*) has been examined by investigating the channel width (W_c) and the channel height (H_c). The simulation results showed that the increase in (W_c) and (H_c) leads to an increase in thermal resistance (R_{th}) and decrease in pressure drop (ΔP) which could reach up to 10.22% and 94.92%, respectively, for $H_c = 3 \text{ mm}$ and $W_c = 1.5 \text{ mm}$ with $\dot{m} = 2 \text{ g/s}$.
- In the same chapter, the deterministic and probabilistic optimisation strategies have been carried out to obtain the optimum design and robust design for the serpentine heat sink. The results of the optimisation under uncertainty, which taken in consideration the variability in the dimensions of the W_c and H_c due to manufacturing tolerance, showed that the performance criteria for the robust design have higher values than the global optimum design. For example, the single-objective optimisations revealed that the R_{th} and ΔP for the robust design are higher than the global optimum design by 0.3% and 4.1%, respectively.

8.2.2 Vortex generators

Furthermore, vortex generators have been added to the sidewalls (*VVGs*) and to the base of the minichannel (*HVGs*) to investigate their effect on the hydrothermal performance of the considered heat sink. The following conclusions have been drawn:

- The vortex generators have been integrated to the sidewalls (*VVGs*) and distributed on both sides of the channel in two arrangements, staggered and in-lined, to examine their effect on the performance of the considered heat sink. For the same boundary conditions and comparing to the smooth serpentine minichannel heat sink, the maximum reduction in R_{th} was 11.1% and 10.68% whereas the increase in ΔP was 207.73% and 115.20% for the in-lined *VVGs* and staggered *VVGs*, respectively, with $r_{VG} = 0.3 \text{ mm}$ and $Re=2250$.
- For the vortex generators attached to the base of the minichannel (*HVGs*) with $r_{VG} = 0.3 \text{ mm}$, this study achieved a reduction in R_{th} of 54.34%. Unfortunately, it was accompanied by an elevation in pressure drop of 48.46%. This rise in ΔP could be mitigated to be 17.9% by reducing the r_{VG} to 0.1 *mm* and thus the percentage of reduction in R_{th} will be 52%.

8.2.3 Fin Parameters of the *SMHS – CF*

In chapter 6, the hydrothermal performance of the serpentine minichannel heat sink with chevron fins (*SMCHS – CF*) has been studied by considering the effect of the number of fins (F_n), the fin offset (F_o), the impact of the fin's secondary channel lengths ratio ($R_{FS} = \frac{F_l}{l_{sc}}$), channel length (l_{sc}), channel width (W_c) and the fin oblique angle (θ). The following conclusions can be made from this investigation:

- In comparison to the performance of the *SMCHS – PF*, the study revealed that the number of fins (F_n) and the secondary channel length (l_{sc}) have a significant influence on R_{th} and ΔP . By changing F_n from 6 to 18, for example, the ΔP reduced by 28.1% for $l_{sc} = 0.25 \text{ mm}$. Similarly, the reduction in thermal performance of the *SMCHS – CF* reached up to 12% for $l_{sc} = 0.25 \text{ mm}$ with 18 fins.

- The fins arrangement has a slight effect on the performance of the *SMCHS – CF* where it is found that the pressure drop could be reduced by 2.31% through setting the $F_o = 2 \text{ mm}$ for $Re = 500$, whereas it is raised by 3.2% via fixing the $F_o = 0.5 \text{ mm}$ for $Re = 2000$. It is also shown that the effect of F_o on R_{th} was insignificant as R_{th} increased by less than 1.19% in the examined range of F_o .
- Furthermore, the effect of the fin length ratio R_{FS} on the hydrothermal performance of the *SMCHS – CF* has also been investigated. The findings revealed that increasing the R_{FS} caused a decrease and then to an increase in thermal resistance R_{th} . Overall, the improvement was moderated, and the maximum reduction was less than 7.3% for the case of $R_{FS} = 3$. Besides, the results indicated that lowering the R_{FS} ratio from 3 to 1 has led to an improvement in the pressure drop by 14%.
- In chapter 6, the optimisation under uncertainty with l_{sc} , W_c and θ as design variables has also been conducted and compared with the deterministic optimisations. As in chapter 5, the results indicated that the performance criteria for the robust design have higher values than the global optimum design. For instance, the single-objective robust designs have responses higher than those of the global optimum designs by 8.7% and 12.4% for the R_{th} and ΔP , respectively. As the robust design obtained at the minimum standard deviation of the responses, it is less sensitive to the variability in input design parameters.

8.2.4 Fin Parameters of the *SMHS – EF*

Chapter 7 was devoted to investigating numerically the performance of the serpentine minichannel heat sink equipped with the hybrid elliptical-rectangular (*SMCHS – EF*). The study focused on exploring the effect of the semi-minor axis (R_f), the number of fins (F_n) and the fin length to the secondary channel length ratio (R_{FS}) on the overall thermal resistance (R_{th}) and pressure drop (ΔP) for the *SMCHS – EF*. Based on this investigation, the following conclusions have been identified:

- Introducing the hybrid elliptical-rectangular fins helped in reducing the overall thermal resistance and pressure drop for the *SMCHS – EF* in comparison to those of the *SMCHS – PF* by 10.0% and 59.8%.
- Within the studied variables ranges, the numerical results showed that the effect of R_f on R_{th} and ΔP was limited with a maximum reduction reach up to 1.1% and 4.7%, respectively.
- The numerical results of the effect of F_n on *SMCHS – PF* performance indicated that increasing F_n could lead to reducing R_{th} by 3.12% and ΔP by 11.65%.
- Regarding the effect R_{FS} , the results showed that R_{th} could be reduced up to 7.3% by increasing R_{FS} from 3 to 13, which was accompanied by raising ΔP by 46.8%.

8.3 Recommendations for Future Works

In this section, some suggestions for future work have been made and listed as follow:

1. In this study, the heat sink has one inlet and one outlet. Therefore, investigation the effect of using multi-inlets and multi-outlets with different locations could contribute to enhancing the thermal performance and produce a better distribution for the temperature for the serpentine minichannels heat sink.
2. Using a double-layered of the serpentine minichannels heat sink for cooling electronic parts might be effective.
3. Since the microchannel heat sink has small geometric size, the temperature gradient generated within the heat sink can deform the microchannels and produce thermal stress. This might have a negative impact on the stability of the heat transfer performance and even decrease its amount. Consequently, future work can analyse thermal stress of the serpentine heat sink.
4. It is suggested to investigate introducing cylindrical secondary microchannels with different sizes drilled in the main channel walls to improve the hydrothermal performance of the serpentine heat sink.
5. It could also be useful to conduct a comprehensive experimental validation of the CFD predictions.

REFERENCES

- Abdollahi, A., Norris, S.E. and Sharma, R.N., 2020. Fluid flow and heat transfer of liquid-liquid Taylor flow in square microchannels. *Applied Thermal Engineering*, p.115123.
- Adham, A.M., Mohd-Ghazali, N. and Ahmad, R., 2012, June. Cooling of a rectangular microchannel heat sink with ammonia gas. In *AIP Conference Proceedings* (Vol. 1440, No. 1, pp. 57-64). American Institute of Physics.
- Adham, A.M., Mohd-Ghazali, N. and Ahmad, R., 2013. Thermal and hydrodynamic analysis of microchannel heat sinks: A review. *Renewable and Sustainable Energy Reviews*, 21, pp.614-622.
- Agarwal, G., Kazior, T., Kenny, T. and Weinstein, D., 2017. Modeling and analysis for thermal management in Gallium Nitride HEMTs using microfluidic cooling. *Journal of Electronic Packaging*, 139(1).
- Aghakhani, S., Ghasemi, B., Pordanjani, A.H., Wongwises, S. and Afrand, M., 2019. Effect of replacing nanofluid instead of water on heat transfer in a channel with extended surfaces under a magnetic field. *International Journal of Numerical Methods for Heat & Fluid Flow*.
- Ahmed, H.E. and Ahmed, M.I., 2015. Optimum thermal design of triangular, trapezoidal and rectangular grooved microchannel heat sinks. *International Communications in Heat and Mass Transfer*, 66, pp.47-57.
- Ahmed, H.E., Mohammed, H.A. and Yusoff, M.Z., 2012. An overview on heat transfer augmentation using vortex generators and nanofluids: approaches and applications. *Renewable and Sustainable Energy Reviews*, 16(8), pp.5951-5993.
- Ahmed, H.E., Salman, B.H., Kherbeet, A.S. and Ahmed, M.I., 2018. Optimization of thermal design of heat sinks: A review. *International Journal of Heat and Mass Transfer*, 118, pp.129-153.
- Ahmed, M.A., Yusoff, M.Z., Ng, K.C. and Shuaib, N.H., 2014. Effect of corrugation profile on the thermal-hydraulic performance of corrugated channels using CuO-water nanofluid. *Case Studies in Thermal Engineering*, 4, pp.65-75.

- Ahmed, M.Y.M. and Qin, N., 2009, May. Surrogate-based aerodynamic design optimization: Use of surrogates in aerodynamic design optimization. In *International Conference on Aerospace Sciences and Aviation Technology* (Vol. 13, No. AEROSPACE SCIENCES & AVIATION TECHNOLOGY, ASAT-13, May 26–28, 2009, pp. 1-26). The Military Technical College.
- Al-Asadi, M.T., Al-damook, A. and Wilson, M.C.T., 2018. Assessment of vortex generator shapes and pin fin perforations for enhancing water-based heat sink performance. *International Communications in Heat and Mass Transfer*, 91, pp.1-10.
- Al-Asadi, M.T., Alkasmoul, F.S. and Wilson, M.C., 2018. Benefits of spanwise gaps in cylindrical vortex generators for conjugate heat transfer enhancement in micro-channels. *Applied Thermal Engineering*, 130, pp.571-586.
- Al-Asadi, M.T., Alkasmoul, F.S. and Wilson, M.C.T., 2016. Heat transfer enhancement in a micro-channel cooling system using cylindrical vortex generators. *International Communications in Heat and Mass Transfer*, 74, pp.40-47.
- Al-Asadi, M.T.K., 2018. Heat transfer, fluid flow analysis and energy management of micro-channel heat sinks using vortex generators and nanofluids (Doctoral dissertation, University of Leeds).
- Al-Damook, A., Kapur, N., Summers, J.L. and Thompson, H.M., 2015. An experimental and computational investigation of thermal air flows through perforated pin heat sinks. *Applied thermal engineering*, 89, pp.365-376.
- Al-damook, A.J.S., 2016. *Design optimization and analysis of heat sinks for electronic cooling* (Doctoral dissertation, University of Leeds).
- Alfaryjat, A.A., Mohammed, H.A., Adam, N.M., Ariffin, M.K.A. and Najafabadi, M.I., 2014. Influence of geometrical parameters of hexagonal, circular, and rhombus microchannel heat sinks on the thermohydraulic characteristics. *International Communications in Heat and Mass Transfer*, 52, pp.121-131.
- Ali, N., Teixeira, J.A. and Addali, A., 2018. A review on nanofluids: fabrication, stability, and thermophysical properties. *Journal of Nanomaterials*, 2018.
- Alkasmoul, F.S., Al-Asadi, M.T., Myers, T.G., Thompson, H.M. and Wilson, M.C.T., 2018. A practical evaluation of the performance of Al₂O₃-water, TiO₂-water and

- CuO-water nanofluids for convective cooling. *International Journal of Heat and Mass Transfer*, 126, pp.639-651.
- Al-Neama, A.F., Kapur, N., Summers, J. and Thompson, H.M., 2017. An experimental and numerical investigation of the use of liquid flow in serpentine microchannels for microelectronics cooling. *Applied Thermal Engineering*, 116, pp.709-723.
- Al-Neama, A.F., Khatir, Z., Kapur, N., Summers, J. and Thompson, H.M., 2018. An experimental and numerical investigation of chevron fin structures in serpentine minichannel heat sinks. *International Journal of Heat and Mass Transfer*, 120, pp.1213-1228.
- Al-Neama, A.F.M., 2018. Serpentine minichannel liquid-cooled heat sinks for electronics cooling applications (Doctoral dissertation, University of Leeds).
- Al-Waaly, A., 2015. *The effect of heat transfer on temperature measurement and its applications to study microchannel heat sinks* (Doctoral dissertation, University of Glasgow).
- Anandan, S.S. and Ramalingam, V., 2008. Thermal management of electronics: A review of literature. *Thermal science*, 12(2), pp.5-26.
- Aris, M.S., Owen, I. and Sutcliffe, C.J., 2011. The development of active vortex generators from shape memory alloys for the convective cooling of heated surfaces. *International journal of heat and mass transfer*, 54(15-16), pp.3566-3574.
- Arora, J.S., 2004. *Introduction to optimum design*. Elsevier.
- Ben Salem, M., Roustant, O., Gamboa, F. and Tomaso, L., 2017. Universal prediction distribution for surrogate models. *SIAM/ASA Journal on Uncertainty Quantification*, 5(1), pp.1086-1109.
- Bergman, T.L., Incropera, F.P., DeWitt, D.P. and Lavine, A.S., 2011. *Fundamentals of heat and mass transfer*. John Wiley & Sons.
- Bodla, K.K., Murthy, J.Y. and Garimella, S.V., 2013. Optimization under uncertainty applied to heat sink design. *Journal of heat transfer*, 135(1).
- Carballo, J.A., Chan, W.T.J., Gargini, P.A., Kahng, A.B. and Nath, S., 2014, October. ITRS 2.0: Toward a re-framing of the Semiconductor Technology Roadmap. In 2014 IEEE 32nd International Conference on Computer Design (ICCD) (pp. 139-146). IEEE.

- Cavazzuti, M., 2012. *Optimization methods: from theory to design scientific and technological aspects in mechanics*. Springer Science & Business Media.
- Cengel, Y., 2014. *Heat and mass transfer: fundamentals and applications*. McGraw-Hill Higher Education.
- Çengel, Y.A., Turner, R.H., Cimbala, J.M. and Kanoglu, M., 2012. *Fundamentals of thermal-fluid sciences* (Vol. 703). New York: McGraw-Hill.
- Chai, L. and Tassou, S.A., 2018. A review of airside heat transfer augmentation with vortex generators on heat transfer surface. *Energies*, 11(10), p.2737.
- Chai, L., Xia, G. and Qi, J., 2012. Experimental and numerical study of flow and heat transfer in trapezoidal microchannels. *Heat transfer engineering*, 33(11), pp.972-981.
- Chakraborty, S., Chatterjee, T., Chowdhury, R. and Adhikari, S., 2017. A surrogate based multi-fidelity approach for robust design optimization. *Applied Mathematical Modelling*, 47, pp.726-744.
- Chandrupatla, T.R. and Osler, T.J., 2010. The perimeter of an ellipse. *Mathematical Scientist*, 35(2).
- Chen, C., Teng, J.T., Cheng, C.H., Jin, S., Huang, S., Liu, C., Lee, M.T., Pan, H.H. and Greif, R., 2014. A study on fluid flow and heat transfer in rectangular microchannels with various longitudinal vortex generators. *International journal of heat and mass transfer*, 69, pp.203-214.
- Chen, Y., Peng, B., Hao, X. and Xie, G., 2014. Fast approach of Pareto-optimal solution recommendation to multi-objective optimal design of serpentine-channel heat sink. *Applied thermal engineering*, 70(1), pp.263-273.
- Cheng, J.C., Tsay, Y.L., Liu, C.T. and Chang, S., 2020. Heat transfer enhancement of microchannel heat sink with longitudinal vortex generators and bypass jet flow. *Numerical Heat Transfer, Part A: Applications*, 77(8), pp.807-819.
- Cheng, Y.J., 2007. Numerical simulation of stacked microchannel heat sink with mixing-enhanced passive structure. *International communications in heat and mass transfer*, 34(3), pp.295-303.
- Coello, C.C., 2006. Evolutionary multi-objective optimization: a historical view of the field. *IEEE computational intelligence magazine*, 1(1), pp.28-36.
- Communications of the ACM <https://cacm.acm.org/careers/192631-liquid-cooling-moves-onto-the-chip-for-denser-electronics/fulltext>.

- COMSOL Multiphysics forum, "<https://uk.comsol.com/forum/thread/36398/finite-elements-for-fluids-p1-p1-p2-p1>".
- COMSOL Multiphysics Programming Reference Manual. Version 5.4, COMSOL, 2018.
- COMSOL support, "Official COMSOL Multiphysics, support page," <https://www.comsol.com/support/knowledgebase/1261>.
- Cook, L.W., 2018. Effective formulations of optimization under uncertainty for aerospace design (Doctoral dissertation, University of Cambridge).
- Datta, A., Sanyal, D. and Das, A.K., 2016. Numerical investigation of heat transfer in microchannel using inclined longitudinal vortex generator. *Applied Thermal Engineering*, 108, pp.1008-1019.
- David, C. (2019, 09-12-2019). Need for Thermal Management in Electronic Systems. Available: <https://experience.molex.com/need-thermal-management-electronic-systems/>
- Deb, K., 2012. Optimization for engineering design: Algorithms and examples. PHI Learning Pvt. Ltd.
- Dehghan, M., Valipour, M.S. and Saedodin, S., 2016. Microchannels enhanced by porous materials: heat transfer enhancement or pressure drop increment?. *Energy Conversion and Management*, 110, pp.22-32.
- Deng, D., Pi, G., Zhang, W., Wang, P. and Fu, T., 2019. Numerical study of double-layered microchannel heat sinks with different cross-sectional shapes. *Entropy*, 21(1), p.16.
- Deng, T., Zhang, G. and Ran, Y., 2018. Study on thermal management of rectangular Li-ion battery with serpentine-channel cold plate. *International Journal of Heat and Mass Transfer*, 125, pp.143-152.
- Doltsinis, I. and Kang, Z., 2004. Robust design of structures using optimization methods. *Computer methods in applied mechanics and engineering*, 193(23-26), pp.2221-2237.
- Duan, Z., Ma, H., He, B., Su, L. and Zhang, X., 2019. Pressure drop of microchannel plate fin heat sinks. *Micromachines*, 10(2), p.80.
- Ebrahimi, A., Rikhtegar, F., Sabaghan, A. and Roohi, E., 2016. Heat transfer and entropy generation in a microchannel with longitudinal vortex generators using nanofluids. *Energy*, 101, pp.190-201.

- Ebrahimi, A., Roohi, E. and Kheradmand, S., 2015. Numerical study of liquid flow and heat transfer in rectangular microchannel with longitudinal vortex generators. *Applied Thermal Engineering*, 78, pp.576-583.
- Echard, B., Gayton, N. and Lemaire, M., 2011. AK-MCS: an active learning reliability method combining Kriging and Monte Carlo simulation. *Structural Safety*, 33(2), pp.145-154.
- Echard, B., Gayton, N., Lemaire, M. and Relun, N., 2013. A combined importance sampling and kriging reliability method for small failure probabilities with time-demanding numerical models. *Reliability Engineering & System Safety*, 111, pp.232-240.
- Fan, Y., Lee, P.S., Jin, L.W., Chua, B.W. and Zhang, D.C., 2014. A parametric investigation of heat transfer and friction characteristics in cylindrical oblique fin minichannel heat sink. *International Journal of Heat and Mass Transfer*, 68, pp.567-584.
- Fedorov, A.G. and Viskanta, R., 2000. Three-dimensional conjugate heat transfer in the microchannel heat sink for electronic packaging. *International Journal of Heat and Mass Transfer*, 43(3), pp.399-415.
- Forrester, A., Sobester, A. and Keane, A., 2008. *Engineering design via surrogate modelling: a practical guide*. John Wiley & Sons.
- Fröhlich, F., Loos, C. and Hasenauer, J., 2019. Scalable inference of ordinary differential equation models of biochemical processes. In *Gene Regulatory Networks* (pp. 385-422). Humana Press, New York, NY.
- Furmański, P.I.O.T.R., Thualfaqir, K. and Łapka, P.I.O.T.R., 2018. Modelling of a micro-channel heat sink for cooling of high-power laser diode arrays. *Archives of Thermodynamics*, 39(3).
- G. Nellis and S. Klein, 2009, Heat transfer, First Edition ed. USA.
- Gundlapalli, R. and Jayanti, S., 2019. Effect of channel dimensions of serpentine flow fields on the performance of a vanadium redox flow battery. *Journal of Energy Storage*, 23, pp.148-158.
- Gunnasegaran, P., Mohammed, H.A., Shuaib, N.H. and Saidur, R., 2010. The effect of geometrical parameters on heat transfer characteristics of microchannels heat sink with different shapes. *International Communications in Heat and Mass Transfer*, 37(8), pp.1078-1086.

- Haftka, R.T., Villanueva, D. and Chaudhuri, A., 2016. Parallel surrogate-assisted global optimization with expensive functions—a survey. *Structural and Multidisciplinary Optimization*, 54(1), pp.3-13.
- Hamad, H., 2006, December. A new metric for measuring metamodels quality-of-fit for deterministic simulations. In *Proceedings of the 2006 Winter Simulation Conference* (pp. 882-888). IEEE.
- Han, Y., Lau, B.L., Zhang, X., Leong, Y.C. and Choo, K.F., 2014. Enhancement of hotspot cooling with diamond heat spreader on Cu microchannel heat sink for GaN-on-Si device. *IEEE Transactions on Components, Packaging and Manufacturing Technology*, 4(6), pp.983-990.
- Hao, X., Peng, B., Xie, G. and Chen, Y., 2014. Thermal analysis and experimental validation of laminar heat transfer and pressure drop in serpentine channel heat sinks for electronic cooling. *Journal of Electronic Packaging*, 136(3).
- Hosseini-rad, E., Khoshvaght-Aliabadi, M. and Hormozi, F., 2019. Evaluation of heat transfer and pressure drop in a mini-channel using transverse rectangular vortex-generators with various non-uniform heights. *Applied Thermal Engineering*, 161, p.114196.
- Hsiao, K.Y., Wu, C.Y. and Huang, Y.T., 2014. Fluid mixing in a microchannel with longitudinal vortex generators. *Chemical Engineering Journal*, 235, pp.27-36.
- Huang, G.J., Wong, S.C. and Lin, C.P., 2014. Enhancement of natural convection heat transfer from horizontal rectangular fin arrays with perforations in fin base. *International Journal of Thermal Sciences*, 84, pp.164-174.
- Huang, P., Huang, G. and Augenbroe, G., 2017. Sizing heating, ventilating, and air-conditioning systems under uncertainty in both load-demand and capacity-supply side from a life-cycle aspect. *Science and Technology for the Built Environment*, 23(2), pp.367-381.
- Hung, T.C. and Yan, W.M., 2013. Thermal performance enhancement of microchannel heat sinks with sintered porous media. *Numerical Heat Transfer, Part A: Applications*, 63(9), pp.666-686.
- Hung, T.C., Huang, Y.X. and Yan, W.M., 2013. Thermal performance analysis of porous-microchannel heat sinks with different configuration designs. *International Journal of Heat and Mass Transfer*, 66, pp.235-243.

- Hung, T.C., Yan, W.M. and Li, W.P., 2012. Analysis of heat transfer characteristics of double-layered microchannel heat sink. *International Journal of Heat and Mass Transfer*, 55(11-12), pp.3090-3099.
- Husain, A. and K.-Y. Kim (2008). "Optimization of a microchannel heat sink with temperature dependent fluid properties." *Applied Thermal Engineering* 28(8-9): 1101-1107.
- Husain, A. and Kim, K.Y., 2008. Shape optimization of micro-channel heat sink for micro-electronic cooling. *IEEE Transactions on Components and Packaging Technologies*, 31(2), pp.322-330.
- Husain, A. and Kim, K.Y., 2010. Enhanced multi-objective optimization of a microchannel heat sink through evolutionary algorithm coupled with multiple surrogate models. *Applied Thermal Engineering*, 30(13), pp.1683-1691.
- Imran, A.A., Mahmoud, N.S. and Jaffal, H.M., 2018. Numerical and experimental investigation of heat transfer in liquid cooling serpentine mini-channel heat sink with different new configuration models. *Thermal Science and Engineering Progress*, 6, pp.128-139.
- Ismail, M.A., Abdullah, M.Z. and Mujeebu, M.A., 2008. A CFD-based experimental analysis on the effect of free stream cooling on the performance of microprocessor heat sinks. *International Communications in Heat and Mass Transfer*, 35(6), pp.771-778.
- Janusevskis, J. and Le Riche, R., 2010. Simultaneous kriging-based sampling for optimization and uncertainty propagation.
- Jeong, W. and Seong, J., 2014. Comparison of effects on technical variances of computational fluid dynamics (CFD) software based on finite element and finite volume methods. *International Journal of Mechanical Sciences*, 78, pp.19-26.
- Jiang, P.X., Fan, M.H., Si, G.S. and Ren, Z.P., 2001. Thermal-hydraulic performance of small scale micro-channel and porous-media heat-exchangers. *International Journal of Heat and Mass Transfer*, 44(5), pp.1039-1051.
- Jiaqiang, E., Xu, S., Deng, Y., Zhu, H., Zuo, W., Wang, H., Chen, J., Peng, Q. and Zhang, Z., 2018. Investigation on thermal performance and pressure loss of the fluid

- cold-plate used in thermal management system of the battery pack. *Applied Thermal Engineering*, 145, pp.552-568.
- Jin, R., Du, X. and Chen, W., 2003. The use of metamodeling techniques for optimization under uncertainty. *Structural and Multidisciplinary Optimization*, 25(2), pp.99-116.
- Joseph, V.R., 2016. Space-filling designs for computer experiments: A review. *Quality Engineering*, 28(1), pp.28-35.
- Joy, B., Philip, J. and Zachariah, R., 2016. Investigations on serpentine tube type solar photovoltaic/thermal collector with different heat transfer fluids: Experiment and numerical analysis. *Solar Energy*, 140, pp.12-20.
- Kandlikar, S., Garimella, S., Li, D., Colin, S. and King, M.R., 2005. *Heat transfer and fluid flow in minichannels and microchannels*. elsevier.
- Kandlikar, S.G. and Bapat, A.V., 2007. Evaluation of jet impingement, spray and microchannel chip cooling options for high heat flux removal. *Heat Transfer Engineering*, 28(11), pp.911-923.
- Kandlikar, S.G., 2003, April. Microchannels and minichannels-history, terminology, classification and current research needs. In *First International Conference on Microchannels and Minichannels, New York*.
- KAWA, M. J., 2011 "electronicproducts." *Electronic Products Magazine* [Online]. Available:
<https://www.electronicproducts.com/Thermal Management/Heat Sinks and Thermal Materials/Fundamentals of active vs passive thermal management.aspx>.
- Kawano, K., Minakami, K., Iwasaki, H. and Ishizuka, M., 1998. Micro channel heat exchanger for cooling electrical equipment. *ASME Heat Transfer Div Publ Htd*, 361, pp.173-180.
- Khan, W.A., Kadri, M.B. and Ali, Q., 2013. Optimization of microchannel heat sinks using genetic algorithm. *Heat Transfer Engineering*, 34(4), pp.279-287.
- Khattak, Z. and Ali, H.M., 2019. Air cooled heat sink geometries subjected to forced flow: A critical review. *International Journal of Heat and Mass Transfer*, 130, pp.141-161.

- Khoshvaght-Aliabadi, M., Deldar, S. and Hassani, S.M., 2018. Effects of pin-fins geometry and nanofluid on the performance of a pin-fin miniature heat sink (PFMHS). *International Journal of Mechanical Sciences*, 148, pp.442-458.
- Kim, B.S., Kwak, B.S., Shin, S., Lee, S., Kim, K.M., Jung, H.I. and Cho, H.H., 2011. Optimization of microscale vortex generators in a microchannel using advanced response surface method. *International Journal of Heat and Mass Transfer*, 54(1-3), pp.118-125.
- Kim, B.S., Lee, Y.B. and Choi, D.H., 2009. Comparison study on the accuracy of metamodeling technique for non-convex functions. *Journal of Mechanical Science and Technology*, 23(4), pp.1175-1181.
- Kim, J., 2007. Spray cooling heat transfer: The state of the art. *International Journal of Heat and Fluid Flow*, 28(4), pp.753-767.
- Knight, R.W., Hall, D.J., Goodling, J.S. and Jaeger, R.C., 1992. Heat sink optimization with application to microchannels. *IEEE Transactions on Components, Hybrids, and Manufacturing Technology*, 15(5), pp.832-842.
- Kode, T.E., Ogwu, A.A., Walker, A., Mirzaeian, M. and Wu, H., 2018. Manufacturing, Numerical and Analytical Model Limitations in Developing Fractal Microchannel Heat Sinks for Cooling MEMS, Microelectronics and Aerospace Components. In *Micro and Nanomanufacturing Volume II* (pp. 499-543). Springer, Cham.
- Koşar, A., 2010. Effect of substrate thickness and material on heat transfer in microchannel heat sinks. *International Journal of Thermal Sciences*, 49(4), pp.635-642.
- Kumar, D.N., 2009. Classical and advanced techniques for optimization. *Optimization Methods*, 5(2), pp.1-12.
- Léal, L., Miscevic, M., Lavieille, P., Amokrane, M., Pigache, F., Topin, F., Nogarède, B. and Tadrist, L., 2013. An overview of heat transfer enhancement methods and new perspectives: Focus on active methods using electroactive materials. *International Journal of Heat and Mass Transfer*, 61, pp.505-524.
- Lee, J. and Mudawar, I., 2007. Assessment of the effectiveness of nanofluids for single-phase and two-phase heat transfer in micro-channels. *International Journal of Heat and Mass Transfer*, 50(3-4), pp.452-463.

- Lee, J., Kim, J. and Park, H., 2019. Numerical simulation of the power-based efficiency in vanadium redox flow battery with different serpentine channel size. *International Journal of Hydrogen Energy*, 44(56), pp.29483-29492.
- Levac, M.J., Soliman, H.M. and Ormiston, S.J., 2011. Three-dimensional analysis of fluid flow and heat transfer in single-and two-layered micro-channel heat sinks. *Heat and mass transfer*, 47(11), pp.1375-1383.
- Lewis, R.W., Nithiarasu, P. and Seetharamu, K.N., 2004. *Fundamentals of the finite element method for heat and fluid flow*. John Wiley & Sons.
- Li, R. and Sudjianto, A., 2005. Analysis of computer experiments using penalized likelihood in Gaussian Kriging models. *Technometrics*, 47(2), pp.111-120.
- Li, X., Hao, X., Chen, Y., Zhang, M. and Peng, B., 2013, April. Multi-objective optimizations of structural parameter determination for serpentine channel heat sink. In *European Conference on the Applications of Evolutionary Computation* (pp. 449-458). Springer, Berlin, Heidelberg.
- Li, Y.F., Xia, G.D., Ma, D.D., Jia, Y.T. and Wang, J., 2016. Characteristics of laminar flow and heat transfer in microchannel heat sink with triangular cavities and rectangular ribs. *International Journal of Heat and Mass Transfer*, 98, pp.17-28.
- Liou, T.M., Wang, C.S. and Wang, H., 2018. Nusselt number and friction factor correlations for laminar flow in parallelogram serpentine micro heat exchangers. *Applied Thermal Engineering*, 143, pp.871-882.
- Liu, C., Teng, J.T., Chu, J.C., Chiu, Y.L., Huang, S., Jin, S., Dang, T., Greif, R. and Pan, H.H., 2011. Experimental investigations on liquid flow and heat transfer in rectangular microchannel with longitudinal vortex generators. *International Journal of Heat and Mass Transfer*, 54(13-14), pp.3069-3080.
- Manca, O., Nardini, S. and Ricci, D., 2012. A numerical study of nanofluid forced convection in ribbed channels. *Applied Thermal Engineering*, 37, pp.280-292.
- Marano, G.C., Greco, R. and Sgobba, S., 2010. A comparison between different robust optimum design approaches: application to tuned mass dampers. *Probabilistic Engineering Mechanics*, 25(1), pp.108-118.

- Marzec, K. and Kucaba-Pietal, A., 2014. Heat transfer characteristic of an impingement cooling system with different nozzle geometry. In *Journal of Physics: Conference Series* (Vol. 530, No. 1, p. 012038). IOP Publishing.
- Matheron, G., 1963. Principles of geostatistics. *Economic geology*, 58(8), pp.1246-1266.
- McHale, J.P. and Garimella, S.V., 2010. Heat transfer in trapezoidal microchannels of various aspect ratios. *International Journal of Heat and Mass Transfer*, 53(1-3), pp.365-375.
- Mehendale, S.S., Jacobi, A.M. and Shah, R.K., 2000. Fluid flow and heat transfer at micro-and meso-scales with application to heat exchanger design.
- Meng, X., Zhu, J., Wei, X. and Yan, Y., 2018. Natural convection heat transfer of a straight-fin heat sink. *International Journal of Heat and Mass Transfer*, 123, pp.561-568.
- Merriam Webster, Retrieved 11/02/2020, from <https://www.merriam-webster.com/dictionary/optimization>
- Merriam-Webster.com Dictionary, *Electronic resource*. URL: <https://www.merriam-webster.com/dictionary/optimization>. Accessed 4 Dec. 2020.
- Mo, H.L., Ye, C.M., Gadepalli, V.V. and Lin, C.X., 2005, January. Numerical modeling of gas flow in square microchannels. In *International Conference on Nanochannels, Microchannels, and Minichannels* (Vol. 41855, pp. 405-409).
- Mohammadi, H., 2016. *Kriging-based black-box global optimization: analysis and new algorithms* (Doctoral dissertation, Ecole Nationale Supérieure des Mines de Saint-Etienne).
- Mohammed, H.A., Gunnasegaran, P. and Shuaib, N.H., 2011. Influence of channel shape on the thermal and hydraulic performance of microchannel heat sink. *International Communications in Heat and Mass Transfer*, 38(4), pp.474-480.
- Montgomery, D.C., 2017. *Design and analysis of experiments*. John Wiley & sons.
- Moss, R.W., Shire, G.S.F., Henshall, P., Eames, P.C., Arya, F. and Hyde, T., 2017. Optimal passage size for solar collector microchannel and tube-on-plate absorbers. *Solar Energy*, 153, pp.718-731.

- Mudawar, I., 2011. Two-phase microchannel heat sinks: theory, applications, and limitations. *Journal of electronic packaging*, 133(4).
- Murshed, S.S. and De Castro, C.N., 2017. A critical review of traditional and emerging techniques and fluids for electronics cooling. *Renewable and Sustainable Energy Reviews*, 78, pp.821-833.
- Murshed, S.S. ed., 2016. *Electronics Cooling*. BoD–Books on Demand.
- Muthu, P., Dhanalakshmi, V. and Sankaranarayanan, K., 2010. Design and manufacturing tolerances optimization with quality loss functions. *International Journal of Advanced Operations Management*, 2(1-2), pp.90-107.
- Naphon, P. and Nakharintr, L., 2013. Heat transfer of nanofluids in the mini-rectangular fin heat sinks. *International Communications in Heat and Mass Transfer*, 40, pp.25-31.
- Narumanchi, S.V., Hassani, V. and Bharathan, D., 2005. *Modeling single-phase and boiling liquid jet impingement cooling in power electronics* (No. NREL/TP-540-38787). National Renewable Energy Lab.(NREL), Golden, CO (United States).
- NEOS Guide website 2020. Types of Optimization Problems. [Online]. [Accessed 10 July 2020]. Available from: <https://neos-guide.org/optimization-tree>.
- Neto, D.M., Oliveira, M.C., Alves, J.L. and Menezes, L.F., 2019. Numerical study on the formability of metallic bipolar plates for proton exchange membrane (PEM) fuel cells. *Metals*, 9(7), p.810.
- Nonino, C., Savino, S., Del Giudice, S. and Mansutti, L., 2009. Conjugate forced convection and heat conduction in circular microchannels. *International Journal of Heat and Fluid Flow*, 30(5), pp.823-830.
- Oberkampf, W.L. and Trucano, T.G., 2002. Verification and validation in computational fluid dynamics. *Progress in aerospace sciences*, 38(3), pp.209-272.
- Öksüz, S., 2014. Characterization of spray cooling for electronic devices (Master's thesis, MSc thesis, Middle East Technical University).
- O'Malley, R.E., 2014. *Historical developments in singular perturbations*. Cham, Switzerland: Springer International Publishing.

- Palm, S. J., et al. (2006). "Heat transfer enhancement with the use of nanofluids in radial flow cooling systems considering temperature-dependent properties." *26(17-18): 2209-2218.*
- Papadrakakis, M., Lagaros, N.D. and Plevris, V., 2005. Design optimization of steel structures considering uncertainties. *Engineering Structures, 27(9), pp.1408-1418.*
- Parkinson, A.R., Balling, R. and Hedengren, J.D., 2013. Optimization methods for engineering design. *Brigham Young University, 5, p.11.*
- Peles, Y., Koşar, A., Mishra, C., Kuo, C.J. and Schneider, B., 2005. Forced convective heat transfer across a pin fin micro heat sink. *International Journal of Heat and Mass Transfer, 48(17), pp.3615-3627.*
- Phillips, R.J., Glicksman, L.R. and Larson, R., Massachusetts Institute of Technology, 1990. *Forced-convection, liquid-cooled, microchannel heat sinks.* U.S. Patent 4,894,709.
- Pi, Y., Chen, J., Miao, M., Jin, Y. and Wang, W., 2018. A fast and accurate temperature prediction method for microfluidic cooling with multiple distributed hotspots. *International Journal of Heat and Mass Transfer, 127, pp.1223-1232.*
- Pryor, R.W., 2011. Multiphysics modeling using COMSOL®: a first principles approach. Jones & Bartlett Publishers.
- Qiu, L., Dubey, S., Choo, F.H. and Duan, F., 2015. Recent developments of jet impingement nucleate boiling. *International Journal of Heat and Mass Transfer, 89, pp.42-58.*
- Qu, W. and Mudawar, I., 2002. Analysis of three-dimensional heat transfer in micro-channel heat sinks. *International Journal of heat and mass transfer, 45(19), pp.3973-3985.*
- Qu, W., Mala, G.M. and Li, D., 2000. Heat transfer for water flow in trapezoidal silicon microchannels. *International Journal of Heat and Mass Transfer, 43(21), pp.3925-3936.*
- Raimondi, N.D.M., Prat, L., Gourdon, C. and Tasselli, J., 2014. Experiments of mass transfer with liquid–liquid slug flow in square microchannels. *Chemical Engineering Science, 105, pp.169-178.*
- Rao, S.S., 2019. *Engineering optimization: theory and practice.* John Wiley & Sons.

- Rapp, B.E., 2016. *Microfluidics: modeling, mechanics and mathematics*. William Andrew.
- Reddy, S.R., Abdoli, A., Dulikravich, G.S., Pacheco, C.C., Vasquez, G., Jha, R., Colaco, M.J. and Orlande, H.R., 2017. Multi-objective optimization of micro pin-fin arrays for cooling of high heat flux electronics with a hot spot. *Heat Transfer Engineering*, 38(14-15), pp.1235-1246.
- Rhinehart, R.R., 2018. *Engineering Optimization: Applications, Methods and Analysis*. John Wiley & Sons.
- Rohsenow, W.M., Hartnett, J.P. and Cho, Y.I., 1998. *Handbook of heat transfer* (Vol. 3). New York: McGraw-Hill.
- Romero, V.J., Swiler, L.P. and Giunta, A.A., 2004. Construction of response surfaces based on progressive-lattice-sampling experimental designs with application to uncertainty propagation. *Structural Safety*, 26(2), pp.201-219.
- Ruiz, M., 2015. *Characterization of Single Phase and Two Phase Heat and Momentum Transport in a Spiraling Radial Inflow Microchannel Heat Sink* (Doctoral dissertation, UC Berkeley).
- Sachdeva, R.C., 2009. *Fundamentals of Engineering Heat and Mass Transfer (SI Units)*. New Age International Publishers.
- Sadrehaghghi, I., 2017. Mesh generation in CFD. *CFD Open Ser*, 151.
- Sahinidis, N.V., 2004. Optimization under uncertainty: state-of-the-art and opportunities. *Computers & Chemical Engineering*, 28(6-7), pp.971-983.
- Sakanova, A. and Tseng, K.J., 2018. Comparison of pin-fin and finned shape heat sink for power electronics in future aircraft. *Applied Thermal Engineering*, 136, pp.364-374.
- Salman, B.H., Mohammed, H.A. and Kherbeet, A.S., 2014. Numerical and experimental investigation of heat transfer enhancement in a microtube using nanofluids. *International Communications in Heat and Mass Transfer*, 59, pp.88-100.
- Sarangi, S., Bodla, K.K., Garimella, S.V. and Murthy, J.Y., 2014. Manifold microchannel heat sink design using optimization under uncertainty. *International Journal of Heat and Mass Transfer*, 69, pp.92-105.
- Shabany, Y., 2009. *Heat transfer: thermal management of electronics*. CRC press.

- Shah, R.K. and London, A.L., 2014. Laminar flow forced convection in ducts: a source book for compact heat exchanger analytical data. Academic press.
- Shahbaz, M., Han, Z.H., Song, W.P. and Aizud, M.N., 2016, January. Surrogate-based robust design optimization of airfoil using inexpensive Monte Carlo method. In *2016 13th International Bhurban Conference on Applied Sciences and Technology (IBCAST)* (pp. 497-504). IEEE.
- Shi, L., Han, Z.H., Shahbaz, M. and Song, W.P., 2016. Surrogate-based robust airfoil optimization under aleatory flight condition and geometric uncertainties. In *54th AIAA Aerospace Sciences Meeting* (p. 0810).
- Shi, X., Li, S., Mu, Y. and Yin, B., 2019. Geometry parameters optimization for a microchannel heat sink with secondary flow channel. *International Communications in Heat and Mass Transfer*, 104, pp.89-100.
- Sidik, N.A.C., Muhamad, M.N.A.W., Japar, W.M.A.A. and Rasid, Z.A., 2017. An overview of passive techniques for heat transfer augmentation in microchannel heat sink. *International Communications in Heat and Mass Transfer*, 88, pp.74-83.
- Singh, R., Akbarzadeh, A. and Mochizuki, M., 2009. Sintered porous heat sink for cooling of high-powered microprocessors for server applications. *International Journal of Heat and Mass Transfer*, 52(9-10), pp.2289-2299.
- Singh, S., Singh, A. and Chander, S., 2019. Thermal performance of a fully developed serpentine wavy channel solar air heater. *Journal of Energy Storage*, 25, p.100896.
- Skandakumaran, P., Ortega, A., Jamal-Eddine, T. and Vaidyanathan, R., 2004, June. Multi-layered SiC microchannel heat sinks-modeling and experiment. In *The Ninth Intersociety Conference on Thermal and Thermomechanical Phenomena In Electronic Systems (IEEE Cat. No. 04CH37543)* (Vol. 1, pp. 352-360). IEEE.
- Sleiti, A.K. and Kapat, J.S., 2006. An experimental investigation of liquid jet impingement and single-phase spray cooling using polyalphaolefin. *Experimental heat transfer*, 19(2), pp.149-163.
- Sohel, M.R., Khaleduzzaman, S.S., Saidur, R., Hepbasli, A., Sabri, M.F.M. and Mahbubul, I.M., 2014. An experimental investigation of heat transfer enhancement of a minichannel heat sink using Al₂O₃-H₂O nanofluid. *International Journal of Heat and Mass Transfer*, 74, pp.164-172.

- Sohel, M.R., Saidur, R., Sabri, M.F.M., Kamalisarvestani, M., Elias, M.M. and Ijam, A., 2013. Investigating the heat transfer performance and thermophysical properties of nanofluids in a circular micro-channel. *International Communications in Heat and Mass Transfer*, 42, pp.75-81.
- Southall, D., Le Pierres, R. and Dewson, S.J., 2008, June. Design considerations for compact heat exchangers. In *Proceedings of ICAPP* (Vol. 8, pp. 8-12). ICAPP.
- Sui, Y., Lee, P.S. and Teo, C.J., 2011. An experimental study of flow friction and heat transfer in wavy microchannels with rectangular cross section. *International journal of thermal sciences*, 50(12), pp.2473-2482.
- Sui, Y., Teo, C.J., Lee, P.S., Chew, Y.T. and Shu, C., 2010. Fluid flow and heat transfer in wavy microchannels. *International Journal of Heat and Mass Transfer*, 53(13-14), pp.2760-2772.
- Sundar, L. S., et al. (2017). "Hybrid nanofluids preparation, thermal properties, heat transfer and friction factor—a review." 68: 185-198.
- Swiler, L.P. and Giunta, A.A., 2007. *Aleatory and Epistemic Uncertainty Quantification for Engineering Applications* (No. SAND2007-4655C). Sandia National Lab. (SNL-NM), Albuquerque, NM (United States); Sandia National Laboratories, Washington, DC.
- Tabatabaian, M., 2015. *COMSOL5 for Engineers*. Stylus Publishing, LLC.
- Tian, W., Heo, Y., De Wilde, P., Li, Z., Yan, D., Park, C.S., Feng, X. and Augenbroe, G., 2018. A review of uncertainty analysis in building energy assessment. *Renewable and Sustainable Energy Reviews*, 93, pp.285-301.
- Toh, K.C., Chen, X.Y. and Chai, J.C., 2002. Numerical computation of fluid flow and heat transfer in microchannels. *International Journal of Heat and Mass Transfer*, 45(26), pp.5133-5141.
- Topuz, T., 2007, November. Quality assessment of data-based metamodells for multi-objective aeronautic design optimization. In *Second International Conference on CFD in the Minerals and Process Industries, CSIRO, Melbourne, Australia*.
- Tuckerman, D. B. and R. F. W. Pease (1981). "High-performance heat sinking for VLSI." *IEEE Electron device letters* 2(5): 126-129.
- Tullius, J.F., Vajtai, R. and Bayazitoglu, Y., 2011. A review of cooling in microchannels. *Heat Transfer Engineering*, 32(7-8), pp.527-541.

- Vafai, K. and L. Zhu (1999). "Analysis of two-layered micro-channel heat sink concept in electronic cooling." *International Journal of Heat and Mass Transfer* 42(12): 2287-2297.
- Vamvatsikos, D., 2014. Seismic performance uncertainty estimation via IDA with progressive accelerogram-wise latin hypercube sampling. *Journal of Structural Engineering*, 140(8), p.A4014015.
- Versteeg, H.K. and Malalasekera, W., 2007. An introduction to computational fluid dynamics: the finite volume method. Pearson education.
- Vu, K.K., d'Ambrosio, C., Hamadi, Y. and Liberti, L., 2017. Surrogate-based methods for black-box optimization. *International Transactions in Operational Research*, 24(3), pp.393-424.
- Wang, C.C., 2017. A quick overview of compact air-cooled heat sinks applicable for electronic cooling—recent progress. *Inventions*, 2(1), p.5.
- Wang, C.C., Lo, J., Lin, Y.T. and Liu, M.S., 2002. Flow visualization of wave-type vortex generators having inline fin-tube arrangement. *International journal of heat and mass transfer*, 45(9), pp.1933-1944.
- Wang, H., Chen, Z. and Gao, J., 2016. Influence of geometric parameters on flow and heat transfer performance of micro-channel heat sinks. *Applied Thermal Engineering*, 107, pp.870-879.
- Wang, Q., Chen, Q., Wang, L., Zeng, M., Huang, Y. and Xiao, Z., 2007. Experimental study of heat transfer enhancement in narrow rectangular channel with longitudinal vortex generators. *Nuclear Engineering and Design*, 237(7), pp.686-693.
- Wang, Y. and Yu, X., 2006, November. Surrogate-based Aerodynamic Optimization under Uncertainty. In *The Fourth China-Japan-Korea Joint Symposium on Optimization of Structural and Mechanical Systems Kunming Nov* (pp. 6-9).
- Wei, X. and Joshi, Y., 2003. Optimization study of stacked micro-channel heat sinks for micro-electronic cooling. *IEEE transactions on components and packaging technologies*, 26(1), pp.55-61.
- Wikipedia https://en.wikipedia.org/wiki/File:AMD_heatsink_and_fan.jpg
- Woodford, C., 2017. Explainthatstuff.
- Wu, J.M. and Tao, W.Q., 2008. Numerical study on laminar convection heat transfer in a rectangular channel with longitudinal vortex generator. Part A:

- Verification of field synergy principle. *International Journal of Heat and Mass Transfer*, 51(5-6), pp.1179-1191.
- Wu, J.M. and Tao, W.Q., 2008. Numerical study on laminar convection heat transfer in a channel with longitudinal vortex generator. Part B: Parametric study of major influence factors. *International Journal of Heat and Mass Transfer*, 51(13-14), pp.3683-3692.
- Xu, B., Ooti, K.T., Wong, N.T. and Choi, W.K., 2000. Experimental investigation of flow friction for liquid flow in microchannels. *International Communications in Heat and Mass Transfer*, 27(8), pp.1165-1176.
- Y. Joshi and Z. Wan, 2018. "Single-and Multiphase Flow for Electronic Cooling," Handbook of Thermal Science and Engineering, pp. 1973-2029.
- Yazicioğlu, B. and Yüncü, H., 2007. Optimum fin spacing of rectangular fins on a vertical base in free convection heat transfer. *Heat and Mass Transfer*, 44(1), pp.11-21.
- Yu, S.H., Lee, K.S. and Yook, S.J., 2010. Natural convection around a radial heat sink. *International Journal of Heat and Mass Transfer*, 53(13-14), pp.2935-2938.
- Yu, W., France, D.M., Routbort, J.L. and Choi, S.U., 2008. Review and comparison of nanofluid thermal conductivity and heat transfer enhancements. *Heat transfer engineering*, 29(5), pp.432-460.
- Yunus, A.C., 2010. *Fluid Mechanics: Fundamentals And Applications (Si Units)*. Tata McGraw Hill Education Private Limited.
- Zhang Y., 2018. *Heat Pipes: Design, Applications and Technology*. Nova Science Publishers.
(https://books.google.co.uk/books/about/Heat_Pipes.html?id=htrytgEACA&source=kp_book_description&redir_esc=y)
- Zhang, J.F., Jia, L., Yang, W.W., Taler, J. and Oclon, P., 2019. Numerical analysis and parametric optimization on flow and heat transfer of a microchannel with longitudinal vortex generators. *International Journal of Thermal Sciences*, 141, pp.211-221.
- Zhang, S., Sun, Y., Cheng, Y., Huang, P., Oladokun, M.O. and Lin, Z., 2018. Response-surface-model-based system sizing for Nearly/Net zero energy buildings under uncertainty. *Applied Energy*, 228, pp.1020-1031.

- Zhao, J., Huang, S., Gong, L. and Huang, Z., 2016. Numerical study and optimizing on micro square pin-fin heat sink for electronic cooling. *Applied Thermal Engineering*, 93, pp.1347-1359.
- Zhao, K., Gao, Z.H. and Huang, J.T., 2014. Robust design of natural laminar flow supercritical airfoil by multi-objective evolution method. *Applied Mathematics and Mechanics*, 35(2), pp.191-202.
- Zhao, K., Gao, Z.H. and Huang, J.T., 2014. Robust design of natural laminar flow supercritical airfoil by multi-objective evolution method. *Applied Mathematics and Mechanics*, 35(2), pp.191-202.
- Zikanov, O., 2019. *Essential computational fluid dynamics*. John Wiley & Sons.